Topology and volume dependence in $SU(N)$ Yang-Mills theories

Memoria de Tesis Doctoral realizada por

Jorge Luis Dasilva Golán

presentada ante el Departamento de Física Teórica
de la Universidad Autónoma de Madrid
para optar al Título de Doctor en Física Teórica

Tesis Doctoral dirigida por **Margarita García Pérez**,
Cientifica Titular del Instituto de Física Teórica

Departamento de Física Teórica
Universidad Autónoma de Madrid

Instituto de Física Teórica UAM-CSIC

Junio de 2023

Contents

Acknowledgements

I would be lying if I said that writing this dissertation and its contents has been an easy task, but I would also be lying if I did not say that it has been very rewarding. These five years have been a mixture of joys and worries that have ended with the work you are about to read. Of course, I have not done it alone, and there are many people who have helped me along the way, and I would like to thank them.

First of all, I would like to thank **Margarita García Pérez**, my supervisor, for being an excellent guide during these years of Ph.D. Since the first meeting we had during the IFT Master, when you introduced me to the concept of Quantum Field Theory in the Lattice, I was deeply fascinated by the subject. I thought I could not like Quantum Field Theory more than I already did, and there was one of the most intriguing formulations I had ever seen. Since that day you have helped me more than I can say. Thank you for the physical intuition I learned from you in so many discussions, for your work and patience, and most of all for always being there.

I would like to thank **Alberto Ramos** for so many fruitful discussions, for providing me with a technical perspective on science and physics issues, and for being a great collaborator.

Quero agradecer aos meus pais, **José Luis** e **Mary Carmen**, e tomareime a licenza de facelo no meu segundo idioma nativo. Non existe palabras para describir todo o que vos teño que agradecer. Vós entregástesme todas as ferramentas que me trouxeron ata aquí, polo que este traballo é tamén voso. Agradézovos todas as horas de dedicación, a paciencia, as alegrías, os días sen durmir, as conversacións alentadoras e o esforzo. Aínda na distancia, non me faltastes xamais. Fixestes de min quen son hoxe. Moitas grazas!

Agradezco también a mis hermanos, **Gabriel** y **Adriana**. Hay un dicho en el refranero popular que dice que los hermanos son un tesoro, y aunque en muchos casos no es cierto, el mio se cumple con creces. Sois mis confidentes más grandes y me habéis ayudado de tantas maneras que es imposible enumerarlas. Hemos compartido risas, llantos, alegrías, desesperaciones, y secretos de una manera que solo nosotros entenderíamos. Sois dos de las personas más importantes en mi vida y no podría haber terminado esta etapa sin vosotros.

A mis hermanos putativos, **Loly** y **Larry**. Muchas gracias Larry por aportarme siempre esa visión crítica recubierta de un tono jocoso. Contigo cualquier conversación se vuelve interesante. Por otra parte, muchas gracias Loly por estar cuando más lo necesité. Hemos vivido tantas cosas en estos años que no puedo evitar contarte como una hermana mas; mi cabeza lo hace automáticamente. Eres y serás siempre mi compañera de locuras, de bailes y de cocina navideña. Gracias a los!

Agradezo aos meus avós **José**, **Emilia** e **Herminia**. Fixestes ata o imposible porque eu este aquí o día de hoxe. Brindástesme tanta axuda, e de tantas maneiras, que xamais podre devolvelo. Fixestes que na distancia sentíseme como na miña casa, e iso para min será sempre invaluable.

A mi madrina **Josefa** y mis tíos **Luis** y **Rosa**, por haberme acogido en su casa durante tanto tiempo, aún cuando eso significase una situación logística complicada. También agradezco a toda la familia que de alguna u otra manera han contribuido para que el día de hoy tenga escrita mi tesis doctoral, en especial a mis tíos/tías y a mis primos/primas.

Quiero tomarme un párrafo para agradecer especialmente a mis dos mejores amigos, **José** y **Fran**. **Pepe**, hemos vivido tantas cosas juntos que es imposible hacer un recuento. Alegrías, problemas, risas, llantos; hemos pasado por todo, hasta una cuarentena juntos. Muchas gracias por tantas conversaciones sobre la vida y sobre la física, aprendí mucho de ellas y las hecho de menos casi tanto como a ti. Eres de las personas mas brillantes que conozco y da por seguro que llevare siempre tu foto en mi cartera y tu frente en mi móvil. Despedirme de ti fue de las cosas más difíciles que he hecho en estos años, y aún en la distancia, te llevaré siempre en el corazón. **Francho**, eres probablemente la persona más graciosa que conozco y con la que mayor cantidad de gustos comparto. Música, cine, humor, F1, Leclerc. Muchas gracias por todo el apoyo durante estos años y por todo lo que me has enseñado, eres una de las personas mas brillantes que he conocido. No miento cuando digo que no ha habido un solo día en todos estos años en el que no me hayas sacado una carcajada. Me va a costar mucho despedirme de ti, pero llevaré siempre a ti y a tus frases de Lana del Rey en tonos pastel en el corazón. Juntos, habéis hecho que la familia que estaba a 8000 kilómetros de distancia estuviese tan cerca como estabais vosotros.

Durante el doctorado he hecho amigos que llevare por siempre conmigo. **Judit**, eres un sol de persona y me alegra haberte conocido. Me has aportado tanto conocimiento y seguridad en mi mismo que he logrado quererme y respetarme más de lo que lo hacía antes. **Llorenç**, has sido de las mejores cosas que me ha pasado en el despacho 312. Me has enseñado tanto y he aprendido tanto de ti, que tu amistad se ha convertido en un preciado tesoro. **Walter**, te has transformado sin duda mi pareja oficial de fiestas. Ya he perdido la cuenta de las veces que hemos desayunado en el Gago III como plan lamentable volviendo a casa. Aún más, contigo he vuelto a conectar con muchos de mis gustos Venezolanos y latinos. **Sergio**, eres sin duda de las personas mas graciosas que he conocido. Estoy tan acostumbrado a verte, por la medida baja, dos veces al día en mi despacho que los días que eso no ocurre siento que me falta algo. Muchas gracias por siempre sacarme una sonrisa aún cuando no me encontraba bien. **Alejandro**, es una lástima que no te conociese antes porque eres una de las mejores personas que me he encontrado en estos años. Muchas gracias por contagiarme con tu alegría y animo, y por siempre estar ahi cuando lo necesitaba. **Marta**, eres sin duda de las mejores personas que he tenido la suerte de conocer en Madrid. Has aportado a mi vida muchas ideas y puntos de vista fuera del ámbito físico-académico que me han hecho una persona mucho más integral. **Eduardo**, nos conocemos desde hace poco pero eres sin duda un genial compañero de despacho. Cuando se fueron Llorenc y José tenía miedo de la nueva convivencia, pero ese miedo era infundado porque eres una persona genial y con la que disfruto mucho conversando, tanto de física como de la vida. Quiero agradecer

por ultimo a **Juan David**, mi amigo en la distancia. Te quiero dar las gracias por todas las conversaciones, las risas, las noches en casa cocinando, viendo series, y escuchando musica. Tu ayuda ha significado muchísimo para mi durante todos estos años. A todos vosotros, y a todos las personas que he conocido a lo largo del doctorado en el IFT, gracias!

To my thesis brother **Pietro**. We made it! Thank you for so many encouraging conversations, for putting up with my problems, and for helping me become a better physicist. Also to my other "Reticulianos" friends, **Alessandro**, **Fernando** and **Claudio**, thank you for so many fruitful conversations. Thanks to the rest of the lattice group at IFT, it has been a very nice place to develop my Ph.D

Last but not least, I would like to thank all the **maintenance** and **administrative** staff at IFT, this institute could not run without you!

List of publications

This thesis report is based on the following list of publications:

- E. I. Bribian, J. L. D. Golan, M. G. Perez, and A. Ramos, "Memory efficient finite volume schemes with twisted boundary conditions", *Eur. Phys. J. C* **81** no. 10, (2021) 951, arXiv:2107.03747 [hep-lat].
- J. L. D. Golan, M. G. Perez, and A. Ramos, "The SU(N) running coupling in the twisted gradient flow scheme and volume independence.", *PoS* **LATTICE2021** (2022) 310, arXiv:2111.13092 [hep-lat].
- J. Dasilva Golán and M. García Pérez, "SU(N) fractional instantons and the Fibonacci sequence", *JHEP* **12** (2022) 109, arXiv:2208.07133 [hep-th].
- J. L. Dasilva Golan and M. Garcia Perez, "SU(N) fractional instantons", *PoS* **LATTICE2022** (2023) 394, arXiv:2212.01264 [hep-th].

Resumen

En la presente memoria de tesis doctoral, estudiamos algunas implicaciones de la hipótesis *volume independence* para las teorías de Yang-Mills $SU(N)$. En particular, exploramos un esquema de renormalización de volumen finito que combina tres ingredientes principales: una constante de acoplo basada en el *gradient flow*, el uso de condiciones de contorno *twisted* y una geometría asimétrica, que para teorías gauge $SU(N)$ consiste en una caja en 4 dimensiones de tamaño $l^2 \times (Nl)^2$. Tanto el número de colores N como el flujo $\mathbf{Z}_N$ que atraviesa el toro son tomados dentro de la secuencia de Fibonacci, es decir, $N = F_n$ y $k = F_{n-2}$. Varios argumentos basados en trabajos anteriores indican que esta elección de condiciones de contorno evita el rompimiento de *volume independence* en el límite de N grande.

Argumentamos que este esquema tiene varias ventajas que lo hacen particularmente adecuado para determinar la constante de acoplamiento fuerte con alta precisión, incluyendo invariancia traslacional, una expansión analítica en la constante de acoplo y un gasto en memoria reducido en comparación con simulaciones en retículos simétricos, lo que permite un uso más eficiente de los actuales clusters de GPU. El esquema también es adecuado para extraer la dependencia en N del parámetro Λ en las teorías gauge puras $SU(N)$.

Probamos numéricamente el esquema determinando el parámetro Λ para tres valores de $N = 3$, 5, y 8. Mostramos que el uso de una geometría asimétrica no tiene un efecto significativo en el tamaño de las violaciones de escala, obteniendo valores $\Lambda^{N=3}_{\overline{\text{MS}}}\sqrt{8t_0} = 0.603(17)$ y $\Lambda^{N=5}_{\overline{\text{MS}}}/\sqrt{\sigma_0} = 0.560(21)$ compatibles con la literatura existente. Se discute en detalle el papel del *freezing* topológico, que es relevante para la determinación del acoplamiento en este esquema particular. También discutimos el papel del volumen físico como herramienta para explorar la dinámica no-perturbativa y general el crecimiento de la susceptibilidad topológica, interpretando algunas de las características topológicas observadas en términos de una aproximación de gas diluido basada en instantones de carga fraccionaria.

Dado que los instantones de carga fraccionaria desempeñan un papel importante en nuestras determinaciones, utilizamos métodos numéricos para estudiar nuevas soluciones de tipo instantón autodual en $\mathbf{R} \times \mathbf{T}^3$ con carga topológica fraccionaria $Q = 1/N$. Se obtienen en una caja con condiciones de contorno *twisted* con el número de colores y el flujo k escalados como se ha comentado anteriormente. Estas soluciones adquieren relevancia en una formulación hamiltoniana de la teoría gauge, donde representan sucesos de túnel entre vacíos inequivalentes, eliminando la degeneración entre sectores de flujo eléctrico presente en teoría de perturbaciones. Discutimos las propiedades de estas soluciones en el límite de N grande y evaluamos varios invariantes gauge como la densidad de acción o los operadores de Wilson y Polyakov.

Abstract

In the present thesis report, we study some implications of the volume independence hypothesis for $SU(N)$ Yang-Mills theories. In particular, we explore a finite volume renormalization scheme that combines three main ingredients: a coupling based on the gradient flow, the use of twisted boundary conditions and a particular asymmetric geometry, which for $SU(N)$ gauge theories consists of a hypercubic box of size $l^2 \times (Nl)^2$. Both the number of colors N and the 't Hooft $\mathbf{Z}_N$ flux piercing the torus are taken within the Fibonacci sequence, i.e. $N = F_n$ and $k = F_{n-2}$. Various arguments based on previous works indicate that this choice of twist avoids the breakdown of volume independence in the large N limit.

We argue that this scheme has several advantages that make it particularly suitable for precision determinations of the strong coupling constant in QCD, including translational invariance, an analytic expansion in the coupling and a reduced memory footprint compared to standard simulations on symmetric lattices, allowing for a more efficient use of current GPU clusters. The scheme is also suitable for extracting the N dependence of the Λ parameter of $SU(N)$ pure gauge theories.

We test the scheme numerically by determining the Λ parameter for three values of $N = 3$, 5, and 8. We show that the use of asymmetric geometry has no significant effect on the size of the scaling violations, obtaining values $\Lambda^{N=3}_{\overline{\text{MS}}}\sqrt{8t_0} = 0.603(17)$ and $\Lambda^{N=5}_{\overline{\text{MS}}}/\sqrt{\sigma_0} = 0.560(21)$ in good agreement with the existing literature. The role of topology freezing, which is relevant for the determination of the coupling in this particular scheme and for large N applications, is discussed in detail. We also discuss the role of the physical volume as a tool for exploring the non-perturbative dynamics and trigger the onset of the topological susceptibility, interpreting some of the observed topological features in terms of a dilute gas approximation based on fractional charge instantons.

Since fractional charge instantons play an important role in our particular setup, we use numerical methods to study new $SU(N)$ self-dual instanton-like solutions on $\mathbf{R} \times \mathbf{T}^3$ with fractional topological charge $Q = 1/N$. They are obtained on the twisted box with the number of colors and the k-flux scaled as commented before. These solutions become relevant on a Hamiltonian formulation of gauge theory, where they represent vacuum-to-vacuum tunneling events, lifting the degeneracy between electric flux sectors present in perturbation theory. We discuss the large N scaling properties of the solutions and evaluate various gauge invariant quantities such as the action density or the Wilson and Polyakov loop operators.

Introducción

El siglo XX fue sin duda uno de los momentos más importantes en el desarrollo teórico de la física tal y como la conocemos hoy en día, dando lugar a dos teorías sin precedentes: la mecánica cuántica y la relatividad especial.[1]

Por un lado, la mecánica cuántica representa un marcado abandono de la intuición clásica que había regido durante mucho tiempo nuestra comprensión del mundo. A diferencia de la física clásica, que asume el determinismo y la medición exacta, la mecánica cuántica nos enfrenta a la incertidumbre inherente y a resultados probabilísticos. También introduce la llamada dualidad onda-partícula, según la cual objetos cuánticos como los electrones y los fotones presentan propiedades tanto de onda como de partícula, un resultado inconcebible en el marco de las teorías clásicas. La relatividad especial, por su parte, retoma la vieja afirmación de Galileo de que las leyes de la física no cambian cuando los sistemas de referencia inerciales se mueven a velocidades constantes, pero la reformula de modo que la velocidad de la luz sea una constante fundamental. Este postulado fundamental conduce a consecuencias asombrosas como la dilatación del tiempo, la contracción de la longitud o la equivalencia de masa y energía. También conduce a una profunda comprensión de la interacción entre espacio y tiempo, que resultan ser dos caras de la misma moneda, y da lugar al concepto de espacio-tiempo cuatri-dimensional.

A partir de estas dos famosas y relevantes teorías, consideradas hoy en día los dos pilares de la física teórica moderna, se construyó un nuevo, potente y elegante marco teórico: la teoría cuántica de campos. Su papel central en nuestra comprensión de la naturaleza quedó establecido por su éxito en la descripción de fenómenos que van desde el mundo microscópico de la física de partículas hasta las escalas cosmológicas del universo primitivo. El principal cambio de paradigma consistió en dejar de pensar en las partículas como objetos puntuales y reinterpretarlas como excitaciones de campos cuánticos vibrantes que se extienden por el espacio-tiempo. De hecho, el desarrollo de la teoría cuántica de campos comenzó en la década de 1920 con el estudio de las interacciones entre la luz y los electrones, que en aquel momento estaban bien descritas a nivel clásico por la electrodinámica de Maxwell, pero que no describían los fenómenos cuánticos. Dado que el electromagnetismo puro es una teoría libre de un campo de espín 1 sin masa, la cuestión era si era posible construir una teoría de campos con espín 1 en el marco de la teoría cuántica de campos. La respuesta llegó en la década de 1950 con las teorías de Yang-Mills, uno de los avances más importantes para la física de partículas y de altas energías. La descripción de la electrodinámica como teoría de Yang-Mills condujo a la formulación de la electrodinámica cuántica, la primera teoría cuántica de campos abeliana plenamente desarrollada y basada en uno de los principios más importantes de la naturaleza: la invariancia gauge.

Hasta ese momento, era natural preguntarse si las teorías gauge de Yang-Mills podrían describir también otras fuerzas de la naturaleza, como la fuerza débil, responsable de la radiactividad, o la fuerza fuerte, que une protones y neutrones en

[1] Todas las referencias importantes para el contenido de esta introducción se dan en ch. 2.

los núcleos atómicos. Unos años más tarde, en 1954, se construyó la primera teoría gauge no abeliana para explicar la interacción fuerte, denominada cromodinámica cuántica debido a la introducción de un nuevo tipo de carga similar a la eléctrica, denominada carga de color.

Las ecuaciones de Yang-Mills para campos gauge abelianos y no abelianos son un complejo sistema de ecuaciones no lineales acopladas para las que sólo se conocen unas pocas soluciones exactas. Históricamente, una de las formas más accesibles de abordarlas ha sido la conocida teoría de perturbaciones, basada en realizar expansiones en torno a un pequeño parámetro para obtener resultados físicos hasta una incertidumbre dada. Esta técnica, combinada con el estudio de la electrodinámica cuántica, llevó a Richard Feynman a desarrollar su famosa notación de diagramas en la que el pequeño parámetro de expansión es la constante de acoplamiento que representa la interacción entre los campos.

Aunque esta técnica se aplicó con éxito a la electrodinámica cuántica, no ocurrió lo mismo con las interacciones fuertes. Mientras que las teorías abelianas se basan en campos cuya interacción crece con la energía, ocurre lo contrario con las teorías no abelianas, en las que los campos están fuertemente acoplados a bajas energías. En este sentido, las implicaciones físicas de baja energía de la interacción fuerte, correspondientes a la física nuclear y hadrónica, no pueden resolverse mediante la teoría de perturbaciones. Desafortunadamente, aunque las teorías de Yang-Mills proporcionan una manera matemáticamente formal de describir la interacción fuerte, todavía no existe una manera matemáticamente consistente de resolver las ecuaciones en el régimen de baja energía. Este es uno de los famosos problemas abiertos en matemáticas y física propuestos por el Instituto Clay.

Se propusieron dos marcos seminales para resolver el problema del espectro no perturbativo de la interacción fuerte. Aunque ambos trabajos nacieron inicialmente con la misma intención, acabaron siguiendo caminos diferentes.

Por un lado, 't Hooft publicó uno de sus trabajos más famosos en el que exploraba la posibilidad de extender el régimen fuertemente acoplado de las interacciones fuertes en términos de un pequeño parámetro distinto del acoplamiento. El objetivo era realizar expansiones en términos de $1/N$, donde N es el número de cargas de color de la teoría no abeliana, que en el caso de la cromodinámica cuántica es $N = 3$. Sorprendentemente, los diagramas se organizan en grupos ordenados topológicamente, y la expansión suprime de forma natural los que no se pueden dibujar en un plano. Por tanto, la principal contribución procede de los llamados diagramas planos, cuyo número crece exponencialmente en contraste con el número total de diagramas, que crece factorialmente. Se creía que estos diagramas podrían resumarse para obtener resultados analíticos a partir de las expansiones perturbativas, pero esto no fue posible y se descartó la idea de utilizar esta teoría planar para resolver las interacciones fuertes; no obstante, este trabajo pionero inició el estudio de las teorías gauge con un número arbitrariamente grande de colores. Resultó que la teoría es más fácil de manejar en este límite que para valores finitos de N, y el conocido límite de N grande se convirtió en una de las mejores opciones para obtener pistas e indicios sobre el comportamiento de las interacciones fuertes.

Como apunte, la invención del límite de gran N fue también un elemento clave en el descubrimiento de un sector de AdS que describe la supergravedad, conocido como la equivalencia Ads/CFT.

Por otro lado, Keneth Wilson propuso una discretización del espacio-tiempo como una red finita de puntos encerrados en un volumen físico finito. Las integrales divergentes habituales de la teoría cuántica de campos podrían calcularse, ya que la separación de la red y el volumen finito proporcionan un límite natural para las divergencias ultravioleta e infrarroja, respectivamente. En pocas palabras, ambos límites son reguladores naturales de la teoría discretizada. La formulación es equivalente a un sistema de mecánica estadística y, en consecuencia, puede resolverse mediante métodos numéricos como el método de Montecarlo. Wilson fue capaz de demostrar el confinamiento de quarks en la región de acoplamiento fuerte, mostrando que a grandes distancias el potencial que conecta dos quarks no dinámicos tiene un término lineal que crece con la distancia. Esto sentó las bases de lo que se conoció como teoría cuántica de campos en el retículo, el único área de investigación de la física teórica capaz de proporcionar resultados precisos y fiables para cantidades de interés fenomenológico relacionadas con la interacción fuerte.

Con el tiempo, ambos marcos se mezclaron, y el formalismo de la teoría de campos en el retículo comenzó a utilizarse para estudiar teorías de Yang-Mills en el límite N grande.

Una herramienta muy exitosa para estudiar las teorías de Yang-Mills es su formulación en un volumen finito. Entre los fenómenos interesantes que surgen del estudio de las teorías de Yang-Mills de volumen finito se encuentra la interacción entre los grados de libertad espaciales y de color que se produce cuando los campos están dotados de condiciones de contorno *twisted*. Estas condiciones de contorno se refieren al hecho de que los campos gauge en un toro deben ser periódicos sólo hasta una transformación gauge, un hecho que 't Hooft utilizó para demostrar la existencia de nuevos sectores topológicos parametrizados por el llamado tensor de torsión $n_{\mu\nu}$.

Una de las descripciones de volumen finito más famosas de las teorías gauge es la conocida reducción de Eguchi-Kawai, en la que muestran una interesante interacción entre grados de libertad espaciales y de color. Esta propuesta fue modificada posteriormente por González-Arroyo y Okawa en su famosa reducción Twisted Eguchi-Kawai, en la que reformularon la propuesta original para dotar a los campos gauge de condiciones de contorno *twisted*.

La interacción entre los grados de libertad de color y espaciales establece una conexión directa entre las teorías gauge de volumen finito con un *twist* no trivial y las teorías no conmutativas. Formulada por primera vez a nivel perturbativo, esta relación se manifiesta de forma no perturbativa a través de la dualidad de Morita, que establece que las teorías gauge $SU(N)$ sobre un toro *twisted* de tamaño l son físicamente equivalentes a una teoría no conmutativa $U(1)$ sobre un toro de longitud $\tilde{l}$ (combinando en cierto modo grados de libertad espaciales y de color) y un parámetro de no conmutatividad $\theta_{mu\nu}$ (fijado en términos del tensor de *twist* $n_{mu\nu}$). Este mapa conduce a la llamada hipótesis de *volume independence*. En pocas palabras, esta

hipótesis establece que los campos gauge con condiciones de contorno *twisted* en un toro finito de tamaño l tienen una dinámica controlada por una longitud efectiva $\tilde{l}$, que mezcla el tamaño de la caja y el número de colores en una cierta combinación, y al mismo tiempo postula una equivalencia entre diferentes teorías gauge $SU(N)$ con la misma longitud efectiva $\tilde{l}$ y parámetro de no conmutatividad fijo $\theta_{\mu\nu}$.

Debe subrayarse que el límite N grande tomado en la hipótesis de *volume independence* no es el límite N grande habitual de 't Hooft. En volumen infinito, el límite de N grande se toma con un acoplamiento *bare* de 't Hooft fijo $\lambda_0 = Ng_0^2$ llevando el número de colores N a infinito y al mismo tiempo llevando el acoplamiento *bare* g_0 a cero. Esto corresponde a un límite termodinámico en el que las condiciones de contorno se vuelven irrelevantes y la dependencia del parámetro de no conmutatividad desaparece. Por otra parte, para volúmenes finitos, el límite N grande se toma fijando la longitud efectiva $\tilde{l}$, lo que equivale a tomar el límite N grande fijando el acoplamiento renormalizado $\lambda(\tilde{l})$ en lugar del *bare*. Usando esta versión del límite N grande, conocido como límite N grande singular, los observables dependen no sólo del volumen efectivo $\tilde{l}$, sino que también dependen del parámetro de no conmutatividad.

Tomar el límite singular de N grande no está exento de dificultades. Para $n_{\mu\nu}$ y N genéricos, la independencia del volumen se rompe debido a la aparición de inestabilidades taquiónicas. Para evitarlas y tener un límite N grande bien definido, hay que hacer algunas elecciones específicas en el número de colores y en el tensor de *twist*. Sorprendentemente, una elección que evita al máximo la aparición de inestabilidades hace uso, de un modo que se detallará más adelante, de la secuencia de Fibonacci, lo que conduce a un valor del parámetro de no conmutatividad relacionado con la sección áurea.

La presente memoria de tesis está dedicada al estudio de algunas implicaciones físicas de la independencia de volumen utilizando técnicas de teoría de campos en el retículo. Estudiaremos tres teorías gauge diferentes basadas en los grupos gauge $SU(3)$, $SU(5)$ y $SU(8)$, así como algunas nuevas soluciones mínimas de las ecuaciones de movimiento de Yang-Mills.

La memoria está organizada de la siguiente manera. En el capítulo 2, se presentan algunos fundamentos generales sobre temas relacionados con el contenido de la tesis, como la formulación de campos gauge en el toro, el límite singular de N grande, la hipótesis de reducción de volumen e independencia de volumen, y algunas técnicas relacionadas con el procedimiento de renormalización, como la definición formal del *gradient flow* y el ajuste de escala en el retículo.

En el capítulo 3, presentaremos un nuevo esquema de renormalización motivado por la idea de independencia de volumen, llamado *twisted gradient flow*. El esquema mezcla tres ingredientes principales: un acoplamiento definido dentro del *gradient flow*, condiciones de contorno *twisted* para los campos gauge, y una geometría asimétrica. Como veremos, este esquema de renormalización es particularmente adecuado para cálculos perturbativos, por lo que en la segunda parte de la tesis nos centraremos en el estudio del acoplamiento usando *twisted gradient flow* para los tres grupos gauge presentados anteriormente. En particular, el capítulo 4

está dedicado exclusivamente al estudio de la teoría $SU(3)$ pura. Este caso es de crucial importancia ya que, como veremos, se ha demostrado que una determinación de muy alta precisión en el caso $SU(3)$ puro puede traducirse en una determinación de muy alta precisión del acoplamiento fuerte QCD, una cantidad clave para la fenomenología de altas energías. Además, existe un problema de consistencia en la determinación del parámetro Λ gauge puro entre los incluidos en el grupo FLAG, por lo que argumentaremos en este capítulo por qué creemos que el *twisted gradient flow* puede utilizarse sistemáticamente para precisar la incertidumbre en este cálculo y resolver esta tensión. El capítulo 5, por otro lado, está dedicado por completo al estudio de $SU(5)$ y $SU(8)$. Calcularemos el parámetro Λ en estos casos y estudiaremos su dependencia de N. Además, investigaremos el efecto de las condiciones de contorno *twisted* en los efectos de volumen finito.

Dado que las teorías Yang-Mills no abelianas tienen una estructura topológica no trivial, describiremos algunas implicaciones y características topológicas presentes en la descripción en volumen finito de la teoría. En el capítulo 6, estudiaremos la presencia y el efecto de un conocido problema de carácter topológico al que se enfrentan las simulaciones de teoría de campos en el retículo en el límite del continuo, conocido como *critical slowing down*, que es particularmente problemático para nuestro cálculo de la constante de acoplo. También presentaremos y justificaremos nuestras elecciones para evitar este problema. Por otra parte, el capítulo explora la dependencia del volumen en $\tilde{l}$ de algunos observables físicamente importantes como la susceptibilidad topológica.

En el capítulo 8 estudiaremos un tipo de solución de acción mínima muy especial, con la peculiaridad de poseer una carga topológica fraccionaria. Creemos que esta configuración tiene una fuerte influencia en nuestro cálculo de la constante de acoplo. La existencia de estas configuraciones se demostró hace tiempo, pero las únicas soluciones analíticas obtenidas hasta ahora son las abelianas de curvatura constante, que se vuelven autoduales sólo bajo ciertas condiciones. Analizaremos su escalado hacia el límite de N grande y estudiaremos algunos operadores invariantes gauge, como los operadores de Polyakov y Wilson. En la literatura se han obtenido otros tipos de soluciones para diferentes valores de *twist* y geometrías. La tesis termina con algunas conclusiones y futuras direcciones en el capítulo 9.

Part I

Preliminaries

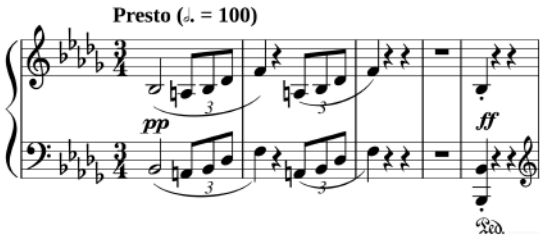

1 Introduction

The 20th century was undoubtedly one of the most important moments in the theoretical development of physics as we know it today, giving rise to two unprecedented and outstanding theories: quantum mechanics and special relativity.[1]

On the one hand, quantum mechanics represents a clear departure from the classical intuition that had long governed our understanding of the world. Unlike classical physics, which assumes determinism and exact measurement, quantum mechanics confronts us with inherent uncertainty and probabilistic results. It also introduces the so-called wave-particle duality, according to which quantum objects such as electrons and photons exhibit both wave and particle properties, a result inconceivable within the framework of classical theories. Special relativity, on the other hand, takes up Galileo's old statement that the laws of physics do not change when inertial reference systems move at constant speeds, but reformulates it so that the speed of light is a fundamental constant. This fundamental postulate leads to astonishing consequences such as time dilation, length contraction, or the equivalence of mass and energy. It also leads to a profound understanding of the interplay between space and time, which turn out to be two sides of the same coin, and gives rise to the concept of four-dimensional spacetime.

From these two famous and relevant theories, now considered the two pillars of modern theoretical physics, a new, powerful and elegant framework was constructed: quantum field theory. Its central role in our understanding of nature was established by its success in describing phenomena ranging from the microscopic world of particle physics to the cosmological scales of the early universe. The major paradigm shift was to stop thinking of particles as point-like objects and to reinterpret them as excitations of vibrating quantum fields that extend through spacetime. In fact, the development of quantum field theory began in the 1920s with the study of the interactions between light and electrons, which at that time were well described at the classical level by Maxwell's electrodynamics, but which did not describe quantum phenomena. Since pure electromagnetism is a free theory of a massless spin-1 field, the question was whether it was possible to construct a theory of spin-1 fields within the framework of quantum field theory. The answer

[1] All important references for the contents of this introduction are given in ch. 2.

came in the 1950s with the Yang-Mills theories, one of the most important breakthroughs for particle and high-energy physics. The description of electrodynamics as a Yang-Mills theory led to the formulation of quantum electrodynamics, the first fully developed abelian quantum field theory based on one of the most important principles of nature: gauge invariance.

Up to this point, it was natural to ask whether Yang-Mills gauge theories could also describe other forces in nature, such as the weak force, which is responsible for radioactivity, or the strong force, which binds protons and neutrons together in atomic nuclei. A few years later, in 1954, the first non-abelian gauge theory was constructed to explain the strong interaction, called quantum chromodynamics due to the introduction of a new type of charge similar to the electric one, called the color charge.

The Yang-Mills equations for abelian and non-abelian gauge fields are a complex system of coupled nonlinear equations for which only a few exact solutions are known. Historically, one of the most accessible ways of dealing with them has been the well-known perturbation theory, based on performing expansions around a small parameter to obtain physical results up to a given uncertainty. This technique, combined with the study of quantum electrodynamics, led Richard Feynman to develop his famous diagram notation in which the small expansion parameter is the coupling constant that represents the interaction between the fields.

Although this technique was successfully applied to quantum electrodynamics, the same was not quite possible for strong interactions. While abelian theories are based on fields whose interaction grows with energy, the opposite is true for non-abelian theories, in which the fields are strongly coupled at low energies. In this sense, the low-energy physics implications of the strong interaction, corresponding to nuclear and hadronic physics, cannot be resolved by means perturbation theory. Unfortunately, although Yang-Mills theories provide a mathematically formal way to describe the strong interaction, there is still no mathematically consistent way to solve the equations in the low energy regime. This is one of the famous open problems in mathematics and physics proposed by the Clay Institute.

Two seminal frameworks were proposed to solve the problem of the non-perturbative spectrum of the strong interaction. Although both works were initially born with the same intention, they ended up following different paths.

On one hand, 't Hooft published one of his most famous paper in which he explored the possibility of extending the strongly coupled regime of strong interactions in terms of a small parameter other than the coupling. The aim was to make expansions in terms of $1/N$, where N is the number of color charges of the non-abelian theory, which in the case of quantum chromodynamics is $N = 3$. Surprisingly, the diagrams were organized in topologically sorted groups, and the expansion naturally suppresses those that could not be drawn in a plane. Therefore, the main contribution came from the so-called planar diagrams, whose number grew exponentially in contrast to the total number of diagrams, which grew factorially. It was believed that these diagrams could be resumed to obtain analytical results from the perturbative expansions, but this was not possible and the idea of using this planar theory

to solve strong interactions was discarded; nevertheless, this pioneering work started the study of gauge theories with an arbitrary large number of colors. It turned out that the theory is easier to handle in this limit than for finite values of N, and the well-known large N limit became one of the best options for obtaining hints and clues about the behavior of the strong interactions. As an aside, the invention of the large N limit was also a key element in the discovery of an AdS sector describing supergravity, known as the Ads/CFT equivalence.

On the other hand, Keneth Wilson proposed a discretization of spacetime as a finite lattice of points enclosed in a finite physical volume. The usual divergent integrals of quantum field theory could be computed since the lattice spacing and the finite volume provide a natural cutoff for the ultraviolet and infrared divergences, respectively. In a nutshell, both cutoffs are natural regulators of the discretized theory. The formulation is equivalent to a statistical mechanics system, and as a consequence it can be solved by numerical methods such as the Monte Carlo algorithm. Wilson was able to demonstrate the confinement of quarks under in the strong coupling region, showing that at large distances the potential connecting two non-dynamical quarks has a linear term that grows with distance. This laid the foundation for what became known as lattice quantum field theory, the only research area in theoretical physics capable of providing accurate and reliable results for quantities of phenomenological interest related to the strong interaction.

Eventually, both frameworks were mixed, and the lattice field theory formalism began to be used to study Yang-Mills theories in the large N limit.

A very successful tool to study Yang-Mills theories is their formulation in a finite volume. Among the interesting phenomena arising from the study of finite volume Yang-Mills theories is the interplay between spatial and color degrees of freedom that occurs when fields are endowed with twisted boundary conditions. These boundary conditions refer to the fact that gauge fields on a torus need to be periodic only up to a gauge transformation, a fact that 't Hooft used to prove the existence of new topological sectors parametrized by the so-called twist tensor $n_{\mu\nu}$.

One of the most famous finite volume descriptions of gauge theories is the well-known Eguchi-Kawai reduction, in which they show an interesting interplay between spatial and color degrees of freedom. This proposal was later modified by Gonzalez-Arroyo and Okawa in his famous Twisted Eguchi-Kawai reduction, in which they reformulated the original proposal to endow the gauge fields with twisted boundary conditions.

The interplay between color and spatial degrees of freedom establishes a direct connection between finite volume gauge theories with a non-trivial twist and non-commutative theories. First formulated at the perturbative level, this relation is manifested non-perturbatively via Morita duality, which states that $SU(N)$ gauge theories on a twisted torus of size l are physically equivalent to a $U(1)$ non-commutative theory on a torus of length $\tilde{l}$ (combining in a certain way spatial and color degrees of freedom) and a non-commutativity parameter $\theta_{\mu\nu}$ (fixed in terms of the twist tensor $n_{\mu\nu}$). This mapping leads to the so-called volume independence hypothesis. In a nutshell, it states that gauge fields with twisted boundary conditions

in a finite torus of size l have dynamics controlled by an effective length $\tilde{l}$, which mixes the size of the box and the number of colors in a certain combination, and at the same time postulates an equivalence between different $SU(N)$ gauge theories with the same effective length $\tilde{l}$ and fixed non-commutativity parameter $\theta_{\mu\nu}$.

It should be emphasized that the large N limit assumed in the volume independence hypothesis is not the usual 't Hooft large N limit. In infinite volume, the large N limit is taken at fixed 't Hooft bare coupling $\lambda_0 = Ng_0^2$ by taking the number of colors N to infinity and at the same time taking the bare coupling g_0 to zero. This corresponds to a thermodynamic limit where the boundary conditions become irrelevant and the dependence on the non-commutativity parameter vanishes. On the other hand, for finite volumes, the large N limit is taken by fixing the effective length $\tilde{l}$, which is equivalent to taking the large N limit by fixing the renormalized coupling $\lambda(\tilde{l})$ instead of the bare one. Using this version of the large N limit, known as singular large N limit, observables depend not only on the effective volume $\tilde{l}$, but also depend on the non-commutativity parameter.

Taking the singular large N limit is not free of difficulties. For generic $n_{\mu\nu}$ and N, volume independence breaks down due to the appearance of tachyonic instabilities. In order to avoid them and to have a well-defined large N limit, some specific choices have to be made on the number of colors and on the twist tensor. Remarkably, a choice that maximally avoids the appearance of instabilities makes use, in a way to be detailed later on, of the Fibonacci sequence, leading to a value of the non-commutativity parameter related to the Golden ratio.

The present thesis report is devoted to the study of some physical implications of volume independence using lattice field theory techniques. We will study three different gauge theories based on the gauge groups $SU(3)$, $SU(5)$, and $SU(8)$, as well as some new minimal solutions of the Yang-Mills equations of motion for large values of N.

The report is organized as follows. In chapter 2, we present some general foundations on topics related to the content of the thesis, such as the formulation of gauge fields on the torus, the singular large N limit, the volume reduction and volume independence hypothesis, and some techniques related to the renormalization procedure, such as the formal definition of the gradient flow and the lattice scale setting.

In chapter 3, we present a new renormalization scheme motivated by the idea of volume independence, called twisted gradient flow. The scheme mixes three main ingredients: a coupling defined within the gradient flow, twisted boundary conditions for the gauge fields, and an asymmetric geometry. As we will see, this renormalization scheme is particularly suitable for perturbative calculations, so in the second part of the thesis we will focus on the study of the twisted gradient flow running coupling for the three gauge groups presented above. In particular, chapter 4 is devoted exclusively to the study of the pure $SU(3)$ theory. This case is of crucial importance since, as we will see, it has been shown that a very high precision determination in the pure $SU(3)$ case can be translated into a very high precision determination of the QCD strong coupling, a key quantity for high-energy

phenomenology. In addition, there is a consistency problem in the determination of the pure gauge Λ parameter among those included in the flavor lattice average group FLAG, so we will argue in this chapter why we believe that twisted gradient flow can be used systematically to pin down the uncertainty in this calculation and resolve this tension. Chapter 5, on the other hand, is devoted entirely to the study of $SU(5)$ and $SU(8)$. We will compute the Λ parameter in these cases and study their N dependence. In addition, we will investigate the effect of twisted boundary conditions on finite volume effects.

Since non-abelian Yang-Mills theories have a non-trivial topological structure, we will describe some implications and features of topological nature present in the finite volume description of the theory when using lattice field theory techniques. In chapter 6, we study the presence and effect of a well-known problem of a topological character that lattice field theory simulations face in the continuum limit, known as critical slowing down, which is particularly problematic for our coupling prescription. We also present and justify our choices to circumvent this problem. On the other hand, ch.7 explores the volume dependence on $\tilde{l}$ of some physically important observables such as the topological susceptibility.

In chapter 8 we study a very special minimal action solution that has the peculiarity of having a fractional topological charge. We believe that this configuration has a strong influence on the running of the coupling in our particular setup. The existence of these configurations was proved long ago, but the only analytic solutions obtained so far are constant curvature abelian ones, which become self-dual only under certain conditions. We analyze their scaling towards the large N limit and study some gauge invariant operators such as the Polyakov and Wilson loops. Other types of solutions have been obtained in the literature for different values of twist and geometries. The thesis ends with some conclusions and future directions in chapter 9.

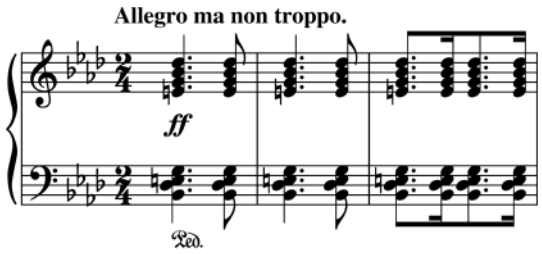

2 Foundations

2.1 Motivation

The use of finite volume descriptions to study the dynamics of non-abelian gauge theories has been very fruitful. In the continuum, the study of $SU(N)$ gauge fields on the hypertorus was initiated by 't Hooft [1–3]. On a small volume, asymptotic freedom guarantees that the theory is weakly coupled and perturbation theory holds. One of the main differences with respect to the infinite volume setup is that in small volumes boundary conditions matter and can significantly influence the behavior of gauge fields; in particular, the choice of boundary conditions determines the allowed field configurations and the resulting spectrum of physical states [1]. In fact, 't Hooft introduced in ref. [1] the notion of twisted boundary conditions, which allowed him to define electric and magnetic fluxes in a gauge invariant way, proving the existence of new topological classes parameterized by the so-called twist tensor $n_{\mu\nu}$.

Also on the lattice, finite volume schemes have been commonly used. The volume is used, for instance, to set the scale for the running of the coupling constant, following the ideas of finite size scaling, and in the same context it can be used to trigger the transition from the perturbative to non-perturbative domains of the theory. As the amount of work done following these ideas is huge, the goal of this chapter is to introduce all the important topics related to these frameworks, with special attention to the interplay of color and spatial degrees of freedom.

The chapter is structured as follows. We start in sec. 2.2.1 with a general description of the 't Hooft large N limit, and in sec. 2.2.2 we go through the factorization properties, the classical interpretation, and the birth of the so-called master field. In addition, insec. 2.2.2 we describe a physical realization of the master field, known as the Eguchi-Kawai (EK) reduction [4], and we present in sec. 2.3 the so-called twisted Eguchi-Kawai (TEK) reduction [5, 6], a modification that aims to solve the breaking of one of the hypothesis required for the original reduction to work. We combine all these ideas to study the hypothesis of volume independence in sec. 2.3, where we also explain the peculiar large N limit used in this thesis report, called the singular large N limit [7–10]. Finally, in sec. 2.4 we present the general method used to define the coupling constant, known as gradient flow [11–14] and some related technicalities such as the lattice scale setting.

2.2 't Hooft large N limit

2.2.1 Generalities

The study of gauge theories in the large N limit was first proposed by 't Hoof in 1970, taking $1/N$ as the expansion parameter of the strong interactions in the non-perturbative regime [15], since at low energies the coupling grows and cannot be used as a parameter for the perturbative expansion. For a complete and technical review of gauge theories in the large N limit, see [16]. In this section we will follow the discussion of that review, highlighting important features and results.

The 't Hooft large N limit is obtained by considering $SU(N)$ gauge theories with an arbitrarily large number of colors $N \to \infty$, and at the same time taking the bare coupling $g_0 \to 0$ in such a way that the combination $\lambda_0 \equiv N g_0^2$ is kept constant, known as the 't Hooft coupling. In the original proposal, the number of flavors n_f does not scale with N, so internal corrections from fermion loops are suppressed and quarks are naturally quenched in this limit.

The 2-loop expansion of the β function with respect to the 't Hooft coupling λ_0 is then

$$\beta(\lambda_0) \equiv \frac{d\lambda_0}{d\log\mu^2} = -\frac{11}{24\pi^2}\lambda_0^2 - \frac{17}{192\pi^4}\lambda_0^3 + \mathcal{O}(\lambda_0^4). \tag{2.1}$$

The 2 universal coefficients (i.e. scheme independent) of equation 2.1 are independent of the specific value of N. It has been shown that, at least in the MS scheme, the dependence of next to leading order coefficients is rather small and tends to become N independent very quickly [17].

One of the key simplifications of the large N theory comes from its insensitivity to non-planar diagrams, i.e. diagrams that cannot be drawn on a plane. The counting rules of the large N theory are such that non-planar diagrams are suppressed by inverse powers of N with respect to the planar ones. Consequently, the 't Hooft limit is commonly referred to as the planar limit.

The number of planar diagrams has been observed to grow exponentially, in marked contrast to the total number of diagrams, which grows factorially [18]. This observation led the scientific community to speculate that it might be possible to sum up the planar diagrams, thus allowing analytical insights into the non-perturbative regime of quantum chromodynamics. However, achieving this summation has remained an impossible task (see [19–22] for more details on this discussion).

With these counting rules, something unexpected happens in the large N limit: all diagrams are organized according to their topology, expressed in terms of their genus and the number of boundaries. In general, the color factor of a given amplitude $\mathcal{M}$ is expressed by the following series:

$$\mathcal{F}(N) = \sum_{g,b=0}^{\infty} N^{2-2g-b}. \tag{2.2}$$

This expansion shows that the leading contribution is indeed of order $\mathcal{O}(N^2)$ and corresponds to the planar limit, with $g = 0$ and no quark loops $b = 0$.

Over the years, the large N limit has become a very powerful mathematical tool for studying the behavior of gauge theories. Notable achievements include, for instance, the formulation of closed Wilson loop equations [23] and a systematic $1/N$ expansion for baryons [24].

In any case, it is important to emphasize that the large N limit used in this thesis report is different from the one discussed in this section. While the 't Hooft large N limit corresponds to a thermodynamic limit in infinite volume, our goal is to study the implications in finite volume scenarios. Therefore, a modified definition is required. For the purposes of the volume independence hypothesis, we will adopt the so-called singular large N limit, which will be discussed in more detail in sec. 2.3.2.

As an aside, it is worth mentioning that the large N limit has interesting connections with several areas of theoretical physics. In particular, there is a fascinating correspondence between the large N limit of certain gauge theories and quantum gravity. This concept, referred to as gauge-gravity duality or the AdS/CFT correspondence [25], proposes that, under certain conditions, the large N limit of a gauge theory is equivalent to a string theory existing in a higher-dimensional spacetime. This correspondence has been studied extensively and has provided many valuable insights into both string and gauge theories.

2.2.2 The master field and the EK reduction

Important aspects of the internal structure of 't Hooft's large N theory are revealed by studying the spectrum of hadrons and mesons. In particular, the primary contribution to any correlation function comes from disconnected diagrams, rather than connected ones. This result leads to a significant suppression of interactions between gluonic and mesonic operators. Furthermore, correlators of gauge invariant operators factorize in the large N limit, so that quantum fluctuations are strongly suppressed [26, 27]. As a consequence, the variance of a single-trace gauge operator $\mathcal{G}$ can be determined as follows:

$$\frac{(\delta\mathcal{G})^2}{\langle\mathcal{G}\rangle^2} \simeq \frac{1}{N^2}. \tag{2.3}$$

An interpretation of this equation suggests a direct correspondence between quantum theories formulated in the large N limit and classical theories. However, it is crucial to keep in mind that while a mapping between the two systems may exist, it does not imply that the quantum theory can be described by solutions of the classical equations of motion. In other words, it is not valid to treat the path integral in the large N limit as a dominant saddle point and use a steepest descent approach, since the number of fields included in the path integral measure also increases and contributes with a term of $\mathcal{O}(N^2)$ [27, 28]. The formulation of this path integral with a steepest descent approach remains an open question, sometimes referred to as the 't Hooft problem.

In any case, the interpretation of a classical theory description in the large N limit suggests the existence of a configuration of gauge fields $A_\mu(x)$ that dominates the path integral. Furthermore, this configuration should exhibit translation invariance, allowing it to be independent of spatial coordinates by an appropriate gauge transformation. Essentially, all relevant information about Yang-Mills theory in the large N limit can be contained in four N^2 matrices. Witten conjectured the existence of such a classical configuration [26], but it was Coleman who named it *the master field* [29]. The master field emerges as the first manifestation of a gauge field that becomes independent of spatial coordinates in the large N limit, providing a framework for describing the theory in terms of a matrix model. For a more technical review of these ideas, see Sections 3.4 and 3.5 of [27].

In the continuum, a set of closed Schwinger-Dyson equations for the expectation values of physical observables was derived [23] by exploiting the suppression of quantum fluctuations in eq. (2.3), allowing the theory to be reformulated in a gauge invariant way. On the other hand, Eguchi and Kawai formulated a lattice version of these equations in their famous EK reduction [4]. The validity of the model rested on two crucial elements: factorization and the absence of spontaneous breaking of the center symmetry. However, subsequent investigations have shown that this symmetry is indeed broken for any number of dimensions greater than 2 [30, 31].

Various proposals have been made to address the issue of the center symmetry breaking of the original reduction. These include the quenched [31] and twisted [32–37] versions, the inclusion of adjoint fermions [38–51] or trace deformations [52, 53], and the so-called continuum large N reduction [54–57]. We will focus only on the twisted version introduced by Gonzalez Arroyo and Okawa, where they modify the boundary conditions to ensure symmetry restoration.

2.3 TEK model and volume independence

In this section we will review the basic properties of the twisted variant of the EK reduction, commonly referred to as the TEK model. As mentioned above, the number of lattice sites becomes irrelevant as the number of colors approaches infinity. In this scenario, the model is completely reduced and the lattice collapses into a single point - an extreme case known as the fully reduced model.

In particular, and following the ideas developed for YM theories in 2+1 dimensions in [8, 58], we will explore an extended version of TEK reduction, known as volume independence, which exploits the interplay between color and spatial degrees of freedom. A notable aspect of this formulation is the fact that in the large N limit the dependence on the gauge group rank N and the torus size l appears intertwined [8, 59–63]. Remarkably, this leads to interesting results even for small values of N. However, there is a subtlety to consider: a residual dependence remains in the form of an additional angular variable, which is closely related to non-commutative theories via Morita duality [7, 64–67]; we will give a more detailed description in sec. 2.3.2.

In the following, we will first introduce twisted boundary conditions and then give an overview of the main ideas behind volume independence.

2.3.1 Twisted boundary conditions

Consider the $SU(N)$ gauge theory defined on a d-dimensional torus with periods l_μ. Gauge fields need to be periodic only up to a gauge transformation, so gauge connections can be introduced as $N \times N$ traceless hermitian matrices satisfying the following periodicity relation

$$A_\mu(x + l_\nu \hat{\nu}) = \Omega_\nu(x) A_\mu(x) \Omega_\nu^\dagger(x) + i\Omega_\nu(x)\partial_\mu \Omega_\nu^\dagger(x). \tag{2.4}$$

The matrices $\Omega_\mu(x)$ are $SU(N)$ matrices satisfying the following consistency relation

$$\Omega_\mu(x + l_\nu \hat{\nu})\Omega_\nu(x) = Z_{\mu\nu}\Omega_\nu(x + l_\mu \hat{\mu})\Omega_\mu(x). \tag{2.5}$$

where the factor $Z_{\mu\nu} = \exp(2\pi n_{\mu\nu}/N)$ is an element of the center of $SU(N)$ and $n_{\mu\nu}$ is an antisymmetric tensor of integers defined modulo N. This tensor has 6 independent components, which can be divided into the electric and the magnetic part of the tensor. The three vectors obtained are

$$n_{0i} = k_i \tag{2.6}$$
$$n_{ij} = \epsilon_{ijk} m_k. \tag{2.7}$$

The case of purely periodic boundary conditions is obtained after imposing $n_{\mu\nu} = 0$ modulo N. The set of eqs. (2.4) and (2.5) are commonly known as twisted boundary conditions, first introduced by 't Hooft [1].

Using gauge symmetry, and for certain choices of the twist tensor, the matrices $\Omega_\mu(x)$ can be brought into a constant form. The constant matrices are called twist eaters $\Omega_\mu(x) = \Gamma_\mu$, and the relations of eqs. (2.4) and (2.5) are then expressed as:

$$A_\mu(x + l_\nu \hat{\nu}) = \Gamma_\nu A_\mu(x) \Gamma_\nu^\dagger, \tag{2.8}$$
$$\Gamma_\mu \Gamma_\nu = Z_{\mu\nu} \Gamma_\nu \Gamma_\mu. \tag{2.9}$$

For a much more detailed discussion of gauge theories on a torus with twisted boundary conditions, see [68].

In four dimensions, the necessary and sufficient condition for these solutions to exist is that the Pfaffian of the twist tensor $\kappa(n) = \varepsilon^{\mu\nu\rho\sigma} n_{\mu\nu} n_{\rho\sigma}/8$ vanishes modulo N, commonly known as orthogonal twist. The twist is irreducible only for certain choices of N and $n_{\mu\nu}$, providing that they are unique module similarity transformations (global gauge transformations) and multiplications by elements of the center. In this case there are N^2 inequivalent solutions [68, 69] which satisfy $\Gamma_\mu^N = \mathbb{I}$, i.e. they are roots of the identity.

In two dimensions, however, n_{12} is the only element of the twist tensor. Thus, the twist is irreducible if n_{12} and N are coprime and there exist N different twist eaters solutions [68, 69] satisfying $\Gamma_\mu^N = \pm\mathbb{I}$ for N even or odd, respectively.

It is convenient to rewrite the twist tensor as

$$n_{\mu\nu} = \epsilon_{\mu\nu}\frac{kN}{\ell_N}, \tag{2.10}$$

where k and $\ell_N \equiv N^{2/d}$ are integers, and $\epsilon_{\mu\nu} = \Theta(\nu-\mu) - \Theta(\mu-\nu)$ is a combination of Heaviside step functions.

A Fourier expansion consistent with twisted boundary conditions is given by:

$$A_\nu(x) = \mathcal{N}\sum_p{}' e^{ip\dot{x}}\hat{A}_\nu(p)\hat{\Gamma}(s(p))\,. \tag{2.11}$$

where $\mathcal{N}^{-2} = \prod_\mu l_\mu$ is a normalization factor. The boundary conditions are automatically satisfied for momenta p_μ quantized as:

$$p_\mu = \frac{2\pi}{\tilde{l}_\mu}m_\mu, \tag{2.12}$$

where $m_\mu \in \mathbb{Z}$. The quantization has the peculiarity of coming in terms of the effective length $\tilde{l}_\nu \equiv l_\nu \times \ell_N$.

We have introduced the set of $N\times N$, d momentum-dependent, $SU(N)$ matrices defined as

$$\hat{\Gamma}(p) = \frac{1}{\sqrt{2N}}e^{i\alpha(p)}\Gamma_0^{s_0(p)}\cdots\Gamma_{d-1}^{s_{d-1}(p)}, \tag{2.13}$$

where $\alpha(p)$ is an complex phase to be determined and $s_\mu(p)$ is a momentum-dependent set of integers given by

$$s_\mu(p) = \tilde{\epsilon_{\mu\nu}}\bar{k}\frac{\tilde{l}_\nu p_\nu}{2\pi}. \tag{2.14}$$

In eq. (2.14) we have used the following definitions: $k\times\bar{k} = 1$, and the following identity:

$$\sum_\nu = \tilde{\epsilon}_{\mu\nu}\epsilon_{\nu\sigma} = \delta_{\mu\sigma}. \tag{2.15}$$

The $\hat{\Gamma}(p)$ matrices span the $SU(N)$ Lie algebra with the following commutation relations

$$\left[\hat{\Gamma}(p),\hat{\Gamma}(p)\right] = i\mathcal{F}(p,q,-p-q)\hat{\Gamma}(p+q) \tag{2.16}$$

with

$$\mathcal{F}(p,q,-p-q) = -\sqrt{\frac{2}{N}}\sin\left(\frac{\theta_{\mu\nu}}{2}p_\mu q_\nu\right) \tag{2.17}$$

and

$$\theta_{\mu\nu} = \frac{\tilde{l}_\mu\tilde{l}_\nu}{2\pi}\tilde{\epsilon}_{\mu\nu}\hat{\theta}. \tag{2.18}$$

The variable $\hat{\theta} \equiv \bar{k}/\ell_N$ will play an important role in the discussion of the singular large N limit of sec 2.3.2. In addition, the complex phase $\alpha(p)$ of eq. (2.13) can be

chosen to satisfy commutation relation of eq. (2.17). Note that these factors play the role of the $SU(N)$ structure constant in this particular basis, and they become momentum-dependent.

It is important to note that the prime in the summation implies the exclusion of momenta with $p_\mu = 0 \mod \ell_N \ \forall \mu$, resulting in traceless gauge fields A_μ and introducing a natural infrared cutoff. This feature has several advantages. First, it automatically eliminates the contribution of zero modes from the dynamics of the theory, effectively introducing a mass gap. Second, it simplifies the perturbative treatment of the theory, leading to a simplified description.

A first glimpse of volume independence comes from the fact that for all orders in the coupling, and up to finite N corrections, the dependence on N and l comes from the combination $\tilde{l} = l \times \ell_N$. If true, this defines an equivalence between different $SU(N)$ gauge theories characterized by the same value of $\tilde{l}$. Note, however, that this is only true if the angular variable $\hat{\theta}$ remains constant, which is not possible while changing N. The solution is to find an appropriate choice of parameters, following a sequential approach to the large N limit that preserves an approximately constant ratio. In sec. 2.3.2 we will discuss an optimal choice of sequence to approach the large N limit.

2.3.2 Singular large N limit

As we sketched in the first part of this chapter, the large N limit considered in our work is not strictly the same as the one introduced by 't Hooft, and the main difference lies in the fact that our setup is a finite volume description closely related to non-commutative gauge theories.

It is worth noting that the coefficients in the expansion of eq. (2.11) are complex numbers without color indices, while the structure constants in eq. (2.17) are momentum dependent, leading to momentum dependent Feynman rules. In fact, this feature was the first derivation of the Feynman rules of non-commutative gauge theories [67].

In the limit we consider here, we take $\ell_N \to \infty$ with $l \to 0$, so $\tilde{l}$ is held constant. This is in contrast to the 't Hooft limit used in standard reduction, where l is held constant while sending $N \to \infty$, so we end up with $\tilde{l} \to \infty$, precisely the thermodynamic limit of gauge theory, where the dependence on $\hat{\theta}$ disappears. In our setup, we will approach the large N thermodynamic limit in a different way, by first taking $N \to \infty$ at fixed $\tilde{l}$, and then taking $\tilde{l} \to \infty$ at fixed $\hat{\theta}$. The large N limit has to be taken along a sequence of choices of N and $\bar{k}$ that tends to a target value of $\hat{\theta}$. The main drawback of this description is that generic sequences are affected by the appearance of so-called tachyonic instabilities related to the condensation of electric fluxes and spontaneous breaking of the center symmetry [70, 71]. It has been shown [10] that a particular choice that maximally avoids these instabilities is based on the Fibonacci sequence [10]. The idea is to scale the number of colors and the k-flux of the twisted boundary conditions as the $n-2$ and n-th terms of the Fibonacci sequence. This sequence naturally saturates the bound and maximizes

the absence of tachyonic instabilities. The parameter $\hat{\theta}$ taken along this sequence, tends to a constant value in the large N limit, which is related to the Golden Ratio φ^{-2}, with $\varphi = (1+\sqrt{5})/2$.

One of the goals of this thesis report is to explore key aspects of the volume independence hypothesis using lattice field theory techniques. Using the 't Hooft running coupling $\lambda = g^2 N$, which will be computed using the gradient flow discussed in sec. 2.4, we aim to investigate the volume dependence of the theory by examining significant quantities such as the topological susceptibility or the Λ parameter. Our approach is to use the volume as a trigger of the dynamics of the system, assuming that the physical volume determines the value of the renormalized coupling. In this sense, the effective length $\tilde{l}$ serves as a natural running scale.

2.3.3 On fractional charge instantons

As a final remark of this section, we will elaborate on some ideas concerning an interesting type of solutions to the YM Euclidean equations of motion with minimal action, whose existence is a direct consequence of twisted boundary conditions. These solutions are studied in detail in ch. 8, and here we will only present the main idea and refer the reader to the appropriate literature.

As mentioned in sec. 2.1, the study of $SU(N)$ gauge fields on the hypertorus $\mathbf{T}^4$ began with the work of 't Hooft [1–3]. 't Hooft provided the existence of new topological classes parameterized by the twist tensor $n_{\mu\nu}$, realizing that non-trivial twists change the way in which the topological charge is quantized. For non-orthogonal twists $\vec{k}\cdot\vec{m} \neq 0$, the topological charge is fractional and quantized in units of $1/N$ [69, 72] as:

$$Q = \frac{1}{16\pi^2}\int d^4x \mathrm{Tr}\left(G_{\mu\nu}(x)\widetilde{G}_{\mu\nu}(x)\right) = \nu - \frac{\vec{k}\cdot\vec{m}}{N},\ \nu \in \mathbf{Z}. \tag{2.19}$$

where $G_{\mu\nu}(x)$ is the standard stress tensor of the gauge potential $A_\mu(x)$.

The existence of solutions with minimal action within each twisted sector was proved by Sedlacek [73]. However, the only $Q = 1/N$ self-dual solutions obtained analytically are constant curvature solutions on the 4-torus [69, 74] which become self-dual only for certain values of the torus periods. Many solutions of this type can be found using the special properties of the Fibonacci numbers assumed in our description, but none of them cover the geometry we will explore in ch.8, where we will look for localized instanton-like configurations on $\mathbf{T}^4$ and $\mathbf{R}\times\mathbf{T}^3$. Configurations of this type have been obtained previously for other values of the twists and geometries, first for $SU(2)$ [75, 76] and then for $SU(N)$ [77, 78].

The dynamical relevance of configurations of this type has been put forward by Gonzalez-Arroyo and collaborators, see i.e. the recent review [79], and is also motivated by their apparent presence in our analysis of the running coupling constant, which will be discussed in chapters 4 and 5. In ch. 7, we will study of their impact on relevant quantities, such as the topological charge.

2.4 The gradient Flow

The gradient flow is a powerful technique used in lattice field theories whose main feature is to smooth the YM fields by evolving them with the so-called flow equations. It was originally introduced to study general YM theories in the continuum [80], but became widely used on the lattice as a method to eliminate ultra ultraviolet divergences [11–14]. Since then it has been systematically used to define renormalized couplings and composite observables [14, 81–83].

Although the GF has been used for various purposes, it is worth mentioning those that combine it with finite size scaling [84] to determine the running coupling and the Λ parameter of $SU(N)$ gauge theories, as for instance [85]. This is one of the main goals of the present work. In addition, it is worth emphasizing that GF has been systematically used to perform scale setting on the lattice [14], due to its precise definition of scales such as t_0 or w_0. In this section, we will present a general overview of the method.

2.4.1 Flow equations

The GF is a renormalization procedure in which the gauge fields $A_\mu(x)$ are replaced by a new set of fields $B_\mu(x,t)$, with an additional dependence on a new coordinate called flow "time" t, with dimensions of squared length. The $B_\mu(x,t)$ fields are then evolved by solving the so-called GF equations. The specific form of these equations depends on the theory being studied, and for the case of continuum $SU(N)$ Yang-Mills theories, they take the following form

$$\partial_t B_\mu(x,t) = D_\nu G_{\nu\mu}(x,t), \quad B_\mu(x,t=0) = A_\mu(x), \tag{2.20}$$

where D_μ and $G_{\mu\nu}$ stand for the usual covariant derivative and the field strength tensor of the flowed $B_\mu(x,t)$ fields:

$$D_\mu B_\nu(x,t) = \partial_\mu B_\nu(x,t) - i[B_\mu(x,t), B_\nu(x,t)]\,, \tag{2.21}$$

$$G_{\mu\nu}(x,t) = \partial_\mu B_\nu(x,t) - \partial_\nu B_\mu(x,t) - i[B_\mu(x,t), B_\nu(x,t)]\,. \tag{2.22}$$

The flow equations drive the gauge fields $B_\mu(x,t)$ towards a stationary point of the classical equations of motion. Note that the right hand side of eq. (2.20) is proportional to the gradient of the action, giving rise to the name *gradient flow*.

The GF equation acts as a heat equation that diffuses the field configurations over the lattice. As the flow time increases, the field configurations approach a smooth limit, eliminating the ultraviolet divergences in a spherical region of size $\sqrt{8t}$, which naturally becomes a renormalization scale $\mu^{-1} = \sqrt{8t}$. This is obtained by solving the leading order of eq. (2.21) with the following heat kernel:

$$B_\mu(x,t) = \int d^d y K_t(x-y) A_\mu(y), \tag{2.23}$$

$$K_t(z) = \frac{1}{(4\pi t)^2} \exp\left(\frac{-z^2}{4t}\right). \tag{2.24}$$

One of the main features of the GF is that any composite observable made of $B_\mu(x,t)$ fields is automatically renormalized for any time $t > 0$ [81]. Even for $t = 0$, the observable decomposes into a finite renormalized part plus an additional term with divergent coefficients. In this sense, renormalized couplings can be easily introduced within the GF by identifying dimensionless observables with a suitable dependence on the energy scale. One such observable is the flowed energy density [14]:

$$E(t) = \frac{1}{2}\mathrm{Tr}\left(G_{\mu\nu}(x,t)G_{\mu\nu}(x,t)\right) . \tag{2.25}$$

Using the flow time t, which has dimensions of length squared, we can construct the dimensionless combination $\langle t^2 E(t)\rangle$. The behavior of this combination with respect to the scale $\mu^{-1} = \sqrt{8t}$ allows to define a renormalized 't Hooft coupling through the following relation:

$$\lambda(\mu) \propto \left\langle t^2 E\left(t\right)\right\rangle \Big|_{\sqrt{8t}=\mu^{-1}} . \tag{2.26}$$

This procedure is usually mixed with finite volume techniques, in particular the so-called finite size scaling [84]. In this context, it is common to relate the renormalization scale μ to the size of the finite volume l. In the standard setup, where the gauge theory is defined on a torus of dimension l^4, the flow time is determined by the relation $\sqrt{8t} = cl$. The parameter c is an arbitrary constant, less than 1, which measures how much the gauge fields are smoothed in units of l. This relation leads to the definition of a coupling as follows:

$$\lambda_{\mathrm{GF}}(\mu) = \mathcal{N}\left\langle t^2 E\left(t\right)\right\rangle \Big|_{\sqrt{8t}=cl=\mu^{-1}} . \tag{2.27}$$

Here the factor $\mathcal{N}$ represents a normalization constant introduced to ensure that $\lambda_{\mathrm{GF}}(\mu)$ approximates $\lambda_{\overline{\mathrm{MS}}}(\mu)$ at leading order in perturbation theory. In this sense, the choice of c is in principle arbitrary and only enters as part of the scheme definition.

We will use these definitions in ch. 3 to present a new renormalization scheme based on the GF, known as twisted gradient flow (TGF). This will be the main computational technique used in most of the thesis report.

2.4.2 Scale setting

Scale setting in lattice field theories plays a crucial role in the determination of physical quantities and in the comparison of lattice results with experimental or theoretical predictions. The discretization of spacetime introduces the lattice spacing a as a natural scale, and therefore all resulting determinations are expressed in terms of it. The scale setting methods aim at establishing a physical scale within lattice theory by relating it to a known physical quantity or dimensional parameter.

When direct comparisons with experimental or theoretical data are possible, lattice simulations can be directly compared with known physical quantities, such as pion masses or decay constants, to determine the lattice spacing. However, in cases

where experimental data are not available, such as more theoretically motivated calculations, alternative scale setting methods are required [86].

One commonly used scale for pure gauge theories is the string tension $\sqrt{\sigma_0}$, but since this approach requires large scale simulations with significant spatial volumes, Rainer Sommer introduced a more precise definition using the so-called Sommer radius r_0 [87]. The scale r_0 is defined by setting a certain value for the force between two static quarks:

$$r^2 F(r) \,|_{r=r_0} = 1.65. \tag{2.28}$$

This approach provides improved accuracy in determining the lattice spacing with fewer configurations required.

It is important to note that scale setting methods can be affected by systematic uncertainties such as lattice artifacts and finite volume effects. These uncertainties must be carefully considered and accounted for to ensure reliable lattice spacing determinations.

Another approach to scale setting is the use of GF. Since the smoothing process of gauge fields can be controlled by varying the flow time t, setting a certain value for an observable, such as the GF energy density of eq. (2.25), allows defining a flow scale t_0 and using it to relate physical quantities on the lattice. The definition of t_0 [14] in $SU(3)$ is the following

$$t^2 \langle E(t) \rangle \,|_{t=t_0} = 0.3\,, \tag{2.29}$$

which can be generalized to $SU(N)$ through:

$$\frac{t^2 \langle E(t) \rangle}{N} \,|_{t=t_0} = 0.1\,. \tag{2.30}$$

Similar ideas can be applied when using the derivative of the energy density, obtaining the following w_0 scale [88]:

$$\left[t \frac{d}{dt} t^2 \langle E(t) \rangle \right] \Big|_{t=w_0^2} = 0.3 \tag{2.31}$$

GF scales provide higher accuracy compared to other methods such as the Sommer radius or the string tension, and require fewer configurations to achieve comparable lattice spacing accuracy. Large volumes are still required to account for finite volume corrections, as distortions can occur for small volumes.

2.5 Summary

We have given a general overview of the background and key aspects relevant to this thesis report. We introduced the concept of the large N limit and its relevance. We initially focused on the 't Hooft large N limit, where the number of colors N is taken to be arbitrarily large, while the bare coupling g_0 is set to zero, keeping the 't Hooft

coupling $\lambda_0 = Ng_0^2$ constant. However, in our particular setup we are interested in studying the large N theory at finite volume, and therefore we have discussed an alternative limit known as the singular large N limit, where the physical volume is held constant instead of the bare coupling.

We have discussed the formulation of $SU(N)$ Yang-Mills theories on a finite torus with twisted boundary conditions. We have shown that the dynamics of the theory is controlled by the effective length of the torus $\tilde{l}$, which equivalently fixes the renormalized coupling. However, there is a residual dependence in the form of the angular variable $\hat{\theta}$, which is not generally fixed by the singular large N limit. Therefore, we have chosen to use N and k scaled within the Fibonacci sequence, which gives a constant $\hat{\theta}$ value in the large N limit related to the Golden ratio. In addition, this choice maximizes the avoidance of tachyonic instabilities associated with the breaking of the center symmetry.

Our main goal is to study the implications of the volume independence hypothesis in the calculation of relevant quantities such as the topological susceptibility or the Λ parameter. To achieve this, we have introduced GF as a useful renormalization procedure to define renormalized couplings. The specific renormalization scheme used in this thesis combines twisted boundary conditions and a coupling definition based on GF, known as twisted gradient flow.

We conclude this introductory chapter by summarizing our general choices. In the following chapters, we will implement $SU(N)$ Yang-Mills theories on an asymmetrical torus of size $l^2 \times \tilde{l}^2$, where the two short directions are endowed with twisted boundary conditions. In this $d = 2$ setup, the effective length $\tilde{l} = l\ell_N$ is given by $\tilde{l} = Nl$, and we choose the values of N and k within the Fibonacci sequence, specifically $N = F_n$ and $k = F_{N-2}$ for any value of n. The details of the coupling definition and the specific finite size scaling realization are given in the chapter 3.

Part II

The N dependence of the running coupling constant

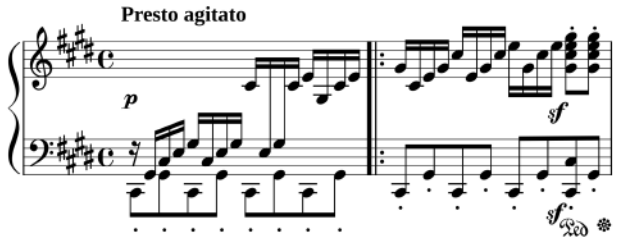

3 Twisted Gradient Flow scheme

3.1 Motivation

Finite volume renormalization schemes [84] are a powerful tool for studying asymptotically free theories. (See [89, 90] for a comprehensive review). Asymptotic freedom [91, 92] predicts weak coupling values at high energies, where perturbation theory becomes a reliable tool for precise determinations. However, in Yang-Mills (YM) theories such as QCD, the approach to the perturbative regime is logarithmic in the running coupling; therefore, the strongly coupled and the perturbative regimes are separated by large energy scales. Accommodating these different scales in a single lattice simulation is challenging and requires compromises (see [93] for a review of strong coupling extraction methods).

Finite volume renormalization schemes solve this multiscale problem by linking the physical volume of the system to the renormalization scale. A single lattice simulation can only study a limited range of scales. However, simulations with different physical sizes can cover large energy scales by using a recursive technique called finite size scaling. This technique has been used to determine the QCD running coupling with $N_{\mathrm{f}} = 2$, 3 [94–96] and 4 [97] flavors as well as in pure gauge theory [85, 98, 99].

This chapter aims to explore a particular finite volume renormalization scheme, first introduced in [100–102], based on three ingredients. First, we choose a non-perturbative coupling based on the gradient flow (GF) [11–14] (see also [103] for a review). Second, we choose twisted boundary conditions [1–3] for the gauge fields. Finally, we use a particular geometry; for $SU(N)$ gauge theories, we choose a hypercubic box of dimensions $l^2 \times \tilde{l}^2$ with $\tilde{l} = lN$.

The logic behind these choices is rooted in the study of the large N limit of YM theories and the ideas of volume reduction with twisted boundary conditions [5, 6, 104] (see [105, 106] for recent reviews). With our choice of geometry $l^2 \times (Nl)^2$ and our particular choice of boundary conditions, perturbation theory indicates that the effective volume of the torus is $(Nl)^4$. As discussed in ch. 2, this equivalence between group degrees of freedom and spatial degrees of freedom (which becomes exact in

the large N limit) lies behind the ideas of volume reduction and non-commutative geometry [67].

Compared to the more common finite volume renormalization schemes based on SF or mixed open SF boundary conditions [83], twisted boundary conditions [107, 108] preserve the invariance under translations and are therefore free of the linear $\mathcal{O}(a)$ cutoff effects present in other schemes. On the other hand, the use of periodic boundary conditions [109, 110] leads to non-analytic coupling definitions, making the extraction of the Λ parameter cumbersome. Instead, twisted boundary conditions do not suffer from these non-analyticities, making them particularly suitable for perturbative calculations. Moreover, the relationship between the Λ parameter of this scheme and the $\overline{\text{MS}}$ scheme is known analytically [100]. Finally, due to the asymmetrical torus, the memory footprint required to simulate this scheme is reduced, although the computational time remains roughly the same due to self-averaging [111]. Conversely, this memory reduction allows for better performance on GPU systems.

Throughout the chapter, we will describe the running of the strong coupling constant in the twisted gradient flow (TGF) renormalization scheme. The chapter is structured as follows. In sec. 3.2, we define the TGF renormalization scheme focusing on our particular choice of coupling and torus geometry. Section 3.3 summarizes the strategy for determining the Λ parameter at some typical hadronic scales. Section 3.4 summarizes the lattice numerical implementation. This setup will be used in chs. 4 and 5 to compute the running coupling constant of several $SU(N)$ gauge groups. We end with some final remarks in section 3.5.

3.2 Twisted gradient flow (TGF) scheme

Definitions of the gauge coupling based on the GF are customary since they can be computed on the lattice to high precision. The GF is a renormalization procedure based on replacing the original gauge fields $A_\mu(x)$ with a new set of smooth, flow-time dependent fields $B_\mu(x,t)$, in terms of which gauge invariant composite observables are automatically renormalized quantities for $t > 0$ [81]. The so-called flow time equations drive these new fields as follows:

$$\partial_t B_\mu(x,t) = D_\nu G_{\nu\mu}(x,t), \quad B_\mu(x,t=0) = A_\mu(x), \tag{3.1}$$

where D_μ and $G_{\mu\nu}$ stand for the covariant derivative and the field strength tensor of the flow fields:

$$D_\mu B_\nu(x,t) = \partial_\mu B_\nu(x,t) - i[B_\mu(x,t), B_\nu(x,t)]\,, \tag{3.2}$$

$$G_{\mu\nu}(x,t) = \partial_\mu B_\nu(x,t) - \partial_\nu B_\mu(x,t) - i[B_\mu(x,t), B_\nu(x,t)]\,. \tag{3.3}$$

The effect of the flow is to smooth the gauge fields on a sphere of radius $\sqrt{8t}$. Renormalized couplings based on the GF can thus be introduced trivially, since one only needs to find dimensionless observables that depend on some energy scale. As

commented in ch. 2.4, the energy density of eq. (2.25) can be used to construct the dimensionless combination $\langle t^2 E(t)\rangle$, which provides one such observable.

As discussed in ch. 2.4.1, in the context of finite size scaling in the standard symmetrical setup, one fixes the renormalization scale in terms of the flow time and the size of the torus as $\mu^{-1} = \sqrt{8t} = cl$, with c standing for an arbitrary, smaller than 1, constant defining the scheme. These choices lead to the coupling definition of eq. (2.27)

Regarding the geometry, the Twisted Gradient Flow (TGF) scheme is defined by introducing $SU(N)$ Yang-Mills (YM) theories on an asymmetrical hypercubic box of size $l^2 \times (Nl)^2$. The plane with two short directions, taken to be the (1,2) plane, is endowed with twisted boundary conditions, i.e.,

$$A_\mu(x + l\hat{\nu}) = \Gamma_\nu A_\mu(x)\Gamma_\nu^\dagger, \text{ for } \nu = 1, 2. \tag{3.4}$$

The gauge field is periodic in the remaining directions with period $\tilde{l} = Nl$. The twist matrices Γ_ν, for $\nu = 1, 2$, satisfy the consistency condition:

$$\Gamma_1\Gamma_2 = Z_{12}\Gamma_2\Gamma_1 \tag{3.5}$$

with

$$Z_{12} = e^{i\frac{2\pi k}{N}}, \tag{3.6}$$

where k and N are coprime integers. As we discussed in sec. 2.3.2, the value of the twist k must be scaled with the number of colors of the gauge group and is best chosen to avoid the appearance of tachyonic instabilities in the large N limit [10,104]. In this work, following ref. [10], the values of the k flux and the number of colors N are scaled as the $n-2$ and n-th terms of the Fibonacci sequence, i.e., $k = F_{n-2}$ and $N = F_n$.

As mentioned above, perturbation theory suggests that the finite volume effects for this choice of twist are controlled by $\tilde{l}$ [8, 9, 100, 112]. Under this assumption, it becomes natural to use the effective size $\tilde{l} = Nl$ rather than l to set the scale of the running coupling [113] as $\mu^{-1} \equiv c\tilde{l}$. Furthermore, and following the prescription introduced in [114], the coupling is defined within the sector of configurations with zero topological charge. This choice aims to circumvent the problems of critical slowing down (CSD) and topology freezing on the lattice [115, 116], which will be discussed in detail in ch. 6. Thus, the coupling is defined as

$$\lambda_{\text{TGF}}(\mu) = \frac{128\pi^2 t^2}{3N\mathcal{A}(\pi c^2)} \frac{\langle E(t)\,\delta_Q\rangle}{\langle \delta_Q\rangle}\Big|_{\sqrt{8t}=c\tilde{l}=\mu^{-1}}, \tag{3.7}$$

where δ_Q stands for a δ-function that restricts the path integral to configurations with zero topological charges Q, and

$$\mathcal{A}(x) = x^2\theta_3^2(0, ix)\left(\theta_3^2(0, ix) - \theta_3^2(0, ixN^2)\right), \tag{3.8}$$

where $\theta_3(0, ix)$ stands for the Jacobi θ_3 function:

$$\theta_3(z, ix) = \sum_{m\in\mathbb{Z}} \exp\left\{-\pi x m^2 + 2\pi i m z\right\} \equiv \frac{1}{\sqrt{x}} \sum_{m\in\mathbb{Z}} \exp\left\{-\pi \frac{(m-z)^2}{x}\right\}, \tag{3.9}$$

is chosen to ensure that the TGF coupling is proportional to the bare coupling at leading order in perturbation theory.

In addition, we will set $c = 0.30$, a standard choice for GF finite volume schemes that aims at reducing the effect of lattice artefacts and minimizing at the same time the statistical errors in the determination of the coupling. We will elaborate more on this choice in ch. 4.2.

3.3 The Λ parameter

The starting point for determining the Λ parameter is the renormalization group (RG) equation in a particular scheme (labeled s)

$$\beta_{\mathrm{s}}(\lambda_{\mathrm{s}}) = \frac{\mathrm{d}\lambda_{\mathrm{s}}}{\mathrm{d}\log(\mu^2)} \,. \tag{3.10}$$

The β function has a perturbative expansion

$$\beta_{\mathrm{s}}(\lambda_{\mathrm{s}}) \overset{\lambda_{\mathrm{s}}\to 0}{\sim} -\lambda_{\mathrm{s}}^2(b_0 + b_1\lambda_{\mathrm{s}}) + \mathcal{O}\left(\lambda_s^{n-1}\right) \,. \tag{3.11}$$

with the first two coefficients $(4\pi)^2 b_0 = 11/3$ and $(4\pi)^4 b_1 = 34/3$ being universal (i.e., scheme independent). The first-order differential equation (3.10) can be integrated exactly

$$\begin{aligned} \frac{\Lambda_{\mathrm{s}}}{\mu} &= \left[b_0\lambda_{\mathrm{s}}(\mu)\right]^{\frac{-b_1}{2b_0^2}} \exp\left(\frac{-1}{2b_0\lambda_{\mathrm{s}}(\mu)}\right) \\ &\times \exp\left[-\int_0^{\lambda_{\mathrm{s}}(\mu)} dx \left(\frac{1}{2\beta_s(x)} + \frac{1}{2b_0x^2} - \frac{b_1}{2b_0^2x}\right)\right] \,, \end{aligned} \tag{3.12}$$

where Λ_{s} is an integration constant (the Λ parameter). As such, it is a renormalization group invariant (i.e., scale independent) but depends on the choice of renormalization scheme. This scheme dependence can be computed exactly via a one-loop computation. In particular, the quotient of the Λ parameters in the $\overline{\mathrm{MS}}$ and the TGF schemes is given by [100]

$$\log\left(\frac{\Lambda_{\mathrm{TGF}}}{\Lambda_{\overline{\mathrm{MS}}}}\right) = \frac{3}{22}\left(\frac{11}{3}\gamma_E + \frac{52}{9} - 3\log 3 + C_1(c)\right) \,, \tag{3.13}$$

where $C_1(c)$ is a finite constant determined for different gauge groups and c values in [100]. For the gauge groups studied in this paper, it takes the values $C_1(c = 0.3) = 0.508(4)$ for $N = 3$ and $k = 1$, $C_1(c = 0.3) = 0.597(14)$ for $N = 5$ and $k = 2$, and $C_1(c = 0.3) = 0.615(14)$ for $N = 8$ and twist $k = 3$.

To determine the Λ parameter, we use the exact relation eq. (3.12) to write

$$\frac{\Lambda_{\mathrm{s}}}{\mu_{\mathrm{had}}} = \frac{\Lambda_{\mathrm{s}}}{\mu_{\mathrm{pt}}} \times \exp\left[-\int_{\lambda_{\mathrm{s}}(\mu_{\mathrm{pt}})}^{\lambda_{\mathrm{s}}(\mu_{\mathrm{had}})} \frac{dx}{2\beta_{\mathrm{s}}(x)}\right] \,, \tag{3.14}$$

where $\mu_{\rm had}$ is a typical hadronic scale, and $\mu_{\rm pt} \gg \mu_{\rm had}$ is a high energy scale where perturbation theory is applicable. Lattice field theory allows us to non-perturbatively determine the running of the coupling in some suitable schemes (like the TGF used here), and thus the second factor on the right-hand side of eq. (3.14). In particular, the technique of finite size scaling [84] allows high-precision determinations. The procedure is implemented by measuring the change of the coupling under a change of the renormalization scale from μ to $s\mu$, where $s > 1$ is the so-called scaling parameter. An iterative procedure allows to link the two scales $\mu_{\rm had}$ and $\mu_{\rm pt}$ by taking into account that at each step:

$$\int_{\lambda(\mu)}^{\lambda(s\mu)} \frac{dx}{\beta(x)} = \log s^2. \tag{3.15}$$

We postpone the concrete implementation for the next section and focus here on evaluating first factor, which requires perturbation theory. If we define

$$I_{\rm s}^{(n)}(\lambda) = \exp\left\{ -\int_0^{\lambda} dx \left(\frac{1}{2\beta_{\rm s}^{(n)}(x)} + \frac{1}{2b_0 x^2} - \frac{b_1}{2b_0^2 x} \right) \right\}, \tag{3.16}$$

where $\beta_{\rm s}^{(n)}(x)$ is the $n-$loop β function, it is easy to see that (cf. eq.(3.12))

$$\frac{\Lambda_{\rm s}}{\mu_{\rm pt}} \overset{\lambda_s(\mu_{\rm pt})\to 0}{\sim} \left(b_0\lambda_s(\mu_{\rm pt})\right)^{\frac{-b_1}{2b_0^2}} \exp\left(\frac{-1}{2b_0\lambda_s(\mu_{\rm pt})}\right) I_{\rm s}^{(n)}\left(\lambda_s(\mu_{\rm pt})\right) + \mathcal{O}\left(\lambda_s^{n-1}(\mu_{\rm pt})\right) . \tag{3.17}$$

The corrections decrease as powers of $\lambda_s(\mu_{\rm pt})$, and therefore logarithmically (i.e., slowly) with the scale $\mu_{\rm pt}$. The extraction of the $\Lambda_{\rm s}$ parameter has to be performed by taking the limit

$$\begin{aligned}\frac{\Lambda_{\rm s}}{\mu_{\rm had}} = \lim_{\lambda_s(\mu_{\rm pt})\to 0} \left(b_0\lambda_s(\mu_{\rm pt})\right)^{\frac{-b_1}{2b_0^2}} \exp\left(\frac{-1}{2b_0\lambda_s(\mu_{\rm pt})}\right) I_{\rm s}^{(n)}\left(\lambda_s(\mu_{\rm pt})\right) \\ \times \exp\left[-\int_{\lambda_s(\mu_{\rm pt})}^{\lambda_s(\mu_{\rm had})} \frac{dx}{2\beta_{\rm s}(x)} \right] .\end{aligned} \tag{3.18}$$

If $\lambda_s(\mu_{\rm pt})$ is sufficiently small for two-loop perturbation theory to hold, one can insert the equation eq. (3.11) and express the integral factor as follows

$$I_s^{(2)}\left(\lambda_s\right) \simeq \left(1 + \frac{b_1}{b_0}\lambda_s\right)^{\frac{b_1}{2b_0^2}} . \tag{3.19}$$

In the TGF scheme, only the two universal coefficients of the β function are known. Therefore, we will evaluate higher-order corrections by determining the β function from the results of our non-perturbative simulations of the running coupling.

Controlling the limit of eq. (3.18) requires simulating large energy scales with our lattice simulations. Finite size scaling allows this by linking the renormalization

scale with the physical size of the lattice simulation (see section 3.2). The change of the coupling when the renormalization scale changes by a factor of two

$$\sigma(u) = \lambda_s(\mu/2)\Big|_{\lambda_s(\mu)=u}, \tag{3.20}$$

is called the step scaling function and can be obtained from lattice simulations by first tuning the value of the bare coupling λ_0 such that $\lambda_s = u$ for several values of the lattice size $\tilde{L} = \tilde{l}/a$, and then determining the value of the coupling in a lattice twice as large at the same values of the bare coupling λ_0. This procedure results in several values of the lattice step scaling function $\Sigma(u, \tilde{L})$, which must be extrapolated to the continuum.

$$\sigma(u) = \lim_{1/\tilde{L}\to 0} \Sigma(u, \tilde{L})\,. \tag{3.21}$$

Since

$$\int_{\lambda_s(\mu)}^{\lambda_s(\mu/2)} \frac{dx}{\beta_s(x)} = \int_u^{\sigma(u)} \frac{dx}{\beta_s(x)} = -2\log 2\,, \tag{3.22}$$

the step scaling function allows us to accurately determine the last factor in eq. (3.18). Once the function $\sigma(u)$ is known, one defines $u_0 = \lambda_s(\mu_{\text{had}})$, and recursively determines

$$u_k = \sigma^{-1}(u_{k-1})\,. \tag{3.23}$$

Each application of the step scaling function changes the renormalization scale by a factor of 2, so that $u_k = \lambda_s(2^k\mu_{\text{had}})$ and

$$\int_{u_k}^{u_0} \frac{\mathrm{d}x}{\beta_s(x)} = -2k\log 2\,. \tag{3.24}$$

As we will see in chs. 4 and 5, after a reasonable number of steps ($\mathcal{O}(10)$), high energy scales have been achieved, where perturbative corrections are expected to be negligible, and one can explore the limit of eq. (3.18) by taking $\lambda_s(\mu_{\text{pt}}) = u_k$ and $\mu_{\text{pt}} = 2^k\mu_{\text{had}} \gg \mu_{\text{had}}$.

Once $\Lambda_{\text{TGF}}/\mu_{\text{had}}$ is computed, all that remains is to change the renormalization scheme to $\Lambda_{\overline{\text{MS}}}$ and relate it to some physical scale μ_0, such as the flow scale $1/\sqrt{8t_0}$, the string tension $\sqrt{\sigma_0}$, or the Sommer radius $1/r_0$:

$$\frac{\Lambda_{\overline{\text{MS}}}}{\mu_0} = \frac{\Lambda_{\overline{\text{MS}}}}{\Lambda_{\text{TGF}}}\frac{\Lambda_{\text{TGF}}}{\mu_{\text{had}}}\frac{\mu_{\text{had}}}{\mu_0}. \tag{3.25}$$

Crucially, large energy scales can be covered with this procedure. In the next section we discuss the numerical determination of the step scaling function in the TGF setup.

3.4 Numerical setup

We simulate pure $SU(N)$ YM theory on asymmetric lattices of size $L^2 \times \tilde{L}^2$, with $\tilde{L} = NL$, corresponding to a torus in the continuum of size $l^2 \times \tilde{l}^2$, with $\tilde{l} = a\tilde{L}$ and a the lattice spacing. Twisted boundary conditions are implemented by taking the following lattice action

$$S_W(U) = Nb \sum_n \sum_{\mu \neq \nu} \mathrm{Tr}\left[1 - Z^*_{\mu\nu}(n) P_{\mu\nu}(n)\right], \tag{3.26}$$

with plaquettes $P_{\mu\nu}(n)$ given in terms of the $SU(N)$ link variables $U_\mu(n)$ as:

$$P_{\mu\nu}(n) = U_\mu(n) U_\nu(n+\hat{\mu}) U^\dagger_\mu(n+\hat{\nu}) U^\dagger_\nu(n), \tag{3.27}$$

and where $b = 1/\lambda_0 = \beta/(2N^2)$ stands for the inverse of the lattice bare 't Hooft coupling, and $Z_{\mu\nu}(n)$ is set to one for all plaquettes except those with coordinates $x_1 = x_2 = 1$, where:

$$Z_{12} = Z^*_{21} = \exp\{i2\pi k/N\}. \tag{3.28}$$

The values of k and N are chosen meticulously to avoid the appearance of tachyonic instabilities in the large N limit. To saturate the limit that maximizes the absence of these instabilities, the twist factor k and the number of colors N must be scaled as the $n-2$ and n-th terms of the Fibonacci sequence [10], i.e., $N = F_n$ and $k = F_{n-2}$ for each value of n. In this thesis, we will use the TGF scheme to study the running of $SU(N)$ YM theories with the following parameter choices: $(N, k) = (3, 1)$, $(5, 2)$, and $(8, 3)$.

We use a hybrid over-relaxation algorithm [117] that combines a single heat bath sweep (HB) [118, 119] followed by several over-relaxation sweeps (OR) [120]. Since flow measurements are computationally expensive, it is best to produce uncorrelated data for all of our coupling values. For this reason, in $SU(3)$ we chose to perform $\tilde{L}$ hybrid sweeps between measurements. The high cost of the simulations for $SU(5)$ and $SU(8)$ forced us to reduce this number and choose only 10 sweeps between measurements. Note, however, that the autocorrelations are taken into account by analyzing the data using two approaches, one based on resampling techniques such as Jacknife, and the other using the Γ method [121] combined with automatic differentiation [122]. Both approaches give similar results in all cases.

All of our simulations were performed by starting from the vacuum configuration, i.e. the so-called cold start. Notice that with twisted boundary conditions, the vacuum configuration does not correspond to all links set to the identity. For more on the concrete construction of twist eaters matrices, see [68].

In our study, we used the so-called Wilson flow discretization of the continuum flow equation and evaluated the energy density through the Plaquette and Clover discretization given by:

$$E_{\mathrm{pl}}(t) = \mathrm{Tr}\left[1 - Z^*_{\mu\nu}(n) P_{\mu\nu}(n,t)\right], \tag{3.29}$$

$$E_{\mathrm{cl}}(t) = \frac{1}{2}\mathrm{Tr}\left[G_{\mu\nu}(n,t) G_{\mu\nu}(n,t)\right], \tag{3.30}$$

where we defined, denoting $U_{-\mu}(n) = U_\mu^\dagger(n-\mu)$:

$$G_{\mu\nu}(n,t) = -\frac{i}{8}\{Z^*_{\mu\nu}(n)P_{\mu\nu}(n,t) + Z^*_{\mu\nu}(n-\hat{\nu})P_{-\nu\mu}(n,t) + Z^*_{\mu\nu}(n-\hat{\mu})P_{\nu-\mu}(n,t) + Z^*_{\mu\nu}(n-\hat{\mu}-\hat{\nu})P_{-\mu-\nu}(n,t) - c.c.\}, \quad (3.31)$$

with $P_{\mu\nu}(n,t)$ the plaquette evaluated in terms of the flowed links at flow time t.

It is well known that simulations at very fine lattice spacings lose ergodicity [123]. This is not a problem in many of our simulations, since they are performed in small physical volumes, where the contributions of the non-trivial topological sectors are strongly suppressed. Nevertheless, for physical volumes of order $\tilde{l} \sim 1$ fm, CSD can severely affect the results of our studies [114]. For this reason, we define the coupling in the zero topological sector as:

$$\lambda_{\text{TGF}}(\mu) = \mathcal{N}(c,\tilde{L})\frac{\langle t^2 E(t)\,\hat{\delta}_Q\rangle}{N\langle\hat{\delta}_Q\rangle}\Big|_{\sqrt{8t}=c\tilde{l}=\mu^{-1}}, \quad (3.32)$$

where the topological charge Q on the lattice is given by

$$Q = \frac{1}{16\pi^2}\sum_n \text{Tr}\left\{G_{\mu\nu}(n,t)\widetilde{G}_{\mu\nu}(n,t)\right\}, \quad (3.33)$$

evaluated at flow time $\sqrt{8t} = c\tilde{l}$. Since the topological charge given by this expression is not an integer, we have set:

$$\hat{\delta}_Q = \begin{cases} 1 & \text{if } |Q| < 0.5 \\ 0 & \text{otherwise} \end{cases}. \quad (3.34)$$

It has to be emphasized that the renormalization of the coupling is different with and without the projection to the trivial topological sector. Note that the projection to the trivial sector is performed with the flowed definition of the topological charge (c.f. eq. (3.33)), which has a well-defined continuum limit. Therefore, there are no further divergences with this definition. Moreover, since both coupling definitions have the same perturbative expansion to all orders in the continuum, we conclude that the difference has to be non-perturbative finite terms: just a different choice of scheme. We will comment more about this projection in ch. 6.

In addition, and to eliminate the leading order lattice artifacts in perturbation theory, the following lattice normalization factor has been used:

$$\mathcal{N}^{-1}_{\text{pl}}(c,\tilde{L}) = \frac{3c^4}{128}{\sum_q}' e^{-\frac{1}{4}c^2\tilde{L}^2\hat{q}^2}, \quad (3.35)$$

$$\mathcal{N}^{-1}_{\text{cl}}(c,\tilde{L}) = \frac{c^4}{128}\sum_{\mu\neq\nu}{\sum_q}' e^{-\frac{1}{4}c^2\tilde{L}^2\hat{q}^2}\frac{1}{\hat{q}^2}\sin^2(q_\nu)\cos^2(q_\mu/2), \quad (3.36)$$

where $\hat{q}_\mu = 2\sin(q_\mu/2)$ stands for the lattice momentum, with $q_\mu = 2\pi n_\mu/\tilde{L}$ and $n_\mu = 0,\cdots,\tilde{L}-1$. The prime in the sum denotes the exclusion of momenta with both components in the twisted plane satisfying $\tilde{L}q_i \propto 2N\pi$.

3.4.1 Determination of the continuum step scaling function

The lattice step scaling function $\Sigma(u, \tilde{L})$ is determined on the lattice by measuring the coupling λ_{TGF}, at fixed values of b, on a lattice $\tilde{L}$ and its double $2\tilde{L}$ for several values of $\tilde{L}$ and b:

$$\Sigma(u, \tilde{L}) = \lambda_{\mathrm{TGF}}(\mu/2, b)|_{\lambda_{\mathrm{TGF}}(\mu,b)=u}\,, \tag{3.37}$$

at a fixed value of u.

Once the lattice step scaling function $\Sigma(u, \tilde{L})$ is determined, it must be extrapolated to the continuum. In our setup, the leading cutoff effects are $\mathcal{O}(a^2)$. Although this leading behavior receives logarithmic corrections [124], our range of lattice sizes spans a factor of two in lattice spacings, so we expect these logarithmic corrections to be small. Since the goal of this chapter is not to provide a precise result, but rather to explore the viability of the TGF scheme, we will rely on simple linear extrapolations. If data exist for fixed values of the coupling u_i $(i = 1, \ldots, N_{\mathrm{points}})$ and their corresponding values of the lattice step scaling function $\Sigma_i(\tilde{L}) \equiv \Sigma(u_i, \tilde{L})$ for different lattice sizes $\tilde{L}$, we can extrapolate them as:

$$\Sigma_i(\tilde{L}) = \sigma_i + \frac{m_i}{\tilde{L}^2}\,. \tag{3.38}$$

Alternatively, we have tried to extrapolate

$$\frac{1}{\Sigma_i(\tilde{L})} = \frac{1}{\sigma_i} + \frac{m_i'}{\tilde{L}^2}\,. \tag{3.39}$$

The difference between the two approaches is a $1/\tilde{L}^4$ term, which turns out to be negligible in our checks. These extrapolations at fixed values of u_i lead to the corresponding values of $\sigma_i = \sigma(u_i)$ of the step scaling function. This approach is described in detail in section 4.2.1, where we apply it to the case of $SU(3)$ YM theory.

Finding a suitable parametrization for the continuum function $\sigma(u)$ is convenient to obtain the sequence of couplings eq. (3.23). Reasonable parametrizations for the functional form $\sigma(u)$ can be found using perturbation theory as a guide. In particular, we will use the simple parametrization

$$\frac{1}{\sigma(u)} = \frac{1}{u} - 2b_0 \log 2 - 2b_1 u \log 2 + \sum_{k=2}^{N_c} p_k u^k \tag{3.40}$$

to fit our data. This parametrization is obtained by inserting the two-loop expansion of the β function (3.11) into the relation (3.22) and taking the coupling u as the expansion parameter. Note that although this functional form imposes the correct perturbative behavior (for $u \to 0$), after determining the fit parameters p_k using our non-perturbative data, we expect it to describe the non-perturbative step scaling function $\sigma(u)$ in our range of couplings.

Alternatively, since $\sigma(u)$ is a one-to-one function in our range of interest, one can use the inverse relation to parameterize the inverse step scaling function σ^{-1}

that goes into eq. (3.23) by taking the coupling in σ as the expansion parameter, i.e.,

$$\frac{1}{u(\sigma)} = \frac{1}{\sigma} + 2b_0 \log 2 + 2b_1 \sigma \log 2 + \sum_{k=2}^{N_c} \hat{p}_k \sigma^k. \tag{3.41}$$

The two parametrizations should give equivalent results.

Finally, we can combine the continuum limit and the step scaling function parametrization in a single global fit. This approach does not require the coupling to be perfectly tuned to constant values of u and amounts to fitting the data for the lattice step scaling function to the functional form

$$\frac{1}{\Sigma(u, \tilde{L})} = \frac{1}{u} - 2b_0 \log 2 - 2b_1 u \log 2 + \sum_{k=2}^{N_c} p_k u^k + \left(\sum_{k=0}^{N_l} \rho_k u^k \right) \times \frac{1}{\tilde{L}^2}, \tag{3.42}$$

and similarly for the parametrization of the lattice inverse function $\mathcal{U}(x, \tilde{L}) = \Sigma^{-1}(x, \tilde{L})$:

$$\frac{1}{\mathcal{U}(\sigma, \tilde{L})} = \frac{1}{\sigma} - 2b_0 \log 2 - 2b_1 \sigma \log 2 + \sum_{k=2}^{4} p_k \sigma^k + \left(\sum_{k=0}^{4} \rho_k \sigma^k \right) \times \frac{1}{\tilde{L}^2}. \tag{3.43}$$

The step scaling sequence starts at low energy and evolves into high energies in steps by which the momentum scale is changed from μ to 2μ. The two different fitting strategies can be classified as the one that uses the coupling at scale μ as the expansion parameter of the Taylor series and the one that uses the coupling at scale 2μ instead. Again, details of this global approach are presented in section 4.2.2 of ch. 4 applied to $SU(3)$ YM theory. This is the same approach we will use for $N = 5$ and 8 in ch. 5.

3.5 Summary

We have introduced a new renormalization scheme, called twisted gradient flow, based on three main ingredients: a coupling definition within the GF (with the effective size of the torus $\tilde{l}$ acting as the running scale), an asymmetrical geometry, and twisted boundary conditions for the gauge fields. One of the aims of the thesis is to use this renormalization scheme to study the evolution of the coupling constant of $SU(N)$ pure YM theories, extracting important quantities such as the Λ parameter and its N scaling, or topological observables such as the topological susceptibility. This is the content of chapters 4, 5, and 7 respectively.

Motivated by the loss of ergodicity as one approaches the continuum limit, we have introduced an additional element into the TGF scheme by projecting the coupling into the zero topological charge sector. In ch. 6 we will analyze the impact of this projection on the calculation of relevant quantities within this scheme. In particular, we will address the question of whether local fluctuations of the topological charge in the $Q = 0$ sector are correctly sampled despite topological freezing.

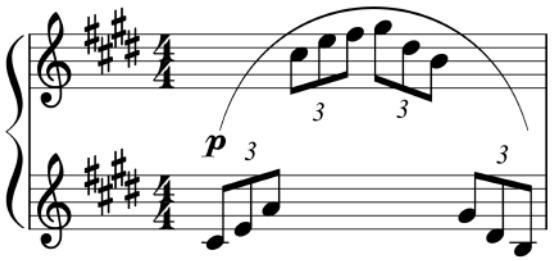

4

$SU(3)$ Λ parameter in the TGF scheme

4.1 Motivation

The goal of this chapter is to compute the Λ parameter of $SU(3)$ pure YM theory using the TGF renormalization scheme [107, 131] introduced in chs. 2 and 3. Throughout the chapter, we will argue that this particular renormalization scheme has several advantages. The running coupling in the pure gauge theory has recently revived interest concerning the quest for precision in the LHC. It has been shown that precise values of the Λ parameter of the zero flavored gauge theory can be used, via a non-perturbative matching between QCD and the pure gauge theory using heavy quarks [132–134], into a precise value for the strong coupling, an essential quantity for phenomenology in high energy physics. Since pure gauge theory is numerically more tractable than QCD, this approach is probably the best way to substantially reduce the uncertainty in the strong coupling. Moreover, it is still necessary to make precise determinations of the running coupling in the pure gauge theory, and this is a challenge in itself.

As well known, there is a consistency problem between the different determinations of the $SU(3)$ pure gauge Λ parameter in the literature. The $r_0\Lambda_{\overline{\text{MS}}}$ values included in the FLAG review [125], displayed in fig. 4.1, are the following: 0.602(48) [126], 0.614(2)(5) [127], 0.637^{+32}_{-30} [128], 0.618(11) [129], 0.621(11) [130], $0.606(9)^{+31}_{-5}$ [99], and 0.660(11) [85]. The most accurate result [85], computed with finite size scaling and within the Schrödinger functional (SF) [135, 136], tends to be larger than, and generally incompatible with, the older determinations included in the FLAG review. Matching with the asymptotic perturbative expansion is the most delicate part of this determination. Substantial deviations between non-perturbative simulations and the expected perturbative behavior have been observed, even when using schemes with known higher-order β function coefficients [85]. A more conservative strategy is to obtain non-perturbatively low couplings and match them to the universal perturbative expansion of the β function. Of course, this has its own trade-off in that it leads to large errors, but it improves the reliability of the result by making no assumptions about the asymptotic behavior. Recently, new results [137, 138] have been obtained with a different method based on the continuous

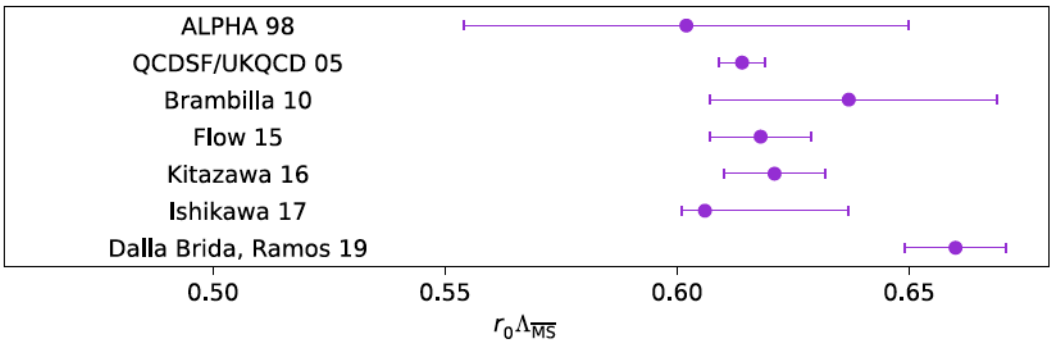

Figure 4.1: Values of $r_0\Lambda_{\overline{\text{MS}}}$ included in the FLAG average [125]. These are: ALPHA 98 [126], QCDSF/UKQCD 05 [127], Brambilla [128], Flow 15 [129], Kitazawa 16 [130], Ishikawa 17 [99], and Dalla Brida, Ramos 19 [85].

β function in the infinite volume limit, where the NNLO β function coefficient b_3 of the GF scheme can be used. However, large lattices are needed to obtain reliable infinite volume extrapolations, and it is not entirely clear whether the matching with perturbation theory is well resolved and how the issue of topology freezing is dealt with. Overall, both results turn out to be compatible with that of [85].

As discussed in ch. 3, the TGF scheme presented in this thesis has several advantages over other more common renormalization schemes, such as the preservation of translation invariance or the absence of zero modes, which directly affects perturbation theory calculations. The use of an asymmetric torus is also advantageous from a computational point of view, as it allows for better performance on the GPU.

As a side note, we emphasize that the TGF scheme is particularly suitable for extracting the N dependence of the Λ parameter of $SU(N)$ gauge theories, since it has a well-defined large N limit and the extraction is computationally cheaper than a brute-force approach on symmetric lattices. These ideas are explored in ch. 5.

In this chapter we explore the viability of the TGF scheme by determining the running of the $SU(3)$ gauge theory coupling, and use it to compute te Λ parameter. We will also check that this particular geometry has no significant effect on the size of scaling violations. In section 4.2 we introduce the lattice calculation of the TGF coupling. In section 4.3 we determine the Λ parameter in the TGF scheme in terms of a hadronic scale μ_{had} and discuss the matching with the SF and $\overline{\text{MS}}$ schemes. Our final result for $\Lambda_{\overline{\text{MS}}}\sqrt{8t_0}$ is presented in section 4.4. We end with some final remarks on the importance of this computation in section 4.5. This computation has been presented in refs. [139, 140].

4.2 $SU(3)$ TGF coupling on the lattice

Table A.1 in Appendix A contains the full set of bare couplings and lattice sizes of our $SU(3)$ pure YM simulations, along with the total number of configurations

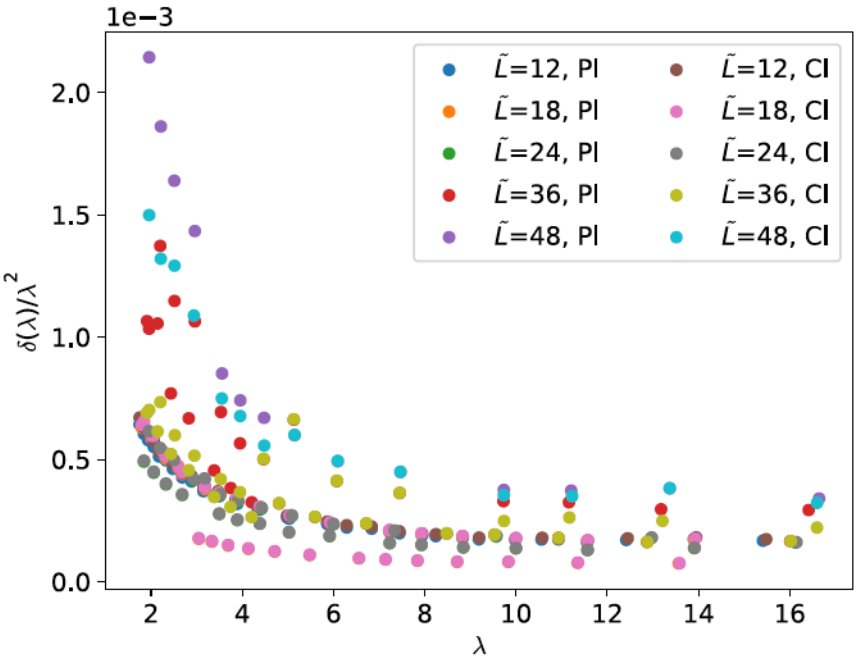

Figure 4.2: Relative errors of the 't Hooft coupling $\delta(\lambda_{\rm TGF})/\lambda^2_{\rm TGF}$ as a function of $\lambda_{\rm TGF}$.

attained in each case. We have used lattices with $\tilde{L} = 12$, 18, 24, 36, and 48 in a range of $b \in [0.33, 1.12]$. Short directions are endowed with twisted boundary conditions with $k = 1$.

The corresponding TGF coupling results, measured at $c = 0.3$, were obtained following the discussion of sec. 3.4, and they are collected in table B.1 in Appendix B for the Clover-like discretization of eq. (3.30). The reason for our choice of scheme parameter c is discussed below.

Since the lattice spacing depends only on the bare lattice coupling, a lattice approximant of the continuum step-scaling function $\sigma(u)$ of eq. (3.20) can be easily evaluated by measuring the renormalized coupling on lattices of size $\tilde{L}$ and $2\tilde{L}$ at the same value of the bare inverse coupling b. We define

$$\Sigma(u, \tilde{L}) = \lambda_{\rm TGF}(\mu/2, b)\Big|_{u=\lambda_{\rm TGF}(\mu,b)} . \tag{4.1}$$

The continuum step scaling function is then obtained as the continuum extrapolation of eq.(3.21) taken at a fixed value of u.

In order to obtain statistical errors of the same order for different values of $\tilde{L}$, we have constrained the uncertainties in all lattices so that the errors of $1/\lambda_{\rm TGF}$ are of the same order for all coupling values. This implies to aim for an statistical accuracy such that the quantity $\delta\lambda_{\rm TGF}/\lambda^2_{\rm TGF}$ is constant for all values of $\lambda_{\rm TGF}$ and $\tilde{L}$. In fig. 4.2, we show the error of $1/\lambda_{\rm TGF}$ as a function of the coupling $\lambda_{\rm TGF}$ for different values of $\tilde{L}$ and for $c = 0.3$. Most lattices are well tunned for $\lambda_{\rm TGF} > 5$ and deviations begin to grow for small coupling values, becoming more significant

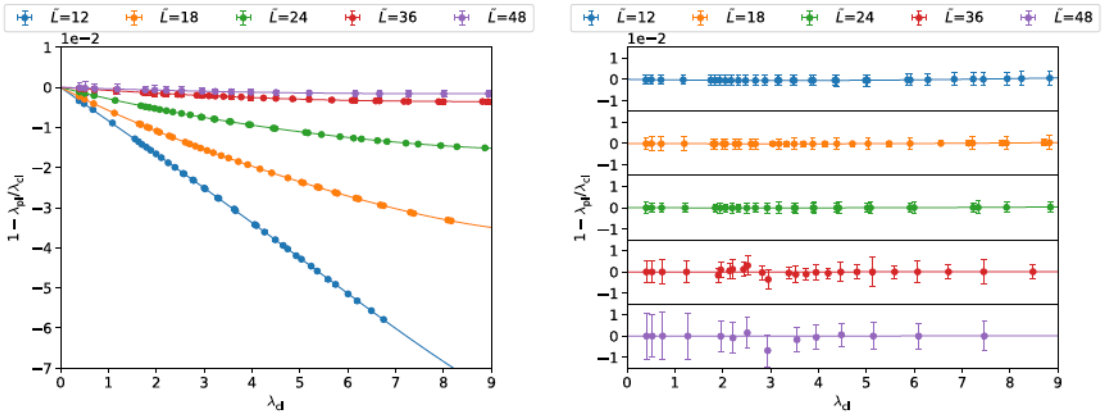

(a) $c = 0.1$ (b) $c = 0.3$

Figure 4.3: Relative size of lattice artifacts for $c = 0.1$ (left) and $c = 0.3$ (right). The couplings $\lambda_{\rm pl}$ and $\lambda_{\rm cl}$ are determined using the Plaquette and Clover discretizations of the energy density of eqs. (3.29) and (3.30) respectively.

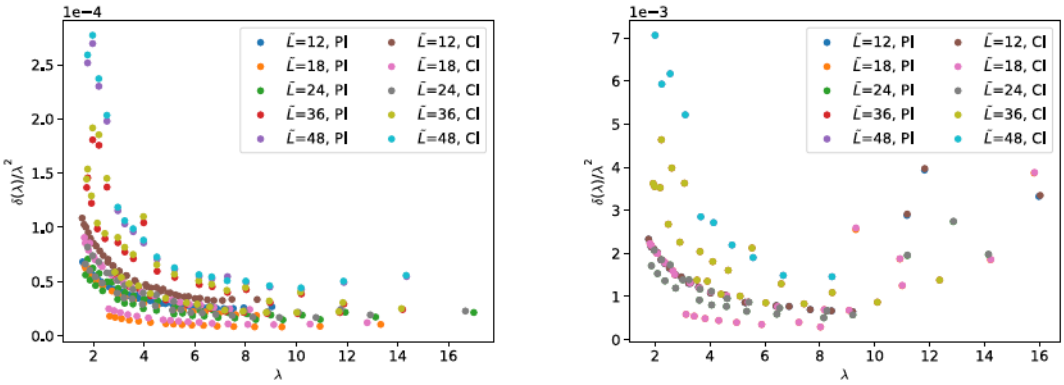

(a) $c = 0.1$ (b) $c = 0.7$

Figure 4.4: Relative errors of $\lambda_{\rm TGF}$ for, from left to right, $c = 0.1$ and $c = 0.7$.

for the largest lattices, where achieving a high level of statistics was not possible. However, we do not expect this to drastically affect the computation of the running coupling.

The choice of c is a compromise between minimizing lattice artifacts without significantly increasing the statistical error. It is well known that small values of c are subject to more significant lattice artifacts, while large values of c lead to higher statistical errors. Our results confirm this observation. To analyze the magnitude of lattice artifacts, we have compared the calculation of the coupling with the Plaquette ($\lambda_{\rm pl}$) and the Clover ($\lambda_{\rm cl}$) discretizations of the energy density – see eq. (3.29) and (3.30). Figure 4.3 compares the relative size of the lattice artifacts between $c = 0.1$ (left) and $c = 0.3$ (right) by plotting $1 - \lambda_{\rm pl}/\lambda_{\rm cl}$ against $\lambda_{\rm cl}$. For $c = 0.3$, the relative difference between the two determinations is less than 5 per mill; however, for c=0.1, the artifacts become as large as 6% in the smallest $\tilde{L} = 12$ lattice.

$u_{\rm tg}$	$\Sigma(u_{\rm tg}, 12)$	$\Sigma(u_{\rm tg}, 18)$	$\Sigma(u_{\rm tg}, 24)$	$\sigma(u_{\rm tg})$
1.8425	1.9503(34)	1.9558(37)	1.9577(61)	1.9602(55)
2.0568	2.1967(38)	2.2002(46)	2.2113(68)	2.2092(65)
2.3270	2.5031(45)	2.5153(50)	2.5147(85)	2.5224(75)
2.6834	2.9271(52)	2.9519(59)	2.9411(99)	2.9607(88)
3.1746	3.5160(66)	3.5278(71)	3.554(11)	3.555(10)
3.4945	3.9068(75)	3.9502(81)	3.955(11)	3.978(11)
3.8881	4.4249(88)	4.475(12)	4.477(12)	4.501(14)
4.3739	5.088(11)	5.113(19)	5.133(17)	5.143(20)
5.0260	5.997(13)	6.058(18)	6.095(20)	6.120(22)
5.9170	7.337(17)	7.453(24)	7.471(27)	7.527(29)
7.2325	9.570(26)	9.758(31)	9.732(37)	9.836(39)
7.9431	10.933(31)	11.202(41)	11.257(48)	11.386(51)
8.8322	12.975(44)	13.223(54)	13.339(73)	13.434(71)
9.9945	16.148(63)	16.575(78)	16.585(96)	16.81(10)
13.91650	32.01(21)	33.21(27)	34.00(25)	34.52(29)

Table 4.1: Values of the lattice step scaling function $\Sigma(u_{\rm tg}, \tilde{L})$ for fixed target values of the coupling $u_{\rm tg}$ and for different values of $\tilde{L}$. We also report the continuum extrapolation $\sigma(u_{\rm tg})$.

Regarding the statistical errors, fig. 4.4 shows the relative errors of the renormalized coupling $\lambda_{\rm TGF}$ for, from left to right, $c = 0.1$ and 0.7. Increasing the value of c removes the lattice artifacts but increases the size of the errors; this is natural since the smearing radius induced by the flow occupies a larger fraction of the box size for large c and the self-averaging within the box decreases, see e.g. [111].

We believe that intermediate values of c are a good compromise, successfully avoiding most of the lattice artifacts without losing control over the statistics (see [107, 136] for more details). Thus, in the rest of this thesis, we will restrict ourselves to the case of $c = 0.3$ unless otherwise specified, and we will also report only the running coupling results for the Clover-like discretization.

4.2.1 Continuum limit on a u-by-u basis

We have tuned the bare coupling b on the $\tilde{L} = 12$, 18, and 24 lattices to attain a few targeted values of the renormalized coupling u (see table C.1 in Appendix C). Once this is achieved, the renormalized coupling is measured on the double-size lattices at the same value as the bare coupling. Since the tuning is not perfect, there is a small mismatch in the tuning of the target couplings, which can be easily corrected by slightly shifting the resulting couplings to a constant value of u.

By using the one-loop perturbative relation

$$\frac{1}{\Sigma(u, \tilde{L})} - \frac{1}{u} = \text{constant}\,, \tag{4.2}$$

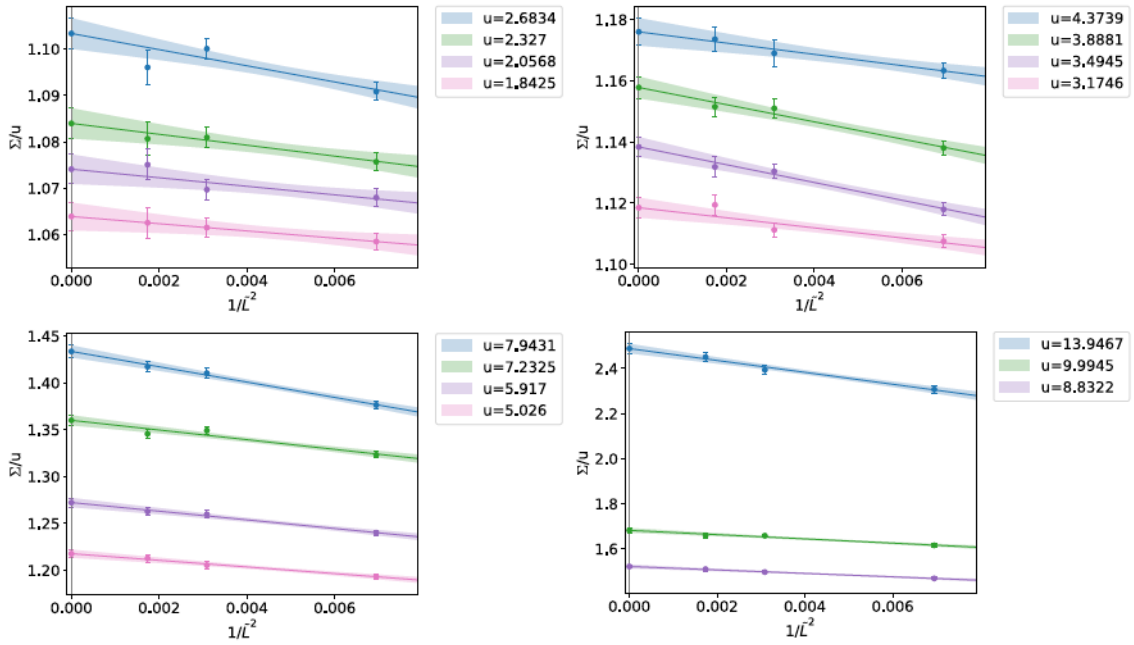

Figure 4.5: We display the continuum extrapolation of $\Sigma(u)/u$, performed at a few selected values of u.

the values of the lattice step scaling function $\Sigma(u, \tilde{L})$ can be shifted to a target value of the coupling $u_{\rm tg}$ using the relation

$$\Sigma(u_{\rm tg}, \tilde{L}) = \Sigma(u, \tilde{L}) + \frac{\Sigma^2(u, \tilde{L})}{u^2}(u - u_{\rm tg})\,. \tag{4.3}$$

Our data set is already well tuned, so the additional shift introduced by this procedure is well below statistical accuracy.

The same one-loop relation can propagate the error of u into an error of the step scaling function. To be precise, we add in quadratures

$$\delta\Sigma(u, \tilde{L}) = \frac{\Sigma^2(u, \tilde{L})}{u^2}\delta u \tag{4.4}$$

to the statistical error of $\Sigma(u, \tilde{L})$. This procedure leads to a set of data at the constant coupling value u for different lattice spacings. The result can be seen in table 4.1, while the raw data is available in table C.1 in Appendix C.

The continuum limit of the step scaling function is obtained by performing a linear extrapolation in $1/\tilde{L}^2$, as illustrated in fig. 4.5. The continuum values of $\sigma(u)$ resulting from these fits are given in table 4.1. The advantage of this procedure over the global fit presented below is that no functional dependence in u is assumed for the terms representing the lattice artifacts (cf. eqs. (3.39) and (3.42)).

The resulting pairs (u, σ) are then fitted to the series expansions given by eqs. (3.40) or (3.41), allowing to parameterize the corresponding step scaling func-

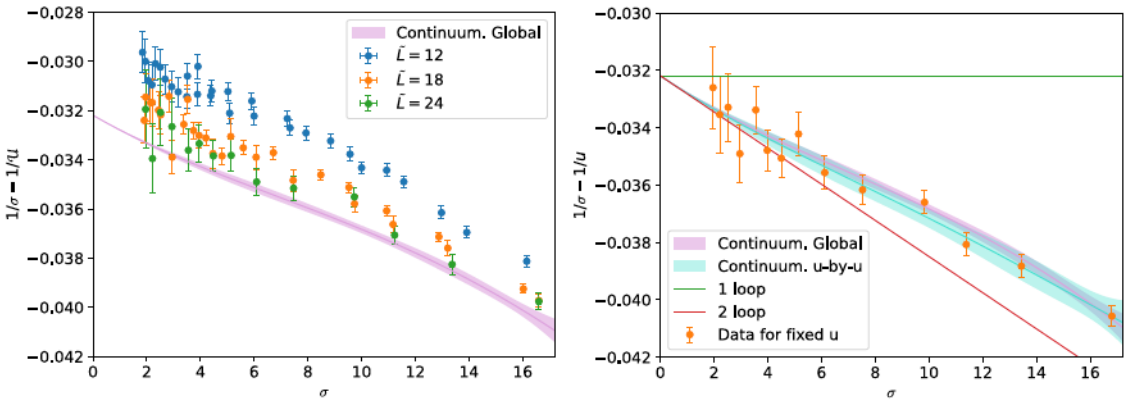

(a) Raw data for $1/\sigma - 1/\mathcal{U}(\sigma, \tilde{L})$ vs σ. (b) Continuum extrapolation of $1/\sigma - 1/u$.

Figure 4.6: (a) Raw data for the inverse step scaling function compared to the continuum extrapolation obtained from the global fit, cf. eqs. (4.7), (4.8). (b) We compare continuum extrapolations of $1/\sigma - 1/u$ as a function of σ. The orange data points correspond to the determination at fixed values of u given in table 4.1. The continuum extrapolations derived from the u-by-u and the global fits described in the text correspond to the blue and pink bands. At the same time, we show continuous lines indicating the one-loop and two-loop perturbative predictions.

tions in the range of couplings under consideration. For completeness, we give the parameters of the fit to eq. (3.41) with $N_c = 4$ and fitting range $\sigma \in [1.5, 17]$:

$$\hat{p}_2 = -2.86020692 \times 10^{-5}, \ \hat{p}_3 = 1.94775566 \times 10^{-6}, \ \hat{p}_4 = -4.21570896 \times 10^{-8}, \quad (4.5)$$

and their covariance:

$$\begin{pmatrix} 9.62610704 \times 10^{-10} & -1.48907565 \times 10^{-10} & 5.49335753 \times 10^{-12} \\ -1.48907565 \times 10^{-10} & 2.37337095 \times 10^{-11} & -8.93899741 \times 10^{-13} \\ 5.49335753 \times 10^{-12} & -8.93899741 \times 10^{-13} & 3.41858249 \times 10^{-14} \end{pmatrix} . \quad (4.6)$$

4.2.2 Continuum limit from a global fit

As an alternative to the u-by-u fit, the continuum limit can be obtained from a combined parametrization of the continuum step scaling function and a continuum extrapolation – see, e.g., eq. (3.42).

The last section shows that the continuum step scaling function is well-parametrized using three parameters in addition to the two universal terms (i.e., $N_c = 4$). Cutoff effects are well described as long as $N_l \geq 3$, with small differences in the continuum results even when the number of parameters is increased to $N_l = 8$. The raw data used in these fits are available in Appendix B. We have fitted the data for $1/\mathcal{U}(\sigma, \tilde{L})$ vs σ in the range $\sigma \in [1.5, 17]$ with the particular choice $N_c = N_l = 4$; the resulting continuum fit parameters are given by:

$$\hat{p}_2 = -3.50622141 \times 10^{-5}, \ \hat{p}_3 = 2.14311070 \times 10^{-6}, \ \hat{p}_4 = -2.97994910 \times 10^{-8}, \quad (4.7)$$

k	TGF	
	$\lambda_{\rm TGF}(2^{k+1}\mu_{\rm had})$	$\Lambda_{\overline{\rm MS}}/(2\mu_{\rm had})$
0	13.9164955	0.18900(10)
1	9.035(13)	0.19019(56)
2	6.7989(88)	0.19271(71)
3	5.4781(96)	0.1948(12)
4	4.5986(99)	0.1965(18)
5	3.9683(96)	0.1978(24)
6	3.4933(89)	0.1989(29)
7	3.1220(81)	0.1998(34)
8	2.8234(74)	0.2005(38)
9	2.5778(67)	0.2011(41)
10	2.3723(60)	0.2017(44)
11	2.1976(55)	0.2021(47)
12	2.0472(50)	0.2026(50)
13	1.9163(45)	0.2029(52)
14	1.8014(41)	0.2032(54)
∞	0.0	0.2082(83)

Table 4.2: We list the couplings along the step scaling sequence starting at $\lambda(2\mu_{\rm had}) = 13.9164955$, computed within the TGF scheme. The final result, quoted in the last line, is obtained from a linear fit to the last 5 steps in the sequence.

with covariance:

$$\begin{pmatrix} 2.87681194\times10^{-10} & -4.50822649\times10^{-11} & 1.69327683\times10^{-12} \\ -4.50822649\times10^{-11} & 7.22888354\times10^{-12} & -2.76073298\times10^{-13} \\ 1.69327683\times10^{-12} & -2.76073298\times10^{-13} & 1.06806168\times10^{-14} \end{pmatrix} . \quad (4.8)$$

The result of this fitting procedure is displayed in fig. 4.6a where the raw data for $1/\mathcal{U}(\sigma,\tilde{L})$ is plotted as a function of σ and compared with the continuum extrapolation resulting from this global fit which is given by the pink band shown in the plot.

Finally, we compare the different continuum extrapolations in fig. 4.6b. The orange points come from the direct extrapolation at fixed target values of u given in table 4.1. The blue and pink bands correspond to the u-by-u and global fits described above, respectively, showing a good agreement in all the range of fitted values. For comparison, the one-loop and two-loop perturbative predictions are also shown in the figure.

4.3 Determination of $\Lambda_{\rm TGF}/\mu_{\rm had}$

The determination of $\Lambda_{\rm TGF}/\mu_{\rm had}$ relies on the use of eq. (3.18), evaluated in terms of a sequence of couplings connecting $\lambda(\mu_{\rm had})$ and $\lambda(\mu_{\rm pt})$. We have performed this

k	MS		SF	
	$\lambda_{\overline{\rm MS}}(2^{k+1}\mu_{\rm had})$	$\Lambda_{\overline{\rm MS}}/(2\mu_{\rm had})$	$\lambda_{\rm SF}(0.9\times 2^{k+1}\mu_{\rm had})$	$\Lambda_{\overline{\rm MS}}/(2\mu_{\rm had})$
0	7.6539(49)	0.11959(18)	7.35(93)	0.207(67)
1	6.3953(76)	0.14936(52)	5.934(36)	0.2263(44)
2	5.3041(72)	0.16265(80)	4.864(11)	0.2212(20)
3	4.5077(69)	0.1708(11)	4.1391(87)	0.2180(22)
4	3.9148(70)	0.1763(16)	3.6138(81)	0.2167(27)
5	3.4591(69)	0.1804(21)	3.2127(75)	0.2164(32)
6	3.0987(66)	0.1836(25)	2.8950(69)	0.2168(36)
7	2.8068(61)	0.1861(29)	2.6364(63)	0.2173(41)
8	2.5656(57)	0.1881(33)	-	-
9	2.3630(52)	0.1898(37)	-	-
10	2.1903(48)	0.1912(40)	-	-
11	2.0414(44)	0.1925(42)	-	-
12	1.9117(41)	0.1935(45)	-	-
13	1.7976(37)	0.1945(47)	-	-
14	1.6965(35)	0.1953(49)	-	-
∞	0.0	0.2097(76)	0.0	0.2175(61)

Table 4.3: We list the couplings along the step scaling sequence starting at $\lambda(2\mu_{\rm had}) = 13.9164955$ for the two remaining strategies ($\overline{\rm MS}$ and SF). The values of $\Lambda_s/(2\mu_{\rm had})$ are obtained by matching to perturbation theory at the corresponding value of $\lambda_s(\mu_{\rm pt})$. Again, the final result is obtained from a linear fit to the last 5 steps of the sequence (3 in the case of SF).

sequence in two steps: an exact step connecting the coupling at scales $\mu_{\rm had}$ and $2\mu_{\rm had}$, followed by a step-scaling sequence, starting at $\lambda(2\mu_{\rm had})$, to be determined by the continuum step scaling functions obtained in the previous sections. Let us now describe these steps in detail.

Determination of $\lambda(\mu_{\rm had})$ We fix the coupling $\lambda(2\mu_{\rm had}) \equiv 13.9164955$ at lattice spacing values corresponding to $\tilde{L} = 12, 18, 24$. The corresponding values of the lattice step scaling function are given in table 4.1 and extrapolate to a continuum value $\lambda(\mu_{\rm had}) = 34.52(29)$.

Determination of $\Lambda_{\overline{\rm MS}}/(2\mu_{\rm had})$ Using the fits of the continuum step scaling function, we determine a sequence of couplings $\lambda_n = \lambda(2^{n+1}\mu_{\rm had})$. The differences between the global and the u-by-u fits in this step are well below our statistical uncertainties. On the other hand, there are several possibilities to determine the ratio $\Lambda_{\overline{\rm MS}}/(2\mu_{\rm had})$:

TGF: One can use the universal coefficients of the β function and the known ratio $\Lambda_{\overline{\rm MS}}/\Lambda_{\rm TGF}$ of eq.(3.18) to determine $\Lambda_{\overline{\rm MS}}/(2\mu_{\rm had})$).

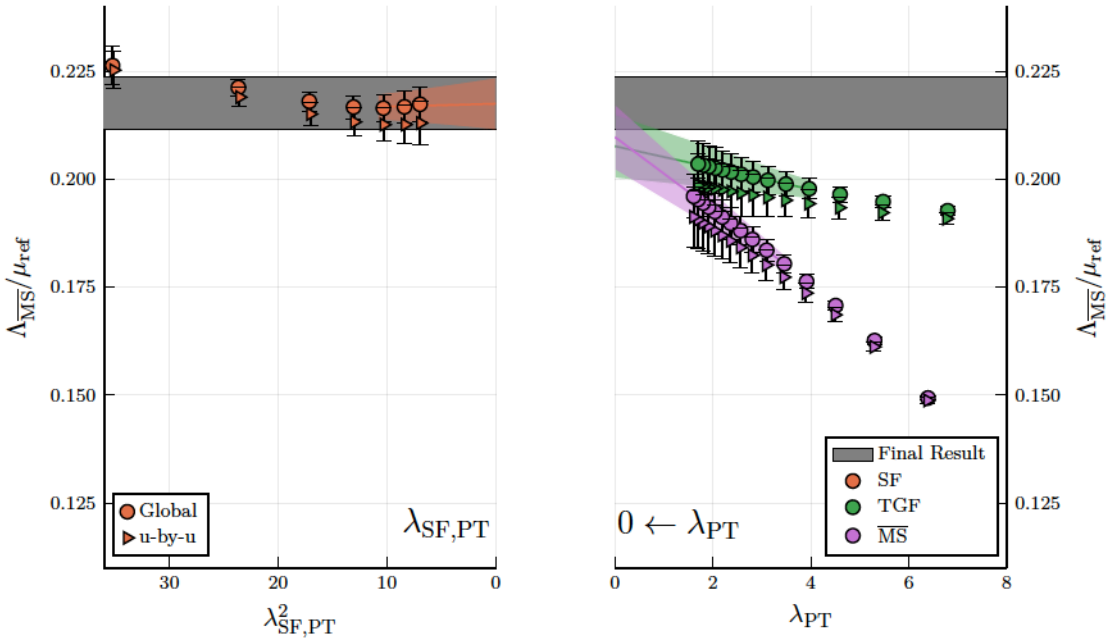

Figure 4.7: Ratio $\Lambda_{\overline{\text{MS}}}/(2\mu_{\text{had}})$ obtained through the different methods explained in the text as a function of the matching scale with perturbation theory ($\mu_{\text{ref}} \equiv 2\mu_{\text{had}}$). The gray band corresponds to the final result obtained from a linear fit to the three last steps of the SF sequence.

MS: One can use the value of the ratio $\Lambda_{\overline{\text{MS}}}/\Lambda_{\text{TGF}}$ to determine the coupling in the $\overline{\text{MS}}$ scheme as follows

$$\lambda_{\overline{\text{MS}}}(2^{n+1}\mu_{\text{had}}) = x + 2b_0x^2\log\left(\frac{\Lambda_{\overline{\text{MS}}}}{\Lambda_{\text{TGF}}}\right) + \mathcal{O}(x^3) \qquad \left(x = \lambda\left(2^{n+1}\mu_{\text{had}}\right)\right). \tag{4.9}$$

Then, using the known 5-loop β function [141] in the $\overline{\text{MS}}$ scheme, one can determine the ratio $\Lambda_{\overline{\text{MS}}}/(2\mu_{\text{had}})$.

SF: High-precision determinations for the SF coupling are available in reference [85]. These computations were performed at the same bare coupling b values as our runs but on lattices of size $\tilde{L}/3$. This allows to non-perturbatively convert the values of $\lambda(2^{n+1}\mu_{\text{had}})$ to values of $\lambda_{\text{SF}}(0.9 \times 2^{n+1}\mu_{\text{had}})$. Details of this matching can be found in Appendix C; here, it is enough to say that this matching is only possible in the region $9 \gtrsim \lambda \gtrsim 3$. After this non-perturbative conversion, the known 3-loop β function in the SF scheme [142–144] can be used to determine the ratio $\Lambda_{\overline{\text{MS}}}/(2\mu_{\text{had}})$.

This procedure is similar to the approach taken in [111], and we encourage the reader interested in the details to consult that reference.

The results for the ratio $\Lambda_{\overline{\text{MS}}}/(2\mu_{\text{had}})$ using the different procedures described above are summarized in tables 4.2 and 4.3, and plotted in figure 4.7. The methods

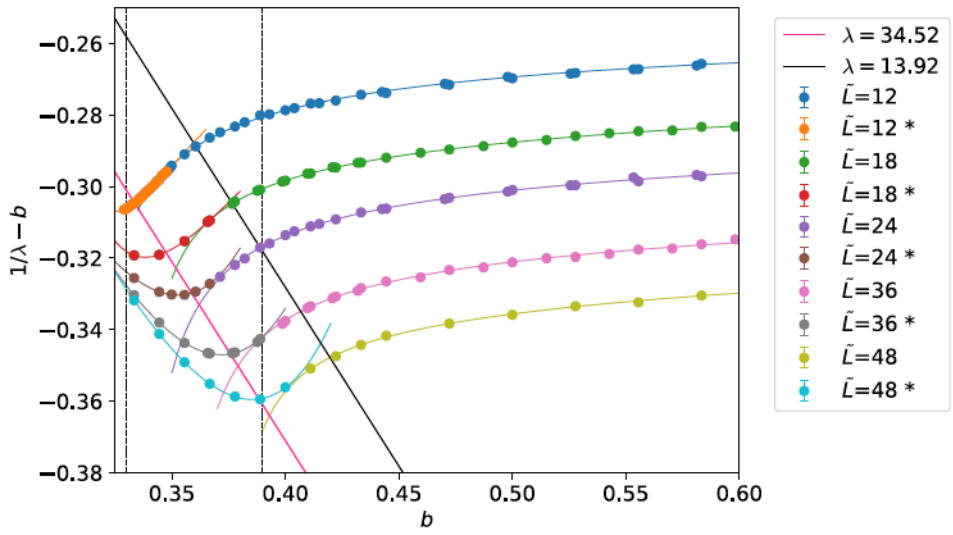

Figure 4.8: We display $1/\lambda - b$ as a function of b. The lines represent Padé fits of the form given in eq. (4.12). The dashed lines with or without $*$ represent different ranges for the Padé-like fits due to the drastic change of coupling behavior around $b \simeq 0.40$. The vertical dotted lines correspond to the maximum and minimum values of t_0/a^2 of table 4.4. Sloped lines correspond to the lines of constant physics at $\lambda(\mu_{\text{had}})$ and $\lambda(2\mu_{\text{had}})$.

labeled TGF and MS carry a perturbative uncertainty $\mathcal{O}(\lambda(2^{n+1}\mu_{\text{had}}))$ (right panel of fig. 4.7), while the SF method carries an uncertainty $\mathcal{O}(\lambda^2(2^{n+1}\mu_{\text{had}}))$ (left panel). Figure 4.7 shows that these perturbative corrections are significant in the methods labeled TGF and MS. Nevertheless, the figure shows a nice agreement between all analysis methods once the limit $\lambda \to 0$ is taken.

Finally, we quote as the central value of the analysis the one labeled as SF since it has the smallest perturbative corrections and is compatible within errors with the other two determinations. We report as final numerical value:

$$\frac{\Lambda_{\overline{\text{MS}}}}{2\mu_{\text{had}}} = 0.2175(61)\,. \tag{4.10}$$

4.4 Computation of $\Lambda_{\overline{\text{MS}}}\sqrt{8t_0}$

To determine the dimensionless combination $\Lambda_{\overline{\text{MS}}}\sqrt{8t_0}$, we must combine our previous results for the ratio $\Lambda_{\overline{\text{MS}}}/\mu_{\text{had}}$ with a determination of $\mu_{\text{had}} \times \sqrt{8t_0}$. This quantity is computed as the continuum extrapolation of

$$\mu_{\text{had}}\sqrt{8t_0} = \lim_{a\to 0}\left(a\mu_{\text{had}} \times \frac{\sqrt{8t_0}}{a}\right), \tag{4.11}$$

where $a\mu_{\text{had}}$ is determined by the lattice size and bare coupling for which the renormalized coupling takes the value $\lambda(\mu_{\text{had}}) = 34.52(29)$ (see table 4.1). Values for

$18 \times b$	t_0/a^2	$18 \times b$	t_0/a^2	$18 \times b$	r_0/a
5.9600	2.7854(62) †	6.4200	11.241(23) †	5.7000	2.9220(90) ††
5.9600	2.7875(53) ‡	6.4500	12.196(21) ‡	5.8000	3.6730(50) ††
6.0500	3.7834(47) ‡	6.5300	15.156(28) ‡	5.9500	4.898(12) ††
6.1000	4.4329(32) ⋆	6.6100	18.714(30) ‡	6.0700	6.033(17) ††
6.1300	4.8641(85) ‡	6.6720	21.924(81) ⋆	6.1000	6.345(13) ⋆
6.1700	5.489(14) †	6.6900	23.089(48) ‡	6.2000	7.380(26) ††
6.2100	6.219(13) ‡	6.7700	28.494(66) ‡	6.3400	9.029(77) ⋆
6.2900	7.785(14) ‡	6.8500	34.819(84) ‡	6.4000	9.740(50) ††
6.3400	9.002(31) ⋆	6.9000	39.41(15) ⋆	6.5700	12.380(70) ††
6.3400	9.034(29) ⋆	6.9300	42.82(11) ‡	6.5700	12.176(97) §
6.3700	9.755(19) ‡	7.0100	52.25(13) ‡	6.6720	14.103(92) ⋆
6.4200	11.202(21) ‡			6.6900	14.20(12) §
				6.8100	16.54(12) §
				6.9000	18.93(15) ⋆
				6.9200	19.13(15) §

Table 4.4: Results for t_0/a^2 and r_0/a for different values of b. For the case of t_0/a^2 the relevant references are † [14], ‡ [145], ⋆ [146]. For r_0/a, the results are instead from †† [147] and ⋆ [146].. The data labeled § is obtained from the values of r_c/a of [148] together with $r_c/r_0 = 0.5133(24)$ which gives the quoted values of r_0/a.

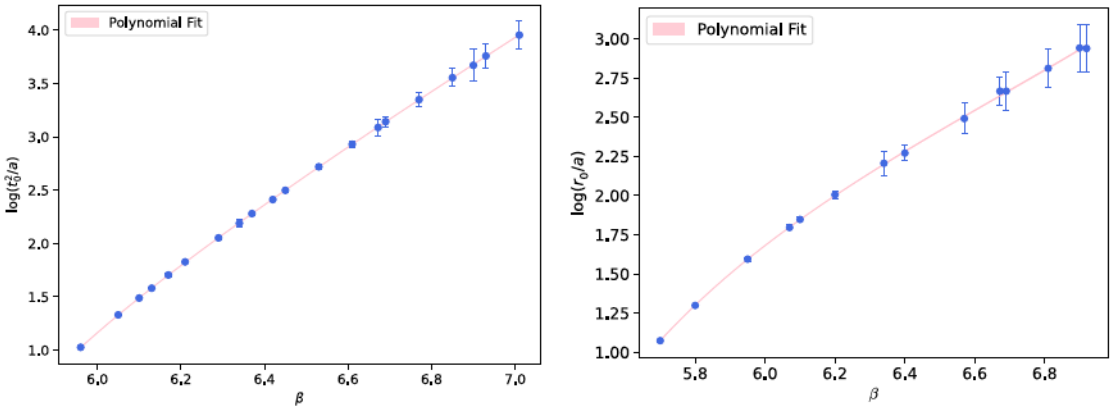

(a) $\log(t_0^2/a)$. **(b)** $\log(r_0/a)$.

Figure 4.9: Polynomial fit of $\log(t_0/a^2)$ and $\log(r_0/a)$ in powers of the bare coupling β. The data is extracted from table 4.4.

$\sqrt{8t_0}/a$ for our choice of Wilson gauge action are available in the literature (see table 4.4).

Two steps were therefore required. First, for each value of $\tilde{L}$, we determined the values of the bare coupling that lead to a renormalized coupling $\lambda(\mu_{\text{had}})$. For

$\tilde{L}$	$18 \times b_{\lambda=34.52}$	$a/\sqrt{8t_0}$	$a\mu_{\text{had}} \times \sqrt{8t_0}/a$	a/r_0	$a\mu_{\text{had}} \times r_0/a$
12	6.0037(26)	0.19637(96)	1.4146(69)	0.1851(20)	1.501(16)
18	6.2518(30)	0.13373(65)	1.3848(68)	0.1256(16)	1.474(18)
24	6.4574(30)	0.10029(47)	1.3848(65)	0.0947(13)	1.467(21)
36	6.7641(36)	0.06683(37)	1.3855(77)	0.0637(15)	1.453(34)
48	6.9908(30)	0.05010(25)	1.3861(70)	0.0471(39)	1.47(12)
∞		0	1.3860(62)	0	1.453(19)

Table 4.5: Values of the bare coupling, lattice spacing and reference scales $\mu_{\text{had}}\sqrt{8t_0}$ and $\mu_{\text{had}}r_0$, corresponding to the renormalization condition $\lambda(\mu_{\text{had}}) = 34.52(29)$ – check sec. 4.3.

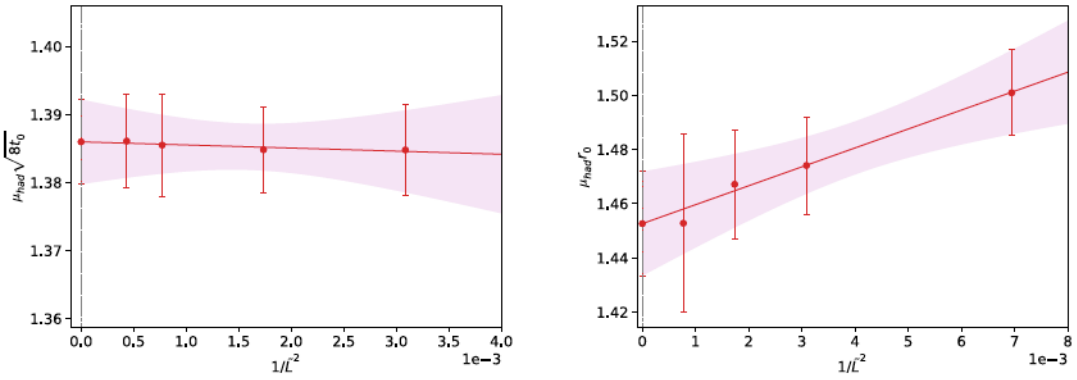

(a) $\mu_{\text{had}} \times \sqrt{8t_0}$. (b) $\mu_{\text{had}} \times r_0$.

Figure 4.10: Continuum extrapolation of the reference scale μ_{had} in units of t_0 and r_0.

this purpose, we fit the dependence of the coupling on b, at fixed $\tilde{L}$, with a Padé fit of the form:

$$b\lambda(b, \tilde{L}) = \frac{a_0 + a_1 b + b^2}{a_2 + a_3 b + b^2}. \tag{4.12}$$

The fits are made to $1/\lambda - b$ with χ^2 tests per degree of freedom ranging from 0.37 to 1.98, as shown in fig. 4.8. The curves marked with a $*$ correspond to different ranges for the Padé approximant due to the drastic change in the b-dependence of the coupling for small values of b. The dotted vertical lines correspond to the window of t_0/a^2 data available on table 4.4. The sloped lines correspond to the lines of constant physics at $\lambda(\mu_{\text{had}})$ and $\lambda(2\mu_{\text{had}})$.

After this, one has to determine $a/\sqrt{8t_0}$ at those values of the bare coupling. Following ref. [85], this is done using the results quoted in refs. [14, 145, 146]. All the values for this quantity given in table 4 of ref. [85] are used to fit $\log(t_0/a^2)$ to a polynomial in b of degree 5 in the range $b \in [0.33, 0.39]$. The polynomial dependence of $\log(t_0/a^2)$ is shown in fig. 4.9a. This fit is then used to determine $a/\sqrt{8t_0}$ at the specific values of the bare coupling corresponding to $\lambda(\mu_{\text{had}})$ on each lattice. The results obtained from this procedure on lattices with $\tilde{L} = 12$, 18, 24, 36, and 48 are given in table 4.5.

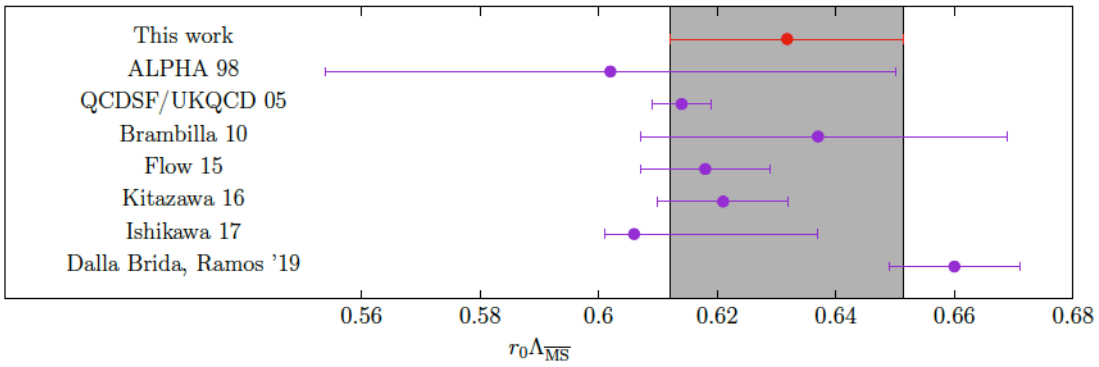

Figure 4.11: Final result for $r_0\Lambda_{\overline{\rm MS}}$ compared with the values included in the FLAG average [125]. These are: ALPHA 98 [126], QCDSF/UKQCD 05 [127], Brambilla [128], Flow 15 [129], Kitazawa 16 [130], Ishikawa 17 [99]. The comparison also includes the recent work Dalla Brida, Ramos 19 [85].

Figure 4.10a shows the continuum extrapolation of $\mu_{\rm had}\sqrt{8t_0}$ obtained using this strategy. We include data points corresponding to the $\tilde{L} = 18$, 24, 36, and 48 lattices. The final continuum extrapolated value is given by:

$$\mu_{\rm had} \times \sqrt{8t_0} = 1.3860(62). \tag{4.13}$$

We can now use these results to express $\Lambda_{\overline{\rm MS}}$ in $\sqrt{8t_0}$ units. Our final result is

$$\sqrt{8t_0} \times \Lambda_{\overline{\rm MS}} = 0.603(17). \tag{4.14}$$

This number is in agreement within errors with the more precise determination obtained in a recent work [85]: $\sqrt{8t_0} \times \Lambda_{\overline{\rm MS}} = 0.6227(98)$. The strategy to obtain the Λ parameter in that work is similar to the one presented here; however, it is based on using a different GF scheme with SF instead of twisted boundary conditions.

A more detailed comparison with the existing literature is better made in terms of the scale r_0 [87], which, although less precise than t_0, is used in most of the previous determinations of the Λ parameter up to date. A similar analysis as the one leading to eq. (4.14) allows determining $r_0 \times \Lambda_{\overline{\rm MS}}$. The values of r_0/a employed in the extrapolation are shown in table 4.4, and the polynomial fit of $\log(r_0/a)$ is shown if fig. 4.9b. The values of the lattice spacing a/r_0 corresponding to the renormalization condition $\lambda(\mu_{\rm had})$ are shown in table 4.5 and the continuum extrapolation is shown in fig. 4.10b, leading to a value of $\mu_{\rm had} \times r_0 = 1.453(19)$. Our final result for the Λ parameter in units of r_0 is:

$$r_0 \times \Lambda_{\overline{\rm MS}} = 0.632(20)\,. \tag{4.15}$$

Figure 4.11 compares this result with the values included in the FLAG average [125]. With the present accuracy, our result comes out compatible with both the FLAG average $r_0 \times \Lambda_{\overline{\rm MS}} = 0.615(18)$ and the result by Dalla Brida and Ramos: $r_0 \times \Lambda_{\overline{\rm MS}} = 0.660(11)$ [85]. We believe that our particular scheme can be efficiently used to pin down the error in the determination of the Λ parameter and clarify the tension among the existing values in the literature.

4.5 Summary

In this chapter, we have studied the running coupling using finite size scaling techniques in a scheme with twisted boundary conditions called twisted gradient flow. We have used a particular choice of geometry, motivated by the study of the large N limit of $SU(N)$ YM theories, in which the size of the four-dimensional torus is asymmetric, with two directions being a factor N larger than the other two.

The chapter is entirely devoted to the $SU(3)$ gauge group. There are many results in the literature for this case, allowing for a more rigorous comparison. Our determination of the $\Lambda_{\overline{\text{MS}}}$ parameter in units of the flow scale $\sqrt{8t_0}$ or the Sommer scale r_0 shows a good agreement with the literature. Our final result is:

$$\begin{aligned}\sqrt{8t_0} \times \Lambda_{\overline{\text{MS}}}^{N=3} &= 0.603(17), \\ r_0 \times \Lambda_{\overline{\text{MS}}}^{N=3} &= 0.632(20)\,.\end{aligned}$$

Even though the precision of our computation does not match the most precise determinations, the systematic associated with the continuum extrapolation is especially taken into account. In addition, the matching with perturbation theory is performed in several ways, using a non-perturbative running that covers large energy scales.

In this respect, it is essential to note that the determination of $\Lambda_{\overline{\text{MS}}}$ is accomplished in two different ways. First, we directly determine the coupling in our finite volume scheme with twisted boundary conditions. In this case, the ratio $\Lambda_{\overline{\text{MS}}}/\Lambda_{\text{TGF}}$ is a crucial piece in the computation. Second, we perform a non-perturbative matching with the SF coupling using available data from the literature. The two determinations show good agreement but with a subtle point. The extraction of the Λ parameter at a specific energy scale μ_{pt} has perturbative corrections $\mathcal{O}(\lambda^k(\mu_{\text{pt}}))$ (with $k = 1$ in the case of the direct extraction, and $k = 2$ for the case of the non-perturbative matching with the SF). A crucial point to obtain compatible results is to remove these subleading perturbative corrections by performing an extrapolation $\lambda(\mu_{\text{pt}}) \to 0$, and at our level of precision (and especially for the case of direct extractions), perturbative corrections are significant, even at large energy scales.

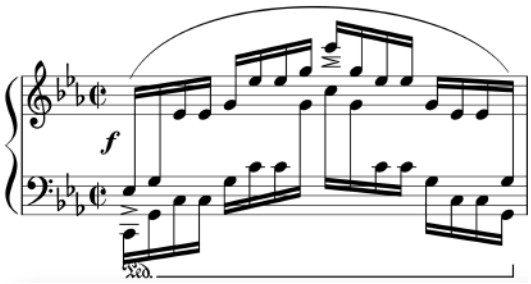

5 $SU(N)$ scaling of the Λ parameter

5.1 Motivation

As discussed in ch. 1, the large N limit emerged as a tool for making expansions in the non-perturbative regime of the strong interactions, in terms of the small parameter $1/N$ [15]. Over the years, it became a powerful tool for understanding the behavior of gauge theories in the presence of many color degrees of freedom, since in this limit the leading correction to the observables comes only from planar diagrams [15]. Although it was initially thought to provide an analytic handle into the low-energy dynamics of strong interactions, these expectations were dashed. However, the approach led to several successful theoretical developments, such as the formulation of closed Wilson loop equations [23], which led to the fundamental concept of the master field [149], a systematic $1/N$ expansion for baryons [24], and several other results not related to the strong interactions, such as the existence of a sector describing supergravity on anti-deSitter spacetimes [25].

In the large N limit, as explained in chapter 2, physical quantities are expected to become volume independent [105], i.e., insensitive to the size of the spacetime volume, as the color and spatial degrees of freedom become entangled. This property has been observed in various gauge theories and led to the famous Eguchi-Kawai (EK) reduction [4].

The concept of volume independence and the related phenomena of EK reduction have been the subject of extensive research over the past few decades [5, 6, 32, 35–51, 54–57, 150, 151]; several of these works are focused on restoring the center symmetry of the EK proposal, which is broken for $d > 2$. These studies have provided valuable insights into the mechanisms underlying volume reduction and the challenges that may arise in its implementation. For a review of volume independence and (twisted) EK reduction, see [105] and references therein. In this chapter, we will use the ideas of volume reduction to study the running coupling properties of YM theories, such as those based on the gauge groups $SU(5)$ and $SU(8)$. Although these values of N are small and cannot be considered as large N limit, our results show the expected N scaling studied in the literature. We will use the TGF renormalization scheme presented in chapter 3. and used in chapter 4

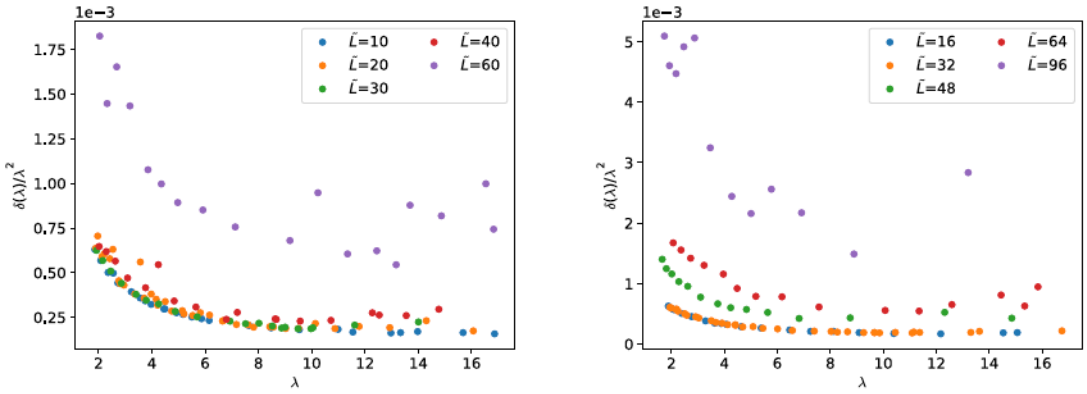

(a) $SU(5)$. (b) $SU(8)$.

Figure 5.1: Relative errors of the 't Hooft coupling $\delta(\lambda)/\lambda^2$ as a function of λ.

to compute the running of $SU(3)$, to obtain the scaling of quantities such as the 't Hooft coupling and the Λ parameter. We will also analyze the effect of boundary conditions and their impact on the determination of the running coupling.

Once again, we want to emphasize that the choice of N and k for the gauge groups studied in this work is not arbitrary, and their values are chosen to avoid the appearance of tachyonic instabilities in the large N limit [9, 10]. Accordingly, we select k and N as the $n-2$ and n-th terms of the Fibonacci sequence, respectively.

The chapter is organized as follows. Section 5.2 contains the computation of the coupling constant and the step scaling function. Section 5.3 summarizes the determination of the $SU(5)$ Λ parameter in physical units. Finally, in section 5.4, we study the dependence of the coupling on the boundary conditions. The chapter ends with some general remarks.

5.2 Step scaling sequence and $\Lambda_{\rm TGF}/\mu_{\rm had}$

5.2.1 Numerical set-up

We have simulated pure $SU(N)$ YM theories on asymmetrical hypercubes of sizes $L^2 \times \tilde{L}^2$, where $\tilde{L} = NL$, with the number of colors taken within the Fibonacci sequence as $N = 5, 8$, with $k = 2$ and 3 respectively. We computed the running of the coupling constant following the same prescription of chapters 3 and 4. The full set of $SU(5)$ configurations for bare coupling raging in $b \in [0.3450, 0.8333]$ and $\tilde{L}$ =10, 20, 30, 40, and 60, are reported in table A.2 of Appendix A. The analogous results for $SU(8)$, with $b \in [0.3555, 0.9445]$ and $\tilde{L}$ =16, 24, 32, 64, and 96, are reported in table A.3 of Appendix A. The results for the renormalized coupling $\lambda_{\rm TGF}$ at $c = 0.30$, for the two values of N and the Clover-like discretization of eq. (3.30), are presented in tables B.2 and B.3 in Appendix B. The results discussed

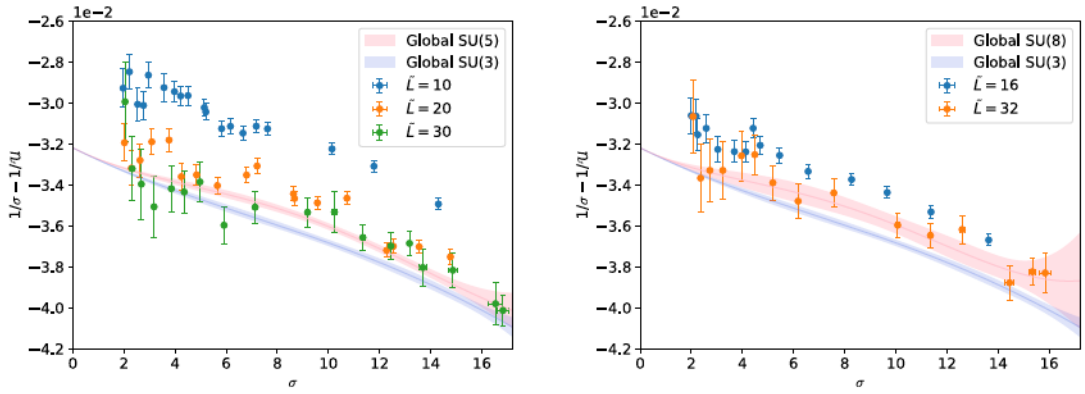

(a) $SU(5)$. (b) $SU(8)$.

Figure 5.2: Raw data for the inverse step scaling function $1/\sigma - 1/\mathcal{U}(\sigma, \tilde{L})$ compared to the continuum extrapolation (pink band) obtained from eqs. (3.43) for $N = 5$ (left) and 8 (right). The blue band represents the continuum extrapolation for $SU(3)$ obtained in ch. 4.

N	$\hat{p}_2$	$\hat{p}_3$	$\hat{p}_4$
5	$-8.11883410 \times 10^{-5}$	$7.75394304 \times 10^{-6}$	$-2.09447526 \times 10^{-7}$
8	$-9.41281947 \times 10^{-5}$	$1.00094809 \times 10^{-5}$	$-3.13446584 \times 10^{-7}$

Table 5.1: Continuum coefficients of the functional form eq. (3.43) of the inverse step scaling function $1/\mathcal{U}(\sigma, \tilde{L})$.

in this chapter are work in progress, and preliminar results have been presented in [140].

Following the same strategy presented in chapter 4, we will restrict the statistical uncertainty in all lattices to satisfy approximately constant errors in the inverse 't Hooft coupling $1/\lambda_{\rm TGF}$. In fig. 5.1 we show the error of $1/\lambda_{\rm TGF}$ as a function of the coupling $\lambda_{\rm TGF}$ for several values of $\tilde{L}$. For the case of $SU(5)$, most lattices are well-tuned except for the largest value of $\tilde{L}$. The case of $SU(8)$ is more delicate, since the computational time needed to obtain high statistics increases significantly, and fig. 5.1 does not show comparable relative errors between the different lattices. For this reason, we present the $SU(8)$ determination as work in progress. Furthermore, the largest lattice for this case, corresponding to $\tilde{L} = 96$, counts with especially low statistics compared to the others, so we will exclude it from the step scaling sequence computation and compute it only with the two smaller values $\tilde{L} = 16$ and 32. Even though these values are large and already close to the continuum, and the fits are made globally to all data simultaneously, we expect the errors associated to the continuum extrapolation to remain relatively large.

k	$SU(5)$		$SU(8)$	
	$\lambda_{\overline{\rm MS}}(2^{k+1}\mu_{\rm had})$	$\Lambda_{\overline{\rm MS}}/(2\mu_{\rm had})$	$\lambda(2^{k+1}\mu_{\rm had})$	$\Lambda_{\overline{\rm MS}}/(2\mu_{\rm had})$
0	13.9164955	0.18672(18)	13.9164955	0.18627(17)
1	9.080(12)	0.18980(54)	9.107(46)	0.1905(20)
2	6.862(12)	0.19535(95)	6.881(33)	0.1964(26)
3	5.541(12)	0.2004(16)	5.557(27)	0.2019(34)
4	4.656(12)	0.2047(22)	4.669(25)	0.2067(47)
5	4.019(11)	0.2082(27)	4.031(24)	0.2107(63)
6	3.5376(94)	0.2112(32)	3.548(23)	0.2141(78)
7	3.1607(83)	0.2137(36)	3.169(21)	0.2170(92)
8	2.8573(74)	0.2158(40)	2.865(19)	0.219(11)
9	2.6077(66)	0.2177(43)	2.615(18)	0.222(12)
10	2.3988(59)	0.2193(46)	2.405(16)	0.223(13)
11	2.2212(53)	0.2207(49)	2.227(15)	0.225(14)
12	2.0683(47)	0.2219(51)	2.073(14)	0.227(15)
13	1.9354(43)	0.2230(53)	1.940(12)	0.228(16)
14	1.8187(39)	0.2240(55)	1.823(11)	0.229(16)
∞	0.0	0.2388(83)	0.0	0.247(27)

Table 5.2: Step scaling sequence of the coupling, starting at $\lambda(2\mu_{\rm had}) = 13.9164955$. The final result, at $k \to \infty$, is obtained from a linear extrapolation with the last 5 steps in the sequence.

5.2.2 Continuum step scaling function

The step scaling function $\sigma(u)$ is obtained as the continuum extrapolation of the lattice step scaling function $\Sigma(u, \tilde{L})$. Of the two strategies followed in the case of $SU(3)$ for obtaining the continuum step scaling function, we will only consider the one that involves a global fit to all data set, since fits on a u-by-u basis require a tuning of the coupling that has not been done in this case.

The function $\Sigma(u, \tilde{L})$ and its inverse $\mathcal{U}(\sigma, \tilde{L})$ can be parametrized using eq. (3.42) and eq. (3.43). These expansions are fitted to the non-perturbatively determined couplings to obtain the step scaling sequence that connects $\mu_{\rm had}$ and $\mu_{\rm pt}$. We have tested that these functions are well described using 3 coefficients p_k for the continuum (in addition to the 2 universal ones) and 5 coefficients for the cutoff effects. Consistent results are obtained between both parametrizations, so we will concentrate on showing the results for the inverse step scaling function $\mathcal{U}(\sigma, \tilde{L})$.

We have fitted the raw data for $1/\mathcal{U}(\sigma, \tilde{L})$ of Appendix B as a function σ to the functional form of eq. (3.43), in a range of coupling $\sigma \in [1.5, 17]$. Table 5.1 contains the results for the continuum fit parameters.

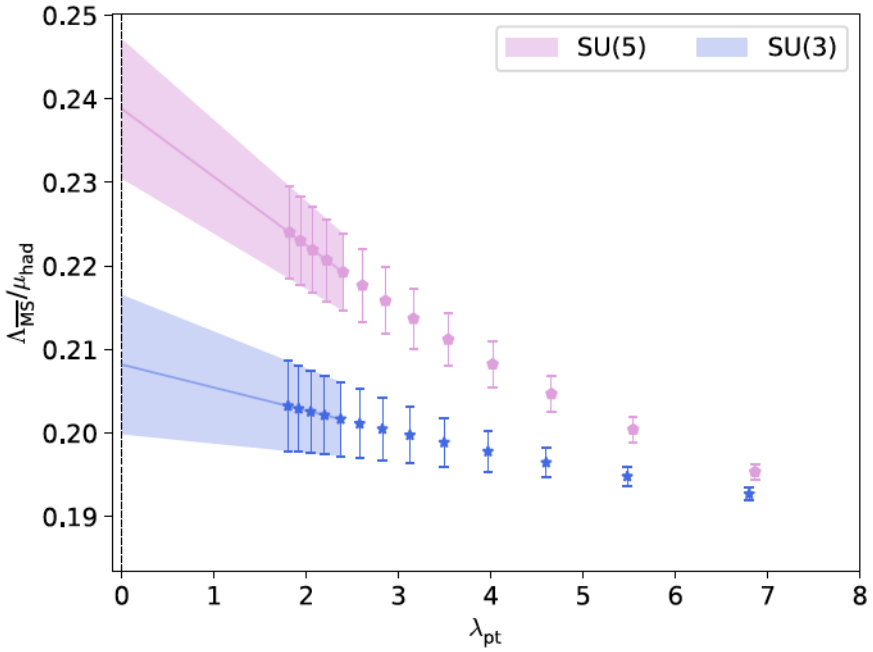

Figure 5.3: Extrapolation of $\Lambda_{\overline{\mathrm{MS}}}/\mu_{\mathrm{had}}$ for $N = 3$ and 5.

For completeness, we also give their corresponding covariance matrices:

$$SU(5) \to \begin{pmatrix} 3.33747650 \times 10^{-10} & -5.37605775 \times 10^{-11} & 2.09862732 \times 10^{-12} \\ -5.37605775 \times 10^{-11} & 8.90180675 \times 10^{-12} & -3.55217046 \times 10^{-13} \\ 2.09862732 \times 10^{-12} & -3.55217046 \times 10^{-13} & 1.44398855 \times 10^{-14} \end{pmatrix}.$$

$$SU(8) \to \begin{pmatrix} 2.45255550 \times 10^{-9} & -4.0419718 \times 10^{-10} & 1.60738054 \times 10^{-11} \\ -4.0419718 \times 10^{-10} & 6.83753802 \times 10^{-11} & -2.77284123 \times 10^{-12} \\ 1.60738054 \times 10^{-11} & -2.77284123 \times 10^{-13} & 1.14197540 \times 10^{-13} \end{pmatrix}.$$

These continuum extrapolations compared to the raw data for $1/\mathcal{U}(\sigma, \tilde{L})$ are shown in fig. 5.2. We also display as a blue band the continuum extrapolation for $SU(3)$ computed in ch. 4.

5.2.3 Step scaling sequence

As for the $SU(3)$ case, we will perform the step scaling sequence in two steps. First, an exact step from μ_{had} to $2\mu_{\mathrm{had}}$, followed by a step scaling sequence starting at $\lambda(2\mu_{\mathrm{had}})$, which will be obtained from the previously determined continuum step scaling function.

For the sake of comparison with $SU(3)$, we will first select $2\mu_{\mathrm{had}}$ through the condition $\lambda(2\mu_{\mathrm{had}}) = 13.9164955$. However, this choice will not allow us to determine the $\overline{\mathrm{MS}}$ in physical units, due to the lack of determinations of the lattice spacing in

$50 \times b$	$a \times \sqrt{\sigma_0}$	$50 \times b$	$a \times \sqrt{\sigma_0}$	$50 \times b$	$a \times \sqrt{\sigma_0}$
16.755	$0.3844(21)^{\dagger}$	17.430	$0.22217(37)^{\dagger\dagger}$	18.040	$0.15622(38)^{\dagger\dagger}$
16.975	$0.3034(20)^{\dagger}$	17.450	$0.2221(17)^{\dagger}$	18.079	$0.14980(67)^{\star}$
16.980	$0.3033(8)^{\dagger\dagger}$	17.567	$0.20070(70)^{\star}$	18.366	$0.12861(82)^{\star}$
17.220	$0.2546(6)^{\dagger\dagger}$	17.630	$0.19636(35)^{\dagger\dagger}$	18.375	$0.13106(30)^{\dagger\dagger}$
17.270	$0.2452(15)^{\dagger}$	17.942	$0.16334(73)^{\star}$	18.859	$0.10070(50)^{\star}$

Table 5.3: Results foR $a\sqrt{\sigma_0}$ as a function of the bare coupling b. for $SU(5)$. The data labeled with † is extracted from [152], the one labeled †† from [153], and the one labeled * from [35]. The highlighted entries are used for the polynomial fit of $\log(a\sqrt{\sigma_0})$ in powers of b.

the appropriate window. A better choice for this purpose will turn out to be, as we will se in sec. 5.3, $\lambda(2\mu_{\rm had}) = 16.062$.

Using as renormalization condition $\lambda(2\mu_{\rm had}) = 13.9164955$, we performed the running up to the lowest simulated coupling of our raw data, i.e., $k = 14$ iterations. Once we reached the perturbative regime, we used the universal coefficients of the β function and the ratio $\Lambda_{\overline{\rm MS}}/\Lambda_{\rm TGF}$ to extrapolate $\Lambda_{\overline{\rm MS}}/(2\mu_{\rm had})$.

The results for $\Lambda_{\overline{\rm MS}}/(2\mu_{\rm had})$ are contained in table 5.2 for all values of $N = 5$ and 8. These results must be compared with the corresponding $SU(3)$ results from table 4.2. For each iteration k we report the corresponding coupling $\lambda(2^{k+1}\mu_{\rm had})$ and the Λ parameter $\Lambda_{\overline{\rm MS}}/(2\mu_{\rm had})$. The last value in each case is obtained by linear extrapolation in λ, taking the last five values of the sequence. Figure 5.3 shows a comparison between $SU(3)$ and $SU(5)$ sequences. As commented before, the errors in the $SU(8)$ calculation are considerably larger than in the other two cases, so we have excluded that sequence from this comparison.

5.3 Computation of $\Lambda_{\overline{\rm MS}}/\sqrt{\sigma_0}$ for $SU(5)$

In this section, we will determine the lattice spacing as a function of the bare coupling b using the data available in the literature; we will then transform the Λ parameter of $SU(5)$ to physical units. We do not perform this computation for the case of $SU(8)$ due to the large uncertainty in our determination of the ratio $\Lambda_{\rm TGF}/(2\mu_{\rm had})$ and the lack of string tension values for a suitable range of bare couplings fitting our determination.

5.3.1 Determination of lattice spacing in physical units: $a\sqrt{\sigma_0}(\beta)$

The flow scale t_0 is commonly used as an intermediate theoretical scale due to its precise definition and high-level statistical determinations. Still, most data in the literature refers to the $SU(3)$ case, and those corresponding to different values of N are restricted to a limited range of bare couplings b. Instead, other physical scales

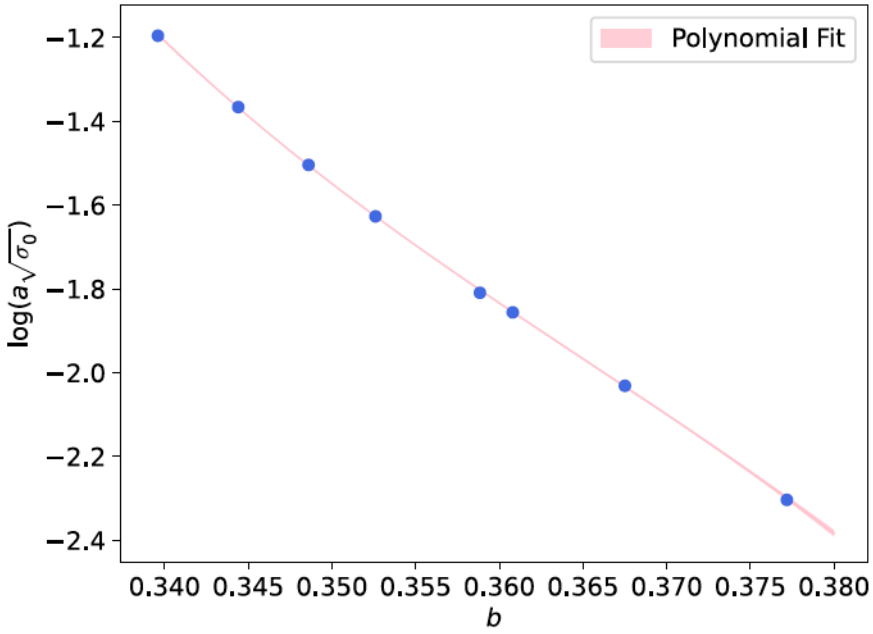

Figure 5.4: Polynomial fit of $\log(a\sqrt{\sigma_0})$ in powers of the bare coupling b. The data is extracted from the highlighted entries of table 5.3.

can be used, as for instance, the string tension $\sqrt{\sigma_0}$ or the Sommer radius r_0. We will use the string tension for our determination.

Table 5.3 contains the values of $a\sqrt{\sigma_0}$ as a function of b found in the literature, and we will use them to fit $\log(a\sqrt{\sigma_0})$ to a polynomial in powers of b. The values in the table are not completely consistent with each other, so we will use the combination that gives the best χ^2 test per degree of freedom. The functional form of the lattice spacing $\log(a\sqrt{\sigma_0})$ is shown in fig. 5.4.

5.3.2 Determination of $\Lambda_{\overline{\text{MS}}}/\sqrt{\sigma_0}$

Once the lattice spacing is determined, the remaining ingredient for computing the Λ parameter in physical units is the corresponding energy scale μ_{had}, i.e., $\mu_{\text{had}}/\sqrt{\sigma_0}$, which is extracted with the following continuum extrapolation

$$\mu_{\text{had}} \times \frac{1}{\sqrt{\sigma_0}} = \lim_{a\to 0} \left(a\mu_{\text{had}} \times \frac{1}{a\sqrt{\sigma_0}} \right) , \tag{5.1}$$

where $a\mu_{\text{had}}$ is fixed with the lattice size $\tilde{L}$ and the bare coupling value b.

The procedure follows the steps described in sec. 4.4 for $SU(3)$. First, for each value of $\tilde{L}$, we extracted the corresponding bare coupling b for which $\lambda_{\text{TGF}} = \lambda(\mu_{\text{had}})$. For this purpose, we fit the dependence of λ_{TGF} on the bare coupling b with the Padé-like fit of eq. (4.12). The fits of $1/\lambda - b$ are shown in fig. 5.5. Finally, we can evaluate

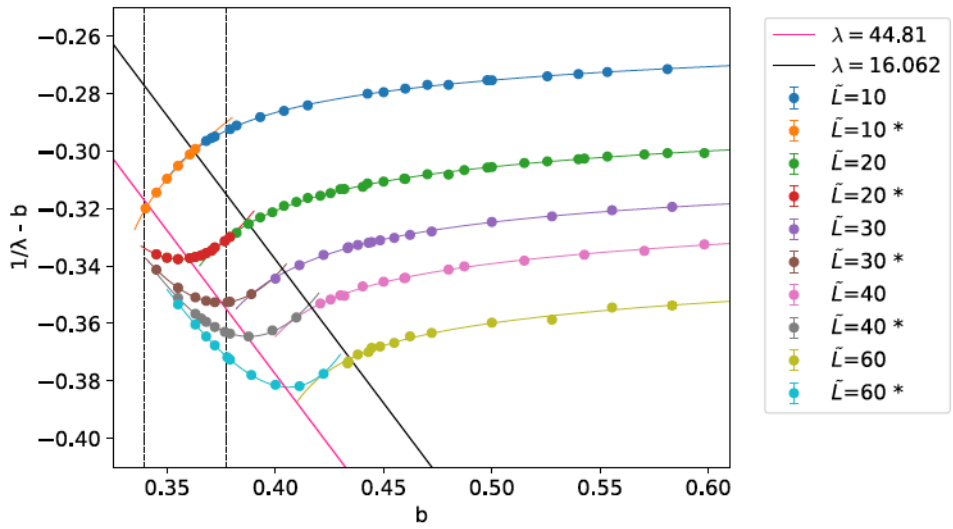

Figure 5.5: Padé-like fits of $1/\lambda - b$ as a function of b given in eq. (4.12), for the case of $SU(5)$. The two vertical dashed lines correspond to the window of b values for which we have $a\sqrt{\sigma_0}$ data.

$\tilde{L}$	$b_{\lambda=43.62}$	$a\sqrt{\sigma_0}$	$a\mu^*_{\rm had} \times 1/(a\sqrt{\sigma_0})$
10	17.0511(11)	0.2875(22)	1.1595(88)
20	17.9853(15)	0.1611(10)	1.0348(66)
30	18.7518(19)	0.1066(22)	1.042(22)
∞		0	1.0027(80)

Table 5.4: Values of the bare coupling, lattice spacing, and reference scale $\mu_{\rm had}/\sqrt{\sigma_0}$, corresponding to the renormalization condition $\lambda(\mu^*_{\rm had}) \equiv 44.81(23)$.

these bare couplings in the polynomial form of fig. 5.4 and extract the corresponding values of tha lattice spacing. The value of $\mu_{\rm had}/\sqrt{\sigma_0}$ is obtained, following the same procedure as in sec. 4.4, as the continuum extrapolation of these results.

At this point it becomes clear that the renormalization condition chosen in the previous section is not optimal for this calculation. The corresponding values of b do not fall in the window for which we have measurements of the lattice spacing in physical units $b \in [0.3390, 0.3772]$, shown between the 2 vertical dotted lines in fig. 5.5.

For this reason we have chosen a new renormalization condition, $\lambda(2\mu^*_{\rm had}) = 16.062$, which corresponds to a simulated value in a lattice of $\tilde{L} = 20$ and $b = 0.3876$ (see tab. B.2). We have extracted from the Padé-like fits of fig. 5.5 the corresponding bare couplings for the lattices of $\tilde{L} = 10$ and 30, and with these values we reevaluate the fits to obtain $\Sigma(u, \tilde{L})$ in the double lattices. Finally, we extrapolate to the continuum these values in fig. 5.6a to obtain $\lambda(\mu^*_{\rm had}) = 44.81(23)$ as in sec. 4.4 for $SU(3)$.

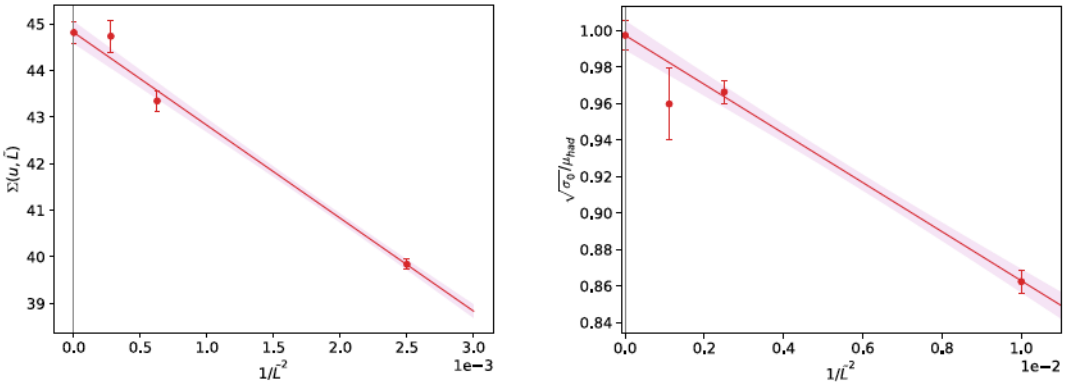

(a) Extrapolation of $\Sigma(u, \tilde{L})$. **(b)** Extrapolation of $\sqrt{\sigma_0}/\mu_{\text{had}}$.

Figure 5.6: (a) Continuum extrapolations of the step scaling function. The continuum value is $\lambda(\mu^*_{\text{had}}) \equiv 44.81(23)$, corresponding to $\lambda(2\mu^*_{\text{had}}) = 16.062$. (b) Continuum extrapolation of the reference scale μ_{had} in units of $\sqrt{\sigma_0}$.

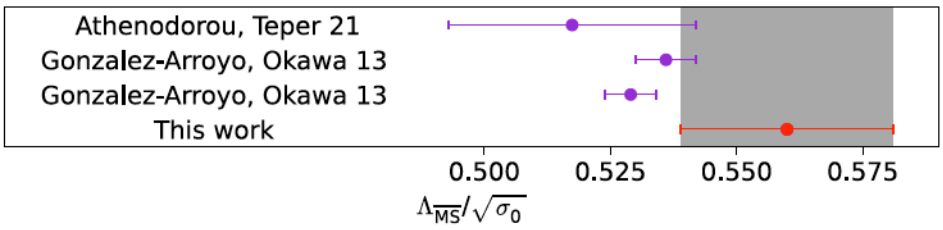

Figure 5.7: Comparison of our result for $\Lambda_{\overline{\text{MS}}}/\sqrt{\sigma_0}$. They correspond to [153] and [35]. The two results from ref [35] come from different ways of determining the value of the Λ parameter. This gives an idea of the size of systematic errors in their calculation.

Table 5.4 contains the results obtained with this procedure. Finally, a continuum extrapolation, shown in fig. 5.6b, gives us the following scale setting:

$$\mu^*_{\text{had}} \times \frac{1}{\sqrt{\sigma_0}} = 1.0027(80). \tag{5.2}$$

Using the same procedure of sec. 4.4, we have repeated the step scaling sequence for $\Lambda_{\overline{\text{MS}}}/2\mu_{\text{had}}$ starting at coupling $\lambda(2\mu^*_{\text{had}}) = 15.753(40)$. We only quote the results of the extrapolation:

$$\frac{\Lambda_{\overline{\text{MS}}}}{2\mu^*_{\text{had}}} = 0.279(10). \tag{5.3}$$

We can now express $\Lambda_{\overline{\text{MS}}}$ for $SU(5)$ in physical units by multiplying eq. (5.2) and eq. (5.3). Our final result is

$$\Lambda_{\overline{\text{MS}}} \times \frac{1}{\sqrt{\sigma_0}} = 0.560(21). \tag{5.4}$$

Figure 5.7 compares our results with some determinations in the literature. With our present accuracy, our results turn out to be compatible with all other calculations, although with rather large errors. The two determinations of [35] come from different ways of determining the Λ parameter, which gives an idea of the systematic uncertainties involved in their calculation.

5.4 Coupling dependence with the boundary conditions

We have used the fact that in the large N limit finite volume effects are controlled by an effective size $\tilde{l} = Nl$ to argue that our boxes are effectively symmetric. This is only true in the large N limit, and there will be finite N corrections which we will try to estimate in this section. In addition, it should be noted that the box we use has different boundary conditions in the different planes, and this also introduces an asymmetry. This effect is irrelevant in the thermodynamic limit, but it has an important effect when working on finite volumes, where boundary conditions are important. This is reflected, for example, in the dependence of physical quantities on the non-commutativity parameter $\hat{\theta}$.

As discussed in ch. 2, the dependence of $\log(\Lambda_{\rm TGF}/\Lambda_{\overline{\rm MS}})$ on $\hat{\theta}$ can be analytically determined in PT for different choices of the scheme parameter c. The infinite volume case corresponds to $c = 0$ with value:

$$\frac{\Lambda_{\rm TGF}}{\overline{\rm MS}} = 1.87208787\,. \tag{5.5}$$

For $c = 0.3$, and the values of N and k used in this thesis, we obtain instead

$$\frac{\Lambda_{\rm TGF}}{\Lambda_{\overline{\rm MS}}} = \begin{cases} 2.0063(11) & \text{for } \hat{\theta} = 1/3 \\ 2.0309(39) & \text{for } \hat{\theta} = 2/5 \\ 2.0359(39) & \text{for } \hat{\theta} = 3/8 \end{cases}.$$

In this section, we will quantify the effect of boundary conditions by selecting coupling schemes corresponding to our asymmetric volume setup, but where instead of averaging the coupling over all possible planes, we do it over a restricted set of planes, classified into 4 different sets:

APA (***All-Plane-Averaged***) – Calculation of sec. 5.2, where we have averaged the coupling in all 6 different planes of the twisted box.

TT (***Twisted-Twisted***) – One plane having a non-trivial twist in both directions; for our choice of twist, this is the 12 plane and both directions have size L in lattice units.

PT (***Periodic-Twisted***) – Four planes sharing one direction with the twisted plane, i.e. $01, 02, 13, 23$. In this case, one direction has length L and the other NL, both in lattice units.

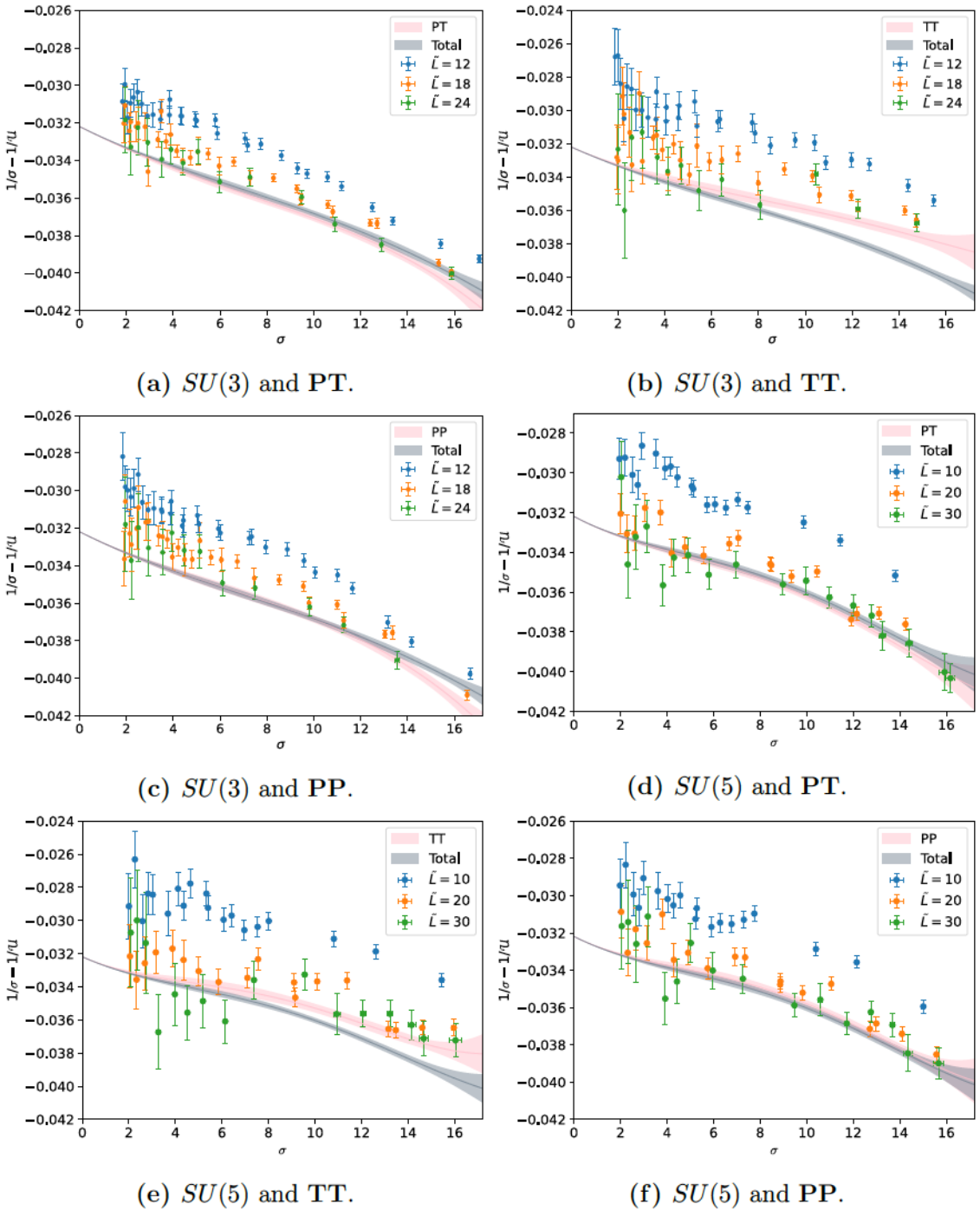

(a) $SU(3)$ and **PT**. (b) $SU(3)$ and **TT**.

(c) $SU(3)$ and **PP**. (d) $SU(5)$ and **PT**.

(e) $SU(5)$ and **TT**. (f) $SU(5)$ and **PP**.

Figure 5.8: Continuum step scaling function $1/\sigma - 1/\mathcal{U}(\sigma, \tilde{L})$ as a function of the coupling σ for $SU(3)$ and $SU(5)$. We have excluded the computation of $SU(8)$ due to its low statistics.

PP (***Periodic-Periodic***) – The last one is the orthogonal plane to the twisted one; for our choice of twist, this corresponds to the 03 plane, and both directions have size NL in lattice units.

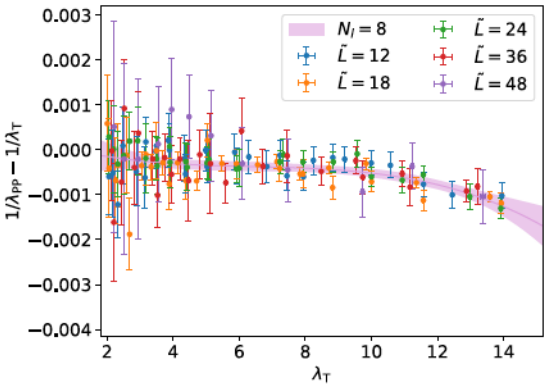

(a) SU(3).

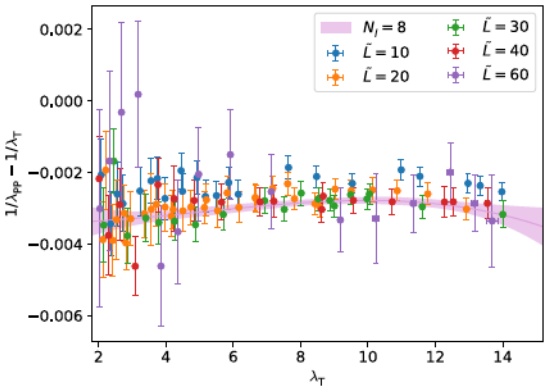

(b) SU(5).

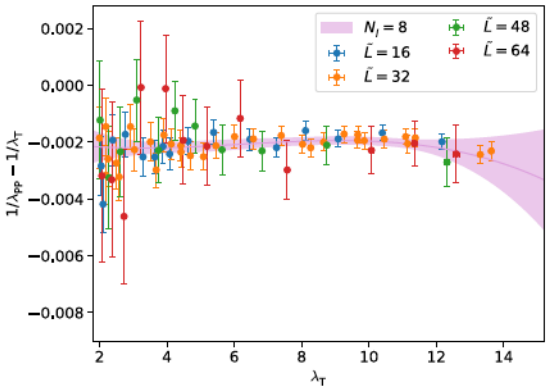

(c) SU(8).

Figure 5.9: Non-perturbative matching between **PP** and **APA** coupling. The purple band is a continuum extrapolation based on a functional form given by eq. (5.7).

Notice that since the boundary conditions are different between the non-equivalent sets of planes, each of them represents a different renormalization scheme, and the one-loop factor $\Lambda_{\overline{\text{MS}}}/\Lambda_{\text{TGF}}$ of eq. (3.13) (calculated in the scheme averaged over all planes) cannot be used to transform the computation of the Λ parameter into the $\overline{\text{MS}}$ scheme. Instead, reproducing the calculation of $\Lambda_{\text{TGF}}/\mu_{\text{had}}$ per plane gives us a numerical estimate of these factors, which have not yet been calculated in perturbation theory.

To ensure the correct leading behavior of the coupling in each set of planes, the normalization factor of eq. (3.32) must be corrected as follows

$$\mathcal{N}_{cl}(c,\tilde{L})_{\mu\nu} = \frac{c^4}{128}\sum_{q}{}' e^{-\frac{1}{4}c^2\tilde{L}^2\hat{q}^2}\left(\sin^2(q_\mu)\cos^2\left(\frac{q_\nu}{2}\right)+\sin^2(q_\nu)\cos^2\left(\frac{q_\mu}{2}\right)\right)\frac{1}{\hat{q}^2}\,, \tag{5.6}$$

where we have removed the (μ,ν) sum of the **APA** computation. We show only the correction for the Clover-like discretization. The 't Hooft coupling λ_{TGF} computed with this procedure, for the three different **PP**, **PT** and **TT** determinations is contained in tables B.4 to B.12 of Appendix B.

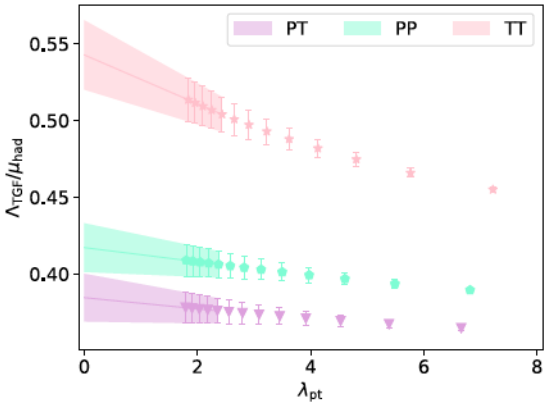

(a) SU(3).

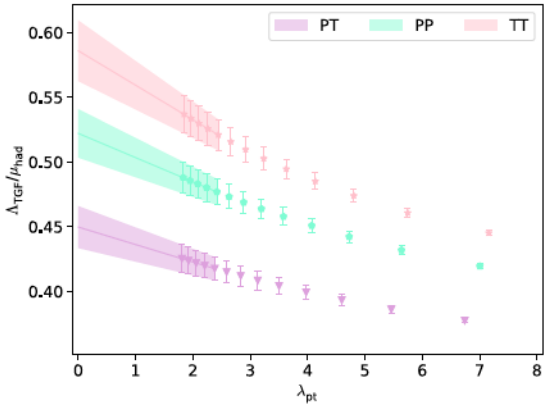

(b) SU(5).

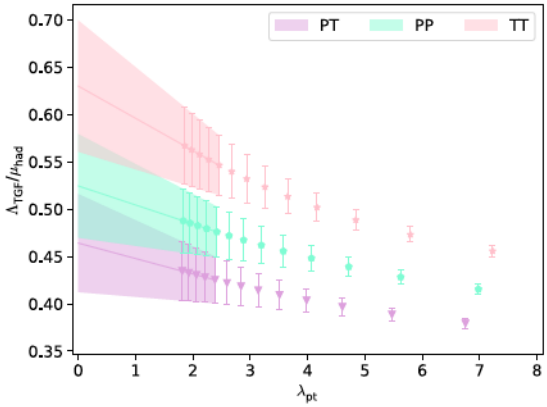

(c) SU(8).

Figure 5.10: Extrapolation of $\Lambda_{\mathrm{TGF}}/\mu_{\mathrm{had}}$ for each set of planes. The starting point of the sequence is $\lambda(2\mu_{\mathrm{had}}) = 13.9164955$.

For completeness, we show in fig. 5.8 the dependence of the continuum step scaling function $1/\sigma - 1/\mathcal{U}(\sigma, \tilde{L})$ on the coupling σ for the three different sets. We show these dependences for $N = 3$ and 5. In fig. 5.8 we see that the **TT** calculation is the one that deviates the most from the **APA** case. We will quantify more precisely this statement later on.

In this case, we will not use the same step scaling procedure to compute the Λ parameter as in section. 5.2.3. Instead, we will perform a non-perturbative matching between the **APA** and the other determinations using the following functional form:

$$\frac{1}{\lambda_{\mathrm{Plane}}(\mu)} - \frac{1}{u(\mu)} = \sum_{n=0}^{3} c_k u^k + \left(\frac{1}{\tilde{L}^2}\right) \times \sum_{n=0}^{8} \rho_k u^k \,, \tag{5.7}$$

where $u(\mu) = \lambda_{\mathbf{APA}}(\mu) = \lambda_{\mathrm{TGF}}(\mu)$ and c_k, ρ_k are coefficients to be determined. This fitting follows the same strategy used in sec. 4.3 for the non-perturbative fitting of TGF and SF schemes. An important advantage of this procedure is that the hadronic scale $1/\mu_{\mathrm{had}} = c\tilde{l}$ is kept constant in all cases; this results from the fact that the matching is done for the same values of bare coupling and lattice sizes

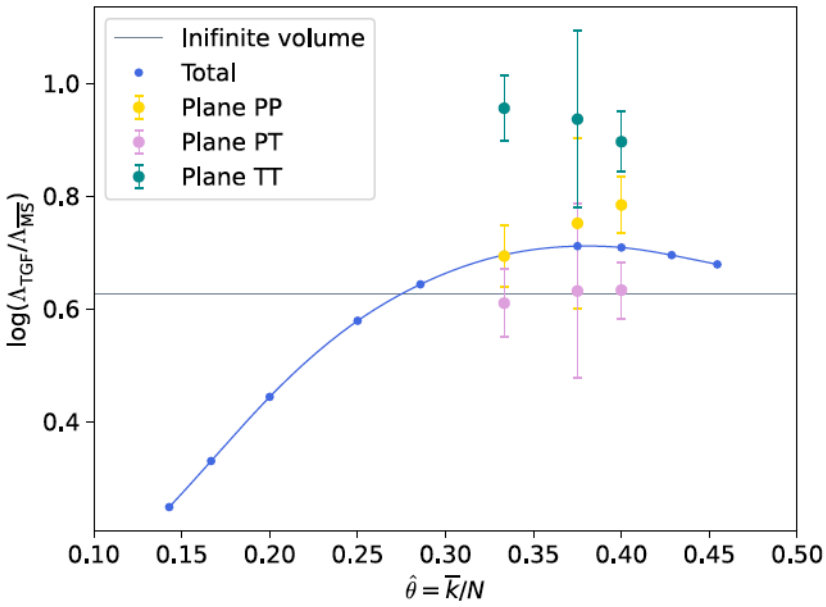

Figure 5.11: Dependence of $\log\left(\Lambda_{\mathrm{TGF}}/\Lambda_{\overline{\mathrm{MS}}}\right)$ with the non-commutativity parameter $\hat{\theta} \equiv \bar{k}/N$, for different values of N and $\bar{k}$. The **APA** determination is extracted from the perturbative computation of [100] for $c = 0.3$. The ratios **TT**, **PT**, and **PP** are determined numerically.

(thus fixing the physical volume $\tilde{l}$). In addition, the matching is done for all data simultaneously, so we can also compute it for the case of $SU(8)$ and exclude only the larger lattice $\tilde{L} = 96$. Figure 5.9 shows the results of the **PP** matching, and fig. 5.10 shows the extrapolation of $\Lambda_{\mathrm{TGF}}/\mu_{\mathrm{had}}$ for our three values of N.

Once the coupling is transformed into the different schemes, and the ratio $\Lambda_{\mathrm{TGF}}/\mu_{\mathrm{had}}$ is determined, the transformation factors relating the $\overline{\mathrm{MS}}$ scheme and each of the TGF schemes are given by:

$$R \equiv \frac{\Lambda_{\mathrm{TGF}}(\mathbf{Plane})}{\Lambda_{\overline{\mathrm{MS}}}} = \frac{\Lambda_{\mathrm{TGF}}(\mathbf{Plane})/\mu_{\mathrm{ref}}}{\Lambda_{\mathrm{TGF}}(\mathbf{APA}\ )/\mu_{\mathrm{ref}}} \times \frac{\Lambda_{\mathrm{TGF}}(\mathbf{APA})}{\Lambda_{\overline{\mathrm{MS}}}}\,. \tag{5.8}$$

The last factor represents the transformation factor to the $\overline{\mathrm{MS}}$ scheme of the **APA** determination, i.e. eq. (3.13). The resulting ratios R, computed for the three values of N, are presented in table 5.5.

In fig. 5.11 we show our results for $\log(\Lambda_{\mathrm{TGF}}/\lambda_{\overline{\mathrm{MS}}})$ as a function of the non-commutativity parameter $\hat{\theta}$ compared to the analytical results for the **APA** determined in ref. [100]. For comparison, we also show the value obtained in the infinite volume GF scheme, represented by the gray horizontal line in the plot and given by $\Lambda_{\mathrm{TGF}}/\Lambda_{\overline{\mathrm{MS}}}(c = 0) = 1.87208787$, which is very close to the PT result. In all cases the dependence on $\hat{\theta}$ is very small, as expected. We recall that the three selected values of (N, k) are the first steps in the Fibonacci sequence, leading in the large N limit to $\hat{\theta} = \varphi^{-2} \simeq 0,38196601$.

N	Plane	$\Lambda_{\rm TGF}/\mu_{\rm had}$	R
3	**APA**	0.418(17)	2.0063(11)
3	**TT**	0.543(23)	2.60(15)
3	**PT**	0.385(16)	1.84(11)
3	**PP**	0.417(16)	2.00(11)

N	Plane	$\Lambda_{\rm TGF}/\mu_{\rm had}$	R	N	Plane	$\Lambda_{\rm TGF}/\mu_{\rm had}$	R
5	**APA**	0.485(17)	2.0309(39)	8	**APA**	0.502(55)	2.0359(39)
5	**TT**	0.586(23)	2.45(13)	8	**TT**	0.630(70)	2.55(40)
5	**PT**	0.450(16)	1.883(94)	8	**PT**	0.464(52)	1.88(29)
5	**PP**	0.522(19)	2.19(11)	8	**PP**	0.524(55)	2.13(32)

Table 5.5: Results for $\Lambda_{\rm TGF}/\mu_{\rm had}$ for **TT**, **PP** and **PT** planes, compared to the **APA** computation. We also show the values of the ratio R between each $\Lambda_{\rm TGF}$ and $\Lambda_{\overline{\rm MS}}$ computed with eq. (5.8).

Finally, we comment on the difference between these results and those obtained for $SU(3)$ using the GF with Schrodinger functional boundary conditions [85]. In this case one can evaluate separately the coupling averaged over the space-time planes and the purely spatial planes, which differ in the boundary conditions. The ratio of the corresponding Λ parameter to the $\overline{\rm MS}$ parameter, for $c = 0.3$, is given by

$$\frac{\Lambda_{\rm GF,m}}{\Lambda_{\overline{\rm MS}}} = 2.0076(69) \qquad \frac{\Lambda_{\rm GF,e}}{\Lambda_{\overline{\rm MS}}} = 1.7756(73). \tag{5.9}$$

where m and e denote the purely spatial and space-time contributions, respectively. The results show differences comparable to those we observe between TGF couplings averaged on different planes.

5.5 Finite volume effects

Finally, we conclude this chapter with a qualitative evaluation of the effect of twisted boundary conditions on the reduction of finite volume effects by examining whether finite corrections are controlled by the effective volume of the lattice $\tilde{l}$. For this purpose, we will compare the computation of the coupling in the **TT** and **PP** planes with the standard setup at large values of c for two $SU(3)$ lattices.

Consider the following couplings computed in the **PP** plane: one obtained at $c = 0.30 \times N$ in a lattice of size L, and another obtained at $c = 0.3$ and size $N \times L$. Without finite volume effects, these two quantities should be equivalent. Accordingly, for a fixed value of the bare coupling, we computed the ratio between the $SU(3)$ **PP** renormalized couplings on lattices with $\tilde{L} = 12$ at $c = 0.90$ and $\tilde{L} = 36$ and $c = 0.30$, so that the renormalization scale is formally kept constant. Figure 5.12a shows this ratio, showing that finite volume effects count for 30% at strong coupling.

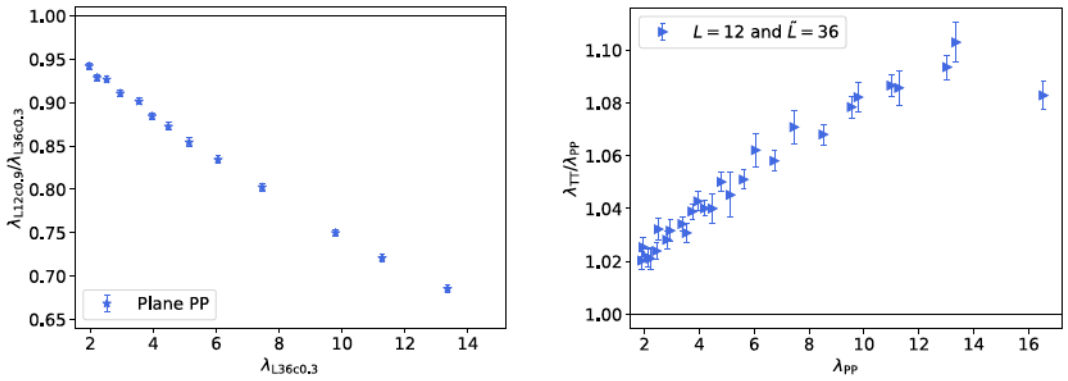

(a) $\tilde{L} = 12|_{c=0.9}$ VS $\tilde{L} = 36|_{c=0.3}$. (b) λ_{TT} VS λ_{PP}.

Figure 5.12: Comparison between finite volume effects in **TT** and **PP** computations with respect to the regular setup for large values of c for $SU(3)$.

On the other hand, we can compare the ratio between **TT** and **PP** calculations for $c = 0.30$. In the twisted plane, the renormalization scale is $1/\mu = c\tilde{l} = \tilde{c}l$, with $\tilde{c} = 0.9$, so in principle one could also expect a 30 % difference with respect to **PP** coupling due to finite volume effects. However, fig. 5.12b shows that the deviation at strong coupling is at most 10 %, indicating that twisted boundary conditions successfully reduce finite volume effects. We are at present working towards performing a similar analysis for $N = 5$ and 8.

5.6 Summary

In the present chapter, we have studied the running coupling of pure $SU(N)$ YM theories for $N = 5$ and 8 by means of the TGF scheme. In order to avoid the appearance of tachyonic instabilities in the large N limit, the values of N studied in this chapter are chosen within the Fibonacci sequence.

We have used the numerical setup of ch. 3 to compute the Λ parameter on the lattice for the gauge groups $SU(5)$ and $SU(8)$. As the value of N increases, the size of the possible lattices $\tilde{L}$ for our asymmetrical geometry also increases significantly, making the step scaling procedure costly. Because of this limitation, it was difficult to obtain high statistics for the $SU(8)$ case, and a precise determination of the Λ parameter was not possible. On the other hand, for the $SU(5)$ case we have obtained the Λ parameter in physical units with a good agreement with the results obtained in the literature. The final result of our determination is:

$$\Lambda_{\overline{\mathrm{MS}}}^{N=5} \times \frac{1}{\sqrt{\sigma_0}} = 0.560(21).$$

Since the boundary conditions are different in each plane of the twisted box, each plane by itself represents a new renormalization scheme. Consequently, we

have also studied the dependence of the Λ parameter on the boundary conditions. In this sense, we have numerically determined the transformation factors R that relate the Λ parameter in the TGF per plane scheme to the $\overline{\text{MS}}$ scheme. This ratio is calculated analytically in perturbation theory only for the All-Plane-Averaged case **APA**. In principle, the factors for **TT**, **PT**, and **PP** can also be computed in perturbation theory by restricting the sums for a given pair of directions (μ, ν), but this computation is far from trivial. Instead, we have provided a numerical determination of these factors by relating the Λ parameter computed in each plane to the **APA** one.

Finally, for the case of $SU(3)$, we have also investigated some finite volume effects. Although we do not count with more values of N for this test, we believe that the twisted boundary conditions significantly reduce the finite volume effects. However, more research needs to be done in this regard to reach a final conclusion.

Part III

Topology and volume dependence of SU(N) Yang-Mills gauge theories

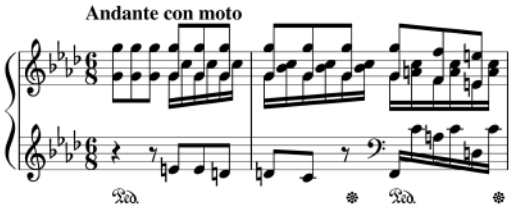

6 Topology freezing and the $Q = 0$ scheme

6.1 Motivation

The continuum limit of any lattice field theory is taken at a critical point where a second-order phase transition occurs, with autocorrelation times diverging power-like as $a^{-\gamma}$, where a is the lattice spacing and γ is a critical exponent that depends on the specific observable and algorithm being studied. For example, for Hybrid Monte Carlo [154] applied to QCD, the critical exponent for the topological charge Q^2 is expected to be $\gamma \simeq 5$ and for Wilson loops $\gamma \simeq 1$ [115]. This effect is called critical slowing down (CSD) [115, 116] (see [155] for a general introduction) and is usually unavoidable since it is characteristic of a phase transition in statistical mechanics systems. At this point, two main questions arise: how strong CSD is, and how fine lattices must be be to obtain reliable continuum extrapolations? Both questions have been studied extensively in the literature over the years, and several methods have been developed to alleviate this problem on the lattice [156–159].

In general, the rate at which autocorrelation times grow depends on the observables, the algorithms, and the accuracy required for each calculation. CSD has been studied in the literature for a wide range of observables, such as topological charge or Wilson loop correlators [152, 160–163]. In particular, the global topological charge is strongly affected, showing large autocorrelations for standard algorithms used in pure YM theory calculations or even QCD [162–165]. As we will see, the coupling defined in the GF scheme is strongly correlated with the topological charge [114], leading to significantly different results depending on the sector in which it is computed. This is particularly problematic in the intermediate volume regime, where the topology starts to become relevant.

In addition, depending on the lattice spacing, the autocorrelation times grow faster than the expected CSD, and transitions in the algorithm become even rarer. For some specific models, such as CP^{N-1}, the autocorrelation times grow exponentially [123]. In the large-volume regime, where the dynamics of the system allow for large topological fluctuations, the problem is less severe. The same is true for

lattices with small physical volumes, where fluctuations are dynamically suppressed. However, in the intermediate volume regime, where only a few configurations with non-trivial topology are expected, this problem is especially severe. This is the well-known topology freezing problem on the lattice, which is expected to occur for large values of the bare coupling $\beta = 2N^2 b$, leading to lattice spacings of order $a \lesssim 0.05$ fm for $SU(3)$ [114, 115, 166, 167]. In our previous computation of the coupling constant (see chs. 4 and 5), these problems were avoided by determining the coupling only in the sector of zero topological charge [85, 107, 114]. Whether the topological fluctuations are also well sampled in the $Q = 0$ sector remains an open question that we will address to some extent in this chapter.

The chapter is organized as follows. In sec. 6.2 we will look for the presence of topological freezing in our simulations, giving some specific representatives for the three values of N studied in this thesis. In sec. 6.3 we analyze the topological charge fluctuations in the sector of $Q = 0$ and present some arguments indicating that they are correctly sampled, supporting our choice to project the determination of the coupling into the trivial topology sector. We end with some general remarks in sec. 6.4.

6.2 Topology freezing and the TGF coupling

As noted above, the topological charge is an observable that is especially sensitive to critical slowing down, with autocorrelation times growing even exponentially in some cases [123]. As we will see, this poses a serious problem for coupling definitions using the GF; in fact large large autocorrelation times of the topological charge may lead to biased determinations of the coupling constant.

Several solutions to mitigate the effects of topological freezing on the lattice have been proposed in the literature; we will briefly discuss below some of them.

The first is based on brute force calculations, where simulations are run for a long time and a large amount of statistics is obtained. For example, this is the strategy used by [99] to determine the $SU(3)$ GF coupling in a scheme similar to ours. They observed large autocorrelation times in the region corresponding to intermediate physical volumes, especially in ensembles such as $\beta = 6.90$ and $\tilde{L} = 24$ of Table 10 of the same paper. The danger of this approach is that GF-based couplings are highly correlated with the topological charge [114], and even with very large statistics it is difficult to obtain an unbiased result with a reliable error estimate.

One possibility is to use open boundary conditions [166]. The idea is to make the boundary open in one direction so that barriers between topological sectors disappear and configurations can jump freely from one sector to another. The approach is expected to work for all algorithms and has been tested several times and used for lattice QCD e.g. in refs. [168]. An important drawback of this approach is that it is subject to large finite volume effects [169, 170].

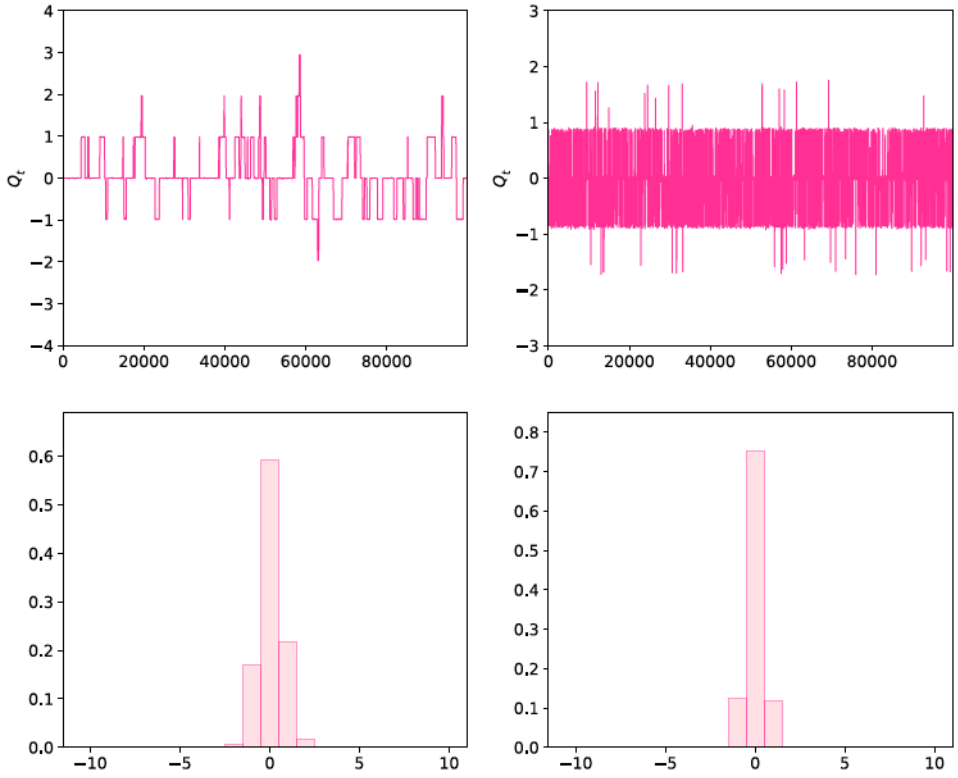

Figure 6.1: Monte Carlo evolution of the topological charge Q, along with the corresponding histograms, for $SU(3)$ lattice spacings $a = 0.0393$ fm (left) and $a = 0.0939$ fm (right), and physical volumes $\tilde{l} = 1.4159$ fm (left) and $\tilde{l} = 1.1263$ fm (right).

Another possible solution to mitigate CSD and freezing is the parallel tempering boundary conditions (PTBC) method [159]. The idea is to replicate multiple copies of the same lattice, interpolating from periodic to open boundary conditions. In a sense, each copy is more open on the boundaries than the previous one. The boundaries are open only in a cube of a certain size, called defect, and after a few Monte Carlo iterations, the configurations are swapped between the closest replicas using a Metropolis accept/reject algorithm. This swapping introduces new configurations associated with the open boundaries in the periodic replica and excites topological fluctuations. PTBC has been successfully used to reduce CSD and topological freezing in pure $SU(N)$ YM gauge theories [171–173]. In the conclusions of the thesis (see ch. 9) we will present some future directions concerning the determination of the running coupling mixing TGF and PTBC.

The last method we will discuss is the one used in eq. (3.32) to determine the renormalized TGF coupling. Since the coupling is not a physical observable, the idea is to modify the scheme and project the coupling into the sector with trivial topology. This idea was first introduced in [114] and is the strategy for the most accurate determination of the pure YM $SU(3)$ Λ parameter [85] of those included in the FLAG review [125]. The projection amounts for a redefinition of the scheme

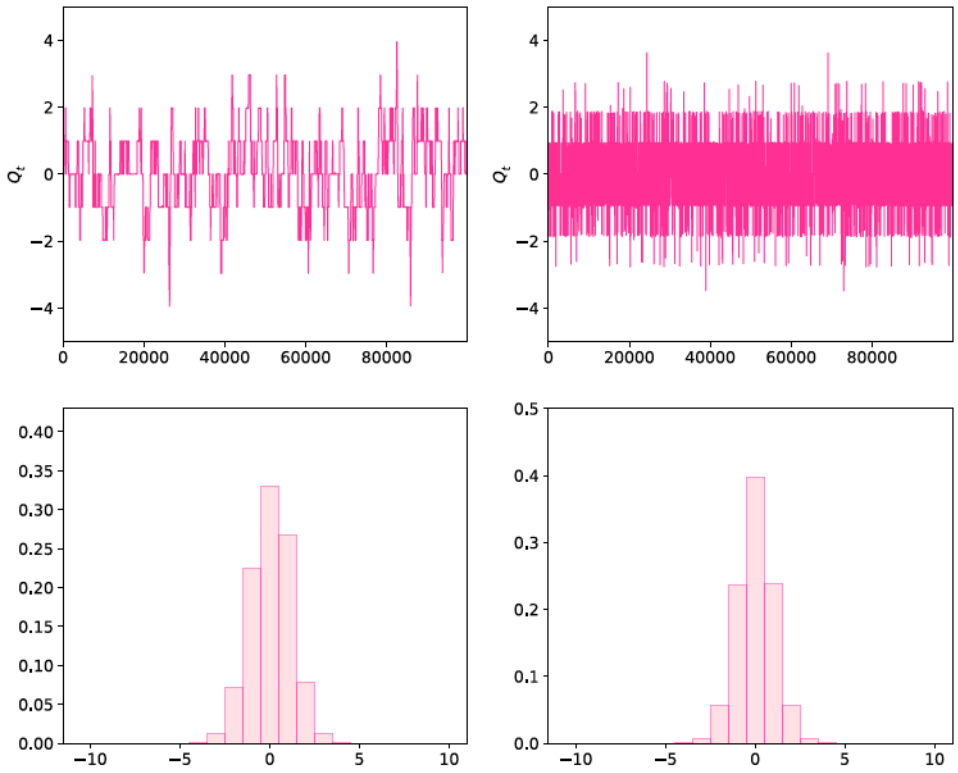

Figure 6.2: Same Monte Carlo evolution as in fig. 6.1, corresponding to the same $SU(3)$ lattice spacings but with larger physical volume: $\tilde{l} = 1.8878$ fm (left) and $\tilde{l} = 1.6895$ fm (right).

and it is not expected to have any effect on the determination of the Λ parameter[1]. In any case, it remains an open question whether topological fluctuations are well sampled in the sector of trivial topology. In sec. 6.2, we will present some arguments supporting this choice.

We present here some figures to illustrate the influence of CSD and topology freezing on our simulations. Again, we note that all our simulations start the Monte Carlo evolution from the vacuum configuration, i.e. cold start. Most of the figures refer to $SU(3)$ cases, but we will also show some results for $N = 5$ and 8. We will not make a strong statement about autocorrelations nor about the scaling with N, as we have not yet studied its effects quantitatively; this chapter aims only to show its influence on the determination of the coupling and to motivate our choice to project into the trivial topology sector.

Figure 6.1 shows the evolution of the topological charge Q with Monte Carlo time for two $SU(3)$ lattices with lattice spacings $a = 0.0393$ fm (left) and $a = 0.0939$ fm (right), both with comparable physical volumes. The same is shown in fig. 6.2 for the same lattice spacings but larger physical volumes. We see that the

[1]Note that the projection has no effect in perturbation theory since non trivial topology only appears at a non-perturbative level. Therefore, projected and unprojected schemes are identical in PT; in particular, $\Lambda_{\mathrm{TGF}}/\Lambda_{\overline{\mathrm{MS}}}$ is the same in both schemes.

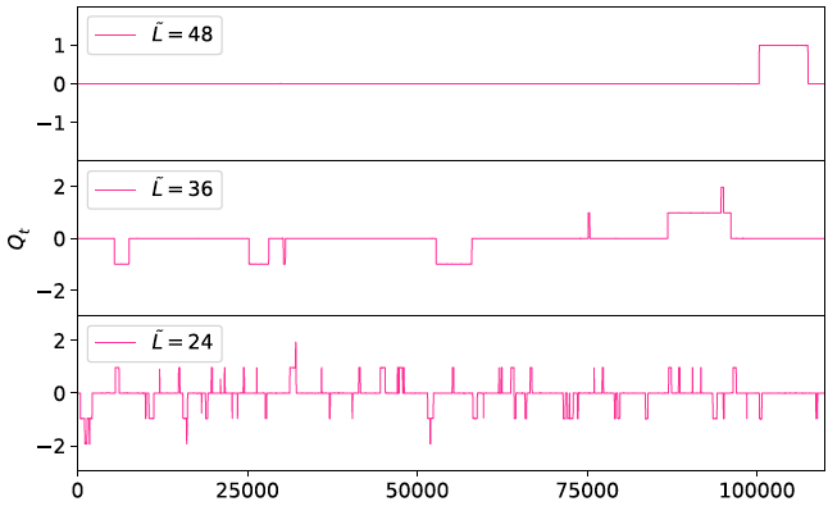

Figure 6.3: Monte Carlo evolution of the topological charge Q for $SU(3)$ lattice with, from top to bottom, $\tilde{L} = 48$, 36 and 24, corresponding to an approximately fixed physical size of $\tilde{l} \sim 1.1$ fm ($\lambda \sim 34.52$), and lattice spacings: $a = 0.023524(96)$, $0.031141(11)$, $0.045691(92)$ fm respectively.

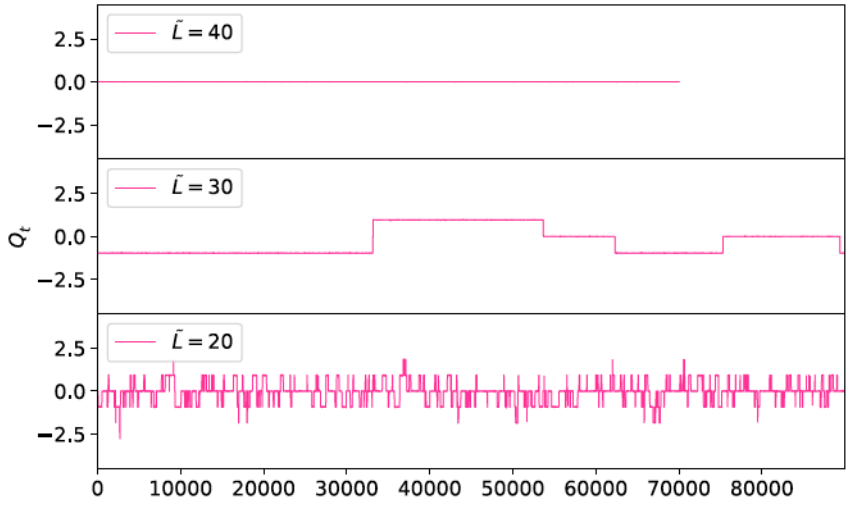

Figure 6.4: Monte Carlo evolution of the topological charge Q for $SU(5)$ lattices with, from top to bottom, $\tilde{L} = 40$, 30 and 20, corresponding to an approximately fixed physical size of $\tilde{l} \sim 1.8$ fm ($\lambda \sim 80$), and lattice spacings: $a = 0.0414(11)$, $0.0599(33)$, $0.08679(53)$ fm respectively. We used the standard string tension which is set to $\sqrt{\sigma_0} = 2.230$ fm^{-1}.

autocorrelations increase as we decrease the lattice spacing; however, even on the finer lattice, several topological sectors are explored and we cannot talk about severe

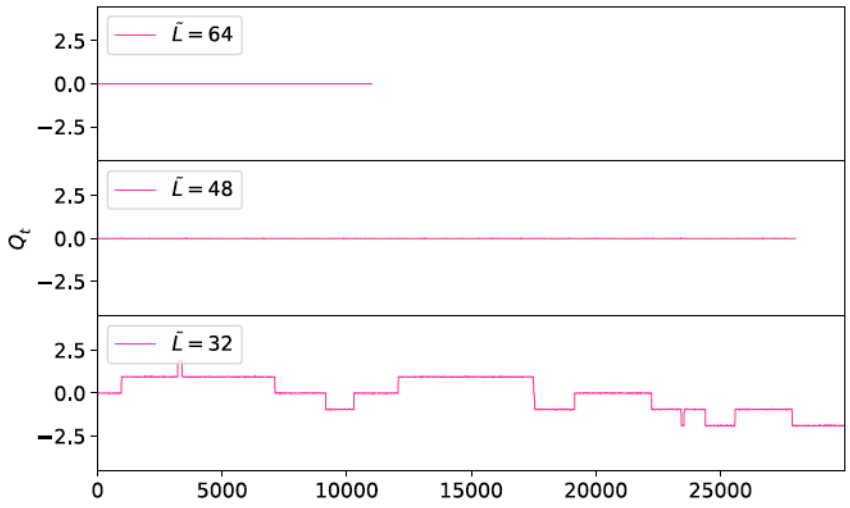

Figure 6.5: Monte Carlo evolution of the topological charge Q for $SU(8)$ lattices with, from top to bottom, $\tilde{L} = 64$, 48 and 32, corresponding to an approximately fixed physical size of $\tilde{l} \sim 3.1$ fm ($\lambda \sim 300$), and lattice spacings: $a = 0.04761(69)$, $0.06348(49)$, $0.1015(12)$ fm respectively. We used the standard string tension which is set to $\sqrt{\sigma_0} = 2.230$ fm^{-1}.

CSD or even topology freezing. A better example is given in fig. 6.3, where we plot the value of the topological charge as a function of the Monte Carlo time for $SU(3)$ lattices with $\tilde{L} = 24, 36, 48$ and a physical volume $\tilde{l} \sim 1.1$ fm, corresponding to a coupling $\lambda \approx \lambda(\mu_{\rm had})$ at the renormalization scale $\mu_{\rm had}$ used in ch. 4.10 for the calculation of the $SU(3)$ Λ parameter. It is clear that autocorrelations dramatically increase on the finer lattice.

We observe that the freezing increases strongly with N. In particular, for $N = 8$ all our lattices except those for $b = 0.3555$, corresponding to lattice spacing $a = 0.097$ fm, remain in the zero topology sector. Some illustrations for $SU(5)$ and $SU(8)$ are shown in figs. 6.4 and 6.5. The value of the coupling determines the volume in each figure, and each sub-figure represents a different value of the lattice spacing determined with respect to the string tension $\sqrt{\sigma_0} = 2.230$ fm^{-1}. As already mentioned, for large values of N we observe a strong increase in freezing, and even for lattice spacings as large as $a = 0.1$ fm we observe very large autocorrelation times for the topological charge. Note that even for large volumes, the charge remains frozen as N grows.

CSD and topological freezing pose a difficult problem for coupling definitions in renormalization schemes based on the GF. It has been shown [114] that the renormalized coupling within the GF is strongly correlated with the topological charge and has substantially different values when calculated in different topological sectors. Since the value of the coupling changes strongly from one topological sector to another, when freezing takes place one effectively ends up with only a handful of independent configurations, leading to poor estimates of the statistical uncertainties.

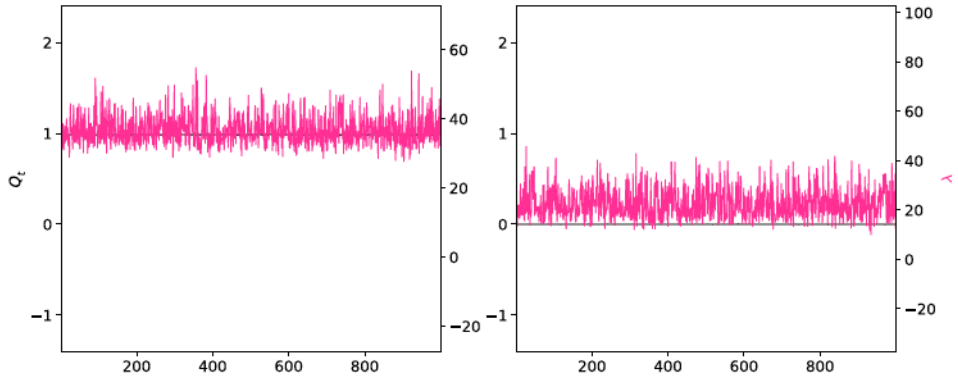

Figure 6.6: 't Hooft coupling λ_{TGF} and topological charge Q as a function of the Monte Carlo time for two $SU(3)$ lattices with the same parameters but in different topological sectors: Q=1 on the left plot and Q=0 on the right one.

Q	$\lambda(\tilde{L}=24)$	$\lambda(\tilde{L}=36)$	$\lambda(\tilde{L}=48)$
0	32.18(10)	33.29(19)	34.00(19)
1	42.92(25)	43.85(56)	43.94(49)
-1	43.07(20)	44.11(50)	-
2	59.1*	56.6*	-
-2	56.4*	-	-

Table 6.1: Values of the TGF coupling of $SU(3)$ measured on sectors with fixed value of the topological charge Q. Entries with a $*$ correspond to cases where the number of configurations with charge Q is less than 20 and a correct estimation of the errors is not feasible.

This effect is illustrated in figs. 6.6 and 6.7, where we display jointly the evolution with MC time of the coupling and the topological charge. Figure 6.6 shows qualitatively the large difference between couplings calculated in sectors with charge $Q = 0$ and $Q = 1$ for the same value of the physical volume. On the other hand, fig. 6.7 shows the correlation for four different values of the physical volume. We observe that the correlation between charge and coupling is enhanced at small and intermediate volumes, and is reduced as the volume increases. A long autocorrelation in the topological charge thus directly affects the measurement of the coupling. We show this correlation in a more quantitive way in table 6.1, where we give the average coupling of ensembles in fig. 6.3 computed in different topological sectors. The correlation between the topological charge and the coupling is very large: values of the coupling averaged over the $Q = 0$ or $|Q| = 1$ sectors differ by as much as 30%.

.

In ch. 7 we will make an attempt to explain the correlation observed in the intermediate volume regime in semiclassical terms, relying on the fact that the partition function in this regime is dominated by a dilute gas of instantons.

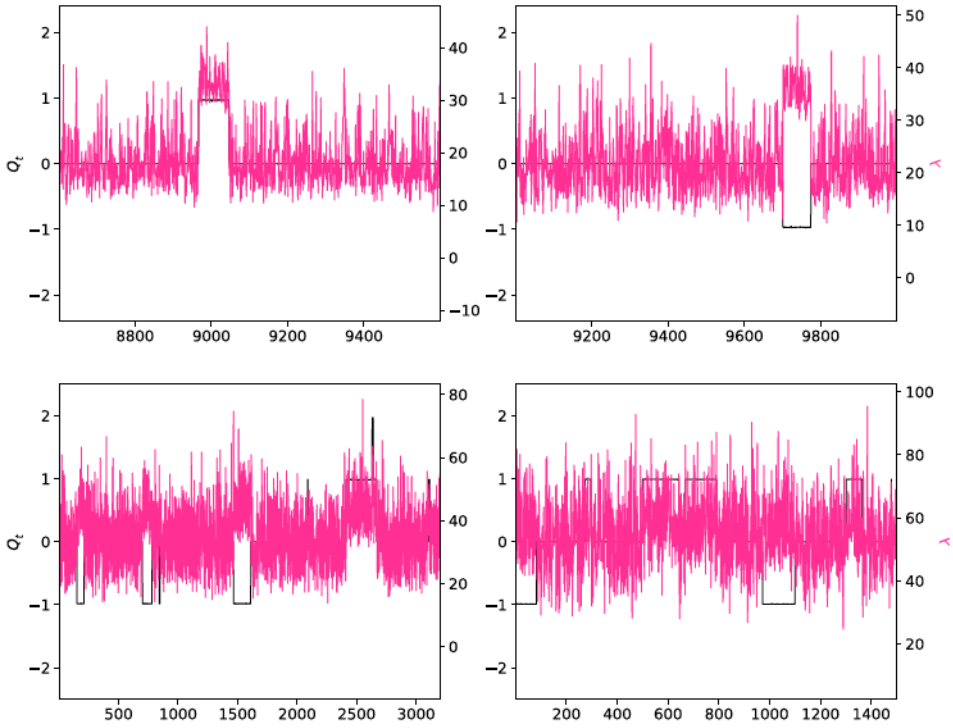

Figure 6.7: 't Hooft coupling λ_{TGF} and topological charge Q as a function of the Monte Carlo time for four $SU(3)$ lattices with different physical volumes – physical volume increases from left-top to right-bottom.

In this section, we have presented some qualitative evidence that our lattice simulations suffer from topology freezing. As noted above, there are several ways to mitigate these effects, and the one chosen in this thesis is the projection into the sector of zero topological charge. This choice is only valid if the sampling of the trivial sector is correct; we will test this statement in the next section by analysing the topological charge correlators computed in the sector of trivial topology (see [174] for a study in the Schwinger model).

6.3 Topological charge fluctuations in the sector of trivial topology

To determine whether local fluctuations of topological charge are correctly sampled in the trivial topology sector, we have computed the two-point function of the operator:

$$q(x_0, t) = \int d\vec{x}\, q(\vec{x}, x_0, t), \tag{6.1}$$

obtained by integrating the topological charge density, smeared over a flow time t, over three directions, including the two short ones. This operator has been determ-

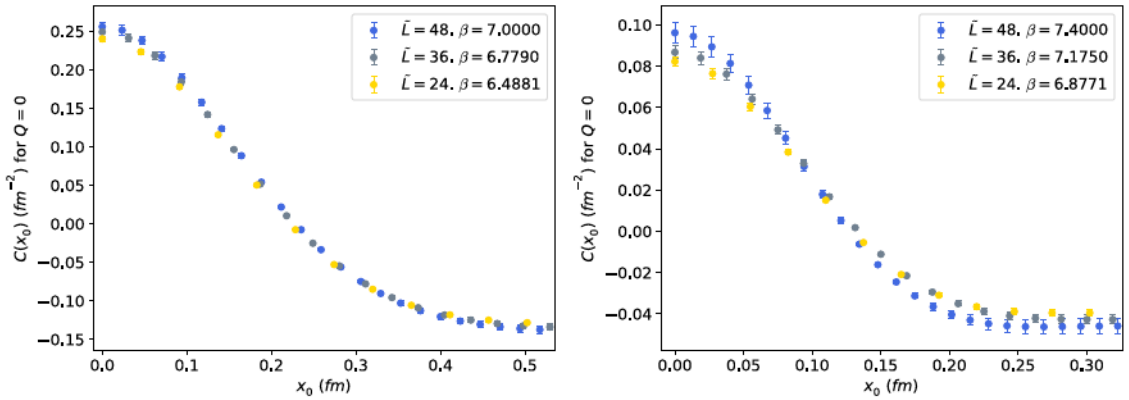

(a) $\tilde{l} \sim 1.1$ fm. (b) $\tilde{l} \sim 0.66$ fm.

Figure 6.8: We display the correlator of topological charge in the trivial topology sector, defined in eq. (6.3), for two different volumes of $SU(3)$, corresponding to those in fig.6.3.

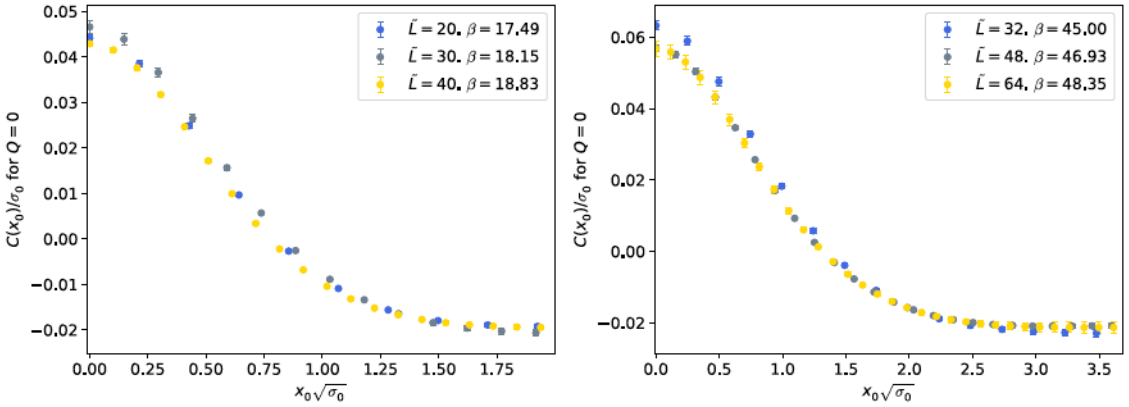

(a) $SU(5)$. (b) $SU(8)$

Figure 6.9: Topological charge correlator in the trivial topology sector, for $SU(5)$ and $SU(8)$ lattice with the same physical volumes of fig. 6.4 and 6.5, respectively.

ined on the lattice using the theoretical field definition of the charge density, cf. eq. (3.31),

$$q(x_0 = n_0 a, t) = \frac{a^{-1}}{16\pi^2} \sum_{\vec{n}} \mathrm{Tr} \left\{ G_{\mu\nu}(\vec{n}, n_0, t) \widetilde{G}_{\mu\nu}(\vec{n}, n_0, t) \right\} , \tag{6.2}$$

evaluated at flow time $\sqrt{8t} = 0.3\tilde{l}$. In terms of this operator, we have computed the correlator:

$$C(x_0) = \frac{\langle q(x_0, t)\, q(0, t)\, \hat{\delta}_Q \rangle}{\langle \hat{\delta}_Q \rangle} \Big|_{\sqrt{8t}=0.3\tilde{l}} \tag{6.3}$$

defined over the sector with trivial topology.

Figure 6.8a shows the time dependence of the correlator evaluated on the $SU(3)$ Monte Carlo ensembles shown in fig. 6.3. Although topology is frozen on the

largest lattice with $\tilde{L} = 48$, we do not observe any significant deviation from scaling; the structure of the charge correlation is the same on the three lattices. These good scaling properties are independent of the physical size of the box and are preserved at smaller volumes; an example for $\tilde{l} \sim 0.66$ fm is shown in fig. 6.8b. These results indicate that local fluctuations of the topological charge are correctly implemented in the trivial topology sector, even when the total topological charge is frozen to zero in the Monte Carlo ensemble. Figure 6.9 shows the topological charge correlators computed for the $SU(5)$ and $SU(8)$ lattices of figs. 6.4 and 6.5, respectively. Again, there are no large deviations between the three lattices.

We conclude this section with a final qualitative test. We have computed, for some $SU(3)$ lattices, the evolution as a function of the Monte Carlo time of the charge density averaged only over half of the lattice size, i.e. by summing the profile of eq. (6.2) in the half-boxes $n \in [0, \tilde{L}/2]$ and $n \in [\tilde{L}/2, \tilde{L}]$. The result is shown in fig. 6.10. Even in regions where the topology is completely frozen with a total charge $Q = 0$, the fluctuations in the half-box are large. Some more examples of these calculations can be found in appendix. D.

6.4 Summary

Critical slowing down and topology freezing represent a challenging problem to lattice simulations. As the lattice spacing decreases, some observables exhibit large, sometimes exponentially increasing, autocorrelation times.

In this chapter we have shown how topological charge freezing affects our simulations. Our prescription for calculating the running coupling in the TGF scheme (first introduced in [114]) projects the coupling into the sector of trivial topological charge. This prescription works as another part of the renormalization scheme as long as the topological fluctuations in the sector of trivial topology are correctly sampled. We have presented some qualitative and quantitative arguments in support of this assumption. In particular, we have computed the topological charge correlators for several lattices and checked that the topological fluctuations are well sampled even in the frozen lattice. This has been checked for the three values of N studied in this work. On the other hand, we have presented evidence for topological fluctuations even in ensembles where the total charge is completely frozen. We did this by looking at the charge density integrated over half of the lattice.

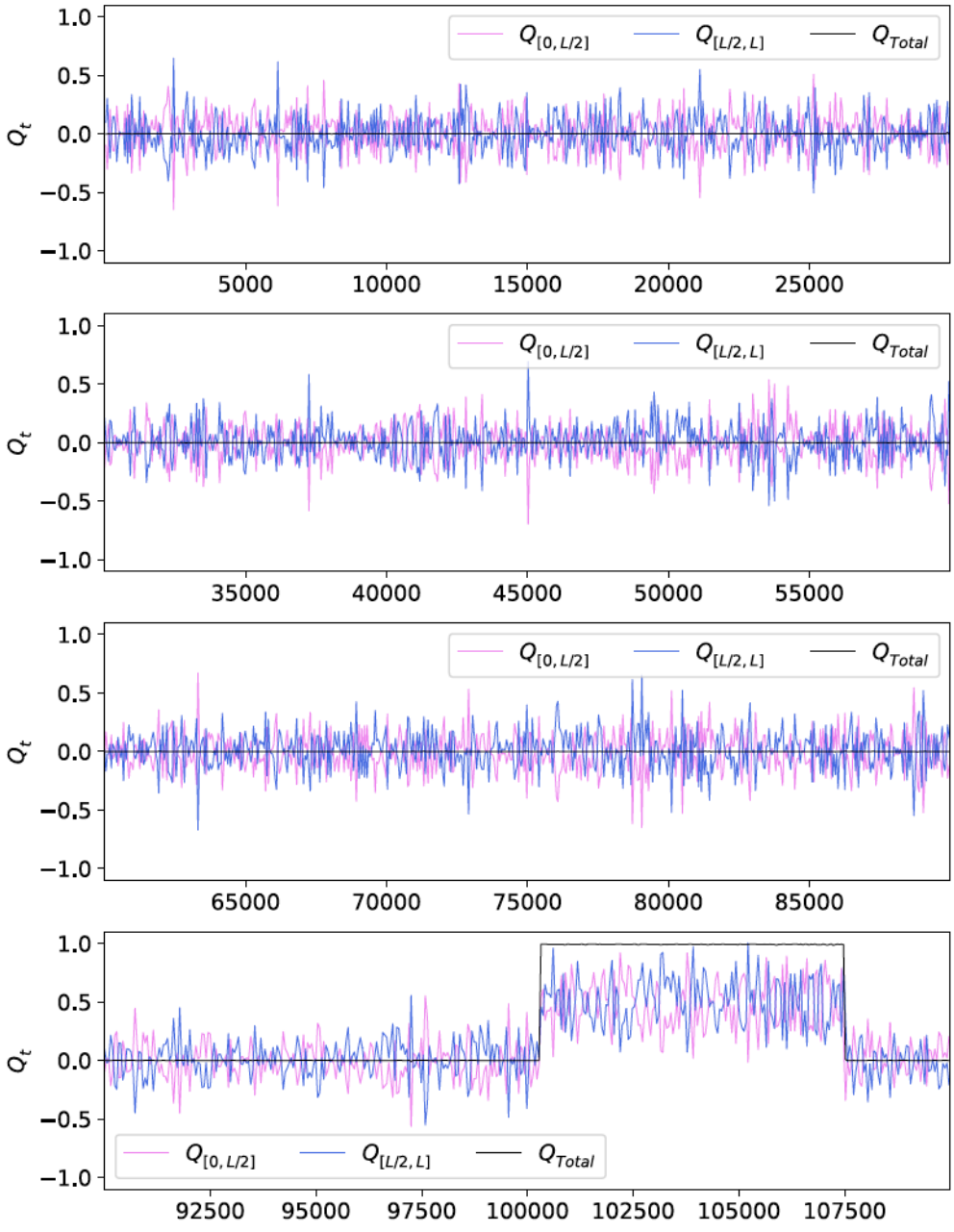

Figure 6.10: Topological charge in half-boxes of size $[0, \tilde{L}/2]$ and $[\tilde{L}/2, \tilde{L}]$ for a $SU(3)$ lattice.

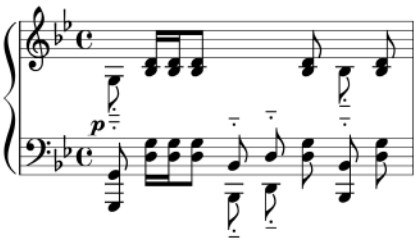

7 Volume dependence

7.1 Motivation

Following the discussion of ch. 6 about the implications of topology in the determination of the TGF coupling, there is another important effect of topological nature that directly affects our computations: the physical volume. Unlike CSD or topology freezing, this effect has nothing to do with the discretization nor the continuum extrapolation; on the contrary, it is directly related to the dynamics of the system.

We will explore in this setup the dependence on the effective size $\tilde{l}$ of some observables, in particular the topological susceptibility. For small volumes, the theory is in the perturbative regime and the topological sector $Q = 0$ dominates. This is a dynamical suppression and should not be interpreted in the same way as the CSD or the topology freezing, where the suppression is due to an incorrect sampling of the configuration space as a consequence of large autocorrelations. As $\tilde{l}$ grows, the probability of reaching sectors with $Q \neq 0$ also increases, and in the thermodynamic limit the charge distribution is determined by the value of the topological susceptibility $\chi = \langle Q^2 \rangle / V$, which in this limit, like all physical observables, tends to a constant value [175, 176]. The onset of the susceptibility in the region of intermediate volumes can be studied with a semiclassical approximation. In this chapter we will analyze the dependence of the $SU(3)$ topological susceptibility with respect to the effective volume $\tilde{l}$, and we will use the semiclassical approximation to understand the dependence of the TGF coupling on the topological charge.

The chapter is organized as follows. Section 7.3 studies the dependence of the 't Hooft coupling in the TGF scheme with the physical volume for different values of N. In sec. 7.4 we study the volume dependence of the topological susceptibility, with particular interest in its semiclassical behavior. We confirm that some of our simulations respect the expected volume dependence and reproduce the infinite volume results for the topological susceptibility [177]. In addition, in sec. 7.4.2 we give a reliable interpretation of the transition from the small to the large volume regime in terms of a dilute instanton gas approximation and use it to qualitatively explain the strong correlation of the coupling constant with the topological sector observed in ch. 6. We conclude the chapter in sec. 7.5 with a brief summary.

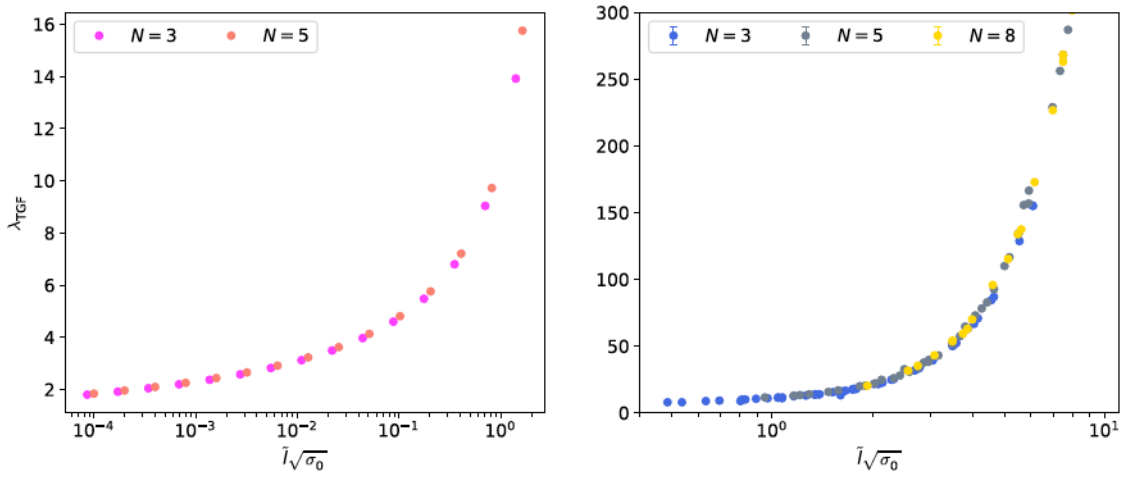

Figure 7.1: Volume dependence of the 't Hooft coupling λ for several values of N. The left plot correspond to coupling values along the step-scaling sequence of ch. 4 and 5. The right extends into the large volume regime.

7.2 Dependence of the coupling with the effective volume

As we have discussed throughout this thesis, the idea of volume independence has strong implications. We recall that we use very different lattice geometries for the $N = 3$, 5 and 8 simulations. For example, $SU(8)$ and $SU(3)$ theories in boxes with effective physical sizes in the range of a fermi ($\tilde{l} \sim 1$ fm) have torus periods in the 01 plane of order 0.3 and 0.125 fm, respectively, yet have very similar finite volume dynamics.

A nice summary of the results presented in the previous chapter is provided by fig. 7.1 where we show the dependence of the TGF 't Hooft coupling on the effective physical volume, given in terms of string tension $\sqrt{\sigma_0}$. The left plot shows the range of scales used in our step-scaling study, while the right plot extends into the large volume domain. The results for the three different values of N are remarkably similar, indicating that the magnitude of the finite N corrections is small. This plot supports the conjecture that a well-defined singular large N limit for the coupling can be obtained from the Fibonacci sequence, although much larger values of N would be required to really substantiate this statement. However, we would like to emphasize that the computational effort involved in this determination is considerable and that obtaining results even for the next value in the Fibonacci sequence is far from trivial.

7.3 Physical volume as topology trigger

It is well known that the topological susceptibility in YM theories depends strongly on the physical volume. On a small box, perturbation theory holds and non-zero

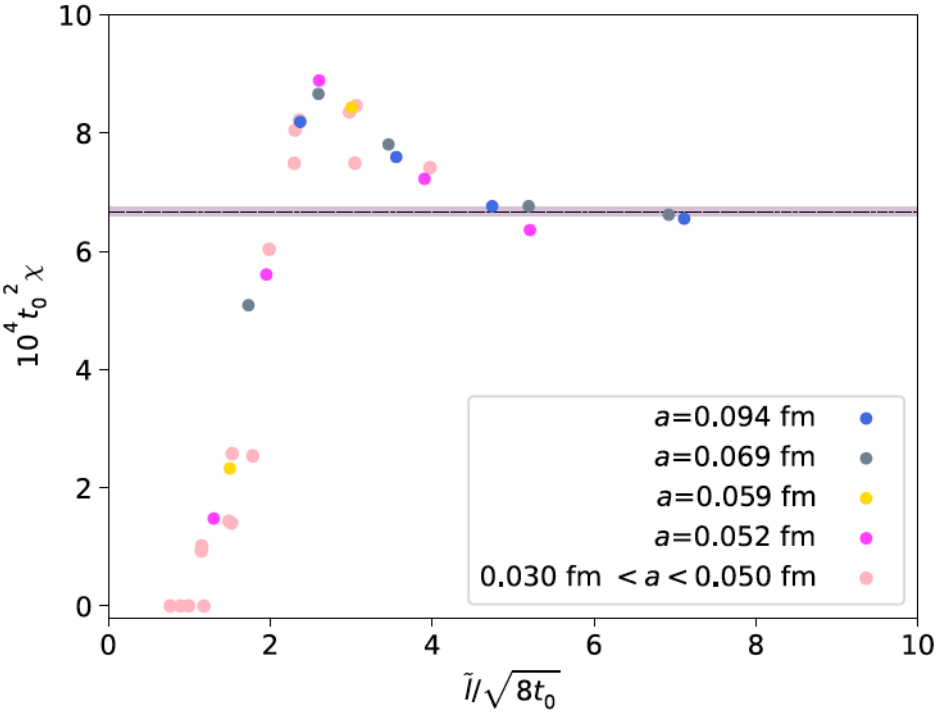

Figure 7.2: Volume dependence of the topological susceptibility evaluated from flowed fields at $8t = (0.3\tilde{l})^2$. The orange horizontal band corresponds to the value of the, continuum extrapolated, large-volume $SU(3)$ susceptibility $t_0^2\chi = 6.67(7) \times 10^{-4}$ [177].

topological charges are suppressed. This suppression is reduced when increasing the volume, leading to a constant topological susceptibility for lattices well above the characteristic QCD scale Λ^{-1}.

The topological susceptibility measures the fluctuations of the topological charge:

$$\chi = \int d^4x \, \langle q(x)q(0)\rangle \,, \tag{7.1}$$

with $q(x)$ the topological charge density. On the lattice, it can be determined by measuring:

$$\chi = \frac{\langle Q^2\rangle}{V} \tag{7.2}$$

with Q determined using eq. (3.33).

An illustration of the volume dependence of the topological susceptibility is provided in fig. 7.2 where we display $t_0^2\chi$ as a function of $\tilde{l}/\sqrt{8t_0}$. The results shown correspond to simulations with lattice spacing $a > 0.03$ fm (we refrain from giving errors in this plot since our determination of the susceptibility may be affected by freezing, particularly for values of $a < 0.05$ fm). The onset of the susceptibility is abrupt and takes place for values of $\tilde{l}/\sqrt{8t_0} \in [1, 3]$, overlapping with the region covered by the step scaling sequence of ch. 4. After that, χ stabilizes to the constant

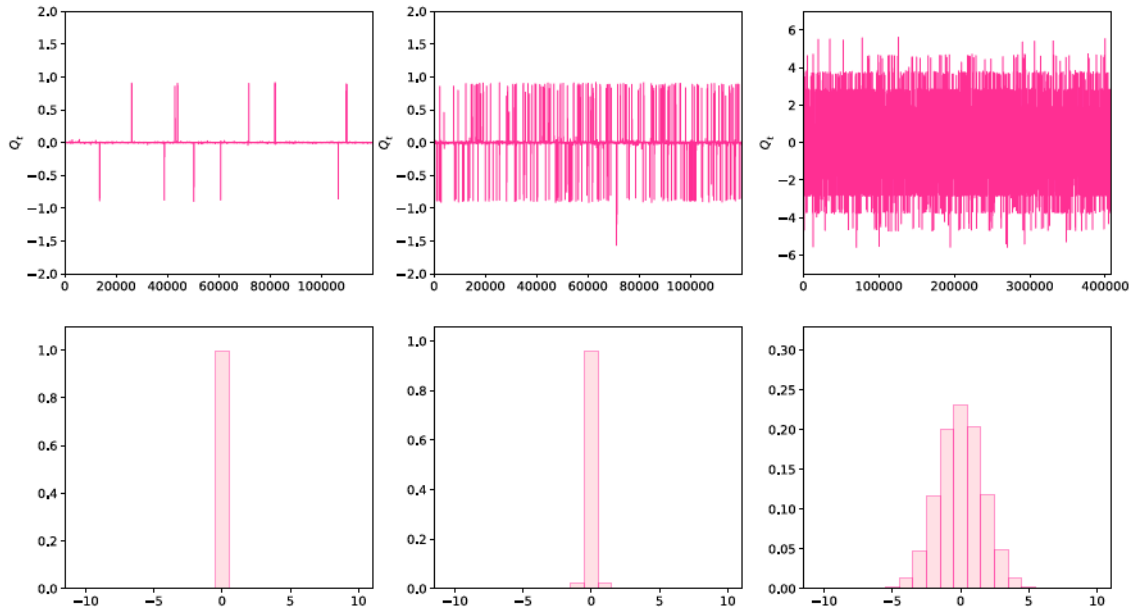

Figure 7.3: Monte Carlo evolution and histograms of the topological charge Q for three $SU(3)$ simulations with physical volumes varying, from left to right, $\tilde{l}/\sqrt{8t_0} = 1.30209$, 1.73085, and 4.74241. They correspond to topological susceptibilities of $10^4 t_0^2 \chi = 1.48059$, 5.08826, and 6.76309 respectively.

large volume value, given in $SU(3)$ by $t_0^2\chi = 6.67(7) \times 10^{-4}$ [177], corresponding in the figure to the orange horizontal band.

To illustrate how our large $SU(3)$ volume simulations reproduce the value of the infinite volume susceptibility, we show in fig. 7.3 the Monte Carlo evolution and topological charge histograms for three SU(3) lattices with physical volumes, from left to right, of $\tilde{l}/\sqrt{8t_0} = 1.30209$, 1.73085, and 4.74241, corresponding to topological susceptibilities $10^4 t_0^2 \chi = 1.48059$, 5.08826, and 6.76309, respectively. Unfortunately, due to topology freezing, we are not able to produce a similar plot for $SU(5)$ and $SU(8)$.

7.4 Semiclassical region

As commented several times in the text, the intermediate volume region, which mediates the transition between small and large volume regimes, is of great interest and at the same time very delicate. Few configurations with non-trivial topological charges are expected for intermediate volumes, since the perturbative solutions with $Q = 0$ dominate. Therefore, semiclassical arguments based on instantons are expected to hold. This section describes a semiclassical approximation based on a dilute gas of instantons. We will use it to qualitatively describe the transition of the topological susceptibility from small to large volumes and the strong correlation of coupling and topological charge discussed in ch. 6. This discussion should not be

interpreted as a rigorous proof, but as a compelling qualitative picture of the role of instantons in this context.

In sec 7.4.1 we will discuss how to apply the dilute instanton gas picture to compute the leading semiclassical contribution to the TGF coupling in a fixed topological charge sector. The derivation is based on the observation that the flow removes short-range fluctuations but preserves classical solutions of the Euclidean equations of motion. This includes instantons, but not instanton-anti-instanton pairs, which are preserved only at typical distances larger than $\sqrt{8t} = c\tilde{l}$. The leading contribution to the TGF coupling in the semiclassical approximation can be therefore estimated by taking into account that:

$$\langle E(t)\rangle = \frac{1}{2}\langle \mathrm{Tr}\left(G^2_{\mu\nu}(x,t)\right)\rangle = \frac{1}{V}\left\langle \frac{1}{2}\int d^4x \mathrm{Tr}\left(G^2_{\mu\nu}(x,t)\right)\right\rangle . \tag{7.3}$$

This expression can be combined with the fact that the classical Euclidean action of a configuration with well-separated instantons and anti-instantons can be approximated by $S_0(n+\bar{n})$, with $n(\bar{n})$ the number of instantons(anti-instantons) and S_0 the one-instanton action. Therefore, at the lowest order in the dilute gas approximation, the energy density receives a (semi-)classical contribution proportional to the average number of instantons plus anti-instantons, which adds to the perturbative one. One can as well evaluate in this approximation the average value of any observable, in particular $\langle n+\bar{n}\rangle$, restricted to the sector of topological charge $\tilde{Q}$ by using:

$$\langle O\rangle_{\tilde{Q}} = \frac{\langle O\,\delta_{Q-\tilde{Q}}\rangle}{\langle \delta_{Q-\tilde{Q}}\rangle}, \tag{7.4}$$

where Q is the total topological charge, analogous to what we did to define the coupling in the zero topological sector in eq. (3.7). In sec. 7.4.2 we will compare these predictions with the results of our numerical simulations.

7.4.1 Dilute instanton gas approximation

We present the derivation of the dependence of the coupling on the topological charge in the dilute gas approximation. The starting point is the continuum expression of the TGF coupling:

$$\lambda(\mu) = \frac{128\pi^2t^2}{3N\mathcal{A}(\pi c^2)}\langle E\,(t)\rangle\Big|_{\sqrt{8t}=c\tilde{l}=\mu^{-1}} . \tag{7.5}$$

By setting $\mathcal{A}(x) = x^2\widehat{\mathcal{A}}(x)$ of eq. (3.8), and $(8t)^2 = c^4\tilde{l}^4 = c^4N^2V$, where V is the volume of the asymmetric box, one gets:

$$\lambda(\mu) = \frac{2NV}{3\widehat{\mathcal{A}}(\pi c^2)}\langle E(t)\rangle\Big|_{\sqrt{8t}=c\tilde{l}=\mu^{-1}} . \tag{7.6}$$

The idea is to evaluate the energy density of $\langle E(t)\rangle_Q$ of eq. (7.3) in the dilute gas approximation and see what the dependence of the coupling with the topological

charge is. In a configuration with well-separated instantons and anti-instantons, the classical Euclidean action can be approximated by $S_0(n+\overline{n})$, with S_0 the one-instanton action and $n(\overline{n})$ the number of instantons(anti-instantons). Therefore, one can compute the contribution to the expectation value of the energy density at leading order in this approximation by estimating the average number of instantons plus anti-instantons in the flowed ensemble:

$$\langle E(t)\rangle^{\text{dig}} \sim \frac{S_0}{V}\langle n+\overline{n}\rangle\,. \tag{7.7}$$

Finally, the evaluation of the coupling can be restricted to sectors of certain topological charge Q, cf. eq. (7.4), leading to:

$$\lambda_Q^{\text{dig}}(c) \sim \frac{2NS_0}{3\widehat{\mathcal{A}}(\pi c^2)}\langle n+\overline{n}\rangle_Q\,. \tag{7.8}$$

To determine the average number of instantons in the dilute gas approximation, we will consider two possibilities: a dilute gas of ordinary instantons with action $S_0 = 8\pi^2$, and one of fractional instantons [69] with instanton action $S_0 = 8\pi^2/N$. The derivation follows the standard treatment, see e.g. [178]. In this context, the semiclassical picture based on the less standard case of fractional instantons follows the ideas of González-Arroyo and collaborators in a series of papers [179–183], see also [184–186] and [79] for a detailed review. We will study this type of configurations in ch. 8.

Ordinary instantons

The basic assumption in the dilute gas approximation is that the gas consists of objects with positive (+1) and negative (-1) topological charges, which are otherwise equally likely; the probability of producing either of them per unit volume is given by $R = K\exp(-NS_0/\lambda)$, where K is the fluctuation determinant around the instanton. Under this hypothesis, it is easy to determine the partition function restricted to the sector of the topological charge Q, which is given by

$$Z_Q = \mathcal{C}\sum_{n,\overline{n}}\frac{1}{n!\overline{n}!}(RV)^{n+\overline{n}}\delta(n-\overline{n}-Q) = \mathcal{C}\int_0^{2\pi}\frac{d\theta}{2\pi}e^{-iQ\theta}\exp\{2RV\cos\theta\}\,, \tag{7.9}$$

where we have used the integral representation of the δ function:

$$\delta(x) = \frac{1}{2\pi}\int_0^{2\pi}d\theta e^{i\theta x}\,. \tag{7.10}$$

Setting $x = 2RV$, a solution for the partition function is $Z_Q = \mathcal{C}I_Q(x)$, where $I_Q(x)$ stands for the modified Bessel function of the first kind.

The total number of instantons and anti-instantons $\langle n+\overline{n}\rangle_Q$ in the dilute gas approximation is computed as follows

$$\langle n\rangle_Q = \frac{RV}{Z_Q}\sum_{n,\overline{n}}\frac{1}{n!\overline{n}!}(RV)^{n+\overline{n}}\delta(n-\overline{n}-(Q-1)) = \frac{x}{2}\frac{I_{Q-1}(x)}{I_Q(x)}\,. \tag{7.11}$$

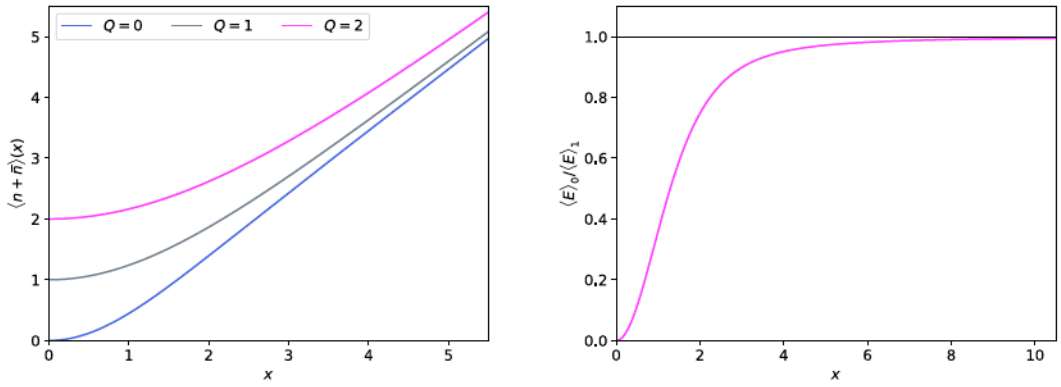

(a) $\langle n+\overline{n}\rangle_Q$. (b) $\langle E\rangle_0/\langle E\rangle_1$

Figure 7.4: (a) The quantity $x\left(I_{Q-1}(x)+I_{Q+1}(x)\right)/(2I_Q(x))$ is displayed vs x for $Q=0,1,2$. (b) We display the ratio of the expectation values of $\langle E(t)\rangle_Q$ between $Q=0$ and $Q=1$.

and, analogously:

$$\langle\overline{n}\rangle_Q = \frac{x}{2}\frac{I_{Q+1}(x)}{I_Q(x)}\,. \tag{7.12}$$

Subtracting eq. (7.11) and (7.12), one derives the total topological charge:

$$\langle n-\overline{n}\rangle_Q = Q\,, \tag{7.13}$$

where we have used the recursion relation of modified Bessel functions of the first kind:

$$I_{n-1}(x) - I_{n+1}(x) = \frac{2nI_n(x)}{x}\,. \tag{7.14}$$

On the other hand, adding eq. (7.11) and (7.12) gives us the total number of instantons and anti-instantons:

$$\langle n+\overline{n}\rangle_Q = \frac{\partial \log I_Q(x)}{\partial \log x} = x\left(\frac{I_{Q-1}(x)+I_{Q+1}(x)}{2I_Q(x)}\right) = Q + x\,\frac{I_{Q+1}(x)}{I_Q(x)}\,, \tag{7.15}$$

leading to the final form of the expectation value of the energy density

$$\langle E(t)\rangle_Q \sim \frac{S_0}{V}\,x\left(\frac{I_{Q-1}(x)+I_{Q+1}(x)}{2I_Q(x)}\right)\,. \tag{7.16}$$

According eq. (7.8), the non-perturbative correction to the coupling coming from the dilute gas of instantons is the following:

$$\lambda_Q^{\text{dig}}(c) = \frac{2NS_0}{3\mathcal{A}(\pi c^2)}\,x\left(\frac{I_{Q-1}(x)+I_{Q+1}(x)}{2I_Q(x)}\right)\,. \tag{7.17}$$

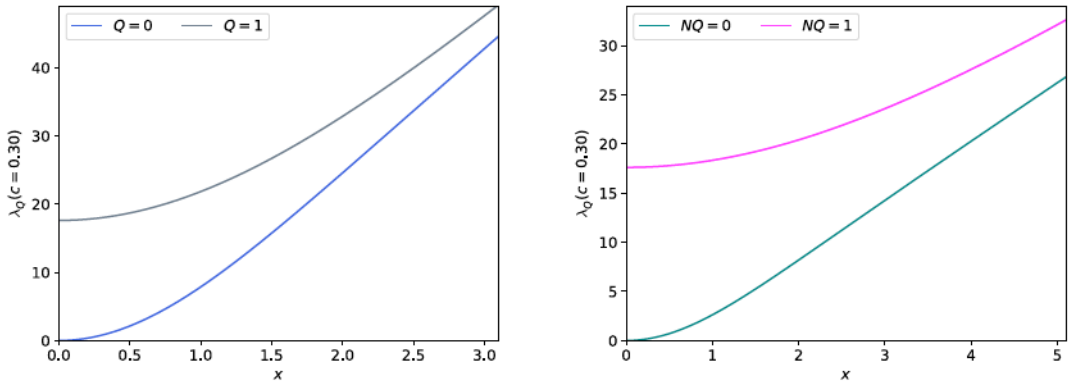

(a) Ordinary instantons. (b) Fractional instantons.

Figure 7.5: (a) We display the non-perturbative contribution to $\lambda_Q(c = 0.3)$ as a function of x for $Q = 0$ and $Q = 1$, for $S_0 = 8\pi^2$. (b) We display the non-perturbative contribution to $\lambda_Q(c = 0.3)$ as a function of x for $Q = 0$ and $Q = 1$, for fractional instantons with $NS_0 = 8\pi^2$.

which, in principle, should be added to the perturbative contribution. Figure 7.4a shows $\langle n+\overline{n}\rangle_Q$ of eq. (7.15) as a function of x for charges $Q = 0, 1, 2$. The expectation value starts at the corresponding charge $|Q|$ and grows almost linear for large x. We also show in fig. 7.4b the ratio of the expectation values of eq. (7.3). Finally, figure 7.5a shows the dependence of the coupling $\lambda_Q^{\text{dig}}(c)$ as a function of x for these two topological sectors.

We can also compute the topological susceptibility in this approximation. The partition function in the θ vacuum is given by:

$$Z(\theta) = \mathcal{C} \sum_{n,\overline{n}} \frac{1}{n!\overline{n}!} (RV)^{n+\overline{n}} e^{i(n-\overline{n})\theta} = \mathcal{C} e^{2RV\cos\theta}\,, \tag{7.18}$$

and the topological susceptibility can be computed from:

$$\chi = \left\langle \frac{(n-\overline{n})^2}{V} \right\rangle = -\frac{1}{VZ(\theta)} \frac{\partial^2 Z(\theta)}{\partial^2 \theta}\Big|_{\theta=0} = 2R\,. \tag{7.19}$$

In the dilute gas approximation, R is determined from the determinant of the fluctuation operator around one instanton. The result at one-loop order in infinite volume reads

$$R = A\,\left(\lambda(\mu)\right)^{-\frac{n_c}{2}}\, e^{-NS_0/\lambda(\mu)} \int_0^\infty \frac{d\rho}{\rho^5}\,(\rho\mu)^{2Nb_0S_0}\,, \tag{7.20}$$

where n_c is the number of collective coordinates, equals to $4N$ for ordinary $SU(N)$ instantons. The formula up to two loops, including the prefactor, has been computed in ref. [187]. The resulting expression is infrared divergent, although on a finite volume, it would be cut off by the box size. Note however, that to determine λ_Q^{dig} we only need the relation $x = 2RV = \chi V$, where one can use the measured topological

susceptibility to determine the input parameter x and evaluate the coupling using eq. (7.15).

Fractional instantons

In the case of fractional instantons, the only difference is that instantons with charge $\pm 1/N$ contribute to the partition function. Note that the twist used in our simulations belongs to the class of so-called orthogonal twists, satisfying $n_{\mu\nu}\tilde{n}_{\mu\nu}/4 = 0 \pmod N$, and thus the total topological charge is still quantized in integer units. This fact has to be taken into account when formulating the dilute gas partition function for fractional instantons, and thus

$$Z_Q = \mathcal{C} \sum_{n,\overline{n}} \frac{1}{n!\overline{n}!} (RV)^{n+\overline{n}} \delta(n - \overline{n} - NQ)\,. \tag{7.21}$$

We can now use that:

$$I_\alpha(x) = \sum_n \frac{1}{n!\Gamma(n+\alpha+1)} \left(\frac{x}{2}\right)^{2n+\alpha}\,, \tag{7.22}$$

to obtain ($x = 2RV$):

$$Z_Q = \mathcal{C} I_{NQ}(x)\,, \tag{7.23}$$

and

$$\langle n + \overline{n} \rangle_Q = x \left(\frac{I_{NQ-1}(x) + I_{NQ+1}(x)}{2I_{NQ}(x)} \right) = NQ + x \frac{I_{NQ+1}(x)}{I_{NQ}(x)}\,. \tag{7.24}$$

The coupling in this approximation is given by:

$$\lambda_Q^{\text{dig}}(c) = \frac{2NS_0}{3\mathcal{A}(\pi c^2)}\, x \left(\frac{I_{NQ-1}(x) + I_{NQ+1}(x)}{2I_{NQ}(x)} \right) \tag{7.25}$$

where, for fractional instantons, $NS_0 = 8\pi^2$.

Figure 7.5b sows the dependence of λ_Q as a function of x for the sectors $Q = 0$ and $Q = 1$. As for the topological susceptibility, using:

$$Z(\theta) = \sum_{Q\in\mathbf{Z}} e^{iQ\theta} Z_Q = \mathcal{C} \sum_{Q\in\mathbf{Z}} e^{iQ\theta} \sum_{n,\overline{n}} \frac{1}{n!\overline{n}!} (RV)^{n+\overline{n}} \delta(n - \overline{n} - NQ)\,, \tag{7.26}$$

and the following representation for the Kronecker delta function:

$$\delta(n - \overline{n} - NQ) = \frac{1}{N} \sum_{k=1}^{N} e^{2\pi i \frac{k}{N}(n-\overline{n})}\,, \tag{7.27}$$

one arrives at:

$$Z(\theta) = \frac{\mathcal{C}}{N}\sum_{k=1}^{N}\sum_{n,\overline{n}}\frac{1}{n!\overline{n}!}(RVe^{i(\theta+2\pi k)/N})^n(RVe^{-i(\theta+2\pi k)/N})^n$$
$$= \frac{\mathcal{C}}{N}\sum_{k=1}^{N}\exp\left\{x\cos\left(\frac{\theta+2\pi k}{N}\right)\right\} \tag{7.28}$$

Finally, eq. (7.28) can be used to derive the general form of the topological susceptibility:

$$\chi = \left\langle\frac{(n-\overline{n})^2}{N^2V}\right\rangle = -\frac{1}{VZ(\theta)}\frac{\partial^2 Z(\theta)}{\partial^2\theta}\Big|_{\theta=0}$$
$$= \frac{2R\mathcal{C}}{N^3Z(\theta=0)}\sum_{k=1}^{N}\left(\cos\left(\frac{2\pi k}{N}\right) - x\sin^2\left(\frac{2\pi k}{N}\right)\right)\exp\left\{x\cos\left(\frac{2\pi k}{N}\right)\right\} \tag{7.29}$$

The relation between $x = 2RV$ and χV is more complicated in this case than for ordinary instantons, but it can still be numerically inverted to obtain x in terms of χV.

In the dilute gas approximation, see i.e. [179, 180]:

$$R = \widehat{C}\ \left(\lambda(\mu)\right)^{-2}\ e^{-NS_0/\lambda(\mu)}\frac{1}{\rho^4}\left(\rho\mu\right)^{2Nb_0S_0}, \tag{7.30}$$

where ρ is the characteristic fractional instanton size. The peculiarity of fractional instantons compared to ordinary ones is that the collective coordinates include only the instanton location; in particular, the size is not a moduli parameter, and in a finite volume it is fixed with respect to the volume of the box. Therefore we expect $\rho \propto \tilde{l}$ in the small volume regime and $\rho \propto 1/\Lambda_{QCD}$ for large volumes. When $\rho \propto \tilde{l}$, and setting $\mu = 1/(c\tilde{l})$, we can write:

$$x = 2RV = C\frac{V}{(c\tilde{l})^4}\ \left(\lambda(\mu)\right)^{-2}\ e^{-8\pi^2/\lambda(\mu)}\Big|_{\mu=(c\tilde{l})^{-1}}, \tag{7.31}$$

and determine x, up to an overall normalization constant, from the measurement of the TGF coupling.

7.4.2 Comparing the semiclassical predictions with the numerical results

Let us use the semiclassical approximation of sec. 7.4.1 to reproduce some important features observed in our simulations. In that section, we computed the contribution to the coupling derived in this approximation when restricted to the sector of topological charge Q, that we collect in the following equation:

$$\lambda_Q^{\text{dig}}(c) = \frac{2NS_0}{3\widehat{\mathcal{A}}(\pi c^2)}\left(\nu + x\frac{I_{\nu+1}(x)}{I_\nu(x)}\right) + \cdots, \tag{7.32}$$

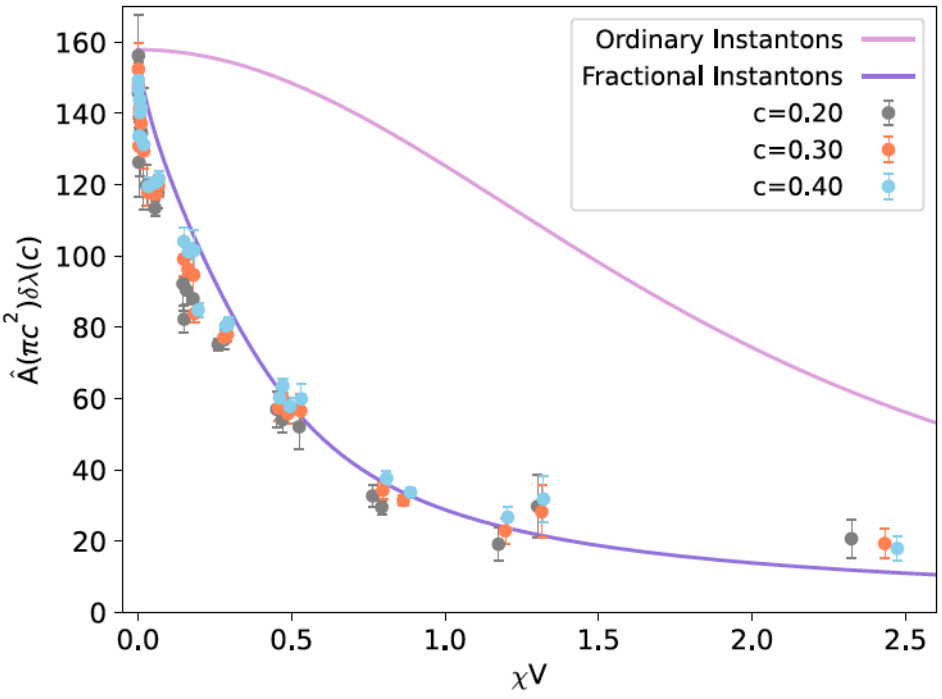

Figure 7.6: We display $\widehat{\mathcal{A}}(\pi c^2)\delta\lambda(c) = \widehat{\mathcal{A}}(\pi c^2)\left(\lambda_{Q=1}(c) - \lambda_{Q=0}(c)\right)$ as a function of χV for couplings obtained at flow time $8t = (c\tilde{l})^2$, with $c = 0, 2,\ 0.3$ and 0.4. The lines correspond to the estimate using the leading semi-classical contribution from fractional or ordinary instantons. Note that these lines are not fit to the data, they are directly given by eq. (7.32) with the parameter x determined from the measured value of the susceptibility.

with $\nu = Q$ for ordinary instantons, and $\nu = NQ$ for fractional ones. We recall that $x = 2RV$, with R the probability of generating one instanton, or anti-instanton, per unit volume, which is a priori unknown. One way to determine R from the numerical simulations is to measure the topological susceptibility.

We have worked a bit more on the case of $SU(3)$, so we will present this analysis by itself, followed by some results for $SU(5)$ and $SU(8)$ gauge groups.

Semiclassical approximation for $N = 3$

In the dilute gas approximation and for the case of ordinary instantons, the relation between R and χ is given by: $\chi = 2R$, while for $SU(3)$ fractional instantons, one obtains from eq. (7.29):

$$\chi = \frac{2R}{9}\left(1 - \frac{3(1+RV)}{2+e^{3RV}}\right) . \tag{7.33}$$

By fixing x in terms of the measured susceptibility, one can evaluate the dilute gas contribution to $\delta\lambda(c) = \lambda_{Q=1}(c) - \lambda_{Q=0}(c)$ and compare the result to the values of $\delta\lambda(c)$ determined in the simulations. This has been done for the set of simulations with $\beta \in [6, 6.8]$ where topology seems to be properly sampled and the number of

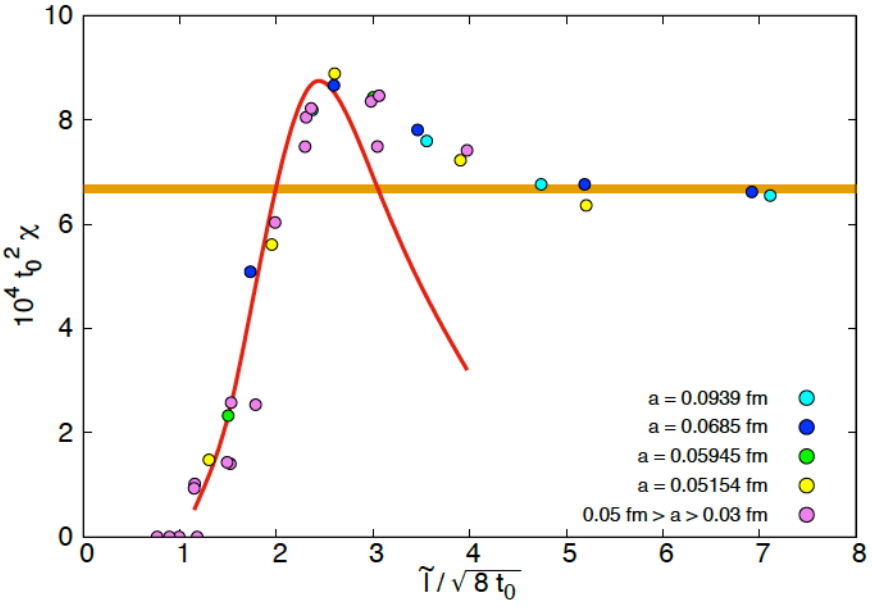

Figure 7.7: Volume dependence of the topological susceptibility. The red line gives the dilute gas estimate discussed in sec. 7.4, cf. eq. (7.34) with $C = 880$.

$Q = 1$ configurations is sufficiently large. In addition, the calculation has been done for various values of the flow time: $8t = (c\tilde{l})^2$, with $c = 0.2$, 0.3, and 0.4. We observe that the quantity $\widehat{\mathcal{A}}(\pi c^2)\delta\lambda(c)$ is quite independent of the value of c. Our results are displayed as a function of χV in fig. 7.6 and compared with the dilute gas predictions for ordinary and fractional instantons, derived from eq. (7.32). Surprisingly, the dependence predicted by the fractional instanton formula matches our results remarkably well in a large range of volumes. We stress that the lines displayed in the figure do not have any free parameter, they are directly given by eq. (7.32) with the input parameter x fixed in terms of the measured value of the susceptibility.

In the dilute gas approximation, one can also obtain a prediction for the parameter $x = 2RV$ in terms of the renormalized coupling. As explained in sec. 7.4.1, the result for fractional instantons at one loop order, obtained from eq. (7.31), reads:

$$x = 2RV = C\,\frac{V}{\rho^4}\,\big(\lambda(1/\rho)\big)^{-2}\; e^{-8\pi^2/\lambda(1/\rho)} \tag{7.34}$$

where ρ is the characteristic fractional instanton size, proportional to $\tilde{l}$ in the small volume regime, and C is an unknown normalization constant. Ignoring this fact, we have used this functional form to get a qualitative idea of the volume dependence of the topological susceptibility in this approximation. The calculation requires the input of the renormalized coupling constant on a scale of $\rho \propto \tilde{l}$; differences in the

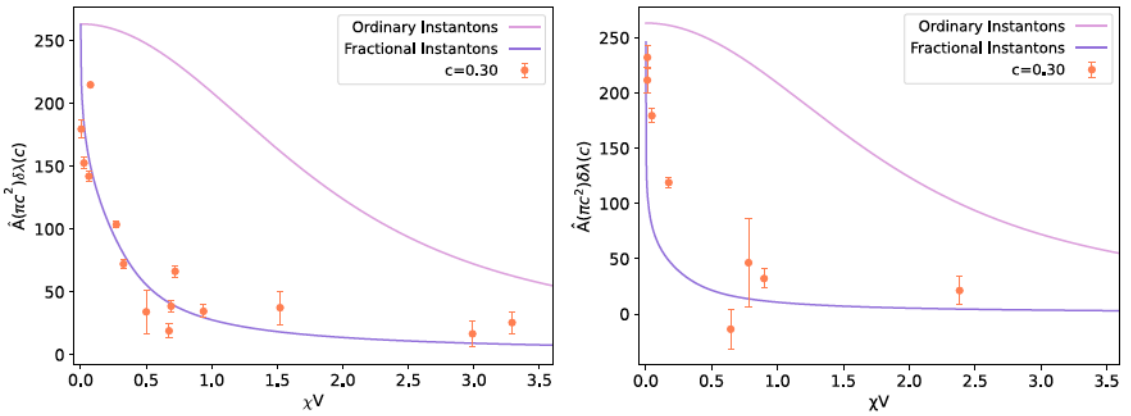

(a) $SU(5)$. (b) $SU(8)$.

Figure 7.8: We display, for $SU(5)$ and $SU(8)$, the contribution $\widehat{\mathcal{A}}(\pi c^2)\delta\lambda(c)$ as a function of χV for couplings obtained at flow time $8t = (c\tilde{l})^2$, with $c = 0, 3$. The lines correspond to the estimate using the leading semi-classical contribution from fractional or ordinary instantons.

scheme dependence translate at this order into a change in the value of C, which depends on the ratio of the Λ parameters. We have tested the formula setting $\rho = c\tilde{l}$ and used the coupling in the TGF scheme with $c = 0.2$, 0.3 and 0.4. The one with $c = 0.2$ better describes our small volume results. A fit of the dependence on $\tilde{l}$ of the topological susceptibility with x given by eq. 7.34, gives $C = 880$ and leads to the red line depicted in fig. 7.7 which describes qualitatively well our data. The saturation to the infinite volume value is expected to take place, as discussed in sec. 7.4.1, when the characteristic size of the fractional instantons becomes of order $1/Lambda_{\rm QCD}$ [79].

Semiclassical approximation for $N = 5$ and 8

As in the case of $SU(3)$, the relation between R and χ for ordinary instantons is given by $\chi = 2R$, while for fractional instantons we get:

$$\chi V = \frac{-x\left(2+2\sqrt{5}-4e^{\frac{(5+5\sqrt{5})x}{4}}+x(5-\sqrt{5})+e^{\frac{\sqrt{5}}{2}x}\left(2-2\sqrt{5}+(5+\sqrt{5})x\right)\right)}{100\left(2+2e^{\frac{\sqrt{5}}{2x}}+e^{\frac{(5+\sqrt{5})x}{4}}\right)} \tag{7.35}$$

for $SU(5)$, and:

$$\chi V = \frac{x\left(-x-x\cosh\frac{x}{\sqrt{2}}+\sinh x+\sqrt{2}\sinh\frac{x}{\sqrt{2}}\right)}{64\left(1+\cosh x+2\cosh\frac{x}{\sqrt{2}}\right)} \tag{7.36}$$

for $SU(8)$.

Again, by fixing x in terms of the numerically computed susceptibility, one can evaluate the contribution to $\delta\lambda(c = 0.30) = \lambda_{Q=1}(c = 0.30) - \lambda_{Q=0}(c = 0.30)$ and compare it with the values of $\delta\lambda(c = 0.30)$ determined in the simulations for $Q = 0$ and $Q = 1$. The results are shown in figs. 7.8a and 7.8b. We only have simulated results for $c = 0.3$. Nevertheless, we see the same tendency of the results to follow the predictions of the fractional instanton approximation instead of the ordinary one, and both curves tend to a universal behavior as the large N limit is approached.

7.5 Summary

The volume dependence of some important quantities in our setup has been studied in this chapter. First, we have analyzed the dependence of the TGF coupling on the effective physical volume (in units of $\sqrt{\sigma_0}$) for the 3 gauge groups studied in this work. The results are largely N independent, with small corrections to this leading behavior, providing support for the volume independence conjecture.

We also computed the topological susceptibility in cases where freezing did not interfere with its determination. As expected, the topological susceptibility starts from zero for small values of the physical volume and grows up to the infinite volume result [177]. We then studied the intermediate volume regime with a dilute approximation based on instantons of different types. The only remaining parameter of this approximation is the probability R of generating an instanton or an anti-instanton, which was extracted from the numerical results of the topological susceptibility. In the case of $SU(3)$, we have obtained compelling evidence that the correlation between topological charge and coupling observed at intermediate volumes in our simulations can be understood in terms of the contribution of fractional instantons. Although the results for $N = 5$ and 8 are still very preliminary, they follow the same tendency as observed for the case of $SU(3)$.

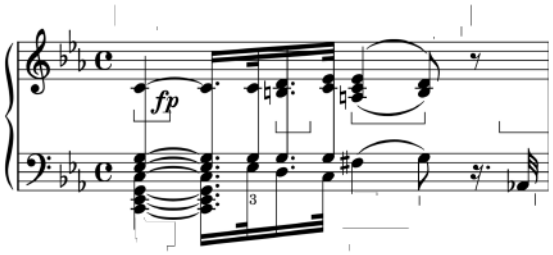

8 $SU(N)$ fractional instantons and the Fibonacci sequence

8.1 Motivation

Although the boundary conditions in our running coupling simulations of chs. 4 and 5 correspond to the so-called orthogonal twist, where $\vec{k} \cdot \vec{m} = 0$ leads to a topological charge that is still quantized in integer units according to eq. (2.19), in ch. 7 we have seen clear evidence that instantons with fractional topological charge play an important role in establishing the low-energy dynamics of the theory. In this chapter we will study an interesting type of solution that is present in our asymmetric geometry when non-orthogonal twists ($\vec{k} \cdot \vec{m} \neq 0$) are considered, which has the peculiarity of having a topological charge quantized in units of $1/N$.

The setup in this chapter will be slightly different from the previous ones in that we will discuss the Hamiltonian limit of gauge theory, i.e. we will consider a geometry $R \times T^3$ instead of T^4. From a physical point of view, the spatial part of the twist, with components $m_i = \epsilon_{ijk} n_{jk}$, can be interpreted in the Hamiltonian limit as the introduction of abelian $\mathbf{Z}_N$ magnetic fluxes piercing the 3-dimensional spatial torus, while the remaining part ($k_i = n_{0i}$) is dual to the electric flux, a vector of quantum numbers characterizing the physical Hilbert space on the theory.

The use of the torus size to explore the dynamics of Yang-Mills theories from the perturbative regime to the onset of confinement was advocated in the 80s, starting with the work by Lüscher [188, 189]. With twisted boundary conditions, this line of thought was explored by González-Arroyo and collaborators, beginning with the perturbative analysis of the pure Yang-Mills spectrum on a small twisted box [190,191] and followed by the study of the dynamical role of fractional instantons in $SU(2)$ Yang-Mills theory beyond the purely semiclassical regime [77,180,192–195] – see also refs. [139,196] for some results on $SU(3)$. For a detailed discussion on the role of instantons with fractional topological charge, we recommend a recent review by Gonzalez-Arroyo [79]. A parallel path for periodic boundary conditions was followed by van Baal and collaborators, leading to a piece of work nicely summarized in ref. [185].

In this chapter, we will introduce a new class of self-dual $SU(N)$ fractional charge solutions, which are localized in time and can be interpreted as tunneling events between inequivalent flat connections on $\mathbf{T}^3$. They are obtained numerically by a minimization scheme based on the gradient flow [11–14] and scale nicely towards the large N limit. As commented in ch. 2, similar fractional charge solutions have been obtained previously, and the first example was obtained for $SU(2)$ in refs. [75, 76] with a magnetic twist $\vec{m} = (1, 1, 1)$; subsequently these solutions were generalized to an arbitrary number of colors for certain choices of the torus periods and twist [77, 78].

The solutions presented in this chapter have a different type of twist which becomes relevant in the large N limit. As in the previous chapters, we choose both the magnetic flux and the number of colors within the Fibonacci sequence, i.e., $N = F_n$ and $\vec{m} = (0, 0, F_{n-2})$ [10], and consider an asymmetric torus geometry where two periods scale as $1/N$. We will elaborate on these choices in section. 8.2, where we summarize some well-known facts about the formulation of gauge theories on a twisted box; for reviews on this topic the reader is referred to refs. [68, 106, 185, 197].

The chapter is structured as follows. First, in section 8.2 we revisit and discuss gauge fields on a torus and reconstruct the main lines of research where twisted boundary conditions have played an influential role. Some of these topics have already been covered in ch. 2. The importance of fractional instantons in this context is especially emphasized. Next, section 8.3 discusses some explicit examples available in the literature for constant curvature self-dual solutions with topological charge $1/N$ for our particular setup. Finally, in section 8.4 we present the fractional instanton solutions on $\mathbf{R} \times \mathbf{T}^3$ obtained by a numerical minimization approach. We end with some final remarks and conclusions. Throughout the chapter, several figures are presented showing the energy density of the solutions, as well as various other gauge invariant observables. In addition, the reader will find in appendix D a list of complementary plots that have not been included in the text to facilitate the reading of the chapter. The results of this chapter are contained in [198, 199].

8.2 General considerations

In this section, we will focus on the solutions with twisted boundary conditions and collect some well-known facts and references that will allow us to contextualize the relevance of fractional instantons. For further details, the interested reader can consult the original references or the review articles [68, 79, 106, 185, 200].

We start by reviewing the Hamiltonian formulation of $SU(N)$ Yang-Mills theory on $\mathbf{R} \times \mathbf{T}^3$, with $\mathbf{T}^3$ a 3-dimensional torus endowed with twisted boundary conditions (TBC). The discussion will be focused on the particular setup that we consider for this paper:

- $SU(N)$ Yang Mills theory defined on an asymmetric torus of sizes $l_1 = l_2 = l/N$ and $l_3 = l$. The number of colors N is the *nth* integer in the Fibonacci sequence, i.e., $N = F_n$.

- Twisted boundary conditions on the three-torus with chromo-magnetic flux $\vec{m} = (0, 0, m)$. The flux m is a coprime of N, and equal to F_{n-2}.

It is important to note that in this chapter we will introduce a change in our notation, referring to the effective volume of the torus as l, whereas in the previous chapters it was referred to as $\tilde{l}$.

There are various reasons behind these particular choices; most were already discussed in chapter 5, but we briefly elaborate on each of them below and refer the reader to the series of works [10, 58, 100, 112, 201] and the review [197] for further details.

We recall that with our choice of twist and torus geometry, the effective large N dynamics is that of a symmetric torus of size l^3 [201]. The parameter that controls the onset of non-perturbative effects in this setup is Λl, where Λ is the non-perturbative dynamical scale of the theory, even in the large N limit (taken at a fixed value of l), where two of the torus periods shrink to zero; it is precisely this *singular* large N limit [7], already introduced in chs. 2 and 7, in which we will center the discussion of this chapter.

The concrete choice of magnetic flux m is driven as well by various considerations. First, a non-zero flux m coprime with N guarantees the perturbative potential to have N isolated gauge-inequivalent minima. In those configurations, the classical potential energy vanishes [190], in contrast with the case of periodic boundary conditions where infinitely many gauge inequivalent configurations have zero vacuum energy [30]. Perturbation theory in this second case is non-analytic in the coupling constant [189], considerably complicating the small volume dynamics analysis. Second, the particular choice of m and N as integers in the Fibonacci sequence aims, as we already know, at avoiding large N phase transitions that invalidate volume independence. Let us recall that, following Morita duality, our setup is equivalent to a non-commutative $U(1)$ gauge theory defined on an l^3 torus with dimensionless non-commutativity parameter given by $\hat{\theta} = \overline{m}/N$, with $\overline{m}$ the modular inverse of m, i.e., $m \times \overline{m} = 1 \bmod N$. It is easy to see that with our choices for N and m, one gets $\overline{m} = (-1)^n F_{n-2}$ and the non-commutativity parameter becomes $|\hat{\theta}| = F_{n-2}/F_n$, which in the large N limit approaches φ^{-2}, with $\varphi = (1 + \sqrt{5})/2$ the Golden Ratio. We will adopt this special twist for the rest of this chapter.

Once our choice of twist and torus geometry has been fixed, we move on to the Hamiltonian description of the gauge theory on the 3-torus with twisted boundary. We recall that the effective torus size l can be tuned to make the theory analytically tractable in the regime in which $\Lambda l << 1$. In what remains, we will summarize what is known about the gauge theory dynamics in this small-volume domain.

Let us collect some particular results concerning the twisted algebra discussed in chapter 2, and adapted to the Hamiltonian setup. Twisted boundary conditions on $\mathbf{R} \times \mathbf{T}^3$ are implemented at the level of the gauge potential by imposing the following periodicity conditions:

$$A_\mu(x + l_i \hat{e}_i) = \Omega_i(x) A_\mu(x) \Omega_i^\dagger(x) + i\, \Omega_i(x) \partial_\mu \Omega_i^\dagger(x), \tag{8.1}$$

where Ω_i are $SU(N)$ transition matrices subject to the consistency conditions:

$$\Omega_i(x + l_j\hat{e}_j)\,\Omega_j(x) = Z_{ij}\,\Omega_j(x + l_i\hat{e}_i)\,\Omega_i(x), \tag{8.2}$$

with $Z_{ij} = \exp\{i2\pi n_{ij}/N\}$. An appropriate choice of gauge to analyze the Hamiltonian limit is $A_0 = 0$. In this gauge, the residual, space-dependent gauge invariance is used to bring the three spatial twist matrices to constant $SU(N)$ matrices satisfying the consistency conditions imposed by the magnetic twist [202,203]. With our choice $\vec{m} = (0, 0, m)$, this gives:

$$\Gamma_1\Gamma_2 = e^{i\frac{2\pi m}{N}}\Gamma_2\Gamma_1, \tag{8.3}$$
$$\Gamma_3\Gamma_i = \Gamma_i\Gamma_3, \text{ for } i = 1, 2, \tag{8.4}$$

reducing the periodicity conditions to:

$$A_i(x + l_j\widehat{e}_j) = \Gamma_j A_i(x)\Gamma_j^\dagger. \tag{8.5}$$

In 3 dimensions, a particularly suitable basis for our choice of twist is the following:

$$\Gamma_1 = Q_N^m, \tag{8.6}$$
$$\Gamma_2 = P_N^\dagger, \tag{8.7}$$
$$\Gamma_3 = z_3\mathbb{I}, \tag{8.8}$$

with

$$Q_N|lj = z\delta_{l,j}\exp\left(\frac{2\pi l}{N}\right), \tag{8.9}$$
$$P_N|lj = z\delta_{l,j+1}. \tag{8.10}$$

The Fourier expansion consistent with this choice is given by [5]:

$$A_i(x_0, \vec{x}) = \frac{1}{\sqrt{l_1 l_2 l_3}}\sum_{\vec{p}}{}' \hat{A}_i(x_0, \vec{p})e^{i\vec{p}\cdot\vec{x}}\widehat{\Gamma}(\vec{p}), \tag{8.11}$$

with:

$$\widehat{\Gamma}(\vec{p}) = \frac{1}{\sqrt{2N}}e^{i\alpha(\vec{p})}\Gamma_1^{-\overline{m}n_2}\Gamma_2^{\overline{m}n_1}, \tag{8.12}$$

with momenta quantized as $p_i = 2\pi n_i/l$, $n_i \in \mathbf{Z}$ in all three directions, and where the prime in the sum indicates the exclusion of the cases where both n_1 and n_2 are equal to zero modulo N. At the perturbative level, the fact that momentum is quantized in units of l in the short directions (with $l_1 = l_2 = l/N$) is, as we know, the first signal of volume independence, indicating that the 3-dimensional box has the same effective size l in all three spatial directions. Note moreover that the fact that Γ_1 and Γ_2 span the algebra of the $SU(N)$ group, together with the consistency condition eq. (8.4), implies that necessarily Γ_3 has to belong to the center of $SU(N)$,

i.e., $\Gamma_3 = z_3 \mathbb{I}$, and therefore there are N different choices of Γ_3 compatible with our boundary conditions.

Gauge fixing is not complete once the constant twist matrices have been chosen. In addition, space-dependent gauge transformations subject to the periodicity condition:

$$\Omega(\vec{x} + l_i \hat{e}_i) = \Gamma_i \Omega(\vec{x}) \Gamma_i^\dagger, \tag{8.13}$$

are still allowed. On top of those, one can as well consider so-called *singular gauge transformations*, satisfying:

$$\Omega_{\vec{s}}(\vec{x} + l_i \widehat{e}_i) = e^{i\frac{2\pi s_i}{N}} \Gamma_i \Omega_{\vec{s}}(\vec{x}) \Gamma_i^\dagger, \; s_i \in \mathbf{Z}_N. \tag{8.14}$$

These transformations commute with the Hamiltonian and can be simultaneously diagonalized with it. States in the Hilbert space can therefore be parameterized by how their wave function transforms under $\Omega_{\vec{s}}$:

$$\Psi_{\vec{e}}\left([\Omega_{\vec{s}}]A\right) = e^{i\frac{2\pi \vec{e}\cdot\vec{s}}{N}} \Psi_{\vec{e}}(A). \tag{8.15}$$

The vector of integers $\vec{e} = (e_1, e_2, e_3)$, defined modulo N, characterizes the state and receives the name of electric flux [1]. There are N^3 different electric flux sectors, and the Hamiltonian can be diagonalized independently. With our choice of boundary conditions, all sectors different from $\vec{e} = \vec{0}$ are lifted in perturbation theory, except the ones of the form $\vec{e} = (0, 0, e_3)$, which remain degenerate with the vacuum [190]. This degeneracy is removed non-perturbatively by the effect of fractional instantons; the general expression for the instanton-induced energy splitting can be found in ref. [184] – see also [185] – and has been tested for SU(2) against numerical simulations in refs. [180, 192].

It is crucial at this stage to recall that the semiclassical weight, $\exp\{-NS/\lambda\}$, remains non-zero in the large N 't Hooft limit for $Q = 1/N$ fractional instantons with action $NS = 8\pi^2$. In what follows, we consider that the quantity that *scales* adequately in the large N limit (in the sense of becoming N-independent) is NS for the action and NQ for the topological charge.

In the Hamiltonian limit, these fractional instantons have a well-defined interpretation as tunneling events interpolating between two pure gauge configurations, which can be characterized in terms of the holonomies (the spatial Polyakov loops at $x_0 = \pm\infty$). With our choice of twist, the only holonomies that can be different from zero are those that wind non-trivially in the x_3 direction. Let us see how this comes about. We start by noticing that with twisted boundary conditions, the appropriate definition of Polyakov loops winding once along a torus period is given by [184]:

$$P_i(x_0, \vec{x}) \equiv \frac{1}{N} \mathrm{Tr} \left(P \exp \left\{ -i \int_0^{l_i} dx_i A_i(x_0, \vec{x}) \right\} \Gamma_i \right), \tag{8.16}$$

a definition that combined with eqs. (8.14) and (8.15), immediately shows that P_i transforms a state with electric flux $\vec{e}$ into one with flux $\vec{e} + \hat{e}_i$. This allows us to

understand the previous statement that the only electric flux sectors not lifted in perturbation theory are those with $e = (0, 0, e_3)$. The argument is as follows. We can find a relationship between electric flux and momentum in the twisted directions by using the periodicity properties of Polyakov loops, obtaining:

$$\hat{e}_i = \frac{N l_i}{2\pi} \epsilon_{ij} \bar{m} p_j \ (\text{mod } N) \text{ for i=1,2.} \tag{8.17}$$

In the third direction, the Polyakov loop is periodic; therefore, zero momentum is allowed. Consequently, all states differing only in the value of the electric flux in the third direction $\hat{e}_3$ are energy degenerate in perturbation theory. Moreover, this degeneracy is also reflected in the vacuum of the theory, and states with flux $(0, 0, \hat{e}_3)$ are degenerate at all orders in perturbation theory. As mentioned before, only tunneling through fractional instantons removes removes the N-folded degeneracy.

We continue with the observation that a gauge potential $A_i(\vec{x}) = 0$ is compatible with the choice of constant twist matrices and leads to holonomies given by:

$$P(\gamma, w_1, w_2, w_3) = \frac{1}{N} \text{Tr} \left(\Gamma_1^{w_1(\gamma)} \Gamma_2^{w_2(\gamma)} \Gamma_3^{w_3(\gamma)} \right), \tag{8.18}$$

where γ represents a closed curve and $w_i(\gamma)$ denotes its winding number in the *ith* direction, defined modulo N.

In our particular case, this implies $P(\gamma, 0, 0, 1) = z_3$ and $P(\gamma, w_1, w_2, 0) = 0$, unless w_1 and w_2 are both equal to zero (mod N). Therefore, the holonomy value parameterizes flat connections in the third direction, which takes values over the N roots of unity. The corresponding gauge potentials are mapped into one another by the action of singular gauge transformations of the form given in eq. (8.14), spanning a group isomorphic to $\mathbf{Z}_N$.

It is worth mentioning that states with the nontrivial flux in the twisted plane are already lifted in perturbation theory. At a tree level, the lowest such states correspond to the fluxes $(\pm\bar{k}, 0, \hat{e}_3)$ and $(0, \pm\bar{k}, \hat{e}_3)$, with momenta $(0, \pm 2\pi/(N l_2)$, $0)$ or $(\pm 2\pi/(N l_1), 0, 0)$. At the next order in perturbation theory, and for moments $(p1, p2, 0)$, there are two transverse polarizations $\epsilon(1) \propto (0, p_2, -p_1, 0)$, and $\epsilon(2) = (0, 0, 0, 0, 1)$. The self-energy correction has been calculated for $\mathbf{T}^2 \times \mathbf{R}^2$ (see, e.g., ref. [197] and references therein). Still, a generalization for the case at hand seems straightforward by simply replacing the integral over the third spatial direction with a discrete sum.

With these preliminaries, we are ready to discuss the numerical approach used to obtain self-dual fractional instantons on the lattice and to characterize the solutions resulting from our study. The Hamiltonian limit is achieved through a limiting process: we start by looking at minimal action solutions on a 4-dimensional torus and analyze their behavior when the torus period in the time direction is sent to infinity. In addition, the fractional topological charge is enforced by introducing a twist in time, i.e., by working with gauge potentials periodic in the time direction up to gauge transformations, i.e.:

$$A_i(x + l_0 \hat{e}_0) = \Omega_0(\vec{x}) A_i(x) \Omega_0^\dagger(\vec{x}) + i \Omega_0(\vec{x}) \partial_i \Omega_0^\dagger(\vec{x}). \tag{8.19}$$

These boundary conditions act as the generators of singular gauge transformations if Ω_0 is taken to satisfy eq. (8.14) [1]. The only additional condition one has to impose is that these boundary conditions support the fractional topological charge. For our choice of magnetic twist ($N = F_n$, $m = F_{n-2}$), and using the formula for the quantization of Q with twisted boundary conditions [72, 184], one obtains:

$$Q = \frac{1}{16\pi^2}\int d^4x \mathrm{Tr}\left(G_{\mu\nu}(x)\widetilde{G}_{\mu\nu}(x)\right) = \nu - \frac{\vec{k}\cdot\vec{m}}{N} = \nu - \frac{F_{n-2}\,k_3}{F_n},\ \nu \in \mathbf{Z}. \quad (8.20)$$

It is easy to see that the minimal fractional topological charge $1/N$ is obtained by taking: $k_3 = -\overline{m} = (-1)^{n+1}F_{n-2}$ and $\nu = (-1)^{n+1}F_{n-4}$. Therefore, we select a space-time twist: $\vec{k} = (0, 0, -\overline{m})$.

In section 8.4, we will present new localized-in-time numerical solutions compatible with our setup and discuss their scaling properties in the singular large N limit mentioned before. As we will see, they resemble the vortex-like configurations obtained for $\mathbf{T}^2 \times \mathbf{R}^2$ in refs. [204–206] but exhibit different large N scaling.

8.3 Fibonacci construction of constant curvature solutions on $\mathbf{T}^4$

This section discusses some solutions of the Yang-Mills equations of motion on $\mathbf{T}^4$ with topological charge $Q = 1/N$ and compatible with our choice of twisted boundary conditions. They have constant curvature and become self-dual for specific values of the torus aspect ratios. Although the Hamiltonian limit of interest is not included in this set, we provide concrete examples that, up to our knowledge, were not previously known in the literature. They are obtained by applying the general construction of constant curvature solutions in the 4-torus recently presented in ref. [74], which generalizes the original one by 't Hooft [69]. We start with a brief review following the notation introduced in ref. [74] and then discuss the particular implementation when both N and the 't Hooft fluxes belong to the Fibonacci sequence.

The construction starts by decomposing the number of colors as $N = N_1 + N_2$ and correspondingly the twist tensor as:

$$n_{\mu\nu} = n^{(1)}_{\mu\nu} + n^{(2)}_{\mu\nu}, \quad (8.21)$$

where the $n^{(a)}_{\mu\nu}$ are taken as orthogonal twists in $SU(N_a)$. Defining:

$$\Delta_{\mu\nu} = n^{(2)}_{\mu\nu}N_1 - n^{(1)}_{\mu\nu}N_2, \quad (8.22)$$

[1] It is trivial to see that they map $A_i = 0$ at $x_0 = -\infty$ to $A_i = i\Omega_0(\vec{x})\partial_i\Omega_0^\dagger(\vec{x})$ at $x_0 = +\infty$, thus interpolating between two flat connections.

the gauge field and the field strength tensor of the constant curvature solutions are given by:

$$A_\mu(x) = \pi \frac{\Delta_{\nu\mu}}{N l_\mu l_\nu} x_\nu T, \tag{8.23}$$

$$G_{\mu\nu}(x) = 2\pi \frac{\Delta_{\mu\nu}}{N l_\mu l_\nu} T, \tag{8.24}$$

where T stands for the hermitian and traceless matrix:

$$T = \begin{pmatrix} \mathbb{I}_1/N_1 & 0 \\ 0 & -\mathbb{I}_2/N_2 \end{pmatrix}, \tag{8.25}$$

with $\mathbb{I}_a$ representing the identity matrix in $SU(N_a)$.

These solutions have constant action density and a topological charge:

$$Q = \frac{\epsilon_{\mu\nu\rho\sigma}\Delta_{\mu\nu}\Delta_{\rho\sigma}}{8 N N_1 N_2}. \tag{8.26}$$

Moreover, it is easy to see that they satisfy twisted boundary conditions on $\mathbf{T}^4$ with transition matrices given by:

$$\Omega_\mu(x) = e^{i\pi\omega_\mu(x)T} \begin{pmatrix} \Gamma_\mu^{(1)} & 0 \\ 0 & \Gamma_\mu^{(2)} \end{pmatrix}, \tag{8.27}$$

where the constant $SU(N_a)$ matrices $\Gamma_\mu^{(a)}$ are twist eaters compatible with the orthogonal twists $n_{\mu\nu}^{(a)}$, i.e., satisfying:

$$\Gamma_\mu^{(a)}\Gamma_\nu^{(a)} = e^{2\pi i n_{\mu\nu}^{(a)}/N_a}\Gamma_\nu^{(a)}\Gamma_\mu^{(a)}, \tag{8.28}$$

and where $\omega_\mu(x)$ stands for the function:

$$\omega_\mu(x) \equiv \frac{\Delta_{\mu\nu}x_\nu}{N l_\nu}. \tag{8.29}$$

We will now consider the case in which the only non-zero components of the twist matrix are $\Delta_{03} \equiv \Delta_A$ and $\Delta_{12} \equiv \Delta_B$ (any other choice can be brought to this form by a change of basis [68]). The self-duality condition ($G_{\mu\nu} = \tilde{G}_{\mu\nu}$) trivially amounts in this case to

$$\frac{l_0 l_3}{l_1 l_2} = \frac{\Delta_A}{\Delta_B}. \tag{8.30}$$

This implies that self-dual constant curvature solutions exist only for a fixed value of the ratio of torus areas in planes 03 and 12.

Given the form of the topological charge, the general minimal action solutions with $Q = 1/N$ can be obtained by choosing $\Delta_A\Delta_B = N_1 N_2$ and [74]:

$$\Delta_A = M_{A1}M_{A2}\ ;\ \Delta_B = M_{B1}M_{B2}\ ;\ N_1 = M_{A1}M_{B1}\ ;\ N_2 = M_{A2}M_{B2}, \tag{8.31}$$

with M_{Ai}, M_{Bi} positive integers. Taking, without loss of generality, N_1 and N_2 to be coprime, compatibility of this choice with eq. (8.22) is easily obtained by selecting [74]:

$$k^{(a)} = M_{Aa}\hat{k}^{(a)}, \tag{8.32}$$
$$m^{(a)} = M_{Ba}\hat{m}^{(a)}, \tag{8.33}$$

satisfying the following relations:

$$\hat{k}^{(2)}M_{B1} - \hat{k}^{(1)}M_{B2} = 1, \tag{8.34}$$
$$\hat{m}^{(2)}M_{A1} - \hat{m}^{(1)}M_{A2} = 1, \tag{8.35}$$

with $\hat{k}^{(a)}$ ($\hat{m}^{(a)}$) coprime with M_{Ba} (M_{Aa}). It is easy to see that this choice leads to orthogonal twists of the required type.

The properties of Fibonacci numbers make them particularly suitable for finding non-trivial examples of this construction. We recall our choice of gauge parameters, with the number of colors set to $N = F_n$ and with 't Hooft fluxes $\vec{m} = (0, 0, m)$ and $\vec{k} = (0, 0, -\overline{m})$, where $m = F_{n-2}$ and $\overline{m} = (-1)^n F_{n-2}$. The starting point is the Honsberger identity:

$$F_n = F_m F_{n-m+1} + F_{m-1}F_{n-m}. \tag{8.36}$$

Setting $N = F_n$, this relation can be mapped in a straightforward way to the decomposition $N = M_{A1}M_{B1} + M_{A2}M_{B2}$. Given the self-duality condition eq. (8.30), many possible identifications are possible. We are interested in those corresponding to the singular large N limit, with l_1 and l_2 scaling as l/F_n, for fixed l. Therefore we obtain:

$$l_0 l_3 = \frac{M_{A_1}M_{A_2}}{F_n^2 M_{B_1}M_{B_2}}, \tag{8.37}$$

where, for simplicity, we have set the reference scale $l = 1$.To keep the area in the 03 plane of order 1 when n tends to infinity, we choose:

$$M_{A_1}M_{A_2} = F_{n-m+1}F_{n-m}, \tag{8.38}$$
$$M_{B_1}M_{B_2} = F_m F_{m-1}. \tag{8.39}$$

with $n - m >> 1$. One can easily work out, in this case, the twist decomposition, c.f. eq. (8.21), compatible with the conditions given in eqs. (8.34), (8.35). The solution for the case of odd $n - m$ is provided below for completeness (for even $n - m$ one just has to exchange $A_1 \leftrightarrow A_2$, $B_1 \leftrightarrow B_2$ and $n_{\mu\nu}^{(1)} \leftrightarrow n_{\mu\nu}^{(2)}$). One takes:

$$M_{B1} = F_m \ ; \ M_{B2} = F_{m-1} \ ; \ M_{A1} = F_{n-m+1} \ ; \ M_{A2} = F_{n-m}, \tag{8.40}$$

with chromo-electric flux given by[2]:

$$\hat{k}^{(1)} = (-1)^{n+1}F_{m-2}, \tag{8.41}$$
$$\hat{k}^{(2)} = (-1)^{n+1}F_{m-3}, \tag{8.42}$$

[2]We use $F_{-m} = (-1)^{m+1}F_m$ to extend the definition of Fibonacci numbers to negative integers.

and magnetic flux by:

$$\hat{m}^{(1)} = F_{n-m-1}, \tag{8.43}$$

$$\hat{m}^{(2)} = F_{n-m-2}. \tag{8.44}$$

Let us study in more detail the possible values of the area in the 03 plane arising from this particular choice. We can express Fibonacci numbers by using the well-known Binet's formula:

$$F_n = \frac{1}{\sqrt{5}}\left(\varphi^n - (\psi)^n\right), \tag{8.45}$$

where φ stands for the Golden Ratio:

$$\varphi = \frac{1+\sqrt{5}}{2}, \tag{8.46}$$

and $\psi \equiv -\varphi^{-1}$. In the limit $n \to \infty$, Fibonacci numbers scale as $\sqrt{5}F_n = \varphi^n$, leading, for $n-m$ large, to:

$$l_0 l_3 = \frac{F_{n-m+1}F_{n-m}}{F_n^2 F_m F_{m-1}} \xrightarrow[n-m\to\infty]{} l_0 l_3 = \frac{\varphi^{1-2m}}{F_m F_{m-1}} \tag{8.47}$$

with the largest value of the area in the 03 plane obtained for $m = 2$. Choosing $l_3 = 1$ leads to a maximum value of $l_0 = \varphi^{-3} \sim 0.236$. If instead one fixes $l_0 = l_3$, the maximal length is $l_0 = l_3 = \varphi^{-3/2} \sim 0.486$. Clearly, under this construction, one cannot approach the Hamiltonian limit ($l_0 \to \infty$, $l_3 = 1$). In the next section, we describe solutions obtained in that limit with a numerical approach. We analyze first the case in which $l_0 = l_3 = 1$ and then look at what happens when the time extent is increased, keeping $l_3 = 1$ fixed. As we will see, in approaching the Hamiltonian limit, the constant curvature configuration is deformed, developing a localized profile in the time direction with tails that tend to flat connections at $x_0 = \pm\infty$.

We end this section by pointing out that one can construct other types of constant curvature solutions by using relations between Fibonacci numbers. Taking for instance $l_1 = l_2 = l_3 = 1/F_n$, constant self-dual solutions exist for any value of l_0 satisfying:

$$l_0 = \frac{F_{n-m+1}F_{n-m}}{F_n F_m F_{m-1}}, \tag{8.48}$$

with arbitrary m. Taking, for instance, the decomposition $n = 4m + q$ and sending n to infinity by taking m to infinity, one obtains:

$$l_0 = \sqrt{5}\varphi^{q+2} \tag{8.49}$$

which can be made arbitrarily large by sending q to infinity. A numerical study of some $SU(N)$ fractional instanton solutions in this geometry has been done in ref. [78]. The choice of twists and geometry taken in that work differ from ours, but the large N scaling properties of some of the solutions agree with those described in the next section.

N	m	$\overline{m}$	L	s	$NS/8\pi^2$	$NS_E/8\pi^2$	$NS_B/8\pi^2$	NQ
3	1	1	6	1	1.000185	0.502579	0.497606	0.965560
3	1	1	8	1	1.000062	0.501413	0.498650	0.980676
3	1	1	10	1	1.000026	0.500892	0.499134	0.987648
3	1	1	20	1	0.999995	0.500216	0.499779	0.996917
3	1	1	4	2	1.000766	0.505760	0.495006	0.921408
3	1	1	6	2	1.000186	0.502393	0.497793	0.965320
3	1	1	8	2	1.000063	0.501309	0.498754	0.980542
5	2	-2	4	1	1.000092	0.501876	0.498216	0.974790
5	2	-2	6	1	1.000019	0.500814	0.499205	0.988820
5	2	-2	12	1	1.000007	0.500203	0.499804	0.997209
5	2	-2	4	2	1.000093	0.501714	0.498379	0.974579
5	2	-2	6	2	1.000019	0.500743	0.499277	0.988727
5	2	-2	12	2	0.999994	0.500179	0.499815	0.997185
8	3	3	2	1	1.000233	0.503091	0.497142	0.959275
8	3	3	4	1	1.000017	0.500734	0.499283	0.989868
8	3	3	6	1	1.000002	0.500322	0.499680	0.995501
8	3	3	8	1	1.000002	0.500181	0.499821	0.997470
8	3	3	2	2	1.000235	0.502842	0.497393	0.958953
8	3	3	4	2	1.000016	0.500673	0.499344	0.989788
8	3	3	6	2	1.000001	0.500294	0.499706	0.995466
13	5	-5	2	1	1.000036	0.501109	0.498926	0.984834
13	5	-5	4	1	1.000001	0.500284	0.499717	0.996187
13	5	-5	2	2	1.000036	0.501015	0.499021	0.984712
13	5	-5	4	2	0.999999	0.500246	0.499752	0.996185
21	8	8	2	1	1.000005	0.500420	0.499586	0.994169
21	8	8	2	2	1.000005	0.500384	0.499621	0.994123

Table 8.1: Value of total action (S) along with its electric (S_E) and magnetic (S_B) parts in units of $8\pi^2/N$. We also give the value of N times the topological charge (NQ). Results are given for all our lattice configurations representing a continuum torus with periods: $l_0 = sNLa$, $l_1 = l_2 = La$ and $l_3 = NLa$, with a the lattice spacing. Quantities are reported with an error of 1 in the last significant digit, taking into account the changes in the last iteration of the flow minimization.

8.4 Fractional instantons on $\mathbf{R} \times \mathbf{T}^3$

This section analyzes a new type of $SU(N)$ instanton configurations with fractional topological charge $Q = 1/N$ compatible with our choice of twisted boundary conditions. They are obtained on the lattice as classical solutions of the lattice equations of motion. In the continuum limit, they lead to self-dual configurations defined on a 4-dimensional torus of periods$l_0 = sl$, $l_1 = l_2 = l/N$, and $l_3 = l$. By changing s,

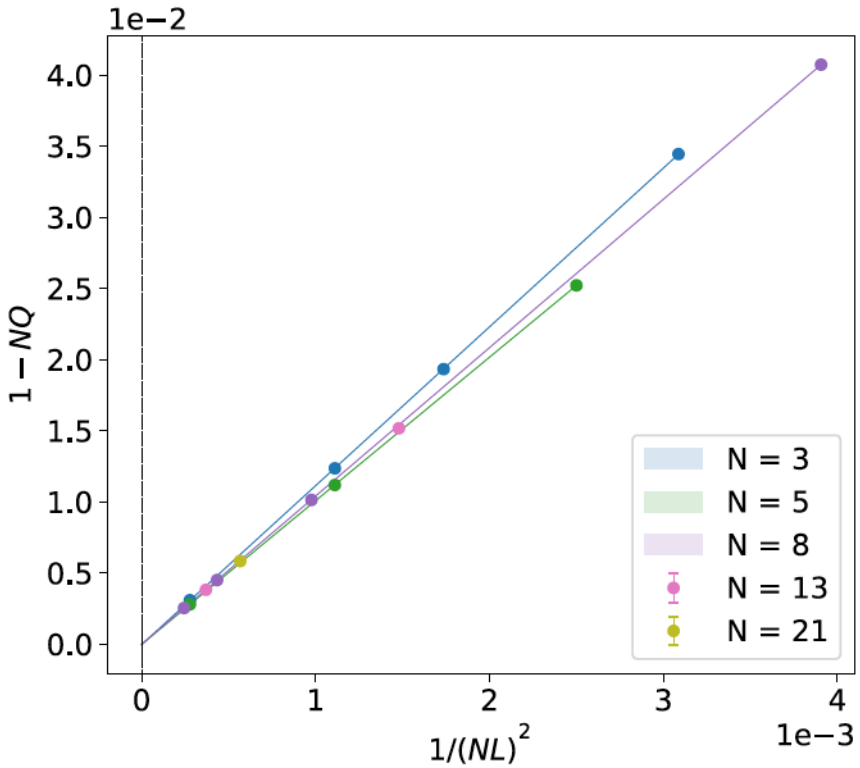

Figure 8.1: Continuum extrapolation of (N-times) the topological charge: $1 - NQ$. Data is extracted from table 8.1 and is extrapolated to the continuum with $a^2 = 1/(NL)^2$ corrections.

we analyze their approach to the Hamiltonian limit: $\mathbf{R} \times \mathbf{T}^3$. As we will see, the resulting configurations are localized in the 03 plane with a characteristic size of order l and interpolate between two flat connections at $x_0 \to \pm\infty$, with holonomies dictated by choice of 't Hooft fluxes, as discussed in section 8.2.

Lattice approximants of the fractional instanton configurations can be obtained by minimizing the lattice equations of motion. There are various standard ways in the literature to attain this goal; in this chapter, we have used the gradient flow [11–14].

On the lattice, the flow equations can be easily discretized; in our study, we have used the Wilson flow discretization, which relies on the minimization of Wilson's plaquette action. It is well known [207] that for the Wilson action, the leading $\mathcal{O}(a^2)$ lattice corrections to the continuum action are negative definite; therefore in the absence of a twist, the only stable solution of the lattice equations of motion is the vacuum configuration. However, with a non-orthogonal twist, a pure gauge configuration is incompatible with the boundary conditions. In our setup, we have selected $\vec{m} = (0, 0, m)$ and $\vec{k} = (0, 0, -\overline{m})$, where $m = F_{n-2}$ and $\overline{m} = (-1)^n F_{n-2}$ for a gauge group $SU(F_n)$. Therefore, the absolute minimum of the lattice action is

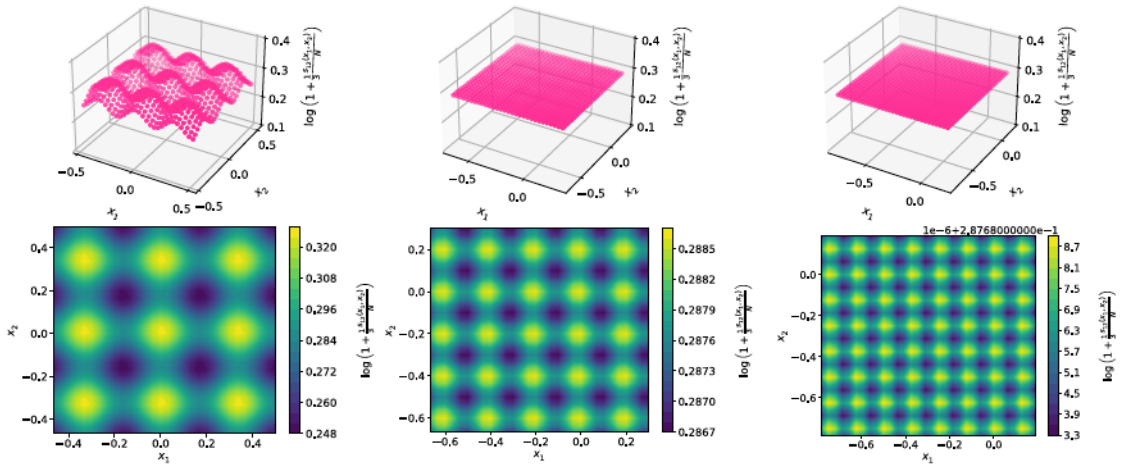

Figure 8.2: We display the profiles obtained by integrating the action density over x_0 and x_3 as a function of x_1/l and x_2/l. The unit of length is set by taking $l = 1$. Gauge groups are, from left to right: $SU(3)$, $SU(5)$ and $SU(8)$. For readability of the plots, the quantity displayed is $\log(1+l^2 s_{12}(x_1, x_2)/(3N))$. In the large N limit, the profiles approach the one of the constant curvature solutions, for which $\log(1 + 1/3) = 0.287682$.

different from zero, corresponding to a discretized version of the $Q = 1/N$ fractional instanton with an action, up to lattice artifacts, equal to $8\pi^2/N$.

To implement the concrete geometry we are interested in, we discretize the $SU(N)$ gauge theory on a lattice $sNL \times L^2 \times NL$, corresponding to a continuum torus of size $sl \times (l/N)^2 \times l$, with $l = NLa$ (a the lattice spacing) and s a positive integer.

To determine lattice observables as the action density, we have considered several ways of discretizing the continuum action, constructed in terms of 1×1 and 2×2 plaquettes, and given by [207]:

$$S(\epsilon) = \frac{4-\epsilon}{3} \sum_{n,\mu,\nu} \mathrm{Tr}\left(\mathbb{I} - Z^*_{\mu\nu}(n) \square\right) + \frac{\epsilon - 1}{48} \sum_{x,\mu,\nu} \mathrm{Tr}\left(\mathbb{I} - \tilde{Z}^*_{\mu\nu}(n) \square\right) \quad . \tag{8.50}$$

In this construction, the link variables are periodic, and the twisted boundary conditions are imposed by introducing the twist-carrying center elements $Z^*_{\mu\nu}(n)$ and $\tilde{Z}^*_{\mu\nu}(n)$. The former is set to one for 1×1 all plaquettes except for the ones with coordinates $n_1 = n_2 = 0$, where we take:

$$Z_{12} = Z^*_{21} = \exp\left\{\frac{i2\pi m}{N}\right\}, \tag{8.51}$$

and for the ones with $n_0 = n_3 = 0$, where we set instead:

$$Z_{03} = Z^*_{30} = \exp\left\{\frac{-i2\pi \bar{m}}{N}\right\}. \tag{8.52}$$

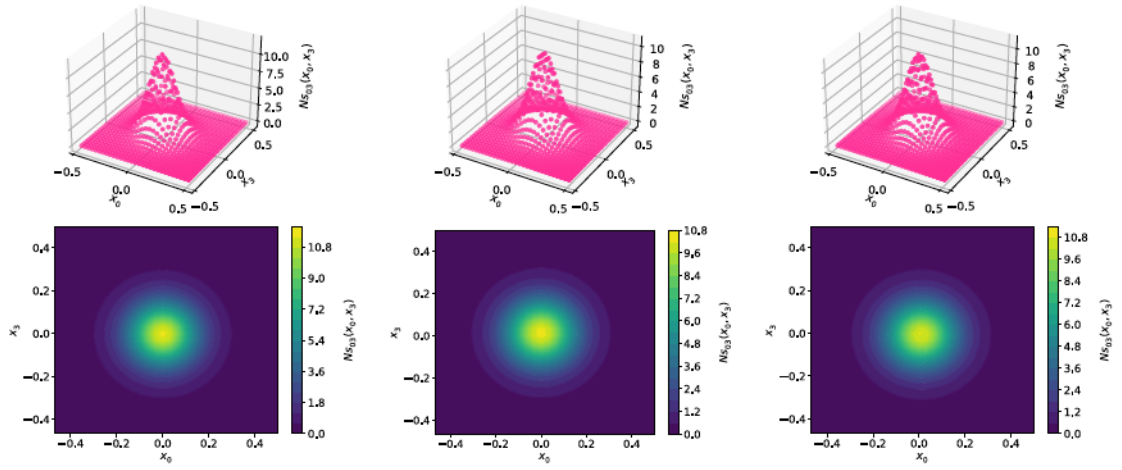

Figure 8.3: We display as a function of x_0/l and x_3/l the profiles obtained by integrating over x_1 and x_2 the action density of the configuration with $l_0 = l_3 = l$ $(s = 1)$. Gauge groups are, from left to right: $SU(3)$, $SU(5)$ and $SU(8)$.

As for $\tilde{Z}_{\mu\nu}(n)$, it is given by the product of all the single plaquette twist factors enclosed in the 2×2 closed loop. The factor ϵ controls the size of $\mathcal{O}(a^2)$ lattice corrections to the continuum action. Wilson's action corresponds to $\epsilon = 1$, while the choice $\epsilon = 0$ is taken so as to ensure that continuum and lattice classical actions differ only by terms of $\mathcal{O}(a^4)$. Our action density corresponds to the one for $\epsilon = 0$ and is clover averaged over the four, 1×1 or 2×2, plaquettes attached to a given lattice point n in each plane.

The observable used to determine the topological charge is constructed out of a lattice discretization of the field strength tensor defined, recalling that $U_{-\mu}(n) \equiv U_\mu^\dagger(n - \hat{\mu})$, as:

$$\begin{aligned} G_{\mu\nu}(n) = -\frac{i}{8}\{ & Z^*_{\mu\nu}(n) P_{\mu\nu}(n) + Z^*_{\mu\nu}(n - \hat{\nu}) P_{-\nu\mu}(n) \\ & + Z^*_{\mu\nu}(n - \hat{\mu}) P_{\nu-\mu}(n) + Z^*_{\mu\nu}(n - \hat{\mu} - \hat{\nu}) P_{-\mu-\nu}(n) - c.c.\}, \end{aligned} \tag{8.53}$$

with $P_{\mu\nu}(n)$ denoting the 1×1 plaquette. In terms of $G_{\mu\nu}$, the topological charge Q is determined from:

$$Q = \frac{1}{16\pi^2} \sum_n \mathrm{Tr}\left\{ G_{\mu\nu}(n) \widetilde{G}_{\mu\nu}(n) \right\} \tag{8.54}$$

This expression has $\mathcal{O}(a^2)$ lattice artifacts.

Finally, let us mention that one practical issue that influences the rate of convergence towards the absolute minimum of the action is the choice of initial configuration, $B_\mu(x, 0)$. A random start is, in most cases, not practical since (especially for large N) the flow tends to get easily trapped in metastable configurations with action higher than the minimum. Instead, it is more efficient to start from a twist eater configuration corresponding to an orthogonal twist, with either m or $\overline{m}$ set to

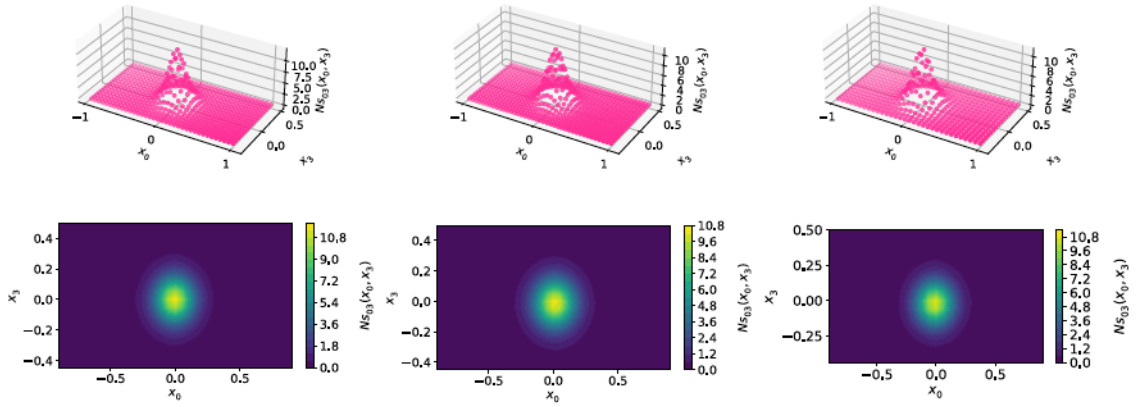

Figure 8.4: The same as in figure 8.3 but for $l_0 = 2l_3 = 2l$ $(s = 2)$.

zero, slightly heated with an immense value of the lattice inverse 't Hooft coupling $b = 1/\lambda$.

The set of lattices employed in our study is given in table 8.1. We have analyzed various gauge groups, with $N = 3, 5, 8, 13, 21$ in the Fibonacci sequence. Setting the scale by fixing $l = 1$, the continuum limit is taken by sending the lattice spacing $a = 1/LN$ to zero at a fixed value of N, i.e., by sending L to infinity. In all cases, except for $N = 21$, we have results at various values of L that allow exploring the continuum limit. Further details on the numerical implementation of the minimization procedure as well as the definition of the lattice observables used to measure the topological charge and action density profiles, are presented in the Appendix. Here, we will only focus on describing the properties of the solutions and the scaling in the singular large N limit.

We have determined the topological charge (Q) and the total action (S) of the minimum action configuration obtained in each case. In addition, to test the solutions' self-duality, we have separately computed the electric (S_E) and magnetic (S_B) contributions to the total action. The resulting values of S, S_E, S_B, in units of $8\pi^2/N$, as well as the topological charge multiplied by N, are given in table 8.1. In all cases, the results are very close to those expected in the continuum for a self-dual solution with fractional topological charge $1/N$ $(NQ = 1,\ NS/(8\pi^2) = 1,$ $NS_E/(8\pi^2) = NS_B/(8\pi^2) = 0.5)$, an indication of the smallness of lattice artifacts and the smoothness of the solutions. We can also use the results at various values of the lattice spacing to obtain a continuum extrapolation of these quantities, and we show in fig. 8.1 the one of NQ. A quadratic extrapolation in the lattice spacing gives values that agree with the continuum result up to one part in 10^4. On the other hand, we point out that anti-instanton configurations with $Q = -1/N$ can also be obtained under time reversal; at the level of boundary conditions, this is implemented by changing the sign of the electric twist $\overline{m}$. In the Hamiltonian limit, both configurations contribute to the semi-classical partition function.

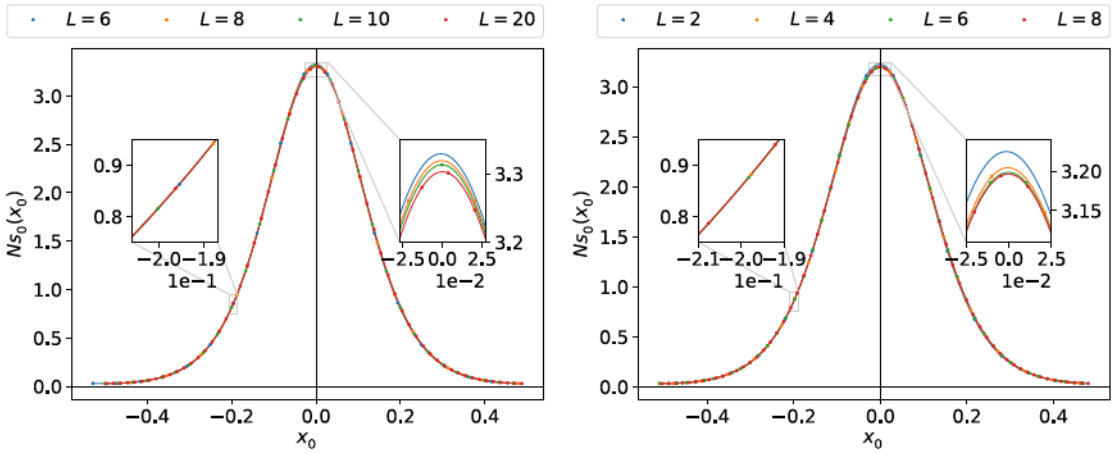

(a) SU(3) (b) SU(8)

Figure 8.5: Continuum extrapolation of the one-dimensional energy profiles, c.f. eq. (8.56) for gauge groups $SU(3)$ and $SU(8)$. The torus has been discretized on a lattice with $l_0 = l_3 = NLa$ and $l_1 = l_2 = La$ with a the lattice spacing. The continuum limit is taken by sending $a = l/NL$ to zero at a fixed value of $l = 1$, i.e., by sending L to infinity .

In addition to these global quantities, we have also studied several gauge invariant observables that can be used to characterize the solution. We first describe the action density profiles and then analyze Polyakov and Wilson loops. Our primary interest will be in analyzing the large N scaling of the solutions.

8.4.1 Action density profiles

We have looked at action density profiles obtained by integrating the 4-dimensional action density (in units of $8\pi^2$) in either two or three directions:

$$Ns_{\mu\nu}(x_\mu, x_\nu) \equiv \left(\prod_{\rho \neq \mu,\nu} \int_0^{l_\rho} dx_\rho \right) Ns(x), \tag{8.55}$$

$$Ns_{\mu}(x_\mu) \equiv \left(\prod_{\rho \neq \mu} \int_0^{l_\rho} dx_\rho \right) Ns(x). \tag{8.56}$$

We have introduced a factor of N in the profiles in agreement with the expected large N scaling discussed in section 8.2, coming from the fact that the N-independent quantity in the large N limit is N times the total action. As a reference point, one can compute these quantities for the constant curvature solutions discussed in the previous section. The action density is given by $Ns(x) = 1/V$, with $V = \prod_\mu l_\mu$. Setting $l_1 = l_2 = l/N$, $l_3 = l$ and $l_0 = \varphi^{-3} l$, as for the Fibonacci construction, we obtain the following scaling with N for the dimensionless density profiles:

$$l^2 s_{12}(x_1, x_2)/N = 1 \ ; \ Nl^2 s_{03}(x_0, x_3) = \varphi^3 \ ; \ Nl s_0(x_0) \sim 1. \tag{8.57}$$

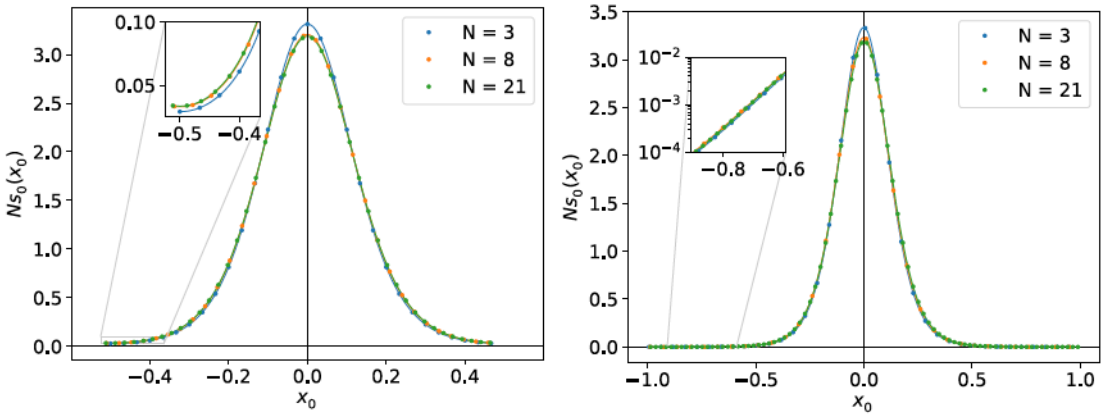

(a) $s = 1$ (b) $s = 2$

Figure 8.6: We compare the time dependence of the energy for various gauge groups N and time extents $l_0 = sl$, with $s = 1$ and 2. The inset in the right plot is in a logarithmic $(y-)$ scale to show that the decay in the tails is exponential in time.

As we will see below, our numerical solutions respect a similar scaling. Once the overall factor of N is considered, the remnant N dependence of the action density profiles turns out to be very small. These minor N corrections indicate that our solutions could perhaps be obtained as a *small* deformation of the constant curvature solution, along with the reasoning presented in refs. [74, 208]; we will return to this point later.

Let us start by analyzing the two-dimensional profiles s_{12}, resulting from integrating the action density along the two large directions. The dependence on x_1/l and x_2/l for various gauge groups is shown in fig. 8.2. In the plot, we have set the scale by taking $l = 1$, a convention that will be used from now on. In addition, we have used periodicity to extend the action density to a box of size l in both directions. It is clear from the plots that at large N, these density profiles approach those of the constant curvature solutions with $l_1 = l_2 = 1/N$.

As for profiles depending on the two large periods, they are displayed for various gauge groups and $l_0 = l_3$ or $l_0 = 2l_3$ in figs. 8.3 and 8.4 respectively. The structure is, in both cases, very similar. The solutions develop a maximum in the 03 plane, which is determined by the effective spatial torus size l. Enlarging the time period by a factor of two modifies the profiles mainly in the time tails, a fact that is best appreciated by looking at the contour plots given in fig. 8.4.

A more quantitative comparison between solutions for different gauge groups can be made by looking at the one-dimensional profiles obtained by integrating the action density in all directions but one. We will focus on profiles where the action density has been integrated over space, giving, therefore, the time dependence of the energy.

We first look at the continuum limit. As an example, on fig. 8.5, we display $Nls_0(x_0)$ as a function of x_0/l for gauge groups $SU(3)$ and $SU(8)$ – similar plots are

N	m	$\overline{m}$	L	w_1/l	w_2/l	w_F/l
3	1	1	6	0.268284	0.268456	0.222222
5	2	-2	12	0.283232	0.289695	0.240000
8	3	3	6	0.279391	0.285402	0.234375
13	5	-5	4	0.286707	0.287152	0.236686
21	8	8	2	0.281166	0.286412	0.235828

Table 8.2: Value of the width at half-maximum for $l_0 = l_3 = l$ (w_1) and $l_0 = 2l_3 = 2l$ (w_2) compared with the value of l_0 for the Fibonacci solution (w_F), given by eq. (8.47) with $m = 2$ and $l_3 = l$.

obtained for the other cases in table 8.1. The plots display our results for various lattice spacings. The continuous lines in each plot are interpolations to the data at a fixed value of L, displayed to guide the eye. As mentioned, the continuum limit is taken by sending $a = l/(LN)$ to zero. The profiles show small dependence on the lattice spacing, indicating relatively small lattice artifacts even for our smaller lattices. One noteworthy point is that discretization effects are controlled by LN in such a way that even the smallest lattices with $L = 2$ show a slight departure from the continuum result if N is large enough.

Let us now study the N dependence of the energy profiles. In figure 8.6a, we display $Nls_0(x_0)$ vs x_0/l for the case in which $l_0 = l_3 = l$. Interpolating curves are displayed to guide the eye. It is clear that the N dependence is rather small, and the curves tend to be a universal one in the large N limit. As seen in fig. 8.6b, enlarging the lattice in the time direction does not change the results appreciably. The energy profile remains localized and displays a shape very similar to the previous one except at the tails, where, as shown in the inset of the plot, it decays exponentially and becomes very close to zero. More quantitatively, we have determined the width at half maximum. The values obtained for all the gauge groups are given in table 8.2. The dependence on N turns out to be very small, and the same happens with the dependence on the time extent of the lattice – compare w_1 and w_2 corresponding to time extents differing by a factor of 2. Our results indicate that the relevant scale parameter for the fractional instanton configurations in this geometry is given by the effective torus size l, set to 1 in our units.

The comparison of the energy profile with the constant-curvature Fibonacci solution discussed in the previous section is very informative. Table 8.2 gives the maximal value of l_0 for which the Fibonacci solution sharing our 3-dimensional torus geometry becomes self-dual (denoted by w_F). It is remarkable that this value, which tends to $w_F = 0.236l$ in the large N limit, agrees surprisingly well with the instanton width. This scaling suggests that when we distort the geometry away from the Fibonacci solution by sending l_0 to infinity, most of the action density remains concentrated within w_F. To test this hypothesis, we have generated a series of numerical solutions starting at $l_0 = 0.25l$, very close to the Fibonacci case, and moving away from it in small steps. The energy profiles for the sequence of solutions with $N = 8$ are displayed in figure 8.7. The change in the first steps is

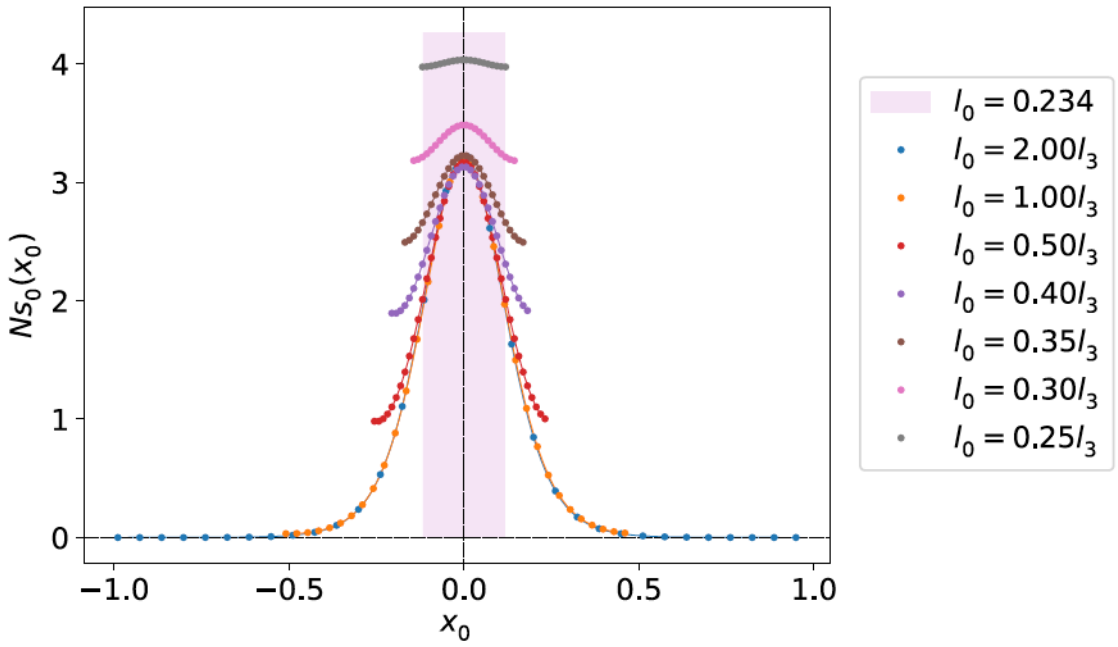

Figure 8.7: Solutions obtained for our spatial torus geometry and various values of the time extent l_0, changing from the Fibonacci constant curvature case ($l_0 = 0.234l$) represented by the pink box to the case $l_0 = 2l$.

speedy. Beyond $l_0 \sim 0.5l$, the solution's central part remains unchanged, and the tails become smaller for larger values of l_0, which is required to maintain the same integral within a larger integration region.

Finally, to test the self-duality of the solution more robustly, we have looked separately at the different components of the electric and magnetic energies. For that purpose, we have computed the spatial integral of $\mathrm{ReTr}(G^2_{\mu\nu})$, with μ and ν fixed, and analyzed their dependence on time. The results for several configurations are displayed in fig. 8.8. The degree of self-duality of the solution is very high and improves as we approach the continuum limit. Notice that for the Fibonacci construction, only the 03 and 12 components of the field strength tensor differ from zero; this is no longer the case for the geometry we are considering, although these two components are the ones that nevertheless remain larger.

8.4.2 Polyakov loops

In addition to the action density, we have also analyzed other gauge invariant quantities like the Polyakov and Wilson loops.

Let us start with a discussion of the Polyakov loops. We use $P_\mu(x)$ to denote ($1/N$ times) the trace of the Polyakov loop winding the torus once in direction μ, and parameterize this quantity in terms of its modulus and phase as:

$$P_\mu(x) = \frac{1}{N}\mathrm{Tr}\Big(P\exp\Big\{-i\int_0^{l_\mu} dx_\mu A_\mu(x)\Big\}\,\Omega_\mu(x)\Big) \equiv |P_\mu(x)|\,e^{i\phi_\mu(x)}. \tag{8.58}$$

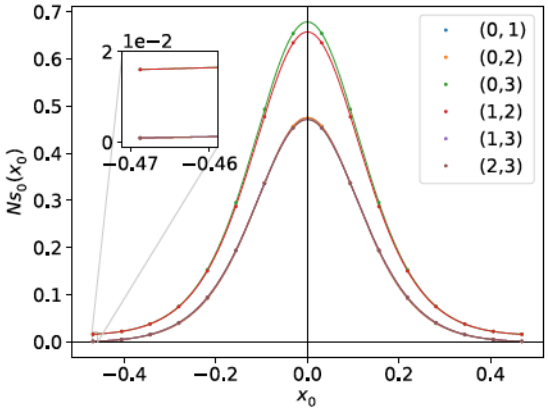

(a) SU(8) with $L = 2$ and $s = 1$

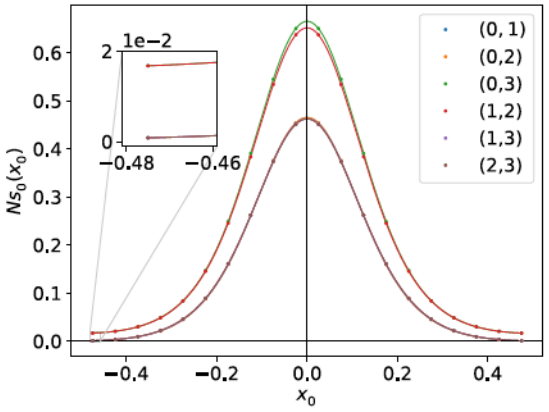

(b) SU(5) with $L = 4$ and $s = 1$

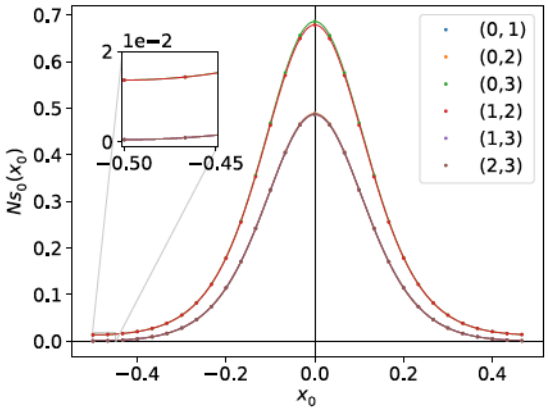

(c) SU(3) with $L = 30$ and $s = 1$

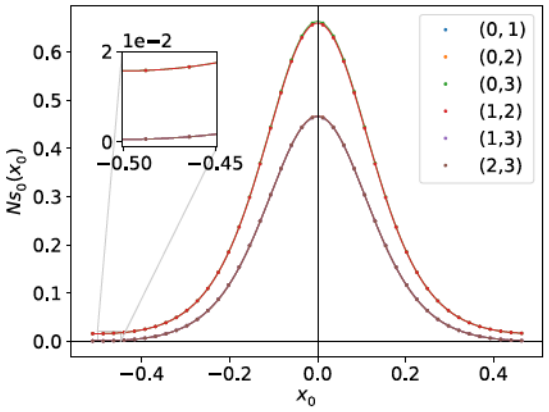

(d) SU(21)with $L = 2$ and $s = 1$

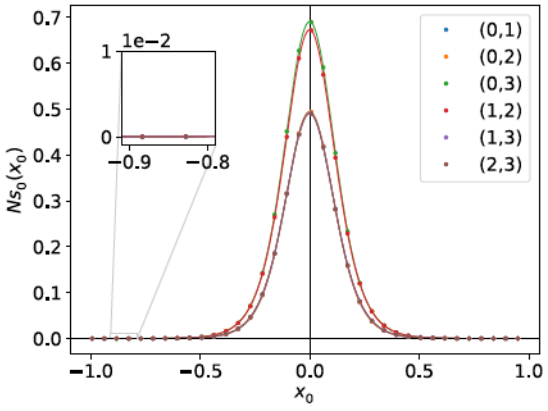

(e) SU(3)with $L = 6$ and $s = 2$

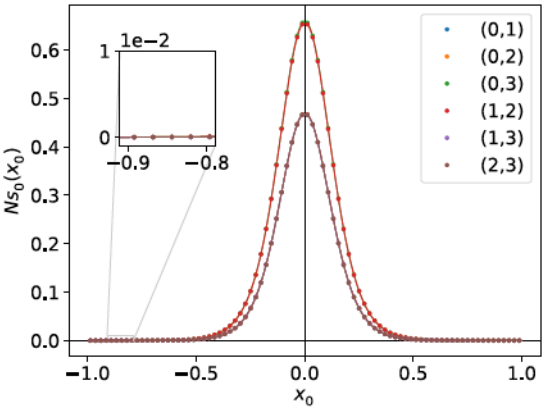

(f) SU(21)with $L = 2$ and $s = 2$

Figure 8.8: Time dependence of the electric and magnetic components of the energy obtained by integrating $\mathrm{ReTr}(G^2_{\mu\nu})$, with (μ, ν) fixed, over the three spatial coordinates. The two most significant components are 03 and 12. Components 01 and 02 are, to an excellent degree, degenerate; the same happens to 23 and 13.

Twisted boundary conditions are reflected in the fact that Polyakov loops satisfy:

$$P_\mu(x + l_\nu \hat{e}_\nu) = e^{i\frac{2\pi n_{\mu\nu}}{N}} P_\mu(x). \tag{8.59}$$

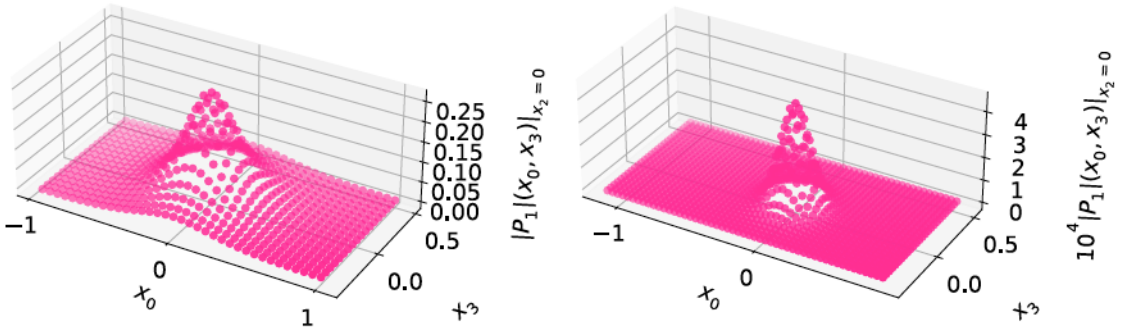

(a) SU(3) (b) SU(13)

Figure 8.9: Modulus of P_1, the Polyakov loop winding once in the x_1 direction, as a function of the coordinates in the 03 plane for x_2 at the instanton center. Data points have been shifted to have the action profile maximum at $x = 0$. Note the change of vertical scale in the case of $SU(13)$.

Under a displacement by a torus period, the modulus is, therefore, periodic, and the phase shifts by an amount that depends on the twist.

As mentioned in section 8.2, in the Hamiltonian limit ($l_0 \to \infty$), the fractional instanton interpolates between two flat connections characterized by the value of the holonomies. Those corresponding to loops in the spatially twisted plane are maximally nontrivial, with $P_i(\vec{x}, x_0 = \pm\infty) = 0$, for $i = 1, 2$. On the other hand, $P_3(\vec{x}, x_0 = \pm\infty)$ is in the center of the gauge group, jumping by a factor $2\pi n_{30}/N$ between $x_0 = -\infty$ and at $x_0 = +\infty$. As we will see below, our numerical configurations successfully match this behavior.

Starting with the holonomies in the two short directions, fig. 8.9 displays, for gauge groups $SU(3)$ and $SU(13)$ and time extent $l_0 = 2l$, the modulus of P_1 as a function of the coordinates in the 03 plane for x_2 at the instanton center. Data points have been shifted to have the action profile maximum at $x = 0$. The value of $|P_1|$ remains everywhere small and tends to zero at $x_0 \to \pm\infty$, as expected. The same behavior is observed for P_2 and all gauge groups.

We move next to describe the results for P_3. In fig. 8.10, we display from top to bottom: the phase of the Polyakov loop multiplied by N/n_{30}, the energy profile as a function of x_0, and the Polyakov loop modulus, all for torus sizes corresponding $l_0 = 2l_3$. We have subtracted the required powers of $2\pi/N$ so as to have the phase at $x_0 = -l_0/2$ close to zero in all cases. For the plot, Polyakov loops are computed with x_1 and x_2 taken as close as possible to the origin; however, we have observed that the dependence of the loop in x_1 and x_2 is small, and the phase becomes independent of these coordinates in the large N limit. The results converge in this limit to a universal function of x_0, which exhibits all the properties discussed previously, i.e.:

- Far from the instanton center, the configuration approaches a vacuum solution with $P_1 = P_2 = 0$ and P_3 equal to a root of unity, exemplified by the fact that the modulus tends to one and the phase becomes an integer multiple of $2\pi/N$.

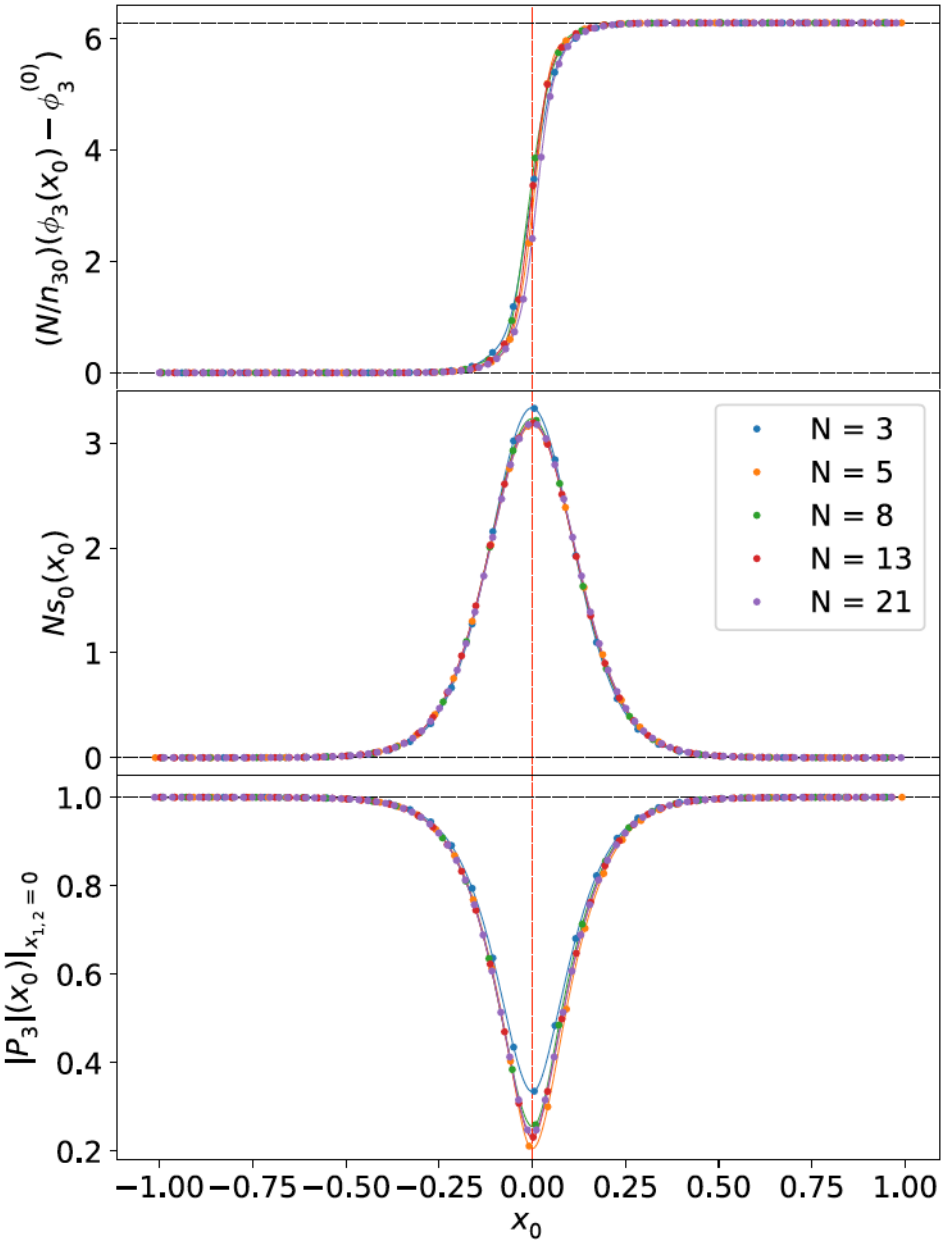

Figure 8.10: For a torus of size $l_0 = 2l_3 = 2l$, we display as a function of time and from top to bottom: the phase of the Polyakov loop P_3 multiplied by N/n_{30} (after subtracting the required powers of $2\pi/N$ to have the zero phase at $x_0 = -l_0/2$), the energy-profile of the instanton, and the modulus of P_3. The phase and modulus of the Polyakov loop are evaluated at $x_1 = x_2 = 0$.

- The fractional instanton interpolates between two vacuum configurations differing in phase by $2\pi n_{30}/N$, as the boundary conditions dictate. With our choice of twist, the jump in phase is given in absolute value by $2\pi F_{n-2}/F_n$ and tends in the large N limit to $2\pi\varphi^{-2}$, with φ the Golden Ratio.

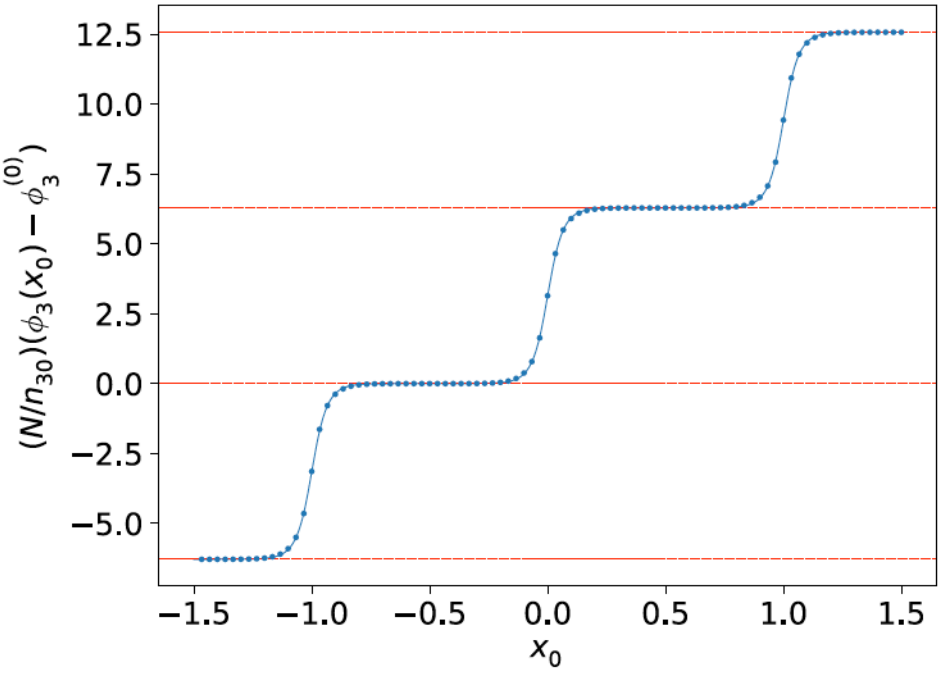

Figure 8.11: We display, for the $SU(3)$ instanton configuration with $l_0 = l_3$, the phase of the Polyakov loop P_3 multiplied by N/n_{30} compared to the ansatz of eq. (8.60) with $\xi = 0.999999999535$.

We have been able to find an ansatz that describes very well the time dependence of ϕ_3. It is given by the following functional form:

$$\phi_3(x_0) = \phi_3^{(0)} + \frac{n_{30}}{N}\left\{\pi + 2\,\mathrm{am}\left(2K(\xi)\frac{x_0 - x_0^{(0)}}{l_0}, \xi\right)\right\} \tag{8.60}$$

where $\mathrm{am}(x, \xi)$ denotes Jacobi's Amplitude Function [209] and

$$K(\xi) = \int_0^{\pi/2} \frac{d\theta}{\sqrt{1 - \xi^2 \sin^2\theta}}. \tag{8.61}$$

with ξ being a tunable parameter taking values between 0 and 1. Using the periodicity properties of the amplitude function:

$$\mathrm{am}(x + 2K(\xi), \xi) = \mathrm{am}(x, \xi) + \pi, \tag{8.62}$$

it is trivial to show that the phases transform as required under displacement by a torus period. An illustration of the quality of the fit for $N = 3$, $l_0 = l_3$ and $\xi = 0.999999999535$ is presented in fig. 8.11.

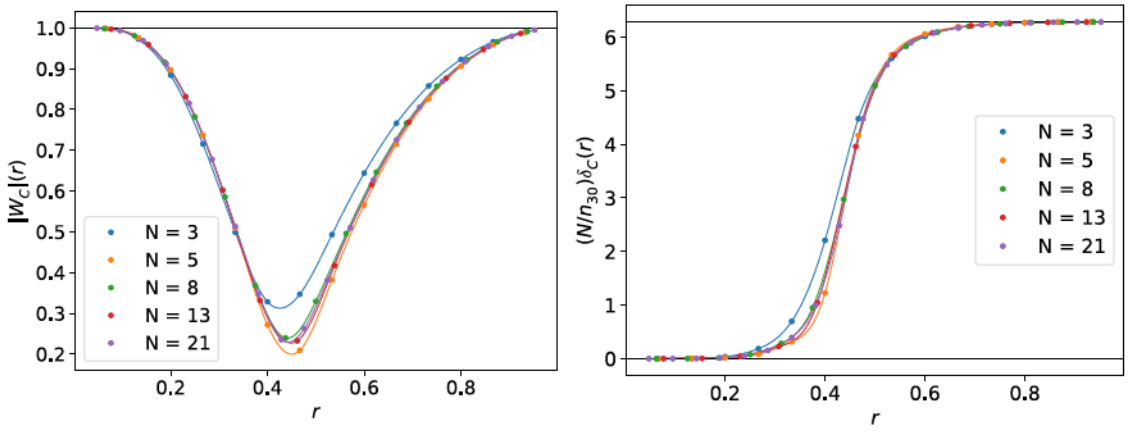

Figure 8.12: We display the modulus (left) and phase (right), multiplied by N/n_{30}, of a square Wilson loop of side r centered at the instanton position.

8.4.3 Wilson loops

Finally, and continuing with the discussion of gauge invariant quantities, we proceed with the analysis of Wilson loops. We denote by $W_C(r)$ the Wilson loop defined as:

$$W_C(r) = \frac{1}{N}\mathrm{Tr}\Big(P\exp\Big\{-i\int_C dx_\mu A_\mu(x)\Big\}\Big) \equiv |W_C(r)|\, e^{i\delta_C(r)}, \tag{8.63}$$

where C stands for a $T \times R$ square loop in the 03 plane, with $T = R = r$, centered around the instanton maximum at $x = 0$.

Figure 8.12 displays as a function of r the Wilson loop modulus and phase (normalized by a factor N/n_{30}) for different gauge groups and $l_0 = l_3 = l$. Several remarks can be extracted from these plots. First, the modulus starts at one for $r = 0$, and as the distance grows, it decreases, reaches a minimum around $r \sim l/2$, and increases again back to 1, becoming a pure complex phase at large r. On the other hand, the phase jumps from $\delta_C(r) = 0$ close to the instanton center to $\delta_C(r) = 2\pi n_{30}/N$ at $r = l$, showing that the Wilson loop around the fractional instanton encloses a nontrivial $\mathbf{Z}_N$ flux – notice that in the large N limit the corresponding phase is dictated by the non-commutativity parameter $|\hat{\theta}| = F_{n-2}/F_n$ and approaches φ^{-2} with φ the Golden Ratio.

8.5 Summary

In this chapter, we have obtained numerical instanton-like solutions for gauge group $SU(N)$ with fractional topological charge $Q = 1/N$. They have minimal action $S = 8\pi^2/N$ and are highly (anti)self-dual. They have been obtained on a 4-torus with twisted boundary conditions given by the magnetic flux $\vec{m} = (0, 0, m)$ and $\vec{k} = (0, 0, -\overline{m})$ where N and $m = |\overline{m}|$ are taken as the $n-2$ and n-th integers in the Fibonacci sequence, i.e., $N = F_n$ and $m = F_{n-2}$. The advantage of this choice is

that it is expected to prevent the appearance of tachyonic instabilities and $\mathbf{Z}_N \times \mathbf{Z}_N$ symmetry breaking in the large N limit.

We have analyzed the scaling of the solutions at large N. The aim was to find fractional charge solutions in the $\mathbf{R} \times \mathbf{T}^3$ Hamiltonian limit representing vacuum-to-vacuum tunneling events. Given that the twist induces an effective entanglement of color and spatial degrees of freedom, we have selected different periods in the planes pierced by non-zero magnetic flux, taking $l_3 = l$ and $l_1 = l_2 = l/N$ and analyzed the resulting solutions in the limit in which $l_0 \to \infty$. Considerations based on TEK reduction and continuum volume independence indicate that the effective size of the spatial torus obtained in this way is l^3. The resulting configurations scale in the large N limit in agreement with this expectation. Action densities become independent of the twisted coordinates (x_1, x_2) and are localized in time with a width determined in terms of the effective length l. The energy profile's width is close to the maximal temporal period for which our asymmetric torus supports abelian constant curvature self-dual solutions.

The scaling of various other physical quantities in the large N limit has been analyzed, including Polyakov and Wilson loop operators. They also scale as expected. The former show how the fractional instanton interpolates in time between two flat connections on the three tori, with a profile that, after an appropriate scaling, becomes N independent in the large N limit. The Wilson loop on the 03 plane is non-trivial around the instanton, acting effectively at a large distance as a $\mathbf{Z}_N$ flux. In the large N limit, the value of the flux is given by the non-commutativity parameter $|\hat{\theta}| = |m|/N = F_{n-2}/F_n$ and approaches φ^{-2} with φ the Golden Ratio.

Part IV

Conclusions

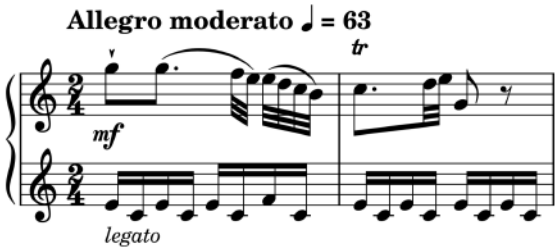

9 Conclusions and Outlook

In this thesis report we have studied SU(N) gauge theories defined on a torus with twisted boundary conditions, exploring and exploiting the relationship between volume and color degrees of freedom induced by the twist. The report is divided into three parts.

In the first part, we gave a general overview of the ideas behind the concepts or volume reduction and volume independence, showing how spatial and color degrees of freedom become entangled, and clarifying the main differences between the 't Hooft large N limit and the one used in this report, known as the singular large N limit. In the former, the bare 't Hooft coupling is held constant as one approaches the large N limit, in contrast to the singular case where we fix the physical volume and hence the renormalized coupling at that scale. We also stressed the close relation between this setup and non-commutative $U(1)$ gauge theories on the torus. Finally, we introduced the general ideas of gradient flow and scale setting on the lattice, which are used throughout the report to compute the renormalized 't Hooft coupling.

The second part is entirely dedicated to the study of the running coupling constant. Mixing the notions of volume independence and gradient flow, in ch. 3 we introduced a particular renormalization scheme, known as twisted gradient flow, which has been the main computational technique of the renormalized 't Hooft coupling throughout this part. The prescription uses finite size scaling techniques in a four-dimensional asymmetrical torus, where short directions are N times smaller than the others and, at the same time, are endowed with twisted boundary conditions.

In ch. 4 we study the $SU(3)$ group within this framework. This case is of great importance for high-energy phenomenology, since it can be non-perturbatively matched to QCD with heavy quarks, and thus has direct relevance for the extraction of the strong coupling constant in QCD. In addition, there are many results in the literature for this case, allowing for a more rigorous comparison. Our determination of the Λ parameter in units of the flow scale $\sqrt{8t_0}$ or the Sommer radius r_0 shows good agreement with the literature. Our final result in units of the flow scale is $\Lambda^{N=3}_{\overline{\text{MS}}}\sqrt{8t_0} = 0.603(17)$. The ratio $\Lambda_{\overline{\text{MS}}}/\Lambda_{\text{TGF}}$ is a key part of the calculation, that has been computed in perturbation theory in the literature. We computed the

Λ parameter within the twisted gradient flow scheme and then used the available Schrodinger functional data, with perturbative corrections of the order of $\mathcal{O}(\lambda^2)$, to perform a non-perturbative matching and extrapolate our final result. The precision of our calculation is not as good as that of the most accurate determinations, but the systematic associated with the continuum extrapolation is taken seriously since our simulations include large lattice sizes. The main contribution to the uncertainty of this calculation is undoubtedly the matching with perturbation theory, since large corrections have been observed even in renormalization schemes where the NNLO coefficients are known. In our determination, the perturbative matching is performed very carefully and in several ways by using a non-perturbative running that covers large energy scales.

Overall, the twisted gradient flow scheme has proven to be a powerful computational technique that can be used in two different directions.

First, the particular choice of geometry shows a smaller memory footprint than the usual symmetrical lattice simulations. This smaller memory footprint implies an increase in the computation-to-memory transfer ratio, and can therefore be executed more efficiently on current hardware accelerators and GPU clusters. In this sense, the twisted gradient flow will allow to optimally pin down the uncertainty in the determination of the Λ parameter and to clarify the existing tension among the determinations in the literature.

Second, this scheme is particularly suitable for extracting the N dependence of the Λ parameter, motivating the analysis of ch. 5. In this chapter we have computed the Λ parameter for the gauge groups $N = 5$ and 8, following the same fine size scaling strategies of ch. 4. The determination in physical units was only possible in the case of $SU(5)$, since there are not enough lattice spacing calculations in the literature for the case of $N = 8$ to fit the range of bare couplings used in our simulations. For $N = 5$ we have calculated the Λ parameter in units of the string tension, yielding: $\Lambda_{\overline{\text{MS}}}^{N=5}/\sqrt{\sigma_0} = 0.560(21)$, which is in good agreement with the literature. Our results show large uncertainties, but again the perturbative extrapolations are carefully taken care of.

In ch. 5 we also investigated the effect of boundary conditions on the determination of the coupling. Following the volume independence hypothesis, we exploited the fact that in the large N limit finite volume effects are controlled by the effective length $\tilde{l}$. This is only true in the large N limit, providing at the same time an approximately constant value of the non-commutativity parameter $\hat{\theta}$. Furthermore, twisted boundary conditions also introduce an asymmetry, since only two directions are equipped with twisted boundary conditions. We explored this asymmetry by restricting the determination of the coupling to certain sets of planes on the twisted box, which in fact represent different renormalization schemes. We then computed the ratio $\log(\Lambda_{\text{TGF}}/\Lambda_{\overline{\text{MS}}})$ for the different planes and found that the dependence of this ratio on the non-commutativity parameter remains very small, as expected when N and k are scaled within the Fibonacci sequence. Moreover, the differences observed in the twisted gradient flow are of the same order as in other schemes, such as the gradient flow with Schrodinger functional boundary conditions.

In the third and final part of this work, we study some topological implications present in our setup and of great interest for the volume independence framework. We point out some important remarks.

As expected, our simulations suffer from critical slowing and freezing at small values of the lattice spacing. It is well known that the topological charge, among all possible observables, is strongly affected by freezing. This is indeed dangerous for definitions of the coupling based on the gradient flow, which are strongly correlated to the topological charge.

We have pointed out the presence of critical slowing down and freezing in our simulations in ch. 6, where we show for the different gauge groups studied in this report how the autocorrelations grow as one approaches the continuum limit. Although we have not computed the autocorrelation times, we have qualitatively observed how this effect is strongly enhanced as the number of colors increases, with the number of configurations with topological charge different from zero being qualitatively reduced for the case of $N = 5$ and having only 6 non-frozen ensembles in the case of $N = 8$.

In this work we have followed the prescription introduced by the ALPHA collaboration to restrict the coupling calculation to the zero topological charge sector. This restriction appears only as a redefinition of the renormalization scheme and is expected to have no impact on the coupling determination as long as the topological fluctuations are well sampled in the sector of trivial topology, which remains an open question. We have presented two different determinations that justify this choice. In one of them we computed the topological charge correlators in the trivial topology sector for several lattices with the same physical volume, i.e. the same renormalized coupling, and checked that even in the completely frozen cases there is no large deviation between the correlators. In the other check, we computed the topological charge density averaged only over half of the box, and showed that even in regions where the topology is completely frozen, there are large fluctuations in the charge density.

We have previously mentioned a promising technique to reduce topology freezing known as parallel tempering boundary conditions, which combines periodic and open boundaries in a parallel tempered manner to induce topology fluctuations. We are currently working on this approach in conjunction with twisted boundary conditions to mitigate the large autocorrelations observed at small lattice spacings. The goal of this project is to address the crucial question of whether the projection into the sector of zero topological charge has any effect on the determination of the Λ parameter. This work is done in collaboration with Massimo D'Elia, Claudio Bonanno, Andrea Giorgieri and Margarita García Pérez. We have already developed functional codes that incorporate both theoretical frameworks (parallel tempering and twisted boundaries), and we will compare the results obtained in ch. 4 with the determination of the coupling within parallel tempering (where freezing is expected to be reduced) when projected onto the zero topological charge sector. If both determinations agree, this is a non-trivial test that even in freezing scenarios, the $Q = 0$ sector is correctly sampled. By defining a scheme in which the coupling is av-

eraged over all sectors, parallel tempering will also allow to show that the projection does not introduce any bias in the results, and that it merely acts as a redefinition of the formulation. This work is in progress.

In ch. 7, we have shown that the dependence of the coupling on the effective torus size follows an almost universal curve for the three values of N studied in this thesis report, with small N-dependent corrections. We have studied the dependence of some physical quantities on the effective length $\tilde{l}$, such as the 't Hooft coupling or the topological susceptibility. As we have seen, the singular large N limit is approached by taking large values of N while keeping the effective length $\tilde{l}$ constant.

On the other hand, we have studied the topological susceptibility as a function of the physical volume, playing special attention to the semiclassical region where the onset of this quantity occurs. We have used a semiclassical approximation based on a dilute gas of instantons to describe the onset of the $SU(3)$ susceptibility and also to explain, at least qualitatively, the strong correlation between the coupling and the topological charge for the three values of N studied in the thesis. Remarkably, the approximation that best fits our data is the one based on a dilute gas of fractional instantons, reaffirming their important role in this framework.

Since fractional topological charge instanton-like solutions seem to have an important relevance in our description, in ch. 8 we have studied numerically (and to some extent analytically) possible solutions of this type within our setup. We have obtained numerical (anti)self-dual solutions to the Euclidian Yang-Mills equations of motion with minimal actions $S = 8\pi^2/N$. They were obtained on a 4-dimensional twisted torus with flux $\vec{m} = (0, 0, m)$ and $\vec{k} = (0, 0, -\overline{m})$, where N and m are taken as the $n-2$ and n-th terms of the Fibonacci sequence. The solutions scale very well towards the large N limit, and we have shown that they can be interpreted as vacuum-to-vacuum tunneling events interpolating between two different pure gauge configurations. We found that the solutions are well concentrated in the plane (x_0, x_3) and practically independent of the twisted coordinates (x_1, x_2). We also checked that gauge invariant operators, such as Wilson and Polyakov loops, scale as expected.

Our solutions share some properties with other $SU(N)$ configurations previously obtained in the literature. Being independent of two of the spatial coordinates and localized in the other two, they resemble the vortex-like structures on $\mathbf{T}^2 \times \mathbf{R}^2$ studied in the literature, but the latter correspond to an N-independent choice of twist $\vec{k} = \vec{m} = (1, 0, 0)$ and show a different large N scaling of the energy profiles and of the Polyakov and Wilson loop operators. Instead, the dependence of our energy profiles on N corresponds to that observed for $SU(N)$ instantons on $\mathbf{T}^3 \times \mathbf{R}$ for a symmetric spatial torus with twist $\vec{m} = (1, 1, 1)$, $\vec{k} = (1, 0, 0)$. It is unclear to us at this point what determines the N dependence in these other cases, and how it relates to the particular choice of twist, a question that certainly deserves further investigation.

We stress that fractional instantons are relevant in the search for analytical computability in Yang-Mills theories, a program which, as mentioned in the intro-

duction, has received renewed attention in recent years. Including their contribution to the partition function is essential to extend analytical calculations on a twisted torus beyond the perturbative regime ($\Lambda\tilde{l} << 1$), where this program has been partially pursued for the case of $SU(2)$. Whether this allows bridging the gap into the confinement regime remains an open question, one way to go might be to exploit the simplifications achieved by volume independence and large N dynamics as done in this work.

Conclusiones y perspectivas

En esta memoria de tesis hemos estudiado teorías gauge $SU(N)$ definidas sobre un toro con condiciones de contorno *twisted*, explorando y explotando la relación entre los grados de libertad de volumen y de color inducidos por el *twist*. La memoria se divide en tres partes.

En la primera parte, dimos una visión general de las ideas que subyacen a los conceptos de reducción de volumen e independencia de volumen, mostrando cómo se entrelazan los grados de libertad espaciales y de color, y aclarando las principales diferencias entre el límite de N grande de 't Hooft y el utilizado en este informe, conocido como límite de N grande singular. En el primero, el acoplamiento *bare* de't Hooft se mantiene constante a medida que uno se aproxima al límite de N grande, en contraste con el caso singular en el que fijamos el volumen físico y, por tanto, el acoplamiento renormalizado a esa escala. También destacamos la estrecha relación entre nuestra descripción y las teorías gauge $U(1)$ no conmutativas en el toro. Por último, introducimos las ideas generales de *gradient flow* y fijación de escala en la red, que se utilizan a lo largo del informe para calcular el acoplamiento renormalizado de 't Hooft.

La segunda parte está enteramente dedicada al estudio de la constante de acoplamiento. Mezclando las nociones de independencia de volumen y *gradient flow*, en el cap. 3 introdujimos un esquema de renormalización particular, conocido como *twisted gradient flow*, que ha sido la principal técnica computacional del acoplamiento 't Hooft renormalizado a lo largo de esta parte. La prescripción utiliza técnicas de escalado de tamaño finito en un toro asimétrico en cuatro dimensiones, donde las direcciones cortas son N veces más pequeñas que las otras y, al mismo tiempo, están dotadas de condiciones de contorno *twisted*.

En ch. 4 estudiamos el grupo $SU(3)$ dentro de este marco. Este caso es de gran importancia para la fenomenología de altas energías, ya que puede ser emparejado no perturbativamente a QCD con quarks pesados, y por tanto tiene relevancia directa para la extracción de la constante de acoplamiento fuerte en QCD. Además, existen muchos resultados en la literatura para este caso, lo que permite una comparación más rigurosa. Nuestra determinación del parámetro Λ en unidades de la escala de *flow* $\sqrt{8t_0}$ o el radio de Sommer r_0 muestra un buen acuerdo con la literatura. Nuestro resultado final en unidades de la escala de *flow* es $\Lambda^{N=3}_{\overline{\text{MS}}}\sqrt{8t_0} = 0,603(17)$. La relación $\Lambda_{\overline{\text{MS}}}/\Lambda_{\text{TGF}}$ es una parte clave del cálculo, que ha sido computada en teoría de perturbaciones en la literatura. Calculamos el parámetro Λ dentro del esquema de *twisted gradient flow* y luego utilizamos los datos del funcional de Schrodinger disponibles, con correcciones perturbativas del orden de $\mathcal{O}(\lambda^2)$, para realizar un ajuste no perturbativo y extrapolar nuestro resultado final. La precisión de nuestro cálculo no es tan buena como la de las determinaciones más exactas, pero la sistemática asociada a la extrapolación del continuo se tiene muy en cuenta, ya que nuestras simulaciones incluyen tamaños de red grandes. La principal contribución a la incertidumbre de este cálculo es sin duda el emparejamiento con la teoría de perturbaciones, ya que se han observado grandes correcciones incluso en esquemas

de renormalización en los que se conocen los coeficientes NNLO. En nuestra determinación, el emparejamiento perturbativo se realiza de forma muy cuidadosa y de varias maneras utilizando una ejecución no perturbativa que cubre grandes escalas de energía.

En general, el esquema de *twisted gradient flow* ha demostrado ser una potente técnica computacional que puede utilizarse en dos direcciones diferentes.

En primer lugar, la geometría elegida ocupa menos memoria que las simulaciones simétricas habituales. Esta menor huella de memoria implica un aumento de la relación de transferencia cálculo-memoria, por lo que puede ejecutarse de forma más eficiente en los actuales aceleradores de hardware y clusters de GPU. En este sentido, el *twisted gradient flow* permitirá acotar de forma óptima la incertidumbre en la determinación del parámetro Λ y aclarar la tensión existente entre las determinaciones en la literatura.

En segundo lugar, este esquema es particularmente adecuado para extraer la dependencia N del parámetro Λ, motivando el análisis de ch. 5. En este capítulo hemos calculado el parámetro Λ para los grupos gauge $N = 5$ y 8, siguiendo las mismas estrategias de escalado fino de ch. 4. La determinación en unidades físicas sólo fue posible en el caso de $SU(5)$, ya que no hay suficientes cálculos de espaciado de red en la literatura para el caso de $N = 8$ que se ajusten al rango de acoplamientos *bare* utilizados en nuestras simulaciones. Para $N = 5$ hemos calculado el parámetro Λ en unidades de la tensión de la cuerda, obteniendo: $\Lambda_{\overline{\text{MS}}}^{N=5}/\sqrt{\sigma_0} = 0,560(21)$, que concuerda bien con la bibliografía. Nuestros resultados muestran grandes incertidumbres, pero de nuevo las extrapolaciones perturbativas se tienen muy en cuenta.

En ch. 5 también investigamos el efecto de las condiciones de contorno en la determinación del acoplamiento. Siguiendo la hipótesis de la independencia del volumen, explotamos el hecho de que en el límite N grande los efectos del volumen finito están controlados por la longitud efectiva $\tilde{l}$. Esto sólo es cierto en el límite de N grande, proporcionando al mismo tiempo un valor aproximadamente constante del parámetro de no conmutatividad $\hat{\theta}$. Además, las condiciones de contorno *twisted* también introducen una asimetría, ya que sólo dos direcciones están equipadas. Exploramos esta asimetría restringiendo la determinación del acoplamiento a ciertos conjuntos de planos en la caja *twisted*, que de hecho representan diferentes esquemas de renormalización. A continuación, calculamos el cociente $\log(\Lambda_{\text{TGF}}/\Lambda_{\overline{\text{MS}}})$ para los distintos planos y observamos que la dependencia de esta relación del parámetro de no conmutatividad sigue siendo muy pequeña, como era de esperar cuando N y k se escalan dentro de la secuencia de Fibonacci. Además, las diferencias observadas en el *twisted gradient flow* son del mismo orden que en otros esquemas, como el *gradient flow* con condiciones de contorno dentro del funcional de Schrodinger.

En la tercera y última parte de este trabajo, estudiamos algunas implicaciones topológicas presentes en nuestra configuración y de gran interés para el marco de independencia de volumen. Señalamos algunas observaciones importantes.

Como era de esperar, nuestras simulaciones sufren de *critical slowing down* y de *topology freezing* a valores pequeños del espaciado de la red. Es bien sabido que la

carga topológica, entre todos los observables posibles, se ve fuertemente afectada por el *freezing*. De hecho, esto es peligroso para las definiciones del acoplamiento basadas en el *gradient flow*, que están fuertemente correlacionadas con la carga topológica.

Hemos señalado la presencia de *critical slowing down* y *topology freezing* en nuestras simulaciones en ch. 6, donde mostramos para los distintos grupos gauge estudiados en esta memoria cómo crecen las autocorrelaciones a medida que uno se aproxima al límite del continuo. Aunque no hemos calculado los tiempos de autocorrelación, hemos observado cualitativamente cómo este efecto se potencia fuertemente a medida que aumenta el número de colores, reduciéndose cualitativamente el número de configuraciones con carga topológica distinta de cero para el caso de $N = 5$ y teniendo sólo 6 conjuntos no congelados en el caso de $N = 8$.

En este trabajo hemos seguido la prescripción introducida por la colaboración ALPHA de restringir el cálculo del acoplamiento al sector de carga topológica cero. Esta restricción aparece sólo como una redefinición del esquema de renormalización y se espera que no tenga impacto en la determinación del acoplamiento siempre que las fluctuaciones topológicas estén bien muestreadas en el sector de topología trivial, lo cual sigue siendo una pregunta abierta. Hemos presentado dos determinaciones diferentes que justifican esta elección. En una de ellas calculamos los correladores de carga topológica en el sector de topología trivial para varias redes con el mismo volumen físico, es decir, el mismo acoplamiento renormalizado, y comprobamos que incluso en los casos completamente congelados no hay grandes desviaciones entre los correladores. En la otra comprobación, calculamos la densidad de carga topológica promediada sólo sobre la mitad de la caja, y mostramos que incluso en las regiones donde la topología está completamente congelada, hay grandes fluctuaciones en la densidad de carga.

Anteriormente hemos mencionado una técnica prometedora para reducir la congelación topológica conocida como condiciones de contorno de templado paralelo, que combina contornos periódicos y abiertos de forma templada paralela para inducir fluctuaciones topológicas. Actualmente estamos trabajando en este enfoque junto con condiciones de contorno *twisted* para mitigar las grandes autocorrelaciones observadas a pequeños espaciamientos de la red. El objetivo de este proyecto es abordar la cuestión crucial de si la proyección en el sector de carga topológica cero tiene algún efecto en la determinación del parámetro Λ. Este trabajo se realiza en colaboración con Massimo D'Elia, Claudio Bonanno, Andrea Giorgieri y Margarita García Pérez. Ya hemos desarrollado códigos funcionales que incorporan ambos marcos teóricos, y compararemos los resultados obtenidos en ch. 4 con la determinación del acoplamiento dentro del temple paralelo (donde se espera que se reduzca la congelación) cuando se proyecta sobre el sector de carga topológica cero. Si ambas determinaciones coinciden, se trata de una prueba no trivial de que, incluso en escenarios de congelación, el sector $Q = 0$ está correctamente muestreado. Al definir un esquema en el que el acoplamiento se promedia sobre todos los sectores, el templado en paralelo también permitirá demostrar que la proyección no introduce ningún sesgo en los resultados, y que simplemente actúa como una redefinición de la formulación. Este trabajo está en curso.

En ch. 7, hemos demostrado que la dependencia del acoplamiento con el tamaño efectivo del toro sigue una curva casi universal para los tres valores de N estudiados en esta memoria de tesis, con pequeñas correcciones dependientes de N. Hemos estudiado la dependencia de algunas magnitudes físicas de la longitud efectiva $\tilde{l}$, como el acoplamiento de 't Hooft o la susceptibilidad topológica. Como hemos visto, el límite singular de N grande se aproxima tomando valores grandes de N mientras se mantiene constante la longitud efectiva $\tilde{l}$.

Por otro lado, hemos estudiado la susceptibilidad topológica en función del volumen físico, prestando especial atención a la región semiclásica donde se produce el establecimiento de esta cantidad. Hemos utilizado una aproximación semiclásica basada en un gas diluido de instantones para describir el inicio de la susceptibilidad $SU(3)$ y también para explicar, al menos cualitativamente, la fuerte correlación entre el acoplamiento y la carga topológica para los tres valores de N estudiados en la tesis. Notablemente, la aproximación que mejor se ajusta a nuestros datos es la basada en un gas diluido de instantones fraccionarios, reafirmando su importante papel en este marco.

Dado que las soluciones tipo instantón de carga topológica fraccionaria parecen tener una relevancia importante en nuestra descripción, en el cap. 8 hemos estudiado numéricamente (y hasta cierto punto analíticamente) posibles soluciones de este tipo dentro de nuestra configuración. Hemos obtenido soluciones numéricas (anti)autoduales para las ecuaciones de movimiento euclidianas de Yang-Mills con acciones mínimas $S = 8\pi^2/N$. Se obtuvieron en un toro *twisted* de 4 dimensiones con flujo $\vec{m} = (0, 0, m)$ y $\vec{k} = (0, 0, -\overline{m})$, donde N y m se toman como los términos $n-2$ y n-ésimo de la sucesión de Fibonacci. Las soluciones escalan muy bien hacia el límite de N grande, y hemos demostrado que pueden interpretarse como sucesos de túnel entre vacío y vacío que interpolan entre dos configuraciones gauge puras diferentes. Encontramos que las soluciones están bien concentradas en el plano (x_0, x_3) y son prácticamente independientes de las coordenadas torcidas (x_1, x_2). También comprobamos que los operadores invariantes gauge, como los operadores de Wilson y Polyakov, escalan como se esperaba.

Nuestras soluciones comparten algunas propiedades con otras configuraciones $SU(N)$ obtenidas previamente en la literatura. Siendo independientes de dos de las coordenadas espaciales y localizadas en las otras dos, se asemejan a las estructuras tipo vórtice en $\mathbf{T}^2 \times \mathbf{R}^2$ estudiadas en la literatura, pero estas últimas corresponden a una elección N-independiente del *twsit* $\vec{k} = \vec{m} = (1, 0, 0)$ y muestran un escalamiento a N grande diferente de los perfiles de energía y de los operadores de Polyakov y Wilson. En cambio, la dependencia de nuestros perfiles de energía con N corresponde a la observada para los instantones $SU(N)$ en $\mathbf{T}^3 \times \mathbf{R}$ para un toro espacial simétrico con *twist* $\vec{m} = (1, 1, 1)$, $\vec{k} = (1, 0, 0)$. No tenemos claro en este momento qué determina la dependencia de N en estos otros casos, y cómo se relaciona con la elección particular de el *twist*, una cuestión que sin duda merece más investigación.

Destacamos que los instantones fraccionarios son relevantes en la búsqueda de computabilidad analítica en teorías de Yang-Mills, un programa que, como se menciona en la introducción, ha recibido renovada atención en los últimos años. In-

cluir su contribución a la función de partición es esencial para extender los cálculos analíticos en un toro *twisted* más allá del régimen perturbativo ($\Lambda\tilde{l} << 1$), donde este programa se ha perseguido parcialmente para el caso de $SU(2)$. Sigue siendo una cuestión abierta si esto permite tender un puente hacia el régimen de confinamiento; una forma de hacerlo podría ser explotar las simplificaciones logradas por la independencia del volumen y la dinámica de N grandes ¡, como se hace en este trabajo.

Part V

Appendices

A

Lattice ensembles

$18 \times b$	$\tilde{L} = 12$	$\tilde{L} = 18$	$\tilde{L} = 24$	$\tilde{L} = 36$	$\tilde{L} = 48$
0.3333	7517(2483)	20248(30694)	3920(13062)	1070(8702)	120(1876)
0.3444	9569(431)	36970(15606)	7869(10087)	1120(4159)	220(1713)
0.3499	9887(113)		5644(4356)		
0.3556	9961(39)	49359(3417)	13050(5356)	3899(6983)	458(1541)
0.3604	9983(17)		8350(1650)		
0.3658		9940(60)		3556(2311)	
0.3667	10000(0)	52807(300)	16713(1287)	6476(4482)	759(1537)
0.3712	10000(0)		9805(195)		
0.3766		10000(0)		2634(569)	
0.3778	10000(0)	51840(67)	17807(193)	9593(1616)	1316(989)
0.3821	10000(0)		10000(0)		
0.3876		10000(0)		4344(1615)	
0.3889	10000(0)	53238(0)	16439(0)	10971(0)	2155(150)
0.3930	10000(0)		10000(0)		
0.3986		10000(0)		6330(0)	
0.4000	10000(0)	50544(0)	18000(0)	10974(0)	2307(0)
0.4040	10000(0)		10000(0)		
0.4097		10000(0)		6421(0)	
0.4111	10000(0)	53406(0)	16763(0)	10981(0)	2603(0)
0.4149	10000(0)		10000(0)		
0.4208		10000(0)		4899(0)	
0.4222	10000(0)	53605(0)	17760(0)	9999(0)	2308(0)
0.4319		10000(0)		6351(0)	
0.4333	10000(0)	53560(0)	17501(0)	8979(0)	2604(0)
0.4426	10000(0)		10000(0)		
0.4444	10000(0)	53602(0)	18000(0)	9720(0)	2610(0)
0.4596		10000(0)		3229(0)	
0.4702	10000(0)		10000(0)		
0.4722	10000(0)	53825(0)	17000(0)	8990(0)	2324(0)
0.4873		10000(0)		3237(0)	
0.4979	10000(0)		10000(0)		
0.5000	10000(0)	53654(0)	18000(0)	9000(0)	2333(0)

0.5150		10000(0)		1602(0)	
0.5256	10000(0)		10000(0)		
0.5278	10000(0)	54178(0)	16483(0)	7998(0)	1966(0)
0.5427		10000(0)		3255(0)	
0.5534	10000(0)		10000(0)		
0.5556	10000(0)	53889(0)	18000(0)	13866(0)	2898(0)
0.5705		10000(0)		8159(0)	
0.5812	10000(0)		10000(0)		
0.5833	10000(0)	53415(0)	17000(0)	12841(0)	2898(0)
0.5982		10000(0)		7714(0)	
0.6111	10000(0)	53679(0)	8640(0)	12800(0)	2584(0)
0.6367	10000(0)		10000(0)		
0.6538		10000(0)		6547(0)	
0.6667	10000(0)	10000(0)	16442(0)	8916(0)	1658(0)
0.6923	10000(0)		10000(0)		
0.7093		10000(0)		6550(0)	
0.7222	10000(0)	10000(0)	16513(0)	8873(0)	1655(0)
0.7478	10000(0)		10000(0)		
0.7649		10000(0)		5643(0)	
0.7778	10000(0)	10000(0)	16340(225)	8400(0)	1663(0)
0.8034	10000(0)		10000(0)		
0.8202		10000(0)		8158(0)	
0.8333	10000(0)	10000(0)	16602(0)	8247(0)	1668(0)
1.1111	10000(0)	5009(0)	11570(0)	1893(0)	401(0)

Table A.1: $SU(3)$ total number of configurations with zero topological charge (within parenthesis, we report those with non-zero charges).

b	$\tilde{L}=10$	$\tilde{L}=20$	$\tilde{L}=30$	$\tilde{L}=40$	$\tilde{L}=60$
0.3300	5826(4174)	1013(8987)	399(9601)	100(3730)	7(933)
0.3350	6189(3811)	1783(8217)	867(9133)	254(5006)	45(1542)
0.3400	8091(1909)	3117(6883)	1439(8561)	539(5821)	62(1438)
0.3450	9550(450)	4385(5615)	1990(8010)	858(6142)	80(1420)
0.3499	9928(72)	5860(3140)			
0.3550	9985(15)	6993(3007)	3978(6022)	1574(5426)	110(1390)
0.3604	9999(1)	8357(643)			
0.3630	9999(1)	9855(145)	2277(7723)	1945(5055)	235(1265)
0.3658		10000(0)		3794(3206)	
0.3680	10000(0)	10000(0)	10000(0)	7000(0)	654(846)
0.3705	10000(0)	8493(507)			
0.3720	10000(0)	8965(1035)	10000(0)	7000(0)	731(769)
0.3766		9439(561)		7000(0)	
0.3778			10000(0)		1500(0)
0.3790	10000(0)	10000(0)	10000(0)	7000(0)	1500(0)

0.3821	10000(0)	7315(685)			
0.3876		10000(0)		8080(0)	
0.3889			10000(0)		1500(0)
0.3930	10000(0)	7116(884)			
0.3986		10000(0)		7000(0)	
0.4000			10000(0)		1500(0)
0.4040	10000(0)	8000(0)			
0.4097		10000(0)		7000(0)	
0.4111			10000(0)		1500(0)
0.4149	10000(0)	7147(853)			
0.4208		10000(0)		7000(0)	
0.4222			10000(0)		1500(0)
0.4255		10000(0)		7000(0)	
0.4300		10000(0)		7000(0)	
0.4319		10000(0)		8230(0)	
0.4333			10000(0)		1500(0)
0.4337			10000(0)		1496(0)
0.4381			10000(0)		1313(0)
0.4404		10000(0)		7000(0)	
0.4426	10000(0)	10000(0)			
0.4430			10000(0)		1313(0)
0.4444			10000(0)		1307(0)
0.4484			10000(0)		1302(0)
0.4500	10000(0)	10000(0)		7000(0)	
0.4549			10000(0)		1000(0)
0.4596		10000(0)		7460(0)	
0.4600	10000(0)	10000(0)		7000(0)	
0.4622			10000(0)		1000(0)
0.4702	10000(0)	8000(0)			
0.4722			10000(0)		1000(0)
0.4800	10000(0)	8000(0)		7000(0)	
0.4873		10000(0)		9260(0)	
0.4979	10000(0)	10000(0)			
0.5000	10000(0)	10000(0)	10000(0)		1000(0)
0.5150		10000(0)		7000(0)	
0.5256	10000(0)	8000(0)			
0.5278			10000(0)		1000(0)
0.5400	10000(0)	10000(0)			
0.5427		10000(0)		7110(0)	
0.5534	10000(0)	8000(0)			
0.5556			10000(0)		1000(0)
0.5705		10000(0)		3500(0)	
0.5812	10000(0)	4309(3691)			
0.5833			10000(0)		1000(0)
0.5982		10000(0)		7080(0)	

0.6111			10000(0)		1000(0)
0.6367	10000(0)	10000(0)			
0.6538		10000(0)		7390(0)	
0.6600	10000(0)	10000(0)			
0.6667			10000(0)		1000(0)
0.6923	10000(0)	6353(1647)			
0.7093		8739(1661)		7360(0)	
0.7222			10000(0)		1000(0)
0.7478	10000(0)	8000(0)			
0.7649		9586(814)		7360(0)	
0.7778			10000(0)		1319(0)
0.8034	10000(0)	7192(808)			
0.8202		9565(835)		8350(0)	
0.8333			10000(0)		1176(0)

Table A.2: $SU(5)$ total number of configurations with zero topological charge (within parenthesis, we report those with non-zero charges).

b	$\tilde{L}=16$	$\tilde{L}=32$	$\tilde{L}=48$	$\tilde{L}=64$	$\tilde{L}=96$
0.3555	9846(154)	2231(7839)	881(1919)		37(163)
0.3594	10000(0)	6800(0)	2800(0)	207(893)	200(0)
0.3633	10000(0)	6800(0)	2800(0)	1100(0)	200(0)
0.3657	10000(0)	10070(0)			
0.3666			2800(0)		200(0)
0.3766	10000(0)	10070(0)			
0.3777		10070(0)		1100(0)	
0.3778			2800(0)		200(0)
0.3876	10000(0)	10070(0)			
0.3888		10070(0)		1100(0)	
0.3891	10000(0)	10070(0)	2800(0)		200(0)
0.3986	10000(0)	10070(0)			
0.4000		9880(0)	2800(0)	1100(0)	200(0)
0.4096	10000(0)	10070(0)			
0.4109			2800(0)		200(0)
0.4111		10070(0)		1100(0)	
0.4207	10000(0)	10070(0)			
0.4219			2800(0)		200(0)
0.4222		10070(0)		1100(0)	
0.4318	10000(0)	10070(0)			
0.4333		10070(0)		1100(0)	
0.4336			2800(0)		150(0)
0.4337		10070(0)		1100(0)	
0.4380		10070(0)		1100(0)	
0.4430		10070(0)		1100(0)	

0.4444		10070(0)		1100(0)	
0.4445	10000(0)	10070(0)	2800(0)		150(0)
0.4484		9880(0)		1100(0)	
0.4548		9880(0)		1100(0)	
0.4595	10000(0)	10070(0)			
0.4622		9880(0)		1100(0)	
0.4722		9690(0)	2800(0)	1100(0)	150(0)
0.4873	10000(0)	10070(0)			
0.5000		9690(0)	2800(0)	1100(0)	150(0)
0.5150	10000(0)	10070(0)			
0.5277		9500(0)		1100(0)	
0.5281			2800(0)		150(0)
0.5427	10000(0)	10070(0)			
0.5555	10000(0)	10070(0)	2800(0)		150(0)
0.5555		9500(0)		1100(0)	
0.5705	10000(0)	10070(0)			
0.5833		9500(0)		1100(0)	
0.5836			2800(0)		150(0)
0.5982	10000(0)	10070(0)			
0.6109			2800(0)		150(0)
0.6111		9120(0)		1100(0)	
0.6538	10000(0)	9500(0)			
0.6664			2800(0)		150(0)
0.6666		9120(0)		1100(0)	
0.7093	10000(0)	10070(0)			
0.7219			2800(0)		150(0)
0.7222		9310(0)		1100(0)	
0.7648	10000(0)	10070(0)			
0.7777		9310(0)		1100(0)	
0.7781	10000(0)	9880(0)	2800(0)		150(0)
0.8202	10000(0)	10070(0)			
0.8333		10070(0)		1100(0)	
0.8336			2800(0)		150(0)
0.8891			2800(0)		150(0)
0.9445			2800(0)		150(0)

Table A.3: $SU(8)$ total number of configurations with zero topological charge (within parenthesis, we report those with non-zero charges).

B

Raw data

b	$\tilde{L}=12$	$\tilde{L}=18$	$\tilde{L}=24$	$\tilde{L}=36$	$\tilde{L}=48$
0.3333	34.80(11)	70.849(96)	128.69(32)	337.0(11)	656.0(50)
0.3444	21.567(67)	39.414(52)	66.69(15)	155.25(66)	309.6(22)
0.3499	17.947(52)		50.75(15)		
0.3556	15.483(42)	24.809(35)	39.530(88)	84.46(24)	155.07(95)
0.3604	13.947(35)		32.18(10)		
0.3658		17.892(50)		52.00(20)	
0.3667	12.448(28)	17.484(22)	25.319(60)	50.06(14)	86.88(55)
0.3712	11.577(23)		21.746(70)		
0.3766		13.931(34)		33.29(19)	
0.3778	10.574(20)	13.585(14)	17.907(41)	31.836(90)	52.44(31)
0.3821	9.994(18)		16.148(42)		
0.3876		11.573(23)		22.67(11)	
0.3889	9.190(15)	11.360(10)	13.916(27)	21.603(63)	34.00(19)
0.3930	8.832(15)		12.975(30)		
0.3986		10.002(18)		16.596(61)	
0.4000	8.243(13)	9.8366(80)	11.571(17)	16.023(43)	22.78(16)
0.4040	7.943(12)		10.933(21)		
0.4097		8.826(15)		13.210(43)	
0.4111	7.444(11)	8.7118(62)	9.999(14)	12.878(27)	16.599(89)
0.4149	7.232(11)		9.570(17)		
0.4208		7.927(12)		11.170(33)	
0.4222	6.836(11)	7.8398(53)	8.846(11)	10.931(21)	13.370(68)
0.4319		7.220(11)		9.736(24)	
0.4333	6.2882(91)	7.1400(47)	7.9290(95)	9.530(17)	11.229(44)
0.4426	5.9170(84)		7.337(11)		
0.4444	5.8619(84)	6.5569(42)	7.2322(83)	8.482(14)	9.731(33)
0.4596		5.9161(85)		7.452(20)	
0.4702	5.0260(68)		5.9971(85)		
0.4722	4.9827(67)	5.4767(33)	5.9142(66)	6.717(11)	7.467(25)
0.4873		5.0356(69)		6.072(15)	
0.4979	4.3739(59)		5.0883(70)		
0.5000	4.3426(57)	4.7096(28)	5.0237(51)	5.5922(83)	6.092(18)

0.5150		4.3850(59)		5.128(17)	
0.5256	3.8881(50)		4.4249(59)		
0.5278	3.8529(50)	4.1335(23)	4.3831(46)	4.8058(74)	5.146(16)
0.5427		3.8813(51)		4.466(10)	
0.5534	3.4945(44)		3.9068(51)		
0.5556	3.4676(44)	3.6895(20)	3.8903(38)	4.2029(47)	4.480(11)
0.5705		3.4943(45)		3.9500(57)	
0.5812	3.1746(40)		3.5160(44)		
0.5833	3.1481(38)	3.3331(18)	3.4938(34)	3.7424(43)	3.954(11)
0.5982		3.1747(39)		3.5280(52)	
0.6111	2.8860(36)	3.0458(17)	3.1720(42)	3.3810(40)	3.5505(94)
0.6367	2.6834(32)		2.9271(36)		
0.6538		2.6817(32)		2.9499(45)	
0.6667	2.4778(30)	2.5955(32)	2.6819(26)	2.8259(36)	2.9393(94)
0.6923	2.3270(28)		2.5031(31)		
0.7093		2.3320(28)		2.5211(38)	
0.7222	2.1738(25)	2.2608(27)	2.3259(22)	2.4370(31)	2.5134(82)
0.7478	2.0568(23)		2.1967(26)		
0.7649		2.0601(25)		2.2038(36)	
0.7778	1.9357(23)	2.0069(23)	2.0584(19)	2.1432(28)	2.2130(65)
0.8034	1.8425(21)		1.9503(23)		
0.8202		1.8449(22)		1.9585(27)	
0.8333	1.7483(20)	1.7971(21)	1.8439(17)	1.9082(25)	1.9593(57)
1.1111	1.1748(13)	1.1988(20)	1.2137(13)	1.2440(32)	1.2705(68)

Table B.1: $SU(3)$ TGF 't Hooft coupling data as a function of the inverse bare coupling $b = 1/\lambda_0$ and the lattice size $\tilde{L} = \tilde{l}/a$.

b	$\tilde{L} = 10$	$\tilde{L} = 20$	$\tilde{L} = 30$	$\tilde{L} = 40$	$\tilde{L} = 60$
0.3499	24.809(87)	78.21(22)			
0.3550	20.036(60)	57.45(17)	134.47(39)	256.17(75)	602.04(419)
0.3604	16.862(45)	43.03(14)			
0.3630	15.678(40)	38.25(13)	82.79(41)	156.88(61)	380.50(210)
0.3658		33.91(11)		133.57(44)	
0.3680	13.975(33)	30.78(11)	63.06(18)	116.65(30)	286.99(149)
0.3705	13.333(29)	27.93(11)			
0.3720	12.971(27)	25.99(10)	51.55(15)	92.77(25)	229.07(149)
0.3766		22.081(81)		73.00(25)	
0.3778			39.71(14)		166.52(84)
0.3790	11.542(22)	20.352(77)	37.64(14)	64.67(26)	155.67(73)
0.3821	10.989(22)	18.648(74)			
0.3876		16.062(45)		43.34(22)	
0.3889			25.58(11)		91.37(80)
0.3930	9.536(16)	14.300(47)			

0.3986		12.927(32)		27.63(17)	
0.4000			17.984(76)		53.65(59)
0.4040	8.475(14)	11.777(28)			
0.4097		10.869(22)		19.31(11)	
0.4111			14.004(44)		34.14(53)
0.4149	7.640(12)	10.136(22)			
0.4208		9.504(17)		14.769(64)	
0.4222			11.613(28)		22.38(28)
0.4255		9.022(15)		13.547(48)	
0.4300		8.563(14)		12.534(41)	
0.4319		8.426(14)		12.272(42)	
0.4333			10.044(19)		16.82(21)
0.4337			9.972(19)		16.53(27)
0.4381			9.484(17)		14.86(18)
0.4404		7.817(12)		10.720(27)	
0.4426	6.1503(88)	7.614(12)			
0.4430			9.002(16)		13.69(16)
0.4444			8.866(15)		13.168(94)
0.4484			8.520(15)		12.441(96)
0.4500	5.8636(83)	7.173(11)		9.566(21)	
0.4549			8.018(14)		11.344(78)
0.4596		6.666(10)		8.670(18)	
0.4600	5.5008(76)	6.652(10)		8.629(18)	
0.4622			7.516(12)		10.232(99)
0.4702	5.1722(71)	6.1650(100)			
0.4722			6.932(11)		9.181(57)
0.4800	4.9237(67)	5.8190(94)		7.206(14)	
0.4873		5.5344(80)		6.795(11)	
0.4979	4.4910(60)	5.2020(73)			
0.5000	4.4503(59)	5.1418(76)	5.7023(82)		7.129(38)
0.5150		4.7411(64)		5.6532(98)	
0.5256	3.9728(51)	4.5030(69)			
0.5278			4.8763(67)		5.913(30)
0.5400	3.7474(47)	4.2159(57)			
0.5427		4.1637(61)		4.8388(80)	
0.5534	3.5592(45)	3.9758(60)			
0.5556			4.2557(59)		4.972(22)
0.5705		3.7126(49)		4.2417(98)	
0.5812	3.2284(41)	3.5650(71)			
0.5833			3.7887(50)		4.356(19)
0.5982		3.3608(43)		3.7630(59)	
0.6111			3.4043(44)		3.853(16)
0.6367	2.7237(33)	2.9542(38)			
0.6538		2.8108(35)		3.0876(45)	
0.6600	2.5513(32)	2.7636(35)			

0.6667			2.8575(36)		3.176(14)
0.6923	2.3559(28)	2.5354(41)			
0.7093		2.4202(34)		2.6289(39)	
0.7222			2.4558(31)		2.679(12)
0.7478	2.0811(25)	2.2122(30)			
0.7649		2.1277(27)		2.2893(32)	
0.7778			2.1546(26)		2.3206(78)
0.8034	1.8596(22)	1.9666(27)			
0.8202		1.8965(23)		2.0187(26)	
0.8333			1.9242(23)		2.0418(76)

Table B.2: $SU(5)$ TGF 't Hooft coupling data as a function of the inverse bare coupling $b = 1/\lambda_0$ and the lattice size $\tilde{L} = \tilde{l}/a$.

b	$\tilde{L} = 16$	$\tilde{L} = 32$	$\tilde{L} = 48$	$\tilde{L} = 64$	$\tilde{L} = 96$
0.3555	53.72(13)	226.12(56)	537.70(159)		1647.83(3045)
0.3594	43.08(11)	172.85(30)	420.81(72)	734.50(416)	1426.25(721)
0.3633	35.25(10)	133.91(28)	330.04(64)	594.95(149)	1178.26(634)
0.3657	31.59(10)	115.28(21)			
0.3666			268.28(60)		1021.115(4033)
0.3766	20.355(68)	62.93(17)			
0.3777		59.30(16)		263.05(114)	
0.3778			137.46(48)		608.00(498)
0.3876	15.060(43)	37.38(13)			
0.3888		35.51(14)		140.08(88)	
0.3891	14.530(39)	35.46(13)	75.26(47)		336.63(482)
0.3986	12.168(25)	24.40(12)			
0.4000		23.23(11)	45.11(33)	77.50(85)	189.49(229)
0.4096	10.396(19)	17.317(67)			
0.4109			28.85(26)		104.596(2033)
0.4111		16.745(61)		46.90(59)	
0.4207	9.086(16)	13.631(39)			
0.4219			20.02(20)		66.06(231)
0.4222		13.305(34)		31.45(49)	
0.4318	8.115(14)	11.375(25)			
0.4333		11.151(25)		20.98(52)	
0.4336			14.851(95)		40.45(426)
0.4337		11.089(23)		20.25(59)	
0.4380		10.455(21)		18.26(39)	
0.4430		9.859(18)		15.84(24)	
0.4444		9.668(18)		15.34(15)	
0.4445	7.253(11)	9.662(18)	12.317(80)		27.75(239)
0.4484		9.260(16)		14.45(17)	
0.4548		8.651(15)		12.59(10)	

0.4595	6.4649(98)	8.268(14)			
0.4622		8.028(13)		11.352(70)	
0.4722		7.393(12)	8.750(33)	10.071(57)	13.20(49)
0.4873	5.3876(77)	6.5671(97)			
0.5000		6.0077(90)	6.822(20)	7.572(35)	8.89(12)
0.5150	4.6315(62)	5.4539(78)			
0.5277		5.0830(75)		6.175(30)	
0.5281			5.635(17)		6.91(10)
0.5427	4.0796(54)	4.6935(63)			
0.5555	3.8811(51)	4.4163(61)	4.834(13)		5.774(85)
0.5555		4.4126(62)		5.189(21)	
0.5705	3.6395(46)	4.1257(55)			
0.5833		3.9113(53)		4.481(18)	
0.5836			4.237(11)		5.007(54)
0.5982	3.2893(42)	3.6812(47)			
0.6109			3.7499(94)		4.279(45)
0.6111		3.5077(47)		3.960(18)	
0.6538	2.7648(35)	3.0356(40)			
0.6664			3.1016(75)		3.466(39)
0.6666		2.9177(38)		3.232(14)	
0.7093	2.3896(28)	2.5824(32)			
0.7219			2.6184(66)		2.874(42)
0.7222		2.4986(31)		2.725(11)	
0.7648	2.1020(25)	2.2513(28)			
0.7777		2.1875(28)		2.3614(87)	
0.7781	2.0486(23)	2.1858(27)	2.2817(54)		2.468(30)
0.8202	1.8817(22)	1.9967(23)			
0.8333		1.9434(23)		2.0665(72)	
0.8336			2.0141(47)		2.175(21)
0.8891			1.8091(41)		1.926(17)
0.9445			1.6525(38)		1.735(15)

Table B.3: $SU(8)$ TGF 't Hooft coupling data as a function of the inverse bare coupling $b = 1/\lambda_0$ and the lattice size $\tilde{L} = \tilde{l}/a$.

b	$\tilde{L} = 12$	$\tilde{L} = 18$	$\tilde{L} = 24$	$\tilde{L} = 36$	$\tilde{L} = 48$
0.3333	32.68(11)	68.106(95)	126.12(32)	336.048(1071)	655.64(513)
0.3444	20.318(61)	37.191(50)	63.98(15)	152.84(66)	308.11(224)
0.3499	17.031(45)		48.24(15)		
0.3556	14.768(37)	23.390(31)	37.302(83)	81.59(24)	152.86(96)
0.3604	13.363(30)		30.311(95)		
0.3658		17.046(33)		49.43(20)	
0.3667	11.963(24)	16.655(19)	23.884(54)	47.53(14)	84.10(55)
0.3712	11.173(21)		20.577(63)		

0.3766		13.380(22)		31.39(18)	
0.3778	10.219(19)	13.056(13)	17.058(36)	30.010(84)	49.95(30)
0.3821	9.682(17)		15.417(39)		
0.3876		11.213(15)		21.434(100)	
0.3889	8.927(15)	10.9884(91)	13.369(23)	20.457(56)	32.05(18)
0.3930	8.580(14)		12.491(27)		
0.3986		9.715(12)		15.867(54)	
0.4000	8.014(13)	9.5499(74)	11.185(16)	15.324(38)	21.55(14)
0.4040	7.731(12)		10.586(19)		
0.4097		8.6130(98)		12.697(37)	
0.4111	7.263(11)	8.4800(59)	9.710(13)	12.410(24)	15.880(80)
0.4149	7.049(10)		9.306(16)		
0.4208		7.737(12)		10.807(30)	
0.4222	6.674(10)	7.6490(51)	8.613(10)	10.594(20)	12.883(57)
0.4319		7.0474(76)		9.448(22)	
0.4333	6.1612(94)	6.9792(45)	7.7413(92)	9.278(17)	10.895(41)
0.4426	5.7935(83)		7.173(11)		
0.4444	5.7384(83)	6.4216(41)	7.0703(80)	8.278(13)	9.480(31)
0.4596		5.8030(59)		7.279(19)	
0.4702	4.9375(49)		5.8834(85)		
0.4722	4.8973(68)	5.3772(33)	5.8018(66)	6.583(10)	7.274(23)
0.4873		4.9481(50)		5.959(15)	
0.4979	4.3107(42)		4.9974(71)		
0.5000	4.2710(57)	4.6335(28)	4.9424(52)	5.4888(83)	5.981(18)
0.5150		4.3187(43)		5.050(18)	
0.5256	3.8340(51)		4.3633(61)		
0.5278	3.8006(52)	4.0753(23)	4.3198(47)	4.7273(76)	5.051(16)
0.5427		3.8288(53)		4.402(10)	
0.5534	3.4462(33)		3.8547(53)		
0.5556	3.4228(46)	3.6413(21)	3.8376(39)	4.1470(47)	4.416(11)
0.5705		3.4531(46)		3.8914(59)	
0.5812	3.1335(28)		3.4748(46)		
0.5833	3.1112(40)	3.2931(19)	3.4529(36)	3.6944(46)	3.903(11)
0.5982		3.1429(41)		3.4867(54)	
0.6111	2.8544(37)	3.0117(17)	3.1370(44)	3.3428(41)	3.5107(100)
0.6367	2.6550(23)		2.8983(38)		
0.6538		2.6534(34)		2.9216(47)	
0.6667	2.4530(31)	2.5674(34)	2.6548(27)	2.7988(39)	2.910(10)
0.6923	2.3073(21)		2.4810(34)		
0.7093		2.3131(30)		2.4981(40)	
0.7222	2.1533(27)	2.2417(28)	2.3054(23)	2.4161(34)	2.4905(86)
0.7478	2.0397(18)		2.1771(28)		
0.7649		2.0424(27)		2.1850(38)	
0.7778	1.9190(25)	1.9909(26)	2.0435(21)	2.1283(32)	2.1926(66)
0.8034	1.8301(16)		1.9362(25)		

0.8202		1.8330(23)		1.9437(28)	
0.8333	1.7344(22)	1.7850(23)	1.8325(19)	1.8932(27)	1.9460(62)
1.1111	1.1684(14)	1.1937(21)	1.2094(14)	1.2374(37)	1.2670(76)

Table B.4: $SU(3)$ TGF 't Hooft coupling data, for planes **PT**, as a function of the inverse bare coupling $b = 1/\lambda_0$ and the lattice size $\tilde{L} = \tilde{l}/a$.

b	$\tilde{L} = 12$	$\tilde{L} = 18$	$\tilde{L} = 24$	$\tilde{L} = 36$	$\tilde{L} = 48$
0.3333	41.51(19)	92.68(15)	174.05(50)	467.0(16)	905.2(82)
0.3444	23.301(100)	47.824(86)	86.53(25)	211.8(10)	431.2(33)
0.3499	18.787(71)		64.13(24)		
0.3556	15.884(59)	27.525(53)	48.11(15)	112.08(39)	211.1(16)
0.3604	14.148(44)		37.59(17)		
0.3658		18.798(51)		65.76(33)	
0.3667	12.605(36)	18.258(31)	28.205(94)	62.99(24)	115.56(85)
0.3712	11.680(28)		23.53(11)		
0.3766		14.165(30)		39.20(32)	
0.3778	10.613(25)	13.781(18)	18.716(58)	37.18(15)	66.06(52)
0.3821	10.024(21)		16.669(57)		
0.3876		11.725(21)		24.70(18)	
0.3889	9.208(19)	11.455(12)	14.173(34)	23.370(96)	40.13(32)
0.3930	8.846(18)		13.152(39)		
0.3986		10.074(15)		17.295(85)	
0.4000	8.259(17)	9.8663(95)	11.646(21)	16.540(62)	24.92(24)
0.4040	7.981(15)		11.014(25)		
0.4097		8.892(13)		13.354(55)	
0.4111	7.477(14)	8.7424(77)	10.060(16)	13.032(33)	17.21(12)
0.4149	7.239(14)		9.578(21)		
0.4208		7.961(16)		11.274(41)	
0.4222	6.854(13)	7.8730(67)	8.867(14)	10.995(26)	13.559(83)
0.4319		7.242(10)		9.794(26)	
0.4333	6.294(12)	7.1534(60)	7.946(12)	9.552(21)	11.276(48)
0.4426	5.930(11)		7.343(14)		
0.4444	5.864(11)	6.5712(54)	7.246(10)	8.516(17)	9.821(41)
0.4596		5.9270(81)		7.459(26)	
0.4702	5.0354(65)		6.012(12)		
0.4722	4.9829(91)	5.4858(44)	5.9292(85)	6.733(14)	7.492(30)
0.4873		5.0302(66)		6.056(22)	
0.4979	4.3842(56)		5.0939(95)		
0.5000	4.3462(80)	4.7250(38)	5.0311(73)	5.615(11)	6.103(24)
0.5150		4.3982(57)		5.136(24)	
0.5256	3.8881(70)		4.4325(82)		
0.5278	3.8497(72)	4.1384(32)	4.3881(64)	4.808(10)	5.138(22)
0.5427		3.8928(70)		4.480(15)	

0.5534	3.4934(45)		3.9110(72)		
0.5556	3.4679(61)	3.6934(28)	3.8891(53)	4.2065(68)	4.465(15)
0.5705		3.4946(62)		3.9586(81)	
0.5812	3.1728(40)		3.5204(63)		
0.5833	3.1542(56)	3.3374(26)	3.4962(47)	3.7447(60)	3.940(14)
0.5982		3.1758(57)		3.5407(74)	
0.6111	2.8901(53)	3.0491(23)	3.1739(65)	3.3833(56)	3.549(13)
0.6367	2.6820(33)		2.9254(54)		
0.6538		2.6953(47)		2.9466(66)	
0.6667	2.4772(43)	2.5963(47)	2.6805(38)	2.8291(54)	2.941(12)
0.6923	2.3336(28)		2.5039(45)		
0.7093		2.3339(42)		2.5153(56)	
0.7222	2.1762(38)	2.2643(40)	2.3276(32)	2.4413(47)	2.515(11)
0.7478	2.0594(26)		2.1966(39)		
0.7649		2.0618(39)		2.2117(53)	
0.7778	1.9376(34)	2.0046(36)	2.0572(28)	2.1433(42)	2.2105(95)
0.8034	1.8447(23)		1.9520(35)		
0.8202		1.8459(34)		1.9563(39)	
0.8333	1.7530(31)	1.7976(32)	1.8441(26)	1.9133(38)	1.9590(92)
1.1111	1.1724(21)	1.2026(31)	1.2163(20)	1.2421(52)	1.268(11)

Table B.5: $SU(3)$ TGF 't Hooft coupling data, for planes **PP**, as a function of the inverse bare coupling $b = 1/\lambda_0$ and the lattice size $\tilde{L} = \tilde{l}/a$.

b	$\tilde{L} = 12$	$\tilde{L} = 18$	$\tilde{L} = 24$	$\tilde{L} = 36$	$\tilde{L} = 48$
0.3333	37.57(13)	67.088(91)	111.17(27)	267.01(87)	517.3(34)
0.3444	24.476(90)	41.603(59)	63.97(14)	131.10(56)	246.0(18)
0.3499	20.328(81)		51.02(15)		
0.3556	17.485(65)	27.703(46)	41.656(98)	77.93(22)	130.59(79)
0.3604	15.654(61)		34.94(12)		
0.3658		20.182(56)		52.30(21)	
0.3667	13.870(49)	19.635(32)	28.173(77)	50.68(14)	79.51(52)
0.3712	12.777(41)		24.394(93)		
0.3766		15.519(40)		35.93(21)	
0.3778	11.661(36)	15.127(23)	20.101(58)	34.54(11)	52.58(31)
0.3821	10.953(34)		18.135(64)		
0.3876		12.775(30)		25.38(15)	
0.3889	10.002(29)	12.465(18)	15.481(44)	24.184(85)	36.61(23)
0.3930	9.613(27)		14.385(50)		
0.3986		10.929(24)		18.479(93)	
0.4000	8.949(26)	10.714(15)	12.732(31)	17.911(62)	25.41(22)
0.4040	8.583(24)		11.968(37)		
0.4097		9.570(19)		14.729(79)	
0.4111	7.992(22)	9.418(12)	10.869(25)	14.251(48)	18.50(13)

0.4149	7.801(22)		10.388(31)		
0.4208		8.500(24)		12.240(59)	
0.4222	7.333(20)	8.416(10)	9.561(21)	11.947(37)	14.74(10)
0.4319		7.728(15)		10.599(45)	
0.4333	6.681(18)	7.6340(91)	8.505(18)	10.301(32)	12.243(77)
0.4426	6.295(17)		7.844(22)		
0.4444	6.246(17)	6.9709(82)	7.730(16)	9.096(27)	10.465(61)
0.4596		6.268(12)		7.988(39)	
0.4702	5.314(10)		6.344(17)		
0.4722	5.249(15)	5.7818(66)	6.256(13)	7.124(22)	8.053(51)
0.4873		5.3070(99)		6.433(30)	
0.4979	4.6039(85)		5.369(14)		
0.5000	4.564(12)	4.9383(56)	5.273(10)	5.902(17)	6.431(36)
0.5150		4.5789(84)		5.368(35)	
0.5256	4.057(10)		4.613(12)		
0.5278	4.018(10)	4.3122(47)	4.5776(92)	5.049(15)	5.445(33)
0.5427		4.039(11)		4.659(20)	
0.5534	3.6272(64)		4.067(10)		
0.5556	3.6070(91)	3.8376(42)	4.0554(78)	4.3752(95)	4.689(22)
0.5705		3.6228(94)		4.128(12)	
0.5812	3.2954(59)		3.6422(94)		
0.5833	3.2595(81)	3.4555(38)	3.6198(69)	3.8905(90)	4.122(23)
0.5982		3.2735(82)		3.650(11)	
0.6111	2.9825(76)	3.1502(35)	3.2801(89)	3.4990(78)	3.676(18)
0.6367	2.7674(47)		3.0179(75)		
0.6538		2.7624(68)		3.0399(97)	
0.6667	2.5554(63)	2.6828(67)	2.7674(56)	2.9089(76)	3.030(19)
0.6923	2.3947(43)		2.5715(65)		
0.7093		2.3899(60)		2.5963(81)	
0.7222	2.2362(55)	2.3183(57)	2.3888(46)	2.4997(66)	2.584(16)
0.7478	2.1124(36)		2.2578(57)		
0.7649		2.1140(52)		2.2583(75)	
0.7778	1.9868(49)	2.0581(51)	2.1056(41)	2.1894(59)	2.278(14)
0.8034	1.8925(33)		1.9933(49)		
0.8202		1.8815(49)		2.0061(57)	
0.8333	1.7891(44)	1.8347(45)	1.8792(36)	1.9522(53)	2.001(13)
1.1111	1.1962(28)	1.2125(42)	1.2256(27)	1.2655(70)	1.283(19)

Table B.6: $SU(3)$ TGF 't Hooft coupling data, for planes **TT**, as a function of the inverse bare coupling $b = 1/\lambda_0$ and the lattice size $\tilde{L} = \tilde{l}/a$.

b	$\tilde{L} = 10$	$\tilde{L} = 20$	$\tilde{L} = 30$	$\tilde{L} = 40$	$\tilde{L} = 60$
0.3300	286.33(28)	1047.0(14)	1717.3(41)	2413(14)	4438(115)
0.3350	125.79(66)	302.63(79)	697.0(17)	1181.2(44)	2282(26)

0.3400	47.64(17)	163.23(43)	397.27(95)	716.7(23)	1458(12)
0.3450	31.08(11)	106.69(28)	261.19(64)	487.2(15)	1057.3(79)
0.3499	23.561(80)	75.64(21)			
0.3550	19.121(54)	55.29(17)	130.56(38)	249.37(73)	592.0(43)
0.3604	16.149(41)	41.17(14)			
0.3630	15.053(37)	36.52(12)	80.13(40)	152.40(60)	371.8(21)
0.3658		32.33(11)		129.78(43)	
0.3680	13.473(31)	29.30(10)	60.85(18)	113.25(28)	279.7(15)
0.3705	12.872(27)	26.60(10)			
0.3720	12.539(26)	24.780(97)	49.52(15)	89.95(24)	222.8(15)
0.3766		21.079(75)		70.65(25)	
0.3778			37.99(14)		161.70(82)
0.3790	11.184(21)	19.458(70)	35.95(13)	62.45(25)	151.27(69)
0.3821	10.661(20)	17.853(65)			
0.3876		15.462(41)		41.52(21)	
0.3889			24.360(99)		88.57(78)
0.3930	9.294(16)	13.805(41)			
0.3986		12.503(28)		26.33(15)	
0.4000			17.239(66)		51.63(57)
0.4040	8.280(13)	11.443(25)			
0.4097		10.572(20)		18.518(96)	
0.4111			13.527(39)		32.48(50)
0.4149	7.475(12)	9.873(21)			
0.4208		9.274(16)		14.241(54)	
0.4222			11.284(24)		21.34(25)
0.4255		8.822(15)		13.109(43)	
0.4300		8.376(14)		12.151(37)	
0.4319		8.242(13)		11.910(37)	
0.4333			9.792(18)		16.18(19)
0.4337			9.726(18)		15.92(23)
0.4381			9.262(16)		14.41(14)
0.4404		7.654(12)		10.451(24)	
0.4426	6.0329(87)	7.462(12)			
0.4430			8.799(15)		13.25(12)
0.4444			8.670(14)		12.794(85)
0.4484			8.335(14)		12.002(68)
0.4500	5.7635(83)	7.034(11)		9.350(20)	
0.4549			7.853(14)		10.979(58)
0.4596		6.554(10)		8.479(17)	
0.4600	5.4091(77)	6.5311(100)		8.436(17)	
0.4622			7.372(12)		9.978(65)
0.4702	5.0896(71)	6.064(10)			
0.4722			6.805(10)		8.981(40)
0.4800	4.8462(68)	5.7230(94)		7.069(14)	
0.4873		5.4536(78)		6.675(11)	

0.4979	4.4262(61)	5.1248(75)			
0.5000	4.3851(61)	5.0664(73)	5.6162(83)		6.971(31)
0.5150		4.6804(66)		5.5710(98)	
0.5256	3.9213(52)	4.4484(70)			
0.5278			4.8129(68)		5.792(23)
0.5400	3.7046(50)	4.1623(57)			
0.5427		4.1130(62)		4.7756(86)	
0.5534	3.5132(47)	3.9237(62)			
0.5556			4.2013(61)		4.905(19)
0.5705		3.6737(51)		4.199(10)	
0.5812	3.1954(43)	3.5221(73)			
0.5833			3.7468(51)		4.298(16)
0.5982		3.3261(45)		3.7221(62)	
0.6111			3.3676(46)		3.827(14)
0.6367	2.6987(35)	2.9247(39)			
0.6538		2.7867(37)		3.0573(47)	
0.6600	2.5283(33)	2.7404(36)			
0.6667			2.8329(38)		3.122(12)
0.6923	2.3384(30)	2.5155(43)			
0.7093		2.4002(36)		2.6070(42)	
0.7222			2.4366(33)		2.651(11)
0.7478	2.0631(28)	2.1955(32)			
0.7649		2.1136(28)		2.2724(35)	
0.7778			2.1400(28)		2.3111(85)
0.8034	1.8478(23)	1.9535(28)			
0.8202		1.8862(25)		2.0076(28)	
0.8333			1.9130(25)		2.0303(67)

Table B.7: $SU(5)$ TGF 't Hooft coupling data, for planes **PT**, as a function of the inverse bare coupling $b = 1/\lambda_0$ and the lattice size $\tilde{L} = \tilde{l}/a$.

b	$\tilde{L} = 10$	$\tilde{L} = 20$	$\tilde{L} = 30$	$\tilde{L} = 40$	$\tilde{L} = 60$
0.3300	405.81(44)	1452.0(23)	2371.5(61)	3325(19)	6070(159)
0.3350	185.4845(10064)	429.1(12)	973.7(26)	1633.8(66)	3138(35)
0.3400	66.19(30)	231.22(68)	560.3(15)	1002.1(35)	2016(18)
0.3450	40.00(19)	149.65(47)	370.7(10)	686.0(21)	1466(13)
0.3499	28.43(14)	104.85(35)			
0.3550	21.893(90)	75.07(28)	184.05(59)	353.7(12)	832.9(61)
0.3604	17.919(65)	54.45(23)			
0.3630	16.433(55)	47.57(21)	111.67(66)	215.82(92)	525.7(34)
0.3658		41.33(19)		183.03(67)	
0.3680	14.489(41)	36.75(18)	83.30(30)	159.06(46)	396.6(21)
0.3705	13.768(39)	32.74(18)			
0.3720	13.370(36)	30.03(16)	66.77(25)	125.53(39)	315.7(21)

0.3766		24.64(13)		97.49(40)	
0.3778			49.57(24)		228.20(12)
0.3790	11.830(29)	22.36(12)	46.60(23)	85.67(41)	214.1(12)
0.3821	11.226(27)	20.20(11)			
0.3876		16.976(66)		54.89(36)	
0.3889			29.52(17)		123.5(121)
0.3930	9.751(20)	15.012(65)			
0.3986		13.452(41)		32.27(27)	
0.4000			19.45(12)		69.77(93)
0.4040	8.629(17)	12.149(34)			
0.4097		11.174(27)		21.14(16)	
0.4111			14.654(65)		41.68(85)
0.4149	7.750(15)	10.398(27)			
0.4208		9.735(22)		15.575(81)	
0.4222			12.026(36)		24.99(46)
0.4255		9.227(19)		14.094(65)	
0.4300		8.786(18)		12.993(52)	
0.4319		8.635(18)		12.713(52)	
0.4333			10.312(24)		17.88(30)
0.4337			10.251(22)		17.58(39)
0.4381			9.726(21)		15.67(20)
0.4404		7.987(16)		11.054(32)	
0.4426	6.250(12)	7.751(15)			
0.4430			9.246(20)		14.35(20)
0.4444			9.090(19)		13.68(11)
0.4484			8.724(19)		12.757(85)
0.4500	5.943(12)	7.301(14)		9.827(27)	
0.4549			8.187(17)		11.725(73)
0.4596		6.790(13)		8.874(22)	
0.4600	5.582(10)	6.774(14)		8.861(22)	
0.4622			7.691(16)		10.588(90)
0.4702	5.245(10)	6.280(14)			
0.4722			7.068(14)		9.470(51)
0.4800	4.9762(92)	5.907(13)		7.354(19)	
0.4873		5.630(12)		6.928(14)	
0.4979	4.5426(82)	5.278(10)			
0.5000	4.4892(82)	5.2218(99)	5.807(11)		7.260(36)
0.5150		4.8087(90)		5.745(13)	
0.5256	4.0163(78)	4.5661(98)			
0.5278			4.9599(95)		5.966(33)
0.5400	3.7781(68)	4.2704(80)			
0.5427		4.2203(79)		4.905(11)	
0.5534	3.5877(65)	4.0232(88)			
0.5556			4.3175(81)		5.023(24)
0.5705		3.7528(72)		4.291(14)	

0.5812	3.2549(59)	3.604(11)			
0.5833			3.8382(71)		4.426(21)
0.5982		3.3967(62)		3.7964(90)	
0.6111			3.4426(64)		3.922(20)
0.6367	2.7452(49)	2.9832(55)			
0.6538		2.8425(51)		3.1323(67)	
0.6600	2.5683(49)	2.7878(51)			
0.6667			2.8886(53)		3.174(15)
0.6923	2.3751(41)	2.5569(59)			
0.7093		2.4433(47)		2.6491(57)	
0.7222			2.4660(45)		2.681(14)
0.7478	2.0901(36)	2.2217(45)			
0.7649		2.1454(40)		2.3092(49)	
0.7778			2.1708(40)		2.330(11)
0.8034	1.8691(33)	1.9779(42)			
0.8202		1.9082(35)		2.0276(40)	
0.8333			1.9290(35)		2.0544(87)

Table B.8: $SU(5)$ TGF 't Hooft coupling data, for planes **PP**, as a function of the inverse bare coupling $b = 1/\lambda_0$ and the lattice size $\tilde{L} = \tilde{l}/a$.

b	$\tilde{L} = 10$	$\tilde{L} = 20$	$\tilde{L} = 30$	$\tilde{L} = 40$	$\tilde{L} = 60$
0.3300	241.31(28)	851.6(13)	1371.0(35)	1915(11)	3547(82)
0.3350	108.27(53)	266.18(76)	585.5(15)	962.9(37)	1820(20)
0.3400	47.19(15)	147.15(39)	347.35(93)	602.9(19)	1171(10)
0.3450	33.63(11)	98.00(27)	232.74(62)	420.4(14)	862.9(59)
0.3499	26.62(10)	71.23(20)			
0.3550	21.823(81)	54.25(15)	118.90(36)	222.79(73)	504.4(39)
0.3604	18.478(65)	42.40(14)			
0.3630	17.190(61)	38.40(12)	74.87(37)	137.85(59)	326.3(21)
0.3658		34.68(11)		117.70(39)	
0.3680	15.246(52)	32.04(11)	58.62(16)	103.51(27)	248.4(14)
0.3705	14.522(48)	29.38(12)			
0.3720	14.088(45)	27.51(12)	49.34(13)	83.22(23)	200.1(14)
0.3766		23.765(92)		66.62(21)	
0.3778			39.54(13)		147.02(76)
0.3790	12.493(39)	22.012(95)	37.86(13)	59.82(21)	136.71(63)
0.3821	11.872(39)	20.25(10)			
0.3876		17.419(67)		42.56(18)	
0.3889			27.18(12)		82.14(68)
0.3930	10.167(30)	15.440(71)			
0.3986		13.951(52)		29.08(18)	
0.4000			19.488(97)		50.93(46)
0.4040	8.995(26)	12.609(47)			

0.4097		11.624(39)		20.78(13)	
0.4111			15.126(64)		35.09(50)
0.4149	8.089(22)	10.808(38)			
0.4208		10.089(31)		15.96(10)	
0.4222			12.407(46)		24.15(37)
0.4255		9.531(28)		14.607(67)	
0.4300		9.022(25)		13.471(64)	
0.4319		8.884(26)		13.155(62)	
0.4333			10.678(35)		18.24(28)
0.4337			10.581(33)		17.84(32)
0.4381			10.040(30)		16.03(24)
0.4404		8.228(22)		11.375(47)	
0.4426	6.459(17)	8.013(23)			
0.4430			9.497(30)		14.67(21)
0.4444			9.349(27)		14.15(17)
0.4484			8.986(27)		13.22(13)
0.4500	6.130(17)	7.533(21)		10.093(36)	
0.4549			8.439(24)		12.07(11)
0.4596		6.948(19)		9.151(33)	
0.4600	5.740(15)	6.962(19)		9.100(32)	
0.4622			7.866(22)		10.93(14)
0.4702	5.388(14)	6.414(19)			
0.4722			7.250(20)		9.554(78)
0.4800	5.135(13)	6.069(18)		7.550(25)	
0.4873		5.733(15)		7.093(20)	
0.4979	4.664(12)	5.400(14)			
0.5000	4.631(12)	5.332(15)	5.912(16)		7.377(58)
0.5150		4.892(13)		5.858(19)	
0.5256	4.108(11)	4.638(14)			
0.5278			5.027(13)		6.141(45)
0.5400	3.8630(99)	4.352(11)			
0.5427		4.290(12)		4.999(15)	
0.5534	3.6861(92)	4.112(12)			
0.5556			4.391(12)		5.184(40)
0.5705		3.8113(98)		4.348(19)	
0.5812	3.3163(84)	3.677(15)			
0.5833			3.892(10)		4.517(30)
0.5982		3.4485(90)		3.872(12)	
0.6111			3.4971(88)		3.976(27)
0.6367	2.7894(68)	3.0298(76)			
0.6538		2.8682(71)		3.1572(92)	
0.6600	2.6131(64)	2.8225(72)			
0.6667			2.9167(75)		3.267(22)
0.6923	2.3991(57)	2.5854(82)			
0.7093		2.4698(66)		2.6859(87)	

0.7222			2.5097(64)		2.724(21)
0.7478	2.1320(54)	2.2587(62)			
0.7649		2.1618(55)		2.3310(70)	
0.7778			2.1911(54)		2.345(15)
0.8034	1.8908(45)	2.0011(59)			
0.8202		1.9219(47)		2.0485(57)	
0.8333			1.9563(49)		2.081(13)

Table B.9: $SU(5)$ TGF 't Hooft coupling data, for planes **TT**, as a function of the inverse bare coupling $b = 1/\lambda_0$ and the lattice size $\tilde{L} = \tilde{l}/a$.

b	$\tilde{L} = 16$	$\tilde{L} = 32$	$\tilde{L} = 48$	$\tilde{L} = 64$	$\tilde{L} = 96$
0.3766	19.411(60)	60.56(16)			
0.3777		57.01(16)		258.2(11)	
0.3778			134.08(47)		599.9(46)
0.3876	14.502(38)	35.54(13)			
0.3888		33.77(13)		136.62(87)	
0.3891	14.001(35)	33.69(12)	72.71(47)		330.6(47)
0.3986	11.771(23)	23.19(10)			
0.4000		22.100(96)	43.12(32)	75.03(83)	185.2(23)
0.4096	10.098(18)	16.597(56)			
0.4109			27.45(24)		101.6(21)
0.4111		16.078(54)		44.79(55)	
0.4207	8.862(15)	13.185(35)			
0.4219			19.14(18)		63.5(23)
0.4222		12.856(30)		29.79(46)	
0.4318	7.938(13)	11.045(23)			
0.4333		10.838(22)		19.99(44)	
0.4336			14.322(83)		38.5(41)
0.4337		10.773(20)		19.37(48)	
0.4380		10.170(20)		17.47(35)	
0.4430		9.603(17)		15.29(21)	
0.4444		9.422(16)		14.76(13)	
0.4445	7.109(11)	9.429(17)	11.941(70)		26.19(218)
0.4484		9.036(15)		13.88(14)	
0.4548		8.454(14)		12.214(90)	
0.4595	6.3396(92)	8.077(13)			
0.4622		7.860(13)		11.044(64)	
0.4722		7.242(11)	8.545(30)	9.819(53)	12.81(46)
0.4873	5.2981(77)	6.4429(95)			
0.5000		5.9082(92)	6.703(19)	7.440(34)	8.68(13)
0.5150	4.5679(65)	5.3717(78)			
0.5277		5.0100(76)		6.064(28)	
0.5281			5.550(16)		6.76(12)

0.5427	4.0242(56)	4.6286(64)			
0.5555	3.8353(53)	4.3545(62)	4.760(14)		5.634(70)
0.5555		4.3516(65)		5.108(22)	
0.5705	3.6022(47)	4.0741(56)			
0.5833		3.8690(55)		4.420(18)	
0.5836			4.180(11)		4.923(53)
0.5982	3.2556(43)	3.6387(51)			
0.6109			3.7141(95)		4.234(42)
0.6111		3.4669(50)		3.925(19)	
0.6538	2.7396(37)	3.0080(42)			
0.6664			3.0683(79)		3.456(39)
0.6666		2.8920(41)		3.207(14)	
0.7093	2.3700(31)	2.5623(34)			
0.7219			2.6045(70)		2.866(46)
0.7222		2.4772(35)		2.692(11)	
0.7648	2.0879(27)	2.2340(28)			
0.7777		2.1711(30)		2.3452(92)	
0.7781	2.0347(26)	2.1705(28)	2.2623(57)		2.440(29)
0.8202	1.8678(25)	1.9817(26)			
0.8333		1.9302(25)		2.0421(74)	
0.8336			2.0008(51)		2.160(22)
0.8891			1.7971(44)		1.913(20)
0.9445			1.6428(42)		1.739(17)

Table B.10: $SU(8)$ TGF 't Hooft coupling data, for planes **PT**, as a function of the inverse bare coupling $b = 1/\lambda_0$ and the lattice size $\tilde{L} = \tilde{l}/a$.

b	$\tilde{L} = 16$	$\tilde{L} = 32$	$\tilde{L} = 48$	$\tilde{L} = 64$	$\tilde{L} = 96$
0.3766	22.13(10)	82.40(27)			
0.3777		77.34(25)		364.0(16)	
0.3778			188.12(72)		843.4(81)
0.3876	15.686(62)	45.73(22)			
0.3888		43.19(23)		191.5(13)	
0.3891	15.085(54)	43.06(22)	100.16(70)		467.0(68)
0.3986	12.469(32)	27.44(18)			
0.4000		25.88(17)	56.86(53)	103.2(12)	261.49(364)
0.4096	10.580(23)	18.378(97)			
0.4109			33.73(43)		141.3(31)
0.4111		17.643(85)		59.5(10)	
0.4207	9.245(19)	14.074(52)			
0.4219			21.85(28)		88.8(28)
0.4222		13.751(45)		37.46(89)	
0.4318	8.221(17)	11.619(32)			
0.4333		11.412(32)		23.05(78)	

0.4336			15.50(14)		50.3(68)
0.4337		11.315(27)		22.23(90)	
0.4380		10.666(26)		19.69(64)	
0.4430		10.052(22)		16.39(28)	
0.4444		9.834(21)		15.83(17)	
0.4445	7.370(14)	9.845(22)	12.74(11)		32.7(37)
0.4484		9.409(20)		15.09(21)	
0.4548		8.803(19)		12.99(13)	
0.4595	6.545(13)	8.421(17)			
0.4622		8.164(17)		11.622(79)	
0.4722		7.491(15)	8.914(41)	10.308(64)	13.88(47)
0.4873	5.436(10)	6.649(13)			
0.5000		6.073(13)	6.931(27)	7.747(49)	9.02(14)
0.5150	4.6741(87)	5.518(11)			
0.5277		5.149(10)		6.220(42)	
0.5281			5.708(23)		6.93(11)
0.5427	4.1202(78)	4.7487(87)			
0.5555	3.9137(73)	4.4626(84)	4.868(18)		5.843(96)
0.5555		4.4542(86)		5.247(30)	
0.5705	3.6732(67)	4.1612(77)			
0.5833		3.9382(75)		4.521(26)	
0.5836			4.253(15)		5.154(84)
0.5982	3.3167(63)	3.7220(68)			
0.6109			3.782(13)		4.353(66)
0.6111		3.5324(68)		3.962(24)	
0.6538	2.7781(51)	3.0566(57)			
0.6664			3.107(12)		3.418(53)
0.6666		2.9301(57)		3.232(20)	
0.7093	2.4007(43)	2.6041(47)			
0.7219			2.6345(88)		2.861(64)
0.7222		2.5158(47)		2.760(14)	
0.7648	2.1207(38)	2.2645(41)			
0.7777		2.2027(41)		2.380(13)	
0.7781	2.0606(36)	2.1928(40)	2.2987(78)		2.431(31)
0.8202	1.8895(34)	2.0041(36)			
0.8333		1.9517(34)		2.080(11)	
0.8336			2.0191(70)		2.174(30)
0.8891			1.8179(61)		1.959(29)
0.9445			1.6564(57)		1.727(31)

Table B.11: $SU(8)$ TGF 't Hooft coupling data, for planes **PP**, as a function of the inverse bare coupling $b = 1/\lambda_0$ and the lattice size $\tilde{L} = \tilde{l}/a$.

b	$\tilde{L}=16$	$\tilde{L}=32$	$\tilde{L}=48$	$\tilde{L}=64$	$\tilde{L}=96$
0.3766	22.294(89)	59.43(15)			
0.3777		56.34(15)		221.622(1089)	
0.3778			119.65(44)		501.59(423)
0.3876	16.446(64)	38.44(14)			
0.3888		36.60(13)		122.13(76)	
0.3891	15.865(61)	36.72(13)	69.30(39)		282.51(419)
0.3986	13.236(43)	26.46(13)			
0.4000		25.25(12)	44.72(30)	70.84(72)	162.5722(20055)
0.4096	11.221(35)	18.966(96)			
0.4109			30.49(28)		93.28(168)
0.4111		18.321(86)		46.46(56)	
0.4207	9.697(28)	14.773(59)			
0.4219			21.76(26)		61.48(225)
0.4222		14.456(57)		33.24(43)	
0.4318	8.604(26)	12.266(40)			
0.4333		11.980(42)		22.91(66)	
0.4336			16.14(14)		40.94(365)
0.4337		11.947(40)		21.85(63)	
0.4380		11.225(36)		19.92(40)	
0.4430		10.551(32)		17.25(31)	
0.4444		10.344(32)		16.88(25)	
0.4445	7.638(21)	10.284(31)	13.25(12)		29.84(243)
0.4484		9.873(30)		15.84(28)	
0.4548		9.178(28)		13.55(16)	
0.4595	6.810(19)	8.779(25)			
0.4622		8.475(24)		12.16(12)	
0.4722		7.810(22)	9.298(59)	10.72(10)	14.07(53)
0.4873	5.639(16)	6.908(19)			
0.5000		6.281(17)	7.134(36)	7.886(62)	9.48(21)
0.5150	4.806(12)	5.674(15)			
0.5277		5.274(14)		6.497(60)	
0.5281			5.859(31)		7.39(17)
0.5427	4.229(11)	4.865(13)			
0.5555	4.005(10)	4.583(12)	5.046(26)		6.17(15)
0.5555		4.579(12)		5.409(41)	
0.5705	3.7366(92)	4.267(11)			
0.5833		4.028(11)		4.651(36)	
0.5836			4.403(22)		5.19(11)
0.5982	3.3789(85)	3.7911(98)			
0.6109			3.844(19)		4.381(85)
0.6111		3.6212(97)		4.070(31)	
0.6538	2.8360(73)	3.1101(81)			

0.6664			3.203(15)		3.527(84)
0.6666		2.9909(79)		3.309(27)	
0.7093	2.4448(61)	2.6327(67)			
0.7219			2.653(12)		2.906(61)
0.7222		2.5557(68)		2.809(24)	
0.7648	2.1356(52)	2.2979(57)			
0.7777		2.2299(57)		2.401(20)	
0.7781	2.0851(51)	2.2297(55)	2.333(11)		2.577(60)
0.8202	1.9206(47)	2.0395(51)			
0.8333		1.9796(49)		2.135(16)	
0.8336			2.053(11)		2.219(47)
0.8891			1.8415(84)		1.947(32)
0.9445			1.6808(87)		1.729(32)

Table B.12: $SU(8)$ TGF 't Hooft coupling data, for planes **TT**, as a function of the inverse bare coupling $b = 1/\lambda_0$ and the lattice size $\tilde{L} = \tilde{l}/a$.

C

Continuum extrapolation of the step scaling function

$\tilde{L}$	$18 \times b$	u	$\Sigma(u)$	$\Sigma(u_{\rm tg})$
12	14.4612	1.8425(21)	1.9503(23)	1.9503(34)
18	14.7634	1.8449(22)	1.9566(40)	1.9558(37)
24	15.0000	1.8439(17)	1.9593(58)	1.9577(61)
∞		$u_{\rm tg}$ =1.8425		1.9602(55)
12	13.4606	2.0568(23)	2.1967(26)	2.1967(38)
18	13.7630	2.0601(25)	2.2038(35)	2.2002(46)
24	14.0000	2.0584(19)	2.2130(64)	2.2113(68)
∞		$u_{\rm tg}$ =2.0568		2.2092(65)
12	12.4606	2.3270(28)	2.5031(31)	2.5031(45)
18	12.7677	2.3320(28)	2.5211(38)	2.5153(50)
24	13.0000	2.3259(22)	2.5134(81)	2.5147(85)
∞		$u_{\rm tg}$ =2.3270		2.5224(75)
12	11.4607	2.6834(32)	2.9271(36)	2.9271(52)
18	11.7682	2.6817(32)	2.9498(44)	2.9519(59)
24	12.0000	2.6819(26)	2.9393(93)	2.9411(99)
∞		$u_{\rm tg}$ =2.6834		2.9607(88)
12	10.4612	3.1746(40)	3.5160(44)	3.5160(66)
18	10.7678	3.1747(39)	3.5280(52)	3.5278(71)
24	11.0000	3.1720(42)	3.5505(94)	3.554(11)
∞		$u_{\rm tg}$ =3.1746		3.555(10)
12	9.96090	3.4945(44)	3.9068(51)	3.9068(75)
18	10.2686	3.4943(45)	3.9500(57)	3.9502(81)

24	10.5000	3.4938(34)	3.954(11)	3.955(11)
∞		$u_{\rm tg}$ =3.4945		3.978(11)
12	9.46150	3.8881(50)	4.4249(59)	4.4249(88)
18	9.76940	3.8813(51)	4.466(10)	4.475(12)
24	10.0000	3.8903(38)	4.480(11)	4.477(12)
∞		$u_{\rm tg}$ =3.8881		4.501(14)
12	8.96290	4.3739(59)	5.0883(70)	5.088(11)
18	9.27040	4.3850(59)	5.128(17)	5.113(19)
24	9.50000	4.3831(46)	5.146(16)	5.133(17)
∞		$u_{\rm tg}$ =4.3739		5.143(20)
12	8.46430	5.0260(68)	5.9971(85)	5.997(13)
18	8.77110	5.0356(69)	6.072(15)	6.058(18)
24	9.00000	5.0237(51)	6.092(18)	6.095(20)
∞		$u_{\rm tg}$ =5.0260		6.120(22)
12	7.96630	5.9170(84)	7.337(11)	7.337(17)
18	8.27210	5.9161(85)	7.452(20)	7.453(24)
24	8.50000	5.9142(66)	7.467(25)	7.471(27)
∞		$u_{\rm tg}$ =5.9170		7.527(29)
12	7.46910	7.232(11)	9.570(17)	9.570(26)
18	7.77340	7.220(11)	9.726(31)	9.758(31)
24	8.00000	7.2322(83)	9.734(36)	9.732(37)
∞		$u_{\rm tg}$ =7.2325		9.836(39)
12	7.27130	7.943(12)	10.933(21)	10.933(31)
18	7.57350	7.927(12)	11.163(41)	11.202(41)
24	7.80000	7.9290(95)	11.210(47)	11.257(48)
∞		$u_{\rm tg}$ =7.9431		11.386(51)
12	7.07390	8.832(15)	12.975(30)	12.975(44)
18	7.37430	8.826(15)	13.185(52)	13.223(54)
24	7.60000	8.846(11)	13.370(68)	13.339(73)
∞		$u_{\rm tg}$ =8.8322		13.434(71)
12	6.87710	9.994(18)	16.148(42)	16.148(63)
18	7.17500	10.002(18)	16.596(61)	16.575(78)
24	7.40000	9.999(14)	16.599(89)	16.585(96)

∞		$u_{\rm tg}$ =9.9945		16.81(10)
12	6.48810	13.947(35)	32.17(11)	32.01(21)
18	6.77900	13.931(34)	33.29(20)	33.21(27)
24	7.00000	13.916(27)	34.00(20)	34.00(25)
∞		$u_{\rm tg}$ =13.91650		34.52(29)

Table C.1: Raw data for the lattice step scaling function $\Sigma(u)$ at the values of u tuned for the u-by-u continuum extrapolation - see sec. 4.2.1. The slight mismatch in fixing the value of u is corrected for by slightly shifting the lattice step scaling functions to a constant value $u_{\rm tg}$, leading to the values $\Sigma(u_{\rm tg})$ given in the table. We also give the continuum step scaling function obtained from the continuum extrapolations displayed in fig. 4.5.

D

Complementary plots

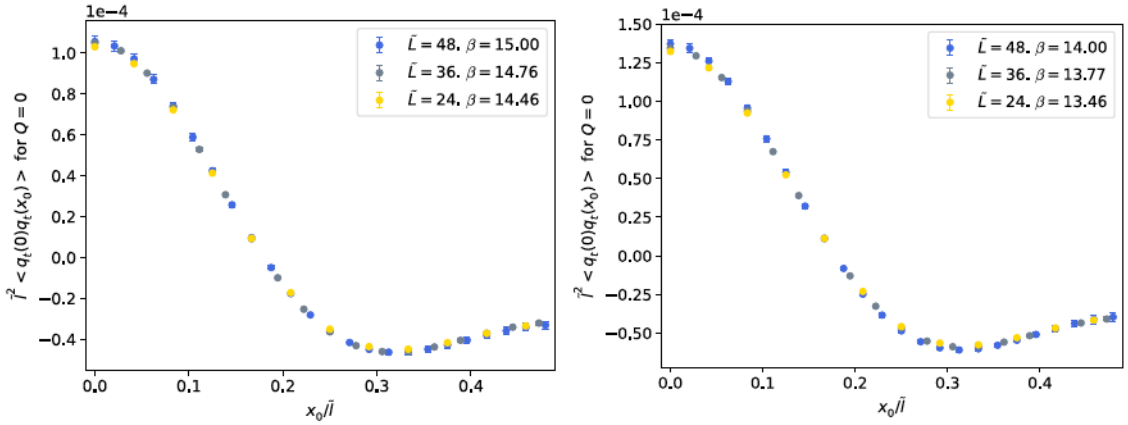

(a) $\sigma = 1.96$.

(b) $\sigma = 2.20$.

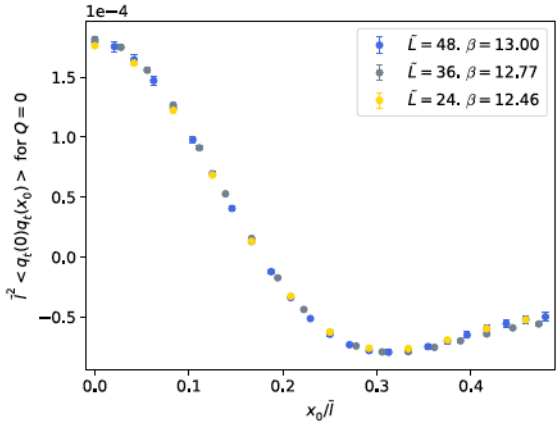

(c) $\sigma = 2.52$.

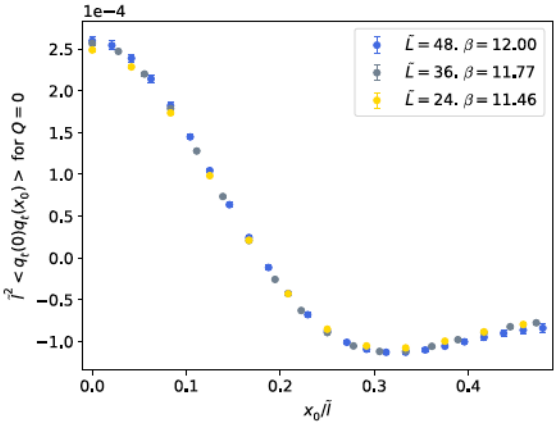

(d) $\sigma = 2.96$.

Figure D.1: Topological charge correlator for $SU(3)$ lattices. The coupling value is almost constant in all cases to those of the continuum extrapolation of tab. C.1, thus, fixing the corresponding physical volume.

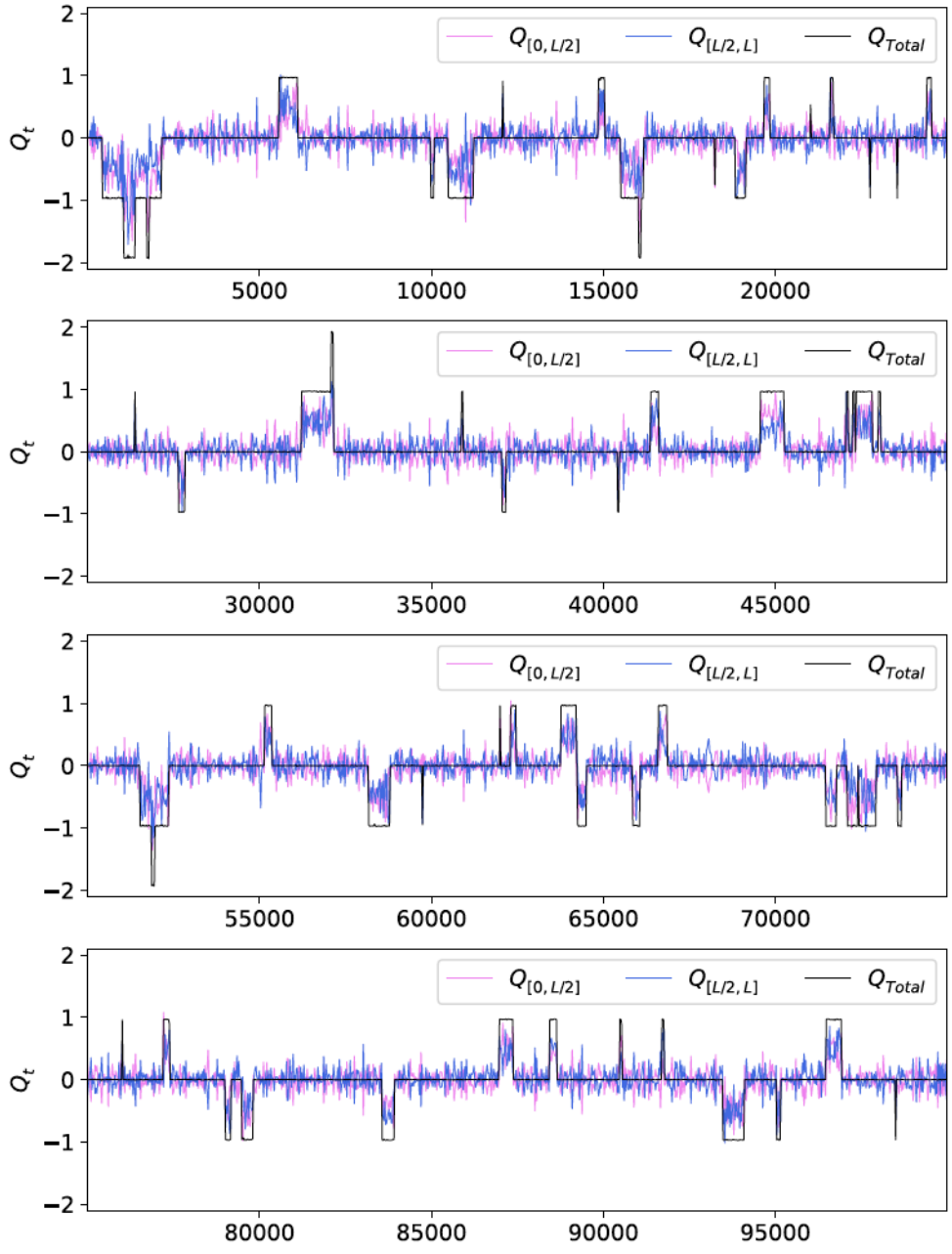

Figure D.2: Topological charge in half-boxes of size $[0, \tilde{L}/2]$ and $[\tilde{L}/2, \tilde{L}]$ for a $SU(3)$ lattice of size $\tilde{L} = 24$ and $\beta = 6.4881$.

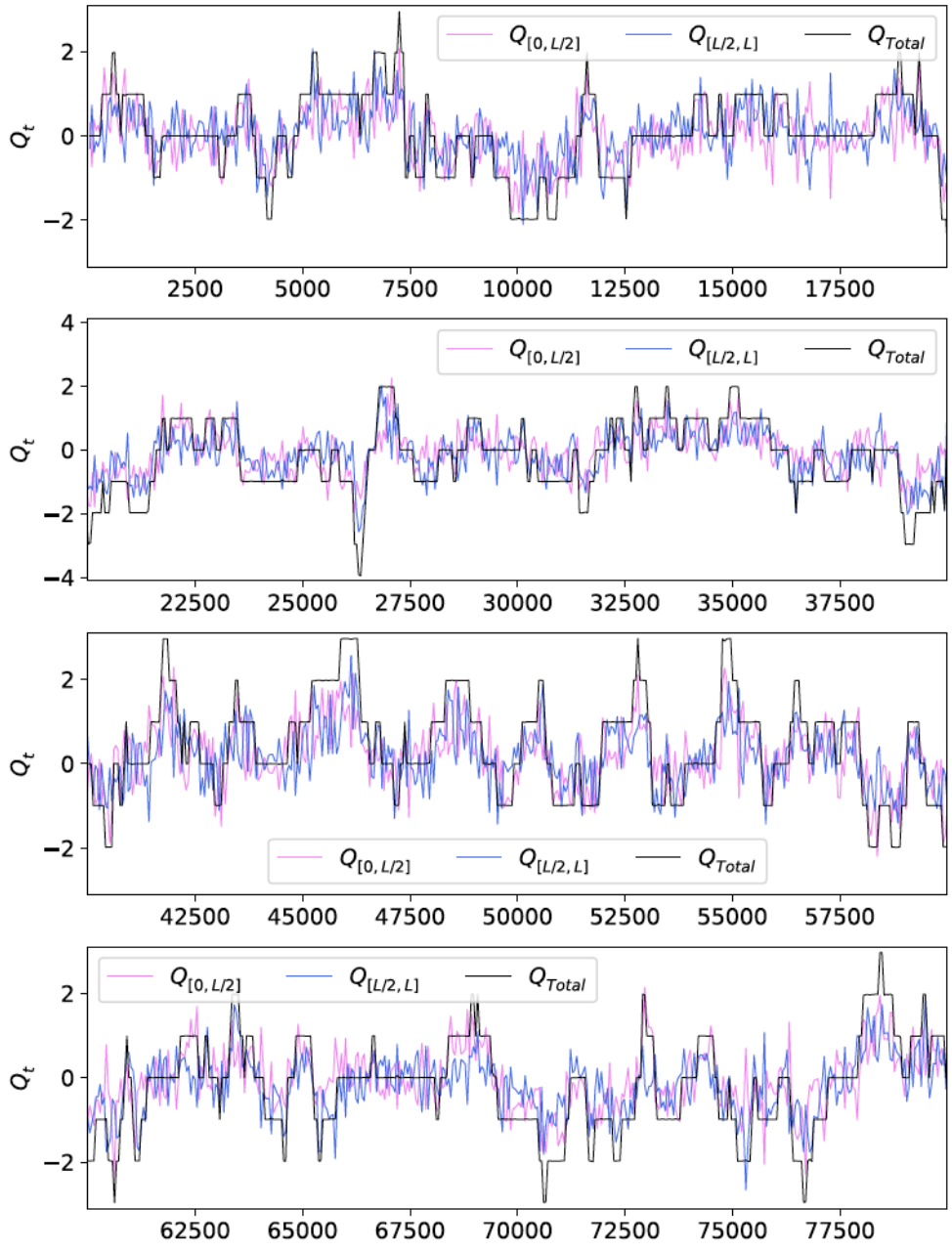

Figure D.3: Topological charge in half-boxes of size $[0, \tilde{L}/2]$ and $[\tilde{L}/2, \tilde{L}]$ for a $SU(3)$ lattice of size $\tilde{L} = 48$ and $\beta = 6.6000$.

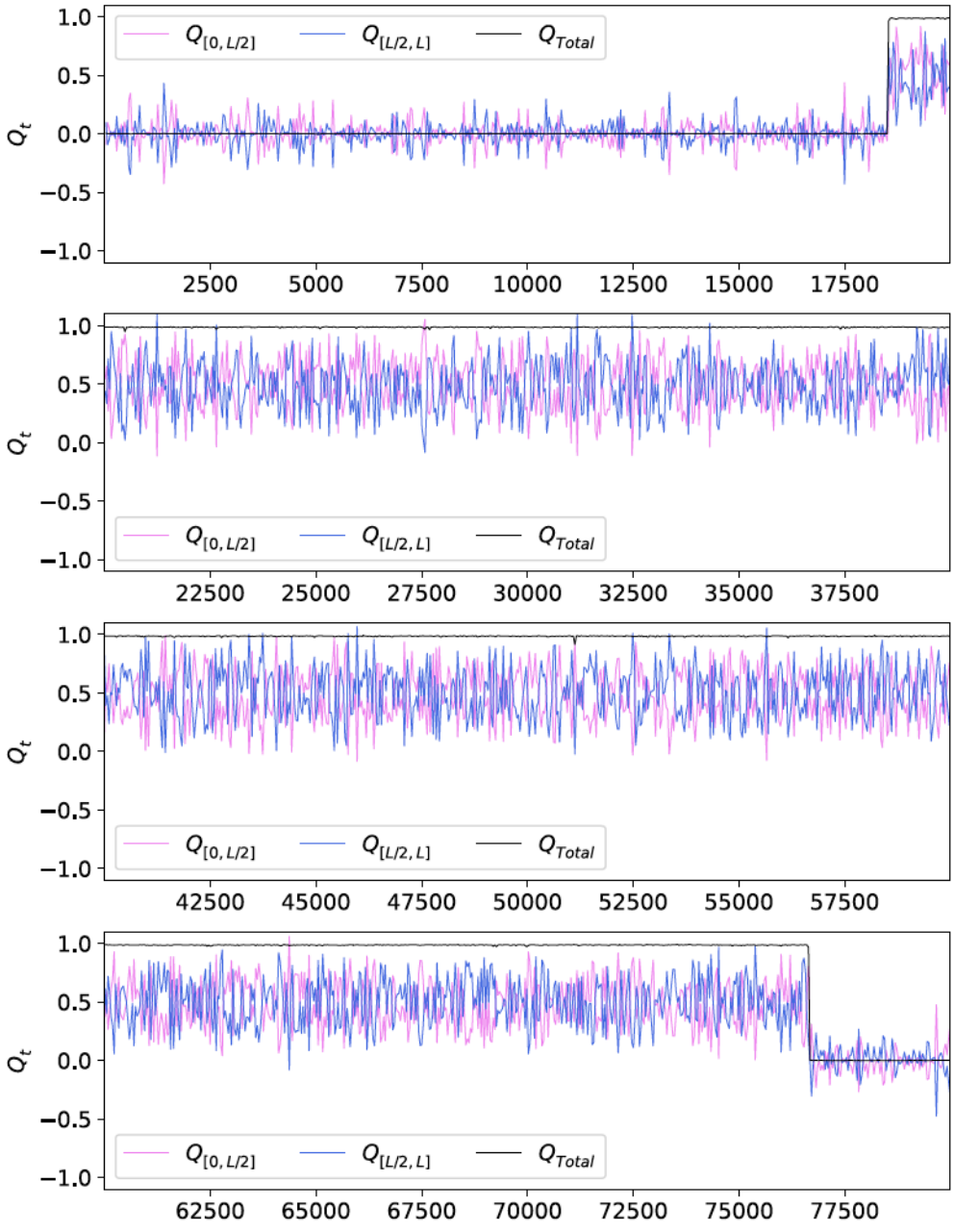

Figure D.4: Topological charge in half-boxes of size $[0, \tilde{L}/2]$ and $[\tilde{L}/2, \tilde{L}]$ for a $SU(3)$ lattice of size $\tilde{L} = 36$ and $\beta = 6.9769$.

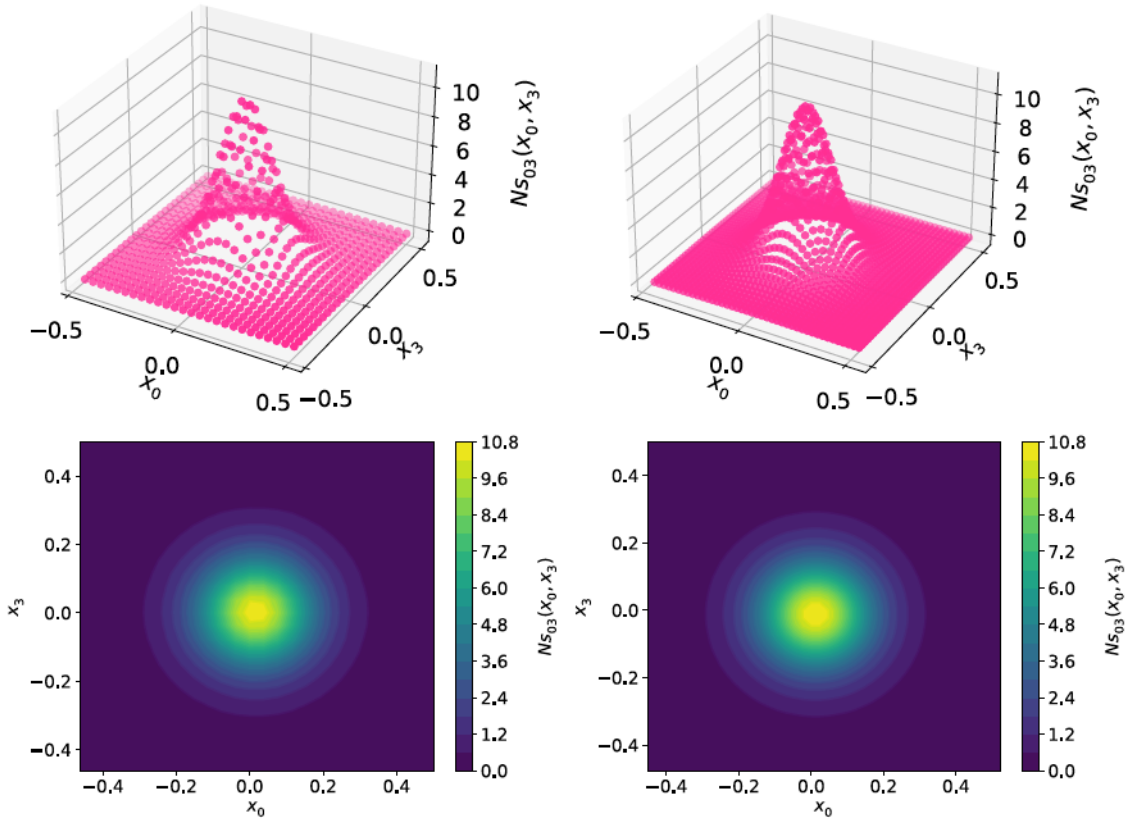

(a) $SU(13)$. (b) $SU(21)$.

Figure D.5: We display as a function of x_0/l and x_3/l the profiles obtained by integrating over x_1 and x_2 the action density of the configuration with $l_0 = l_3 = l$ ($s = 1$). Gauge groups are, from left to right: $SU(13)$ and $SU(21)$.

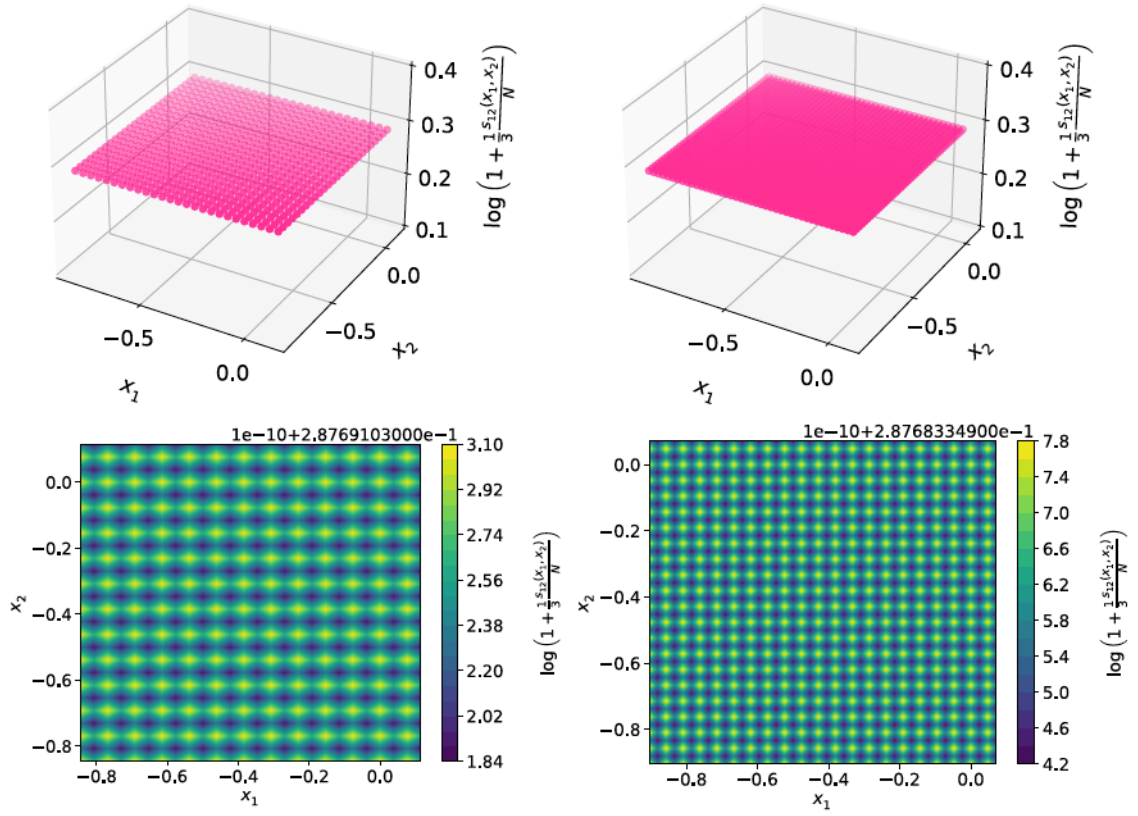

(a) $SU(13)$. (b) $SU(21)$.

Figure D.6: We display the profiles obtained by integrating the action density over x_0 and x_3 as a function of x_1/l and x_2/l. The unit of length is set by taking $l = 1$. Gauge groups are, from left to right: $SU(13)$ and $SU(21)$. For readability of the plots, the quantity displayed is $\log(1+l^2 s_{12}(x_1, x_2)/(3N))$. In the large N limit, the profiles approach the one of the constant curvature solutions, for which $\log(1 + 1/3) = 0.287682$.

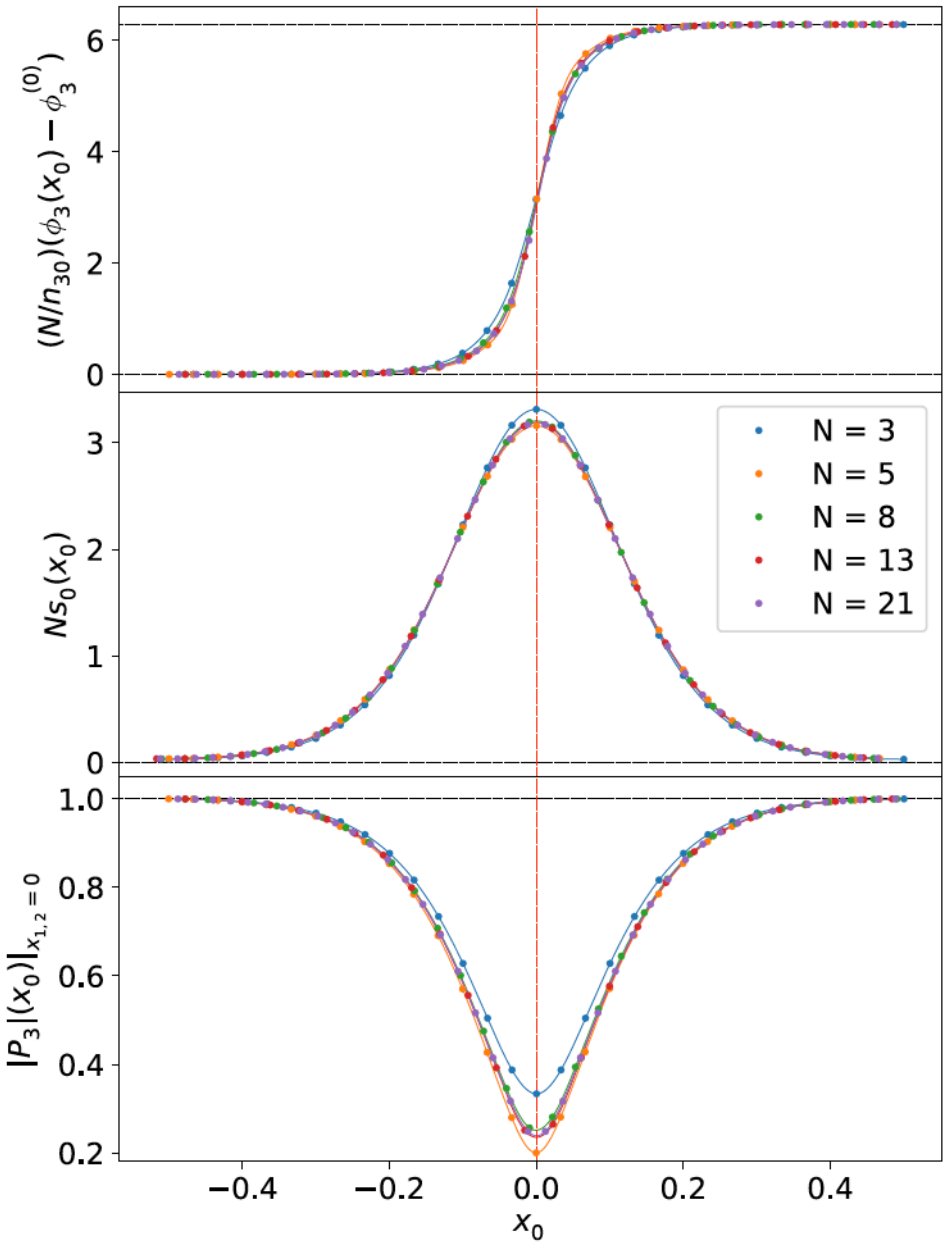

Figure D.7: For a torus of size $l_0 = l_3 = l$, we display as a function of time and from top to bottom: the phase of the Polyakov loop P_3 multiplied by N/n_{30} (after subtracting the required powers of $2\pi/N$ to have the zero phase at $x_0 = -l_0/2$), the energy-profile of the instanton, and the modulus of P_3. The phase and modulus of the Polyakov loop are evaluated at $x_1 = x_2 = 0$.

E

Matching with the SF scheme for $SU(3)$

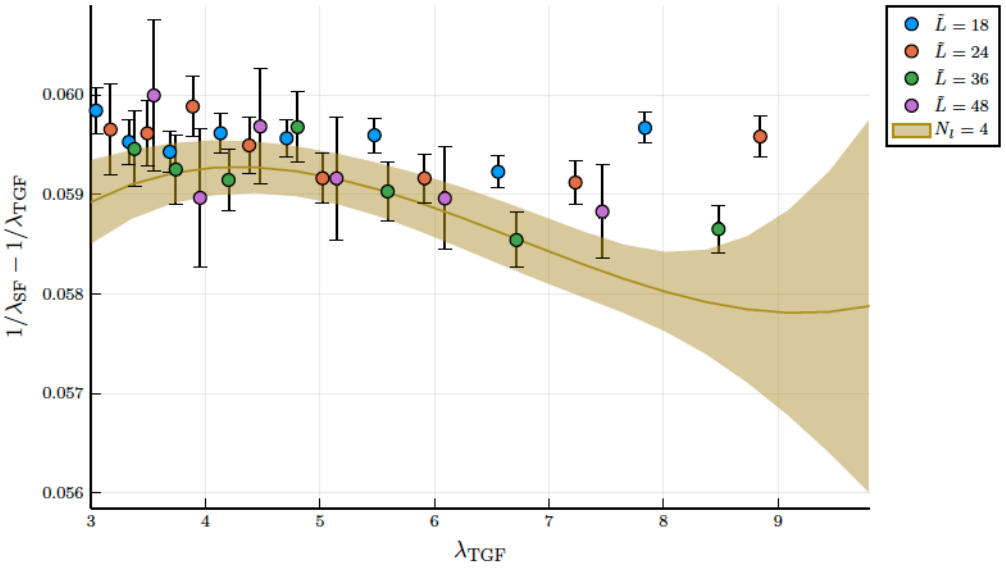

Figure E.1: Non perturbative matching between the SF and the TGF couplings. We use the available data for the SF coupling in [85]. In the fit we discard the data with $\tilde{L} = 18$, but these are plotted to show the consistency of the fit.

In order to match the values of the coupling $\lambda_{\rm TGF}(\mu)$ to the SF scheme, we use a set of simulations performed at the same values of the bare coupling but on a symmetric lattice with size $L_{\rm SF} = \tilde{L}/3$ with SF boundary conditions and an abelian background field [135]. The values of the SF coupling in these simulations can be checked in reference [85] [1].

We perform a fit, discarding the SF data with $\tilde{L} = 18$, of the form

$$\frac{1}{\lambda_{\rm SF}(\mu)} - \frac{1}{u} = \sum_{n=0}^{N_l} c_k u^k + \left(\frac{1}{\tilde{L}^2}\right) \times \sum_{n=0}^{8} \rho_k u^k \,, \tag{E.1}$$

[1] Reference [85] gives the values of the $SU(3)$ Yang-Mills coupling $\bar{g}^2_{\rm SF}$ related to the 't Hooft coupling used in our work through the standard relation: $\lambda_{\rm SF} = 3\bar{g}^2_{\rm SF}$.

where c_k are the fit coefficients and $u = \lambda_{\mathrm{TGF}}(\mu/0.9)$. The result of the fit can be seen in Figure E.1. This fit can only be trusted for $3 < \lambda_{\mathrm{TGF}} < 6$, since data on the SF scheme at higher energies is not available in the literature.

Bibliography

[1] G. 't Hooft, "A Property of Electric and Magnetic Flux in Nonabelian Gauge Theories", *Nucl. Phys. B* **153** (1979) 141–160.

[2] G. 't Hooft, "Confinement and Topology in Nonabelian Gauge Theories", *Acta Phys. Austriaca Suppl.* **22** (1980) 531–586.

[3] G. 't Hooft, "Aspects of Quark Confinement", *Phys. Scripta* **24** (1981) 841–846.

[4] T. Eguchi and H. Kawai, "Reduction of Dynamical Degrees of Freedom in the Large N Gauge Theory", *Phys. Rev. Lett.* **48** (1982) 1063.

[5] A. Gonzalez-Arroyo and M. Okawa, "The Twisted Eguchi-Kawai Model: A Reduced Model for Large N Lattice Gauge Theory", *Phys.Rev.* **D27** (1983) 2397.

[6] A. Gonzalez-Arroyo and M. Okawa, "A Twisted Model for Large N Lattice Gauge Theory", *Phys.Lett.* **B120** (1983) 174.

[7] L. Alvarez-Gaume and J. L. F. Barbon, "Morita duality and large N limits", *Nucl. Phys. B* **623** (2002) 165–200, `arXiv:hep-th/0109176`.

[8] M. García Pérez, A. González-Arroyo, and M. Okawa, "Spatial volume dependence for 2+1 dimensional SU(N) Yang-Mills theory", *JHEP* **1309** (2013) 003.

[9] M. García Pérez, A. González-Arroyo, M. Koren, and M. Okawa, "The spectrum of 2+1 dimensional Yang-Mills theory on a twisted spatial torus", *JHEP* **07** (2018) 169.

[10] F. Chamizo and A. Gonzalez-Arroyo, "Tachyonic instabilities in 2 + 1 dimensional Yang–Mills theory and its connection to number theory", *J. Phys. A* **50** no. 26, (2017) 265401.

[11] R. Narayanan and H. Neuberger, "Infinite N phase transitions in continuum Wilson loop operators", *JHEP* **0603** (2006) 064.

[12] R. Lohmayer and H. Neuberger, "Continuous smearing of Wilson Loops", *PoS* **LATTICE2011** (2011) 249.

[13] M. Lüscher, "Trivializing maps, the Wilson flow and the HMC algorithm", *Commun.Math.Phys.* **293** (2010) 899–919.

[14] M. Lüscher, "Properties and uses of the Wilson flow in lattice QCD", *JHEP* **1008** (2010) 071.

[15] G. 't Hooft, "A Planar Diagram Theory for Strong Interactions", *Nucl. Phys. B* **72** (1974) 461.

[16] B. Lucini and M. Panero, "SU(N) gauge theories at large N", *Phys. Rept.* **526** (2013) 93–163, arXiv:1210.4997 [hep-th].

[17] T. A. Ryttov and R. Shrock, "Higher-Loop Corrections to the Infrared Evolution of a Gauge Theory with Fermions", *Phys. Rev. D* **83** (2011) 056011, arXiv:1011.4542 [hep-ph].

[18] M. Mariño, "Lectures on non-perturbative effects in large N gauge theories, matrix models and strings", *Fortsch. Phys.* **62** (2014) 455–540, arXiv:1206.6272 [hep-th].

[19] G. 't Hooft, "Rigorous Construction of Planar Diagram Field Theories in Four-dimensional Euclidean Space", *Commun. Math. Phys.* **88** (1983) 1.

[20] G. 't Hooft, "Borel Summability of a Four-dimensional Field Theory", *Phys. Lett. B* **119** (1982) 369.

[21] C. B. Thorn, "On the Derivation of Dual Models from Field Theory. 2.", *Phys. Rev. D* **17** (1978) 1073.

[22] E. Brezin, C. Itzykson, G. Parisi, and J. B. Zuber, "Planar Diagrams", *Commun. Math. Phys.* **59** (1978) 35.

[23] Y. M. Makeenko and A. A. Migdal, "Exact Equation for the Loop Average in Multicolor QCD", *Phys. Lett. B* **88** (1979) 135. [Erratum: Phys.Lett.B 89, 437 (1980)].

[24] R. F. Dashen, E. E. Jenkins, and A. V. Manohar, "The 1/N(c) expansion for baryons", *Phys. Rev. D* **49** (1994) 4713, arXiv:hep-ph/9310379. [Erratum: Phys.Rev.D 51, 2489 (1995)].

[25] J. M. Maldacena, "The Large N limit of superconformal field theories and supergravity", *Adv. Theor. Math. Phys.* **2** (1998) 231–252, arXiv:hep-th/9711200.

[26] E. Witten, "The 1/N expansion in atomic and particle physics", *NATO Sci. Ser. B* **59** (1980) 403–419.

[27] Y. Makeenko, "Large N gauge theories", *NATO Sci. Ser. C* **556** (2000) 285–354, arXiv:hep-th/0001047.

[28] O. Haan, "Large N as a thermodynamic limit", *Phys. Lett. B* **106** (1981) 207–210.

[29] S. R. Coleman, "1/N", in *17th International School of Subnuclear Physics: Pointlike Structures Inside and Outside Hadrons*. 3, 1980.

[30] A. Gonzalez-Arroyo, J. Jurkiewicz, and C. P. Korthals-Altes, "Ground State Metamorphosis for Yang-Mills Fields on a Finite Periodic Lattice", 12, 1981.

[31] G. Bhanot, U. M. Heller, and H. Neuberger, "The Quenched Eguchi-Kawai Model", *Phys. Lett. B* **113** (1982) 47–50.

[32] A. Gonzalez-Arroyo and M. Okawa, "A Twisted Model for Large N Lattice Gauge Theory", *Phys. Lett. B* **120** (1983) 174–178.

[33] A. Gonzalez-Arroyo and M. Okawa, "The Twisted Eguchi-Kawai Model: A Reduced Model for Large N Lattice Gauge Theory", *Phys. Rev. D* **27** (1983) 2397.

[34] A. Gonzalez-Arroyo and M. Okawa, "Large N reduction with the Twisted Eguchi-Kawai model", *JHEP* **07** (2010) 043, arXiv:1005.1981 [hep-th].

[35] A. Gonzalez-Arroyo and M. Okawa, "The string tension from smeared Wilson loops at large N", *Phys. Lett. B* **718** (2013) 1524–1528, arXiv:1206.0049 [hep-th].

[36] A. Gonzalez-Arroyo and M. Okawa, "The string tension for Large N gauge theory from smeared Wilson loops", *PoS* **LATTICE2012** (2012) 221, arXiv:1212.3835 [hep-lat].

[37] A. Gonzalez-Arroyo and M. Okawa, "Confinement in large N gauge theories", *PoS* **ConfinementX** (2012) 277, arXiv:1303.4921 [hep-lat].

[38] G. Basar, A. Cherman, D. Dorigoni, and M. Ünsal, "Volume Independence in the Large N Limit and an Emergent Fermionic Symmetry", *Phys. Rev. Lett.* **111** no. 12, (2013) 121601, arXiv:1306.2960 [hep-th].

[39] P. Kovtun, M. Unsal, and L. G. Yaffe, "Volume independence in large N(c) QCD-like gauge theories", *JHEP* **06** (2007) 019, arXiv:hep-th/0702021.

[40] T. Azeyanagi, M. Hanada, M. Unsal, and R. Yacoby, "Large-N reduction in QCD-like theories with massive adjoint fermions", *Phys. Rev. D* **82** (2010) 125013, arXiv:1006.0717 [hep-th].

[41] B. Bringoltz, M. Koren, and S. R. Sharpe, "Large-N reduction with adjoint Wilson fermions", *PoS* **LATTICE2012** (2012) 045, arXiv:1212.0535 [hep-lat].

[42] P. Korcyl and M. Koren, "Preliminary study of two-dimensional SU(N) Yang-Mills theory with adjoint matter by Hybrid Monte Carlo approach", *PoS* **LATTICE2011** (2011) 071, arXiv:1111.4682 [hep-lat].

[43] B. Bringoltz, M. Koren, and S. R. Sharpe, "Large-N reduction with two adjoint Dirac fermions", *PoS* **LATTICE2011** (2011) 072, arXiv:1111.1059 [hep-lat].

[44] B. Bringoltz, M. Koren, and S. R. Sharpe, "Large-N reduction in QCD with two adjoint Dirac fermions", *Phys. Rev. D* **85** (2012) 094504, arXiv:1106.5538 [hep-lat].

[45] A. González-Arroyo and M. Okawa, "Twisted reduction in large N QCD with adjoint Wilson fermions", *PoS* **LATTICE2013** (2014) 099, arXiv:1311.3778 [hep-lat].

[46] M. Garcia Perez, A. Gonzalez-Arroyo, L. Keegan, and M. Okawa, "Mass anomalous dimension from large N twisted volume reduction", *PoS* **LATTICE2013** (2014) 098, arXiv:1311.2395 [hep-lat].

[47] A. González-Arroyo and M. Okawa, "Twisted space-time reduced model of large N QCD with two adjoint Wilson fermions", *Phys. Rev. D* **88** (2013) 014514, arXiv:1305.6253 [hep-lat].

[48] A. Gonzalez-Arroyo and M. Okawa, "Twisted reduction in large N QCD with two adjoint Wilson fermions", *PoS* **LATTICE2012** (2012) 046, arXiv:1210.7881 [hep-lat].

[49] L. Keegan, "Mass Anomalous Dimension at Large N", *PoS* **LATTICE2012** (2012) 044, arXiv:1210.7247 [hep-ph].

[50] R. Lohmayer and R. Narayanan, "Weak-coupling analysis of the single-site large-N gauge theory coupled to adjoint fermions", *Phys. Rev. D* **87** no. 12, (2013) 125024, arXiv:1305.1279 [hep-lat].

[51] A. Hietanen and R. Narayanan, "Numerical evidence for non-analytic behavior in the beta function of large N SU(N) gauge theory coupled to an adjoint Dirac fermion", *Phys. Rev. D* **86** (2012) 085002, arXiv:1204.0331 [hep-lat].

[52] M. Unsal and L. G. Yaffe, "Center-stabilized Yang-Mills theory: Confinement and large N volume independence", *Phys. Rev. D* **78** (2008) 065035, arXiv:0803.0344 [hep-th].

[53] D. Simic and M. Unsal, "Deconfinement in Yang-Mills theory through toroidal compactification with deformation", *Phys. Rev. D* **85** (2012) 105027, arXiv:1010.5515 [hep-th].

[54] J. Kiskis, R. Narayanan, and H. Neuberger, "Proposal for the numerical solution of planar QCD", *Phys. Rev. D* **66** (2002) 025019, arXiv:hep-lat/0203005.

[55] R. Narayanan and H. Neuberger, "Large N reduction in continuum", *Phys. Rev. Lett.* **91** (2003) 081601, arXiv:hep-lat/0303023.

[56] R. Narayanan, H. Neuberger, and F. Reynoso, "Phases of three dimensional large N QCD on a continuum torus", *Phys. Lett. B* **651** (2007) 246–252, arXiv:0704.2591 [hep-lat].

[57] R. Narayanan and H. Neuberger, "Universality of large N phase transitions in Wilson loop operators in two and three dimensions", *JHEP* **12** (2007) 066, arXiv:0711.4551 [hep-th].

[58] M. García Pérez, A. González-Arroyo, M. Koren, and M. Okawa, "The spectrum of 2+1 dimensional Yang-Mills theory on a twisted spatial torus", *JHEP* **07** (2018) 169, arXiv:1807.03481 [hep-th].

[59] Z. Guralnik and J. Troost, "Aspects of gauge theory on commutative and noncommutative tori", *JHEP* **05** (2001) 022, arXiv:hep-th/0103168.

[60] M. Unsal and L. G. Yaffe, "Large-N volume independence in conformal and confining gauge theories", *JHEP* **08** (2010) 030, arXiv:1006.2101 [hep-th].

[61] M. Garcia Perez, A. Gonzalez-Arroyo, and M. Okawa, "Volume dependence in 2+1 Yang-Mills theory", *PoS* **LATTICE2012** (2012) 219, arXiv:1211.0807 [hep-lat].

[62] M. M. Anber and M. Ünsal, "QCD in magnetic field, Landau levels and double-life of unbroken center-symmetry", *JHEP* **12** (2014) 107, arXiv:1309.4394 [hep-th].

[63] M. Garcia Perez, A. Gonzalez-Arroyo, and M. Okawa, "Perturbative analysis of twisted volume reduced theories", *PoS* **LATTICE2013** (2014) 342, arXiv:1311.3465 [hep-lat].

[64] J. Ambjorn, Y. M. Makeenko, J. Nishimura, and R. J. Szabo, "Lattice gauge fields and discrete noncommutative Yang-Mills theory", *JHEP* **05** (2000) 023, arXiv:hep-th/0004147.

[65] J. Ambjorn, Y. M. Makeenko, J. Nishimura, and R. J. Szabo, "Nonperturbative dynamics of noncommutative gauge theory", *Phys. Lett. B* **480** (2000) 399–408, arXiv:hep-th/0002158.

[66] J. Ambjorn, Y. M. Makeenko, J. Nishimura, and R. J. Szabo, "Finite N matrix models of noncommutative gauge theory", *JHEP* **11** (1999) 029, arXiv:hep-th/9911041.

[67] A. Gonzalez-Arroyo and C. P. Korthals Altes, "Reduced Model for Large N Continuum Field Theories", *Phys. Lett. B* **131** (1983) 396–398.

[68] A. Gonzalez-Arroyo, "Yang-Mills fields on the four-dimensional torus. Part 1.: Classical theory", in *Advanced Summer School on Nonperturbative Quantum Field Physics*, pp. 57–91. 6, 1997. arXiv:hep-th/9807108.

[69] G. 't Hooft, "Some Twisted Selfdual Solutions for the Yang-Mills Equations on a Hypertorus", *Commun. Math. Phys.* **81** (1981) 267–275.

[70] M. Hayakawa, "Perturbative analysis on infrared aspects of noncommutative QED on R**4", *Phys. Lett. B* **478** (2000) 394–400, arXiv:hep-th/9912094.

[71] Z. Guralnik, R. C. Helling, K. Landsteiner, and E. Lopez, "Perturbative instabilities on the noncommutative torus, Morita duality and twisted boundary conditions", *JHEP* **05** (2002) 025, arXiv:hep-th/0204037.

[72] P. van Baal, "Some Results for SU(N) Gauge Fields on the Hypertorus", *Commun. Math. Phys.* **85** (1982) 529.

[73] S. Sedlacek, "A direct method for minimizing the Yang-Mills functional over 4-manifolds", *Commun. Math. Phys.* **86** (1982) 515–527.

[74] A. González-Arroyo, "Constructing SU(N) fractional instantons", *JHEP* **02** (2020) 137, arXiv:1910.12565 [hep-th].

[75] M. Garcia Perez, A. Gonzalez-Arroyo, and B. Soderberg, "Minimum Action Solutions for SU(2) Gauge Theory on the Torus With Nonorthogonal Twist", *Phys. Lett. B* **235** (1990) 117–123.

[76] M. Garcia Perez and A. Gonzalez-Arroyo, "Numerical study of Yang-Mills classical solutions on the twisted torus", *J. Phys. A* **26** (1993) 2667–2678, arXiv:hep-lat/9206016.

[77] M. Garcia Perez, A. Gonzalez-Arroyo, A. Montero, and C. Pena, "Yang-Mills classical solutions and fermionic zero modes from lattice calculations", *Nucl. Phys. B Proc. Suppl.* **63** (1998) 501–503, arXiv:hep-lat/9709107.

[78] A. Montero, "Numerical analysis of fractional charge solutions on the torus", *JHEP* **05** (2000) 022, arXiv:hep-lat/0004009.

[79] A. Gonzalez-Arroyo, "On the fractional instanton liquid picture of the Yang-Mills vacuum and Confinement", arXiv:2302.12356 [hep-th].

[80] M. F. Atiyah and R. Bott, "The Yang-Mills equations over Riemann surfaces", *Phil. Trans. Roy. Soc. Lond. A* **308** (1982) 523–615.

[81] M. Lüscher and P. Weisz, "Perturbative analysis of the gradient flow in non-abelian gauge theories", *JHEP* **1102** (2011) 051.

[82] M. Luscher, "Chiral symmetry and the Yang–Mills gradient flow", *JHEP* **04** (2013) 123, arXiv:1302.5246 [hep-lat].

[83] M. Lüscher, "Step scaling and the Yang-Mills gradient flow", *JHEP* **1406** (2014) 105.

[84] M. Lüscher, P. Weisz, and U. Wolff, "A Numerical method to compute the running coupling in asymptotically free theories", *Nucl.Phys.* **B359** (1991) 221–243.

[85] M. Dalla Brida and A. Ramos, "The gradient flow coupling at high-energy and the scale of SU(3) Yang-Mills theory",.

[86] R. Sommer, "Scale setting in lattice QCD", *PoS* **LATTICE2013** (2014) 015, arXiv:1401.3270 [hep-lat].

[87] R. Sommer, "A New way to set the energy scale in lattice gauge theories and its applications to the static force and alpha-s in SU(2) Yang-Mills theory", *Nucl. Phys.* **B411** (1994) 839–854.

[88] **BMW** Collaboration, S. Borsanyi *et al.*, "High-precision scale setting in lattice QCD", *JHEP* **09** (2012) 010, arXiv:1203.4469 [hep-lat].

[89] M. Luscher, "Advanced lattice QCD", in *Les Houches Summer School in Theoretical Physics, Session 68: Probing the Standard Model of Particle Interactions*, pp. 229–280. 2, 1998. arXiv:hep-lat/9802029.

[90] R. Sommer, "Non-perturbative renormalization of QCD",.

[91] H. D. Politzer, "Reliable Perturbative Results for Strong Interactions?", *Phys. Rev. Lett.* **30** (1973) 1346–1349.

[92] D. J. Gross and F. Wilczek, "Ultraviolet Behavior of Nonabelian Gauge Theories", *Phys. Rev. Lett.* **30** (1973) 1343–1346.

[93] L. Del Debbio and A. Ramos, "Lattice determinations of the strong coupling",.

[94] S. Aoki *et al.*, "Precise determination of the strong coupling constant in $N_f = 2 + 1$ lattice QCD with the Schrödinger functional scheme", *JHEP* **0910** (2009) 053.

[95] M. Dalla Brida, P. Fritzsch, T. Korzec, A. Ramos, S. Sint, and R. Sommer, "Slow running of the Gradient Flow coupling from 200 MeV to 4 GeV in $N_\mathrm{f} = 3$ QCD", *Phys. Rev.* **D95** no. 1, (2017) 014507.

[96] M. Bruno, M. Dalla Brida, P. Fritzsch, T. Korzec, A. Ramos, S. Schaefer, H. Simma, S. Sint, and R. Sommer, "QCD Coupling from a Nonperturbative Determination of the Three-Flavor Λ Parameter", *Phys. Rev. Lett.* **119** no. 10, (2017) 102001.

[97] F. Tekin, R. Sommer, and U. Wolff, "The running coupling of QCD with four flavors", *Nucl.Phys.* **B840** (2010) 114–128.

[98] M. Lüscher, R. Sommer, P. Weisz, and U. Wolff, "A precise determination of the running coupling in the SU(3) Yang-Mills theory", *Nucl.Phys.* **B413** (1994) 481–502.

[99] K.-I. Ishikawa, I. Kanamori, Y. Murakami, A. Nakamura, M. Okawa, and R. Ueno, "Non-perturbative determination of the Λ-parameter in the pure SU(3) gauge theory from the twisted gradient flow coupling", *JHEP* **12** (2017) 067.

[100] E. I. Bribian and M. Garcia Perez, "The twisted gradient flow coupling at one loop", *JHEP* **03** (2019) 200, arXiv:1903.08029 [hep-lat].

[101] E. I. Bribian, M. Garcia Perez, and A. Ramos, "The twisted gradient flow running coupling in SU(3): a non-perturbative determination", in *37th International Symposium on Lattice Field Theory (Lattice 2019) Wuhan, Hubei, China, June 16-22, 2019*. 2020.

[102] E. Ibañez Bribián, *Volume (in)dependence in Yang-Mills theories*. PhD thesis, Madrid, Autonoma U., 2019.

[103] A. Ramos, "The Yang-Mills gradient flow and renormalization", *PoS* **LATTICE2014** (2015) 017.

[104] A. Gonzalez-Arroyo and M. Okawa, "Large N reduction with the Twisted Eguchi-Kawai model", *JHEP* **1007** (2010) 043.

[105] M. G. Perez, A. Gonzalez-Arroyo, and M. Okawa, "Volume independence for Yang-Mills fields on the twisted torus",.

[106] M. García Pérez, "Prospects for large N gauge theories on the lattice", *PoS* **LATTICE2019** (2020) 276, arXiv:2001.10859 [hep-lat].

[107] A. Ramos, "The gradient flow running coupling with twisted boundary conditions", *JHEP* **1411** (2014) 101.

[108] L. Keegan and A. Ramos, "(Dimensional) twisted reduction in large N gauge theories", in *Proceedings, 33rd International Symposium on Lattice Field Theory (Lattice 2015)*. 2015. https://inspirehep.net/record/1401229/files/arXiv:1510.08360.pdf.

[109] Z. Fodor, K. Holland, J. Kuti, D. Nogradi, and C. H. Wong, "The Yang-Mills gradient flow in finite volume", *JHEP* **1211** (2012) 007.

[110] Z. Fodor, K. Holland, J. Kuti, D. Nogradi, and C. H. Wong, "The gradient flow running coupling scheme",.

[111] A. Nada and A. Ramos, "An analysis of systematic effects in finite size scaling studies using the gradient flow", *Eur. Phys. J. C* **81** no. 1, (2021) 1.

[112] M. G. Pérez, A. González-Arroyo, and M. Okawa, "Perturbative contributions to Wilson loops in twisted lattice boxes and reduced models", *JHEP* **10** (2017) 150, arXiv:1708.00841 [hep-lat].

[113] M. García Pérez, A. González-Arroyo, L. Keegan, and M. Okawa, "The $SU(\infty)$ twisted gradient flow running coupling", *JHEP* **01** (2015) 038.

[114] P. Fritzsch, A. Ramos, and F. Stollenwerk, "Critical slowing down and the gradient flow coupling in the Schrödinger functional", *PoS* **Lattice2013** (2013) 461.

[115] S. Schaefer, R. Sommer, and F. Virotta, "Critical slowing down and error analysis in lattice QCD simulations", *Nucl. Phys.* **B845** (2011) 93–119.

[116] U. Wolff, "Critical Slowing Down", *Nucl. Phys. B Proc. Suppl.* **17** (1990) 93–102.

[117] U. Wolff, "Dynamics of hybrid overrelaxation in the Gaussian model", *Phys.Lett.* **B288** (1992) 166–170.

[118] M. Creutz, "Monte Carlo Study of Quantized SU(2) Gauge Theory", *Phys.Rev.* **D21** (1980) 2308–2315.

[119] K. Fabricius and O. Haan, "Heat Bath Method for the Twisted Eguchi-Kawai Model", *Phys.Lett.* **B143** (1984) 459.

[120] M. Creutz, "Overrelaxation and Monte Carlo Simulation", *Phys.Rev.* **D36** (1987) 515.

[121] U. Wolff, "Monte Carlo errors with less errors", *Comput.Phys.Commun.* **156** (2004) 143–153.

[122] A. Ramos, "Automatic differentiation for error analysis of Monte Carlo data", *Comput. Phys. Commun.* **238** (2019) 19–35.

[123] L. Del Debbio, G. M. Manca, and E. Vicari, "Critical slowing down of topological modes", *Phys.Lett.* **B594** (2004) 315–323.

[124] N. Husung, P. Marquard, and R. Sommer, "Asymptotic behavior of cutoff effects in Yang-Mills theory and in Wilson's lattice QCD",.

[125] S. Aoki *et al.*, "FLAG Review 2019",.

[126] S. Capitani, M. Lüscher, R. Sommer, and H. Wittig, "Non-perturbative quark mass renormalization in quenched lattice QCD", *Nucl.Phys.* **B544** (1999) 669–698.

[127] M. Gockeler, R. Horsley, A. C. Irving, D. Pleiter, P. E. L. Rakow, G. Schierholz, and H. Stuben, "A Determination of the Lambda parameter from full lattice QCD", *Phys. Rev.* **D73** (2006) 014513.

[128] N. Brambilla, X. Garcia i Tormo, J. Soto, and A. Vairo, "Precision determination of $r_0\Lambda_{\overline{MS}}$ from the QCD static energy", *Phys. Rev. Lett.* **105** (2010) 212001. [Erratum: Phys. Rev. Lett.108,269903(2012)].

[129] M. Asakawa, T. Hatsuda, T. Iritani, E. Itou, M. Kitazawa, and H. Suzuki, "Determination of Reference Scales for Wilson Gauge Action from Yang–Mills Gradient Flow",.

[130] M. Kitazawa, T. Iritani, M. Asakawa, T. Hatsuda, and H. Suzuki, "Equation of State for SU(3) Gauge Theory via the Energy-Momentum Tensor under Gradient Flow", *Phys. Rev.* **D94** no. 11, (2016) 114512.

[131] E. I. Bribian, M. García Pérez, and A. Ramos, "The twisted gradient flow running coupling in SU(3): a non-perturbative determination", *PoS* **LATTICE2019** (2019) 217, arXiv:2001.03735 [hep-lat].

[132] M. Dalla Brida, R. Höllwieser, F. Knechtli, T. Korzec, A. Ramos, and R. Sommer, "Non-perturbative renormalization by decoupling", *Phys. Lett. B* **807** (2020) 135571.

[133] **ALPHA** Collaboration, M. D. Brida, R. Höllwieser, F. Knechtli, T. Korzec, A. Nada, A. Ramos, S. Sint, and R. Sommer, "Results for α_s from the decoupling strategy", *PoS* **LATTICE2021** (2022) 492, arXiv:2112.09623 [hep-lat].

[134] **ALPHA** Collaboration, M. Dalla Brida, R. Höllwieser, F. Knechtli, T. Korzec, A. Nada, A. Ramos, S. Sint, and R. Sommer, "Determination of $\alpha_s(m_Z)$ by the non-perturbative decoupling method", *Eur. Phys. J. C* **82** no. 12, (2022) 1092, arXiv:2209.14204 [hep-lat].

[135] M. Lüscher, R. Narayanan, P. Weisz, and U. Wolff, "The Schrödinger Functional: a renormalizable probe for non-abelian gauge theories", *Nucl.Phys.* **B384** (1992) 168–228.

[136] P. Fritzsch and A. Ramos, "The gradient flow coupling in the Schrödinger Functional", *JHEP* **1310** (2013) 008.

[137] C. H. Wong, S. Borsanyi, Z. Fodor, K. Holland, and J. Kuti, "Toward a novel determination of the strong QCD coupling at the Z-pole", *PoS* **LATTICE2022** (2023) 043, arXiv:2301.06611 [hep-lat].

[138] A. Hasenfratz, C. T. Peterson, J. van Sickle, and O. Witzel, "Λ parameter of the SU(3) Yang-Mills theory from the continuous β function", arXiv:2303.00704 [hep-lat].

[139] E. I. Bribian, J. L. D. Golan, M. G. Perez, and A. Ramos, "Memory efficient finite volume schemes with twisted boundary conditions", *Eur. Phys. J. C* **81** no. 10, (2021) 951, arXiv:2107.03747 [hep-lat].

[140] J. L. D. Golan, M. G. Perez, and A. Ramos, "The SU(N) running coupling in the twisted gradient flow scheme and volume independence.", *PoS* **LATTICE2021** (2022) 310, arXiv:2111.13092 [hep-lat].

[141] P. A. Baikov, K. G. Chetyrkin, and J. H. K̈hn, "Five-Loop Running of the QCD coupling constant", *Phys. Rev. Lett.* **118** no. 8, (2017) 082002.

[142] A. Bode, U. Wolff, and P. Weisz, "Two loop computation of the Schrodinger functional in pure SU(3) lattice gauge theory", *Nucl. Phys.* **B540** (1999) 491–499.

[143] A. Bode, P. Weisz, and U. Wolff, "Two loop lattice expansion of the Schrodinger functional coupling in improved QCD", *Nucl. Phys. Proc. Suppl.* **83** (2000) 920–922.

[144] A. Bode, P. Weisz, and U. Wolff, "Two loop computation of the Schrodinger functional in lattice QCD", *Nucl. Phys.* **B576** (2000) 517–539. [Erratum: Nucl. Phys.B600,453(2001)].

[145] Giusti, Leonardo and Lüscher, Martin, "Topological susceptibility at $T > T_c$ from master-field simulations of the SU(3) gauge theory",.

[146] F. Knechtli, T. Korzec, B. Leder, and G. Moir, "Power corrections from decoupling of the charm quark", *Phys. Lett.* **B774** (2017) 649–655.

[147] M. Guagnelli, R. Sommer, and H. Wittig, "Precision computation of a low-energy reference scale in quenched lattice QCD", *Nucl. Phys.* **B535** (1998) 389–402.

[148] S. Necco and R. Sommer, "The N(f) = 0 heavy quark potential from short to intermediate distances", *Nucl. Phys.* **B622** (2002) 328–346.

[149] E. Witten, "Baryons in the 1/n Expansion", *Nucl. Phys. B* **160** (1979) 57–115.

[150] G. Bhanot, U. M. Heller, and H. Neuberger, "The quenched eguchi-kawai model", *Physics Letters B* **113** no. 1, (1982) 47–50. `https://www.sciencedirect.com/science/article/pii/037026938290106X`.

[151] J. Kiskis and R. Narayanan, "Computation of the string tension in three dimensional Yang-Mills theory using large N reduction", *JHEP* **09** (2008) 080, `arXiv:0807.1315 [hep-th]`.

[152] B. Lucini and M. Teper, "SU(N) gauge theories in four-dimensions: Exploring the approach to N = infinity", *JHEP* **06** (2001) 050, `arXiv:hep-lat/0103027`.

[153] A. Athenodorou and M. Teper, "SU(N) gauge theories in 3+1 dimensions: glueball spectrum, string tensions and topology", *JHEP* **12** (2021) 082, `arXiv:2106.00364 [hep-lat]`.

[154] S. Duane, A. D. Kennedy, B. J. Pendleton, and D. Roweth, "Hybrid Monte Carlo", *Phys. Lett. B* **195** (1987) 216–222.

[155] M. Creutz, *Quantum Fields on the Computer*. WORLD SCIENTIFIC, 1992. https://www.worldscientific.com/doi/abs/10.1142/1634.

[156] A. Ramos, "Playing with the kinetic term in the HMC", *PoS* **LATTICE2012** (2012) 193, arXiv:1212.3800 [hep-lat].

[157] A. S. Gambhir and K. Orginos, "Improved Sampling Algorithms in Lattice QCD", *PoS* **LATTICE2014** (2015) 043, arXiv:1506.06118 [hep-lat].

[158] M. G. Endres, R. C. Brower, W. Detmold, K. Orginos, and A. V. Pochinsky, "Multiscale Monte Carlo equilibration: Pure Yang-Mills theory", *Phys. Rev. D* **92** no. 11, (2015) 114516, arXiv:1510.04675 [hep-lat].

[159] M. Hasenbusch, "Fighting topological freezing in the two-dimensional CPN-1 model", *Phys. Rev. D* **96** no. 5, (2017) 054504, arXiv:1706.04443 [hep-lat].

[160] B. Alles, G. Boyd, M. D'Elia, A. Di Giacomo, and E. Vicari, "Hybrid Monte Carlo and topological modes of full QCD", *Phys. Lett. B* **389** (1996) 107–111, arXiv:hep-lat/9607049.

[161] P. de Forcrand, M. Garcia Perez, J. E. Hetrick, and I.-O. Stamatescu, "Topology of full QCD", *Nucl. Phys. B Proc. Suppl.* **63** (1998) 549–551, arXiv:hep-lat/9710001.

[162] L. Del Debbio, H. Panagopoulos, and E. Vicari, "theta dependence of SU(N) gauge theories", *JHEP* **08** (2002) 044, arXiv:hep-th/0204125.

[163] L. Del Debbio, H. Panagopoulos, P. Rossi, and E. Vicari, "Spectrum of confining strings in SU(N) gauge theories", *JHEP* **01** (2002) 009, arXiv:hep-th/0111090.

[164] C. Jung, "Status of dynamical ensemble generation", *PoS* **LAT2009** (2009) 002, arXiv:1001.0941 [hep-lat].

[165] C. Bernard *et al.*, "Topological susceptibility with the improved Asqtad action", *Phys. Rev. D* **68** (2003) 114501, arXiv:hep-lat/0308019.

[166] M. Luscher and S. Schaefer, "Lattice QCD without topology barriers", *JHEP* **07** (2011) 036, arXiv:1105.4749 [hep-lat].

[167] S. Schaefer, R. Sommer, and F. Virotta, "Investigating the critical slowing down of QCD simulations", *PoS* **LAT2009** (2009) 032, arXiv:0910.1465 [hep-lat].

[168] **ALPHA** Collaboration, M. Bruno, S. Schaefer, and R. Sommer, "Topological susceptibility and the sampling of field space in $N_f = 2$ lattice QCD simulations", *JHEP* **08** (2014) 150, arXiv:1406.5363 [hep-lat].

[169] S. Mages, B. C. Toth, S. Borsanyi, Z. Fodor, S. D. Katz, and K. K. Szabo, "Lattice QCD on nonorientable manifolds", *Phys. Rev. D* **95** (2017) 094512, arXiv:1512.06804 [hep-lat].

[170] N. Husung, M. Koren, P. Krah, and R. Sommer, "SU(3) Yang Mills theory at small distances and fine lattices", *EPJ Web Conf.* **175** (2018) 14024, arXiv:1711.01860 [hep-lat].

[171] C. Bonanno, C. Bonati, and M. D'Elia, "Large-N $SU(N)$ Yang-Mills theories with milder topological freezing", *JHEP* **03** (2021) 111, arXiv:2012.14000 [hep-lat].

[172] C. Bonanno, M. D'Elia, B. Lucini, and D. Vadacchino, "Towards glueball masses of large-N SU(N) pure-gauge theories without topological freezing", *Phys. Lett. B* **833** (2022) 137281, arXiv:2205.06190 [hep-lat].

[173] C. Bonanno, M. D'Elia, B. Lucini, and D. Vadacchino, "Towards glueball masses of large-N SU(N) Yang-Mills theories without topological freezing via parallel tempering on boundary conditions", *PoS* **LATTICE2022** (2023) 392, arXiv:2210.07622 [hep-lat].

[174] D. Albandea, P. Hernández, A. Ramos, and F. Romero-López, "Topological sampling through windings",.

[175] E. Witten, "Current Algebra Theorems for the U(1) Goldstone Boson", *Nucl. Phys. B* **156** (1979) 269–283.

[176] G. Veneziano, "U(1) Without Instantons", *Nucl. Phys. B* **159** (1979) 213–224.

[177] M. CĂ¨, C. Consonni, G. P. Engel, and L. Giusti, "Non-Gaussianities in the topological charge distribution of the SU(3) Yang–Mills theory", *Phys. Rev.* **D92** no. 7, (2015) 074502.

[178] S. Coleman, *Aspects of symmetry*. Cambridge University Press, 1985.

[179] M. Garcia Perez *et al.*, "Instanton like contributions to the dynamics of Yang-Mills fields on the twisted torus", *Phys. Lett. B* **305** (1993) 366–374.

[180] M. Garcia Perez, A. Gonzalez-Arroyo, and P. Martinez, "From perturbation theory to confinement: How the string tension is built up", *Nucl. Phys. B Proc. Suppl.* **34** (1994) 228–230.

[181] A. Gonzalez-Arroyo, P. Martinez, and A. Montero, "Gauge invariant structures and confinement", *Phys. Lett. B* **359** (1995) 159–165.

[182] A. Gonzalez-Arroyo and P. Martinez, "Investigating Yang-Mills theory and confinement as a function of the spatial volume", *Nucl. Phys. B* **459** (1996) 337–354.

[183] M. Garcia Perez, A. Gonzalez-Arroyo, and A. Sastre, "From confinement to adjoint zero-modes", *eCONF* **C0906083** (2009) 06.

[184] P. van Baal, "Twisted Boundary Conditions: A Nonperturbative Probe for Pure Nonabelian Gauge Theories", other thesis, 7, 1984. https://inis.iaea.org/collection/NCLCollectionStore/_Public/16/023/16023246.pdf?r=1&r=1.

[185] P. van Baal, "QCD in a finite volume", arXiv:hep-ph/0008206.

[186] M. Ünsal, "Strongly coupled QFT dynamics via TQFT coupling", *JHEP* **11** (2021) 134, arXiv:2007.03880 [hep-th].

[187] T. R. Morris, D. A. Ross, and C. T. Sachrajda, "Higher Order Quantum Corrections in the Presence of an Instanton Background Field", *Nucl. Phys. B* **255** (1985) 115–148.

[188] M. Luscher, "A New Method to Compute the Spectrum of Low Lying States in Massless Asymptotically Free Field Theories", *Phys. Lett. B* **118** (1982) 391–394.

[189] M. Luscher, "Some Analytic Results Concerning the Mass Spectrum of Yang-Mills Gauge Theories on a Torus", *Nucl. Phys. B* **219** (1983) 233–261.

[190] A. Gonzalez Arroyo and C. P. Korthals Altes, "The Spectrum of Yang-Mills Theory in a Small Twisted Box", *Nucl. Phys. B* **311** (1988) 433–449.

[191] D. Daniel, A. Gonzalez-Arroyo, C. P. Korthals Altes, and B. Soderberg, "Energy Spectrum of SU(2) Yang-Mills Fields With Space - Like Symmetric Twist", *Phys. Lett. B* **221** (1989) 136–142.

[192] **RTN** Collaboration, M. Garcia Perez *et al.*, "Instanton like contributions to the dynamics of Yang-Mills fields on the twisted torus", *Phys. Lett. B* **305** (1993) 366–374, arXiv:hep-lat/9302007.

[193] A. Gonzalez-Arroyo and P. Martinez, "Investigating Yang-Mills theory and confinement as a function of the spatial volume", *Nucl. Phys. B* **459** (1996) 337–354, arXiv:hep-lat/9507001.

[194] A. Gonzalez-Arroyo, P. Martinez, and A. Montero, "Gauge invariant structures and confinement", *Phys. Lett. B* **359** (1995) 159–165, arXiv:hep-lat/9507006.

[195] A. Gonzalez-Arroyo and A. Montero, "Do classical configurations produce confinement?", *Phys. Lett. B* **387** (1996) 823–828, arXiv:hep-th/9604017.

[196] E. Itou, "Fractional instanton of the SU(3) gauge theory in weak coupling regime", *JHEP* **05** (2019) 093, arXiv:1811.05708 [hep-th].

[197] M. Garcia Perez, A. Gonzalez-Arroyo, and M. Okawa, "Volume independence for Yang–Mills fields on the twisted torus", *Int. J. Mod. Phys. A* **29** no. 25, (2014) 1445001, arXiv:1406.5655 [hep-th].

[198] J. Dasilva Golán and M. García Pérez, "SU(N) fractional instantons and the Fibonacci sequence", *JHEP* **12** (2022) 109, arXiv:2208.07133 [hep-th].

[199] J. L. Dasilva Golan and M. Garcia Perez, "SU(N) fractional instantons", *PoS* **LATTICE2022** (2023) 394, arXiv:2212.01264 [hep-th].

[200] M. Garcia Perez, A. Gonzalez-Arroyo, and A. Sastre, "From confinement to adjoint zero-modes", *eCONF* **C0906083** (2009) 06, arXiv:1003.5022 [hep-th].

[201] M. García Pérez, A. González-Arroyo, and M. Okawa, "Spatial volume dependence for 2+1 dimensional SU(N) Yang-Mills theory", *JHEP* **09** (2013) 003, arXiv:1307.5254 [hep-lat].

[202] J. Groeneveld, J. Jurkiewicz, and C. P. Korthals Altes, "Twist as a Probe for Phase Structure", *Phys. Scripta* **23** (1981) 1022.

[203] J. Ambjorn and H. Flyvbjerg, "'T Hooft's non-Abelian magnetic flux has zero classical energy", *Phys. Lett. B* **97** (1980) 241–245.

[204] A. Gonzalez-Arroyo and A. Montero, "Selfdual vortex - like configurations in SU(2) Yang-Mills theory", *Phys. Lett. B* **442** (1998) 273–278, arXiv:hep-th/9809037.

[205] A. Montero, "SU(3) vortex - like configurations in the maximal center gauge", *Nucl. Phys. B Proc. Suppl.* **83** (2000) 518–520, arXiv:hep-lat/9907024.

[206] A. Montero, "Vortex configurations in the large N limit", *Phys. Lett. B* **483** (2000) 309–314, arXiv:hep-lat/0004002.

[207] M. Garcia Perez, A. Gonzalez-Arroyo, J. R. Snippe, and P. van Baal, "Instantons from over - improved cooling", *Nucl. Phys. B* **413** (1994) 535–552, arXiv:hep-lat/9309009.

[208] M. Garcia Perez, A. Gonzalez-Arroyo, and C. Pena, "Perturbative construction of selfdual configurations on the torus", *JHEP* **09** (2000) 033, arXiv:hep-th/0007113.

[209] "NIST Digital Library of Mathematical Functions", http://dlmf.nist.gov/, elease 1.1.6 of 2022-06-30.